

**DEVELOPMENT OF PROGRAMMABLE PEPTIDE CONSTRUCTS FOR  
CONTROLLING THE ASSEMBLY ARCHITECTURE AND PROPERTIES OF GOLD  
NANOPARTICLE SUPERSTRUCTURES AND SOFT MATERIALS**

by

**Andrea D. Merg**

B.S., Winthrop University, 2010

Submitted to the Graduate Faculty of

The Kenneth P. Dietrich School of Arts and Sciences in partial fulfillment

of the requirements for the degree of

Doctor of Philosophy

University of Pittsburgh

2017

UNIVERSITY OF PITTSBURGH  
KENNETH P. DIETRICH SCHOOL OF ARTS AND SCIENCES

This dissertation was presented

by

Andrea D. Merg

It was defended on

April 26<sup>th</sup>, 2017

and approved by

Stephen G. Weber, PhD, Professor, Department of Chemistry

W. Seth Horne, PhD, Associate Professor, Department of Chemistry

Patrick C. A. van der Wel, PhD, Associate Professor, Department of Structural Biology

Dissertation Advisor: Nathaniel L. Rosi, PhD, Professor, Department of Chemistry

Copyright © by Andrea D. Merg

2017

**DEVELOPMENT OF PROGRAMMABLE PEPTIDE CONSTRUCTS FOR  
CONTROLLING THE ASSEMBLY ARCHITECTURE AND PROPERTIES OF  
GOLD NANOPARTICLE SUPERSTRUCTURES AND SOFT MATERIALS**

Andrea D. Merg, PhD

University of Pittsburgh, 2017

This dissertation describes advances in the development of peptide-based methods for assembling nanomaterials. The aim of my work is four-fold: 1) develop methods to rationally tune the metrics of gold nanoparticle superstructures; 2) develop approaches to post-synthetically modify and stabilize gold nanoparticle superstructures; 3) develop an understanding of the underlying peptide assembly scaffold and how it dictates the final nanoparticle assembly architecture; and 4) develop new hybrid materials with peptide conjugate molecules having programmable R-groups.

Specifically, in Chapter 2 I describe methods to tune the assembly of double-helical gold nanoparticle superstructures by modulating the sterics and hydrophobicity of a family of new peptide conjugate molecules. I show that I can tune the assembly metrics of double helices including pitch, nanoparticle size, and interhelical distance. Chapter 3 describes the construction of single-helical gold nanoparticle superstructures that exhibit intense chiroptical activity. I examine their underlying peptide assembly structure and arrive at a molecular-level understanding of their assembly and how it relates to the chiral nanoparticle superstructure. In Chapter 4, I demonstrate a straightforward approach to rationally tune the metrics of hollow spherical gold nanoparticle superstructures including nanoparticle coverage density and sphere diameters. I further demonstrate that their assembly can be stabilized post-synthetically via ligand exchange. Finally, in Chapter 5 I design new peptide conjugate building blocks composed



of peptides and oligonucleotides interlinked by a hydrophobic organic core. I outline design rules that govern their assembly and show that their assembly morphology can be rationally predicted and altered.

## TABLE OF CONTENTS

<b>1.0</b>	<b>INTRODUCTION.....</b>	<b>1</b>
<b>1.1</b>	<b>SELF-ASSEMBLY IN NATURE.....</b>	<b>1</b>
<b>1.2</b>	<b>SELF-ASSEMBLY OF METALLIC NANOPARTICLES.....</b>	<b>3</b>
<b>1.2.1</b>	<b>Properties of metallic nanoparticles and their assemblies.....</b>	<b>3</b>
<b>1.2.2</b>	<b>Biomolecule-directed assembly of metallic nanoparticles.....</b>	<b>5</b>
<b>1.3</b>	<b>PEPTIDE-BASED METHOD FOR ASSEMBLING NANOPARTICLE SUPERSTRUCTURES.....</b>	<b>7</b>
<b>1.3.1</b>	<b>Assembly and substrate-binding properties of peptides.....</b>	<b>7</b>
<b>1.3.2</b>	<b>Methodology background.....</b>	<b>11</b>
<b>1.3.3</b>	<b>Chiroptical properties of helical nanoparticle superstructures.....</b>	<b>13</b>
<b>1.4</b>	<b>OBJECTIVES AND OUTLINES.....</b>	<b>14</b>
<b>2.0</b>	<b>ADJUSTING THE METRICS OF 1D HELICAL GOLD NANOPARTICLE SUPERSTRUCTURES USING MULTIVALENT PEPTIDE CONJUGATES.....</b>	<b>16</b>
<b>2.1</b>	<b>INTRODUCTION.....</b>	<b>16</b>
<b>2.2</b>	<b>RESULTS AND DISCUSSION.....</b>	<b>18</b>
<b>2.2.1</b>	<b>Soft assembly of peptide conjugates.....</b>	<b>20</b>
<b>2.2.2</b>	<b>Nanoparticle assembly studies.....</b>	<b>26</b>
<b>2.3</b>	<b>CONCLUSION.....</b>	<b>33</b>

<b>2.4</b>	<b>EXPERIMENTAL SECTION.....</b>	<b>34</b>
2.4.1	General methods and instrumentations .....	34
2.4.2	Preparation of peptide conjugates .....	36
2.4.3	Preparation of soft assemblies .....	37
2.4.4	Preparation of nanoparticle assemblies.....	37
<b>3.0</b>	<b>PEPTIDE-DIRECTED ASSEMBLY OF SINGLE-HELICAL GOLD NANOPARTICLE SUPERSTRUCTURES EXHIBITING INTENSE CHIROPTICAL ACTIVITY.....</b>	<b>38</b>
<b>3.1</b>	<b>INTRODUCTION .....</b>	<b>38</b>
<b>3.2</b>	<b>RESULTS AND DISCUSSION .....</b>	<b>40</b>
3.2.1	Single helix synthesis and chiroptical properties.....	40
3.2.2	Peptide conjugate assembly studies .....	43
3.2.3	Single helix assembly model.....	51
<b>3.3</b>	<b>CONCLUSION .....</b>	<b>53</b>
<b>3.4</b>	<b>EXPERIMENTAL SECTION.....</b>	<b>54</b>
3.4.1	General materials and methods.....	54
3.4.2	Preparation of $N_3$ -PEP <sub>Au</sub> <sup>M-ox</sup> .....	55
3.4.3	Preparation of C <sub>18</sub> -(PEP <sub>Au</sub> <sup>M-ox</sup> ) <sub>2</sub> .....	55
3.4.4	Preparation of single helices .....	56
3.4.5	Preparation of C <sub>18</sub> -(PEP <sub>Au</sub> <sup>M-ox</sup> ) <sub>2</sub> fibers .....	56
3.4.6	Cryogenic electron tomography and 3D reconstruction.....	56
3.4.7	Atomic force microscopy.....	57
3.4.8	Circular dichroism spectroscopy .....	57

3.4.9	Powder X-ray diffraction.....	58
3.4.10	MAS solid-state NMR spectroscopy .....	58
4.0	<b>POST-SYNTHETIC SURFACE MODIFICATION OF HOLLOW SPHERICAL GOLD NANOPARTICLE SUPERSTRUCTURES WITH TUNABLE ASSEMBLY METRICS.....</b>	<b>60</b>
4.1	<b>INTRODUCTION .....</b>	<b>60</b>
4.2	<b>RESULTS AND DISCUSSION .....</b>	<b>62</b>
4.2.1	Monitoring the assembly formation of HSAuNP superstructures.....	62
4.2.2	Ligand-capped nanoparticle superstructures.....	66
4.3	<b>CONCLUSION AND FUTURE WORK.....</b>	<b>70</b>
4.4	<b>EXPERIMENTAL SECTION.....</b>	<b>71</b>
4.4.1	General materials and methods.....	71
4.4.2	Assembly of HSAuNP superstructures.....	72
4.4.3	PEP <sub>Au</sub> -capped HSAuNP superstructures .....	72
4.4.4	Proteinase K stability studies.....	73
4.4.5	Thiol-capped HSAuNP superstructures.....	73
5.0	<b>PEPTIDE-OLIGONUCLEOTIDE CHIMERAS (POCS): PROGRAMMABLE BIOMOLECULAR CONSTRUCTS FOR THE ASSEMBLY OF MORPHOLOGICALLY-TUNABLE SOFT MATERIALS .....</b>	<b>74</b>
5.1	<b>INTRODUCTION .....</b>	<b>74</b>
5.2	<b>RESULTS AND DISCUSSION .....</b>	<b>75</b>
5.3	<b>CONCLUSION .....</b>	<b>84</b>
5.4	<b>EXPERIMENTAL SECTION.....</b>	<b>85</b>

5.4.1	General materials and methods.....	85
5.4.2	Preparation of O <sub>18</sub> -N <sub>3</sub> and O <sub>6</sub> -N <sub>3</sub> .....	86
5.4.3	Attachment of azido-modified oligonucleotide to diacetylene biphenyl organic core .....	87
5.4.4	Attachment of azido-modified peptide .....	88
5.4.5	POC assembly protocol.....	89
5.4.6	Preparation of DNA-functionalized gold nanoparticles.....	89
5.4.7	Addition of DNA-functionalized gold nanoparticles to PO <sub>18</sub> C vesicles and PO <sub>6</sub> C fibers .....	90
APPENDIX A .....		91
APPENDIX B .....		126
APPENDIX C .....		138
APPENDIX D.....		139
BIBLIOGRAPHY .....		152

## LIST OF TABLES

Table 1.1. Family of 12 peptide conjugate molecules with varying number of peptide head groups and varying aliphatic tail lengths .....	20
Table S3.2 Detailed experimental conditions of the MAS ssNMR experiments. Abbreviations: NS, number of scans; Set Temp, set temperature of cooling gas; MAS, magic angle spinning rate; RD, recycle delay; TPPM, two-pulse phase-modulated <sup>1</sup> H decoupling power during evolution and acquisition. ....	137

## LIST OF FIGURES

Figure 1.1. Several different natural supramolecular protein assemblies. Ring proteins: (a) the  $\beta$ -clamp of *E. coli* (PDB:2POL); (b) the proliferating cell nuclear antigen PCNA of *H. sapiens* (PDB:1AXC); (c) bacteriophage T7 gp4 helicase (PDB:1E0K); (d) bacteriophage  $\lambda$  exonuclease (PDB: 1AVQ); (e) TRAP (PDB: 1QAW); (f) RAD52 (PDB: 1KN0). Non-covalent catenane proteins: (a) RecR (PDB: 1VDD); (b) Cys168Ser variant of Prx III (PDB: 1ZYE); (c) class 1a RNR (PDB: 4ERP); (d) CS<sub>2</sub> hydrolase (PDB:3TEO). Tubular protein assemblies: (k) TMV (PDB: 4UDV). (l)  $\alpha$ -hemolysin pore complex (PDB: 7AHL); (m) anthrax protective antigen pore (PDB: 3J9C); (n) PhiX174 bacteriophage tail (PDB: 4JPP); (o) Hcp1 from *P. aeruginosa* (PDB: 1Y12). Protein cages: (a) maxi-ferritin (PDB: 1BFR); (q) mini-ferritin (PDB:1DPS); (r) superimposition of ribbon structures of mini-ferritin (light) and maxi-ferritin (dark); (s) a surface view of the rat vault shell (PDB: 4HL8); (t) ribbon structure of the major vault protein monomer, showing the structural repeat domains (green), the shoulder domain (blue), the cap-helix domain (red), and the cap-ring domain (magenta); (u) surface-structure of triskelion and zoom showing the  $\alpha$ -helical zigzags (PDB: 1XI4); (v) structure of hexagonal barrel. (All figures adapted from ref. 1)..... 2

Figure 1.2. Tunable optical properties of gold nanorods by changing their aspect ratios. (a) Gold nanorods of different aspect ratios exhibit different dimensions as observed by TEM. (b)

Different colors and (c) different LSPR wavelengths associated with colloidal solutions of nanorods of different aspect ratios. (Adapted from ref. 3) ..... 4

Figure 1.3. Examples of biomolecule-directed assemblies of metallic nanoparticles. (a) 3D crystalline nanoparticle superlattices assembled from DNA-functionalized nanoparticles (adapted from ref. 22). (b) Gold nanoparticles decorated onto a tobacco mosaic virus scaffold (adapted from ref. 36). (c) End-to-end assembly of gold nanorods using streptavidin/biotin linkages (adapted from ref. 34). ..... 6

Figure 1.4. Various structures assembled from peptides and peptide conjugates. (a) AFM images of KFE8 helical assemblies in aqueous solution (adapted from ref. 41). (b) TEM image of vesicles assembled from BP-A<sub>2</sub>-PEP<sub>Au</sub> (BP = biphenyl, A = alanine) (adapted from ref. 59). (c) TEM and SEM (inset) image of nanotubes assembled from N-lauroyl-Aβ(16-22) assembled in 40% CH<sub>3</sub>CN/water with 0.1% trifluoroacetic acid for 1-2 weeks (adapted from ref. 38). (d) Assembly scheme and TEM image of nanosheets assembled from alpha-helical peptides (scale bar = 200 nm; adapted from ref. 45). ..... 8

Figure 1.5. (a) Molecular structures and schematic representation of isomeric peptide amphiphiles. (b-e) Cryo-TEM images of a variety of 1D nanostructures formed by the designed peptides in water after 2 weeks of incubation at room temperature: (b) nanobelts of VEVE; (c) rigid cylindrical nanofibers of VVEE; (d) twisted nanoribbons of EVEV; and (e) flexible and entangled nanofibers of EEVV. (Adapted from ref. 48)..... 9

Figure 1.6. Biomimetic approach to the predictable synthesis of shaped nanocrystals. (a) Schematic illustration of face-specific peptide sequence selection and nanocrystal synthesis: Pt-[100] binding peptide sequence T7 and Pt-[111] binding peptide sequence S7 are selected against [100] faceted and [111] faceted substrates; (b) facet-specific peptides are used to direct the



synthesis of platinum nanocrystal cubes and tetrahedra, respectively. (c) TEM images (scale bar = 20 nm) of platinum nanocrystals obtained in the presence of (c) T7, (d) S7, and (e) BP7A (a peptide previously selected against bulk platinum polycrystalline surfaces). (f) TEM image (scale bar = 20 nm) of platinum nanocrystals obtained in the absence of peptides. All samples were conducted under the same conditions and collected after reacting for 10 min. (Adapted from ref. 56)..... 10

Figure 1.7. Left-handed gold nanoparticle double helices are synthesized and assembled directly in a reaction containing HEPES buffer solutions of chloroauric acid and C<sub>12</sub>-PEP<sub>Au</sub>. TEM image and electron tomography data of the double-helical gold nanoparticle superstructure are shown. (Adapted from ref. 25) ..... 11

Figure 1.8. The peptide conjugate and the various modifications for tuning its assembly..... 12

Figure 1.9. Circular dichroism spectra for left- and right-handed gold nanoparticle double helices (blue and red line, respectively) and the 3D surface rendering of the tomographic volumes revealing the left- and right-handed nature of the double helices are shown. (Adapted from ref. 61) ..... 13

Figure 2.10. (a) Peptide conjugate consisting of a peptide headgroup and an aliphatic chain; (b) peptide conjugates associate in an end-to-end fashion via hydrophobic interactions between aliphatic tails and amino acid side chain interactions between peptide headgroups; (c) assembly scheme illustrating the assembly of twisted fibers from peptide conjugate building blocks (fiber width, w, and fiber thickness, d, are indicated). ..... 18

Figure 2.11. Negatively stained TEM images of the peptide conjugate soft assemblies as a function of peptide valency and aliphatic chain length (scale bar = 100 nm): (a) C<sub>12</sub>-(PEP<sub>Au</sub>)<sub>1</sub>, (b) C<sub>14</sub>-(PEP<sub>Au</sub>)<sub>1</sub>, (c) C<sub>16</sub>-(PEP<sub>Au</sub>)<sub>1</sub>, (d) C<sub>18</sub>-(PEP<sub>Au</sub>)<sub>1</sub>, (e) C<sub>12</sub>-(PEP<sub>Au</sub>)<sub>2</sub>, (f) C<sub>14</sub>-(PEP<sub>Au</sub>)<sub>2</sub>, (g) C<sub>16</sub>-

(PEPAu)<sub>2</sub>, (h) C<sub>18</sub>-(PEPAu)<sub>2</sub>, (i) C<sub>12</sub>-(PEPAu)<sub>3</sub>, (j) C<sub>14</sub>-(PEPAu)<sub>3</sub>, (k) C<sub>16</sub>-(PEPAu)<sub>3</sub>, and (l) C<sub>18</sub>-(PEPAu)<sub>3</sub>. ..... 22

Figure 2.12. Nanofiber width distribution for (a) C<sub>12</sub>-(PEPAu)<sub>1</sub>, 12.6 ± 1.3 nm based on 60 counts; (b) C<sub>14</sub>-(PEPAu)<sub>1</sub>, 12.1 ± 1.7 nm based on 70 counts; (c) C<sub>16</sub>-(PEPAu)<sub>1</sub>, 12.6 ± 1.1 nm based on 100 counts; (d) C<sub>18</sub>-(PEPAu)<sub>1</sub>, 13.8 ± 1.1 nm based on 100 counts; (e) C<sub>14</sub>-(PEPAu)<sub>2</sub>, 8.9 ± 0.9 nm based on 70 counts; (f) C<sub>16</sub>-(PEPAu)<sub>2</sub>, 9.3 ± 1.2 nm based on 100 counts; and (g) C<sub>18</sub>-(PEPAu)<sub>2</sub>, 8.3 ± 0.9 nm based on 100 counts..... 23

Figure 2.13. Packing model of (a) C<sub>18</sub>-(PEPAu)<sub>1</sub>, (b) C<sub>18</sub>-(PEPAu)<sub>2</sub>, and C<sub>18</sub>-(PEPAu)<sub>3</sub> assemblies. (d) C-H vibration bands in the IR spectra of C<sub>18</sub>-(PEPAu)<sub>1</sub> (blue line), C<sub>18</sub>-(PEPAu)<sub>2</sub> (red line), and C<sub>18</sub>-(PEPAu)<sub>3</sub> (green line) assemblies..... 24

Figure 2.14. (a) TEM image showing the twist points used to measure the fiber thickness (scale bar = 100 nm). Fiber thickness distribution of (b) C<sub>12</sub>-(PEPAu)<sub>1</sub>: 8.7 ± 1.0 based on 30 counts; (c) C<sub>14</sub>-(PEPAu)<sub>1</sub>: 8.9 ± 1.2 based on 60 counts; (d) C<sub>16</sub>-(PEPAu)<sub>1</sub>: 8.8 ± 0.9 based on 60 counts; (e) C<sub>18</sub>-(PEPAu)<sub>1</sub>: 10.3 ± 1.9 based on 30 counts..... 25

Figure 2.15. TEM images of the nanoparticle assemblies as a function of peptide valency and aliphatic chain length (scale bar = 100 nm): (a) C<sub>12</sub>-(PEPAu)<sub>1</sub>, (b) C<sub>14</sub>-(PEPAu)<sub>1</sub>, (c) C<sub>16</sub>-(PEPAu)<sub>1</sub>, (d) C<sub>18</sub>-(PEPAu)<sub>1</sub>, (e) C<sub>12</sub>-(PEPAu)<sub>2</sub>, (f) C<sub>14</sub>-(PEPAu)<sub>2</sub>, (g) C<sub>16</sub>-(PEPAu)<sub>2</sub>, (h) C<sub>18</sub>-(PEPAu)<sub>2</sub>, (i) C<sub>12</sub>-(PEPAu)<sub>3</sub>, (j) C<sub>14</sub>-(PEPAu)<sub>3</sub>, (k) C<sub>16</sub>-(PEPAu)<sub>3</sub>, and (l) C<sub>18</sub>-(PEPAu)<sub>3</sub>..... 28

Figure 2.16. Nanoparticle diameters measured from TEM images: (a) C<sub>12</sub>-(PEPAu)<sub>1</sub>: 5.3 ± 0.9 nm based on 100 counts; (b) C<sub>14</sub>-(PEPAu)<sub>1</sub>: 6.6 ± 1.2 nm based on 100 counts; (c) C<sub>16</sub>-(PEPAu)<sub>1</sub>: 7.6 ± 1.5 nm based on 100 counts; (d) C<sub>18</sub>-(PEPAu)<sub>1</sub>: 10.2 ± 2.9 nm based on 50 counts; (e) C<sub>12</sub>-(PEPAu)<sub>2</sub>: 2.9 ± 0.6 nm based on 100 counts; (f) C<sub>14</sub>-(PEPAu)<sub>2</sub>: 4.5 ± 1.1 nm based on 100 counts; (g) C<sub>16</sub>-(PEPAu)<sub>2</sub>: 5.9 ± 1.1 nm based on 100 counts; (h) C<sub>18</sub>-(PEPAu)<sub>2</sub>: 6.1 ± 1.4 nm based on 100

counts; (i) C<sub>12</sub>-(PEP<sub>Au</sub>)<sub>3</sub>: 2.8 ± 0.6 nm based on 50 counts; (j) C<sub>14</sub>-(PEP<sub>Au</sub>)<sub>3</sub>: 2.6 ± 0.5 nm based on 100 counts; (k) C<sub>16</sub>-(PEP<sub>Au</sub>)<sub>3</sub>: 3.0 ± 0.6 nm based on 50 counts; (a) C<sub>18</sub>-(PEP<sub>Au</sub>)<sub>3</sub>: 2.8 ± 0.7 nm based on 100 counts. .... 30

Figure 2.17. QCM binding data for the (a) monovalent and (b) divalent peptide conjugates. (c) The association binding constant, K<sub>a</sub>, dissociation binding constant, K<sub>d</sub>, and equilibrium binding constant, K<sub>eq</sub>, were calculated from the QCM experiments. .... 31

Figure 2.18. TEM images of nanoparticle assemblies showing regions of helicity and pitch measurements from (a) C<sub>16</sub>-(PEP<sub>Au</sub>)<sub>1</sub> and (b) C<sub>18</sub>-(PEP<sub>Au</sub>)<sub>2</sub> (scale bar = 100 nm). .... 33

Figure 3.19. Preparation of (a) double- and (b) single-helical nanoparticle superstructures from C<sub>18</sub>-(PEP<sub>Au</sub>)<sub>2</sub> and C<sub>18</sub>-(PEP<sub>Au</sub><sup>M-Ox</sup>)<sub>2</sub>, respectively, under identical reaction conditions. C<sub>18</sub>-(PEP<sub>Au</sub><sup>M-Ox</sup>)<sub>2</sub> was prepared via oxidation using H<sub>2</sub>O<sub>2</sub>. .... 41

Figure 3.20. Single helix characterization. (a,b) TEM images of single-helical gold nanoparticle superstructures after 15 h of reaction and (c) negative-stained TEM image after 30 min. of reaction. (d) Pitch of the helices, measured from TEM (94.4 ± 6.6 nm; based on 80 counts). The cryo-ET 3D reconstruction of the single helices reveals their (e) left-handed helicity and, when viewed along the helix axis, their (f) core diameter where the fiber resides. (g) CD spectrum of the single-helical superstructures. .... 42

Figure 3.21. C<sub>18</sub>-(PEP<sub>Au</sub><sup>M-ox</sup>)<sub>2</sub> fiber morphology studies. Helical peptide amphiphile fibers typically exhibit either (a) helical ribbon or (b) twisted ribbon morphology. (c) Negative-stained TEM image of C<sub>18</sub>-(PEP<sub>Au</sub><sup>M-ox</sup>)<sub>2</sub> fibers. (d) Fiber widths were 10.2 ± 0.8 nm. (e) AFM reveals the helical ribbon morphology of C<sub>18</sub>-(PEP<sub>Au</sub><sup>M-ox</sup>)<sub>2</sub> fibers with a pitch of 96.2 ± 4.8 nm and (f) a ribbon height of approximately 4 nm (height trace measured along the dashed line). .... 44

Figure 3.22. Spectroscopy studies. (a) FTIR spectrum of  $C_{18}-(PEP_{Au}^{M-ox})_2$  fibers. Peaks at  $1630\text{ cm}^{-1}$  and  $2922\text{ cm}^{-1}$  correspond to the amide I band and C-H stretch, respectively. (b) CD spectrum of  $C_{18}-(PEP_{Au}^{M-ox})_2$  in 10 mM HEPES and 1 mM  $CaCl_2$  after one day, and (c) corresponding negative-stained TEM image of the  $C_{18}-(PEP_{Au}^{M-ox})_2$  fibers. .... 46

Figure 3.23. X-ray data. 2D x-ray diffraction pattern of aligned  $C_{18}-(PEP_{Au}^{M-ox})_2$  fibers reveals a cross- $\beta$  architecture. The colored arrows correlate with the (c) integrated d-spacings of the XRD diffractogram. (c) Figure showing the strand-to-strand and sheet-to-sheet distances as revealed via XRD. .... 47

Figure 3.24. MAS ssNMR results. (a) Position of residue-specific  $^{13}C$ -,  $^{15}N$ -labeling (arrows). (b) 2D  $^{13}C$ - $^{13}C$  MAS ssNMR of labeled  $C_{18}-(PEP_{Au}^{M-ox})_2$  assemblies. Dashed and colored lines connect sets of peaks from labeled P10 (black dashed line) and A1 residues (solid lines). Three A1 conformations are marked with red (A1a), blue (A1b), and green (A1c) lines. (c) Secondary structure analysis of A1 ssNMR signals, showing A1a and A1b to be part of the  $\beta$ -sheet core. (d) Secondary structure distribution in the three peptide conformers observed by ssNMR, along with their relative ssNMR peak intensities (right). (e) Amyloid core model based on a class 3 steric zipper architecture. The compact Ala/Ser/Gly interface and the aromatic interface present intersheet distances of  $\sim 6.5$  and  $\sim 9$  Å, respectively. Alternating peptides have distinct structures (blue/red coloring) that explain the observed peak doubling in the A1  $\beta$ -sheet peaks. .... 49

Figure 3.25. Single helix assembly model. (a) Proposed assembly model of  $C_{18}-(PEP_{Au}^{M-ox})_2$  helical ribbons.  $\beta$ -sheets run along the length of the fiber (interstrand distance =  $4.6$  Å). The width of the ribbon,  $w$ , is determined by the number of stacked  $\beta$ -sheets with lamination spacings of  $\sim 6.5$  and  $\sim 9$  Å. PPII helices are exposed at the outer surface of the helical ribbon. The blue and red layers correspond to the type 'a' and type 'b'  $\beta$ -sheets, respectively, shown in Figure

3.24. The aliphatic tails have been omitted for clarity. (b) AFM (amplitude image) and (c) TEM image aligned to highlight the structural similarity between the fiber assembly and nanoparticle assembly, alongside (d) the proposed single helix assembly model with gold nanoparticles bound to the outer face of the helical ribbon. The arrows show directionality similarities of the nanoparticle orientation. .... 52

Figure 4.26. TEM images of HSAuNP superstructures assembled with 0.7 uL HAuCl<sub>4</sub>/TEAA after (a) 30 min., (b) 1 hr., (c) 3 hrs., and (d) 24 hrs. TEM images of HSAuNP superstructures assembled with 0.9 uL HAuCl<sub>4</sub>/TEAA after (e) 30 min., (f) 1 hr., (g) 3 hrs., and (h) 24 hrs. TEM images of HSAuNP nanoparticle superstructures assembled with 1.1 uL HAuCl<sub>4</sub>/TEAA after (i) 30 min., (j) 1 hr., (k) 3 hrs., and (l) 24 hrs. (scale bars = 100 nm) ..... 64

Figure 4.27. (a) Distribution of sphere diameters of HSAuNP superstructures after 10 min., 1 hr. and 3 hrs. for samples assembled with 1.1 μL of HAuCl<sub>4</sub>/TEAA. (b) Distribution of sphere diameters (collected after 1 hr. of assembly time) as a function of the amount of HAuCl<sub>4</sub>/TEAA added to the C<sub>6</sub>-AA-PEP<sub>Au</sub> solution in HEPES. .... 66

Figure 4.28. TEM images of HSAuNP superstructures formed with (a) 0.7 μL and (b) 1.1 μL of HAuCl<sub>4</sub>/TEAA, after 1 day of incubation with PEP<sub>Au</sub>, and (c,d) their corresponding UV-Vis absorption spectra, respectively. TEM images of HSAuNP superstructures formed with (e) 0.7 μL and (f) 1.1 μL of HAuCl<sub>4</sub>/TEAA after 1 day of incubation with proteinase K, and (g,h) their corresponding UV-Vis absorption spectra, respectively. .... 67

Figure 4.29. TEM images of HSAuNP superstructures after 1 day of incubation in (a) 2 μM, (b) 20 μM, and (c) 200 μM MHA. TEM images of HSAuNP superstructures after 1 day of incubation in (d) 2 μM, (e) 20 μM, and (f) 200 μM PEG-SH (MW = 1000). (scale bars = 200 nm) ..... 70

Figure 5.30. Modular synthesis of POCs: i) covalent attachment of an azido-modified oligonucleotide sequence to a biphenyl organic linker followed by ii) covalent attachment of an azido-modified peptide. .... 76

Figure 5.31. PO<sub>18</sub>C assemblies at varying CaCl<sub>2</sub> concentrations. TEM images of PO<sub>18</sub>C assemblies formed in (a) 10 mM, (b) 50 mM, (c) 150 mM, and (d) 300 mM CaCl<sub>2</sub>. TEM samples were prepared after 15-20 hrs. of assembly time. .... 77

Figure 5.32. PO<sub>18</sub>C assembly characterization. (a) SEM images of PO<sub>18</sub>C vesicles assembled in 50 mM CaCl<sub>2</sub>. (b) AFM image of PO<sub>18</sub>C vesicles deposited on mica. (c) AFM image of a vesicle and (d) corresponding height profile along the dashed line shown in c. (e) Phase image of the vesicle shown in c. (f) UV-Vis spectrum of free 15 nm gold nanoparticle functionalized with complementary O<sub>18</sub> sequence (black line) and gold nanoparticle-decorated vesicles after addition of the complementary functionalized gold nanoparticles to a solution containing PO<sub>18</sub>C vesicles (red line). (g) TEM images of the gold nanoparticle-decorated vesicles after addition of 15 nm gold nanoparticles functionalized with complementary O<sub>18</sub> to a solution of PO<sub>18</sub>C vesicles. (h) Proposed assembly model of PO<sub>18</sub>C vesicles. The vesicles are composed of a PO<sub>18</sub>C monolayer, with the oligonucleotides exposed on the outer surface. .... 78

Figure 5.33. Role of charge shielding. (a) Greater charge shielding can allow for tighter packing of POCs, which can lead to fiber formation. (b) Greater repulsion due to less charge shielding favors the formation of vesicles. .... 80

Figure 5.34. PO<sub>6</sub>C assemblies at varying CaCl<sub>2</sub> concentrations. TEM images of PO<sub>6</sub>C assemblies formed in (a) 10 mM, (b) 50 mM, (c) 150 mM, and (d) 300 mM CaCl<sub>2</sub>. TEM samples were prepared after 15-20 hrs. .... 81

Figure 5.35. FTIR spectra of PO <sub>18</sub> C vesicles (red line) and PO <sub>6</sub> C fibers (blue line) assembled in 50 mM CaCl <sub>2</sub> . .....	82
Figure 5.36. (a) The charge ratio value is the ratio of positive to negative charges of the assembly solution (N = number of oligonucleotide bases; the '+2' results from the azido-functionalized T residue, Figure S5.68, and the deprotonated COO- terminus of the peptide. (b) The charge ratio of the assembly solution as a function of CaCl <sub>2</sub> concentration and oligonucleotide length. TEM images of PO <sub>18</sub> C vesicles (c) before and (d) after conc. CaCl <sub>2</sub> addition. ....	83
Figure S2.37. Plasmonic circular dichroism signal as a function of helical pitch, calculated according to reported methods. <sup>61</sup> .....	91
Figure S2.38. Chemical structure of N <sub>3</sub> -PEP <sub>Au</sub> .....	92
Figure S2.39. Scheme detailing the construction of the monovalent, divalent, and trivalent alkyne-modified aliphatic substrates. Briefly, the experimental details include: a) EDC-mediated NHS activation of the carboxylic acid, b) amide bond formation, and c) propargylation under basic conditions.....	93
Figure S2.40. MALDI-TOF mass spectra of purified monovalent and divalent peptide conjugates: (a) C <sub>12</sub> -(PEP <sub>Au</sub> ) <sub>1</sub> , m/z = 1649.5 (M + Na <sup>+</sup> ); (b) C <sub>14</sub> -(PEP <sub>Au</sub> ) <sub>1</sub> , m/z = 1677.3 (M + Na <sup>+</sup> ); (c) C <sub>16</sub> -(PEP <sub>Au</sub> ) <sub>1</sub> , m/z = 1693.2 (M + Na <sup>+</sup> ); (d) C <sub>18</sub> -(PEP <sub>Au</sub> ) <sub>1</sub> , m/z = 1733.1 (M + Na <sup>+</sup> ), m/z = 1748.9 (M + K <sup>+</sup> ); (e) C <sub>12</sub> -(PEP <sub>Au</sub> ) <sub>2</sub> , m/z = 3063.4 (M + Na <sup>+</sup> ); (f) C <sub>14</sub> -(PEP <sub>Au</sub> ) <sub>2</sub> , m/z = 3092.2 (M + Na <sup>+</sup> ); (g) C <sub>16</sub> -(PEP <sub>Au</sub> ) <sub>2</sub> , m/z = 3119.0 (M + Na <sup>+</sup> ); (h) C <sub>18</sub> -(PEP <sub>Au</sub> ) <sub>2</sub> , m/z = 3147.8 (M + Na <sup>+</sup> ). .....	94
Figure S2.41. LCMS spectra of purified trivalent peptide conjugates: (a) C <sub>12</sub> -(PEP <sub>Au</sub> ) <sub>3</sub> , m/z = 1484 (m/3), m/z = 1113 (m/4), m/z = 890 (m/5); (b) C <sub>14</sub> -(PEP <sub>Au</sub> ) <sub>3</sub> , m/z = 1494 (m/3), m/z = 1120	

(m/4); (c) C<sub>16</sub>-(PEP<sub>Au</sub>)<sub>3</sub>, m/z = 1505 (m/3), m/z = 1129 (m/4); (d) C<sub>18</sub>-(PEP<sub>Au</sub>)<sub>3</sub>, m/z = 1513 (m/3), m/z = 1134 (m/4), m/z = 907 (m/5). ..... 95

Figure S2.42. ATR-FTIR spectra of (a) C<sub>18</sub>-(PEP<sub>Au</sub>)<sub>1</sub> and (b) its corresponding negatively stained TEM image of the soft assembly. ATR-FTIR spectra of (c) C<sub>18</sub>-(PEP<sub>Au</sub>)<sub>2</sub> and (d) its corresponding negatively stained TEM image of the soft assembly. ATR-FTIR spectra of (e) C<sub>18</sub>-(PEP<sub>Au</sub>)<sub>3</sub> and (f) its corresponding negatively stained TEM image of the soft assembly (scale bar = 100 nm)..... 96

Figure S2.43. Pitch measurements of selected fibers from negatively stained TEM images of (a) C<sub>12</sub>-(PEP<sub>Au</sub>)<sub>1</sub>; (b) C<sub>14</sub>-(PEP<sub>Au</sub>)<sub>1</sub>; (c) C<sub>16</sub>-(PEP<sub>Au</sub>)<sub>1</sub>; and (d) C<sub>18</sub>-(PEP<sub>Au</sub>)<sub>1</sub> (scale bar = 100 nm). Note: in general, the measurements from TEM confirm the trend determined from the AFM data. However, the TEM pitch measurements can vary widely between different fibers, as is clear for the C<sub>12</sub>-(PEP<sub>Au</sub>)<sub>1</sub> assemblies. .... 97

Figure S2.44. (a) AFM images of C<sub>12</sub>-(PEP<sub>Au</sub>)<sub>1</sub> assemblies and (b) corresponding height traces. The pitch length was calculated by averaging the distances between every other peak in the height traces. Average pitch is 186 ± 13 nm based on 18 counts. .... 98

Figure S2.45. (a) AFM image of C<sub>14</sub>-(PEP<sub>Au</sub>)<sub>1</sub> assemblies and (b) corresponding height traces. The pitch length was calculated by averaging the distances between every other peak in the height traces. Average pitch is 196 ± 11 nm based on 20 counts. It is clear that some fibers intertwine, but the pitch measurements were only made on single fibers. .... 99

Figure S2.46. (a) AFM image of C<sub>16</sub>-(PEP<sub>Au</sub>)<sub>1</sub> assemblies and (b) corresponding height traces. The pitch length was calculated by averaging the distances between every other peak in the height traces. Average pitch is 214 ± 7 nm based on 10 counts. It is clear that some fibers intertwine, but the pitch measurements were only made on single fibers. .... 100



Figure S2.47. (a) AFM image of C<sub>18</sub>-(PEP<sub>Au</sub>)<sub>1</sub> assemblies and (b) corresponding height traces. The pitch length was calculated by averaging the distances between every other peak in the height traces. Average pitch is 228 ± 30 nm based on 8 counts. It is clear that some fibers intertwine, but the pitch measurements were only made on single fibers. .... 101

Figure S2.48. AFM image of C<sub>14</sub>-(PEP<sub>Au</sub>)<sub>2</sub> assemblies. Only spherical assemblies/aggregates were observed. .... 102

Figure S2.49. (a) AFM image of C<sub>16</sub>-(PEP<sub>Au</sub>)<sub>2</sub> assemblies and (b) corresponding height traces. The pitch length was calculated by averaging the distances between every other peak in the height traces. Average pitch is 178 ± 20 nm based on 20 counts. It is clear that some fibers intertwine, but the pitch measurements were only made on single fibers. .... 103

Figure S2.50. (a) AFM image of C<sub>18</sub>-(PEP<sub>Au</sub>)<sub>2</sub> assemblies and (b) corresponding height traces. The pitch length was calculated by averaging the distances between every other peak in the height traces. Average pitch is 184 ± 15 nm based on 9 counts. It is clear that some fibers intertwine, but the pitch measurements were only made on single fibers. .... 104

Figure S2.51. Molecular structure of the (a) mono- and (b) divalent peptide conjugates used for the QCM experiments. MALDI-TOF mass spectra of (c) monovalent peptide conjugate, m/z = 1424 (M + Na<sup>+</sup>), m/z = 1440.0 (M + K<sup>+</sup>) and (d) divalent peptide conjugate, m/z = 2866.1 (M + Na<sup>+</sup>). .... 105

Figure S2.52. (a) TEM image showing the interchain distances (scale bar = 50 nm). Interchain distances of (b) C<sub>14</sub>-(PEP<sub>Au</sub>)<sub>1</sub>: 5.9 ± 1.2 nm based on 65 counts; (c) C<sub>16</sub>-(PEP<sub>Au</sub>)<sub>1</sub>: 5.6 ± 1.2 nm based on 65 counts; (d) C<sub>16</sub>-(PEP<sub>Au</sub>)<sub>2</sub>: 4.6 ± 1.2 nm based on 55 counts; (e) C<sub>18</sub>-(PEP<sub>Au</sub>)<sub>2</sub>: 5.0 ± 1.4 nm based on 35 counts. .... 106

Figure S2.53. Possible locations for particle association to fibers: (a) fiber faces or (b) fiber edges. ....	107
Figure S2.54. TEM images indicating helical segments of assemblies constructed from (a,b) C <sub>14</sub> -(PEP <sub>Au</sub> ) <sub>1</sub> and (c) C <sub>16</sub> -(PEP <sub>Au</sub> ) <sub>2</sub> (scale bar = 100 nm). The red arrows indicate points of helicity. ....	107
Figure S3.55. Chemical structure of (a) C <sub>18</sub> -(PEP <sub>Au</sub> ) <sub>2</sub> and (b) C <sub>18</sub> -(PEP <sub>Au</sub> <sup>M-ox</sup> ) <sub>2</sub> . ....	126
Figure S3.56. LCMS spectra of (a) C <sub>18</sub> -(PEP <sub>Au</sub> ) <sub>2</sub> , m/z = 1562 (m/2) and C <sub>18</sub> -(PEP <sub>Au</sub> <sup>M-ox</sup> ) <sub>2</sub> , m/z = 1578 (m/2). ....	127
Figure S3.57. Additional TEM images of the single-helical superstructure at different magnifications. ....	128
Figure S3.58. The nanoparticle length and widths of the single-helical superstructure were 16.6 ± 3.0 nm and 9.6 ± 1.9 nm, respectively, after 15 hours of reaction (based on 125 counts each). ....	129
Figure S3.59. Negative-stained TEM images of the single helices after (a) 0 min., (b) 30 min., (c) 2 hrs., (d) 5 hrs., (e) 8 hrs., and (f) 2 days of reaction at room temperature (scale bars = 50 nm) ....	129
Figure S3.60. Structural parameters of single helices from cryo-ET: (a) the helical pitch was 102.0 ± 2.5 nm, based on 20 counts; (b) rotation angle was 34.3 ± 4.9 degrees, based on 20 counts; and (c) inner diameter was 10.1 ± 0.6 nm, based on 10 counts. ....	130
Figure S3.61. (a) CD spectrum of PEP <sub>au</sub> <sup>M-ox</sup> capped gold nanoparticles and (b) their corresponding TEM image (scale bar = 100 nm). Both single particles and particle aggregates are observed. ....	131
Figure S3.62. (a) TEM image of helices formed with 10 min. of sonication and 20 min. of incubation prior to H <sub>Au</sub> Cl <sub>4</sub> /TEAA addition. (b) The particle width and lengths were 12.1 ± 3.0	

nm and  $23.9 \pm 3.9$  nm, respectively (based on 75 counts each). (c) CD spectrum of the optimized single helices exhibit a very strong CD signal. (d) UV-Vis extinction spectrum, and (e) g-factor graph showing absolute g-factor values up to 0.04. g- factor =  $\Delta\epsilon/\epsilon$ , where  $\Delta\epsilon$  is the molar circular dichroism and  $\epsilon$  is the molar extinction. .... 132

Figure S3.63. (a-d) AFM images of  $C_{18}-(PEP_{Au}^{M-ox})_2$  fibers dispersed on APTES-functionalized mica (scale bars = 200 nm) and (e) height traces of the labeled segments. .... 133

Figure S3.64. (a)  $C_{18}-(PEP_{Au}^{M-ox})_2$  in 10 mM HEPES as a function of time. Negative-stained TEM images after (b) 15 min., (c) 3 hrs., and (d) 72 hrs. are shown (scale bars = 500 nm). Under these conditions, fibers form very slowly, and very few fibers are observed at early time points. .... 134

Figure S3.65. Additional ssNMR results and structural reference. (a) Aliphatic  $^{13}C$  1D MAS ssNMR spectrum of the site-specifically labeled  $C_{18}-(PEP_{Au}^{M-ox})_2$  assemblies (top), with the P10 peaks indicated. Bottom: ssNMR spectrum of fibrillar huntingtin exon1-derived peptide htt<sup>NT</sup> Q<sub>30</sub>P<sub>10</sub>K<sub>2</sub>, with  $^{13}C$ -,  $^{15}N$ -labeled Pro P48 (adapted from ref. <sup>119</sup>). In both cases the labeled Pro is part of a PPII helix that flanks the  $\beta$ -sheet amyloid core. (b) Long-mixing 500ms PDS 2D ssNMR spectrum on the labeled  $C_{18}-(PEP_{Au}^{M-ox})_2$  assemblies. Compared to the short-mixing spectrum (Figure 3.24b) only new intra-residue P10 peaks are observed, with no contacts between the distinct A1 conformers. (c) Compact zipper interfaces mediated by Ser and other small amino acids in amyloid-like crystals of peptides SSTSAA and SSTNVG from RNase and IAPP.<sup>120</sup> The compact 6 Å inter-sheet distance is indicated. (d) Tyr ring stacking in GNNQQNY in-register parallel (IP)  $\beta$ -sheets.<sup>166</sup> (e) Amyloid interfaces featuring aromatic residues generate wider 9-10 Å inter-sheet distances. Illustrated for Phe in this Class-2 amyloid-like crystal of

peptide ANFLVH.<sup>167</sup> The PDB entries for the four peptide crystal structures are 2ONW, 3DG1, 1YJP, and 5E5X..... 135

Figure S3.66. Length of the different extended segments of C<sub>18</sub>-(PEP<sub>Au</sub><sup>M-ox</sup>)<sub>2</sub>. The total length of the extended molecule is ~7.5 nm. The length measurements of the peptide portion takes into account the average length spanned by one amino acid in both the parallel β-sheet (3.25 Å)<sup>168</sup> and the PPII (3.1 Å)<sup>169</sup> secondary structure..... 136

Figure S4.67. TEM images of HSAuNP superstructures assembled after 10 min. with (a) 0.7 μL H<sub>2</sub>AuCl<sub>4</sub>/TEAA, (b) 0.9 μL H<sub>2</sub>AuCl<sub>4</sub>/TEAA, and (c) 1.1 μL H<sub>2</sub>AuCl<sub>4</sub>/TEAA (scale bars = 100 nm). ..... 138

Figure S5.68. Structure of the (a) 18-base azido-modified oligonucleotide (O<sub>18</sub>-N<sub>3</sub>) and (b) 6-base azido-modified oligonucleotide (O<sub>6</sub>-N<sub>3</sub>)..... 139

Figure S5.69. Chemical structure of the azido-modified peptide (N<sub>3</sub>-C<sub>4</sub>H<sub>8</sub>CO-AAAYSSGAPPMPPF)..... 140

Figure S5.70. (a) Reverse-phase HPLC trace and (b) MALDI spectrum of PO<sub>18</sub>C. (c) Reverse-phase HPLC trace and (d) MALDI spectrum of PO<sub>6</sub>C. Note: m/1 and m/2 peaks were observed in the MALDI spectra. .... 140

Figure S5.71. TEM images of 500 μM PO<sub>18</sub>C in 50 mM CaCl<sub>2</sub> after 15-20 hrs. Spherical assemblies were observed. .... 141

Figure S5.72. TEM images of 500 μM PO<sub>18</sub>C in 150 mM CaCl<sub>2</sub> after 15-20 hrs. Spherical/pseudo-spherical assemblies were the major products. Few fiber assemblies were also observed. .... 141

Figure S5.73. TEM images of 500 μM PO<sub>18</sub>C in 300 mM CaCl<sub>2</sub> after 15-20 hrs. Fibers were observed. .... 141

Figure S5.74. AFM images of PO<sub>18</sub>C vesicles deposited on APTES-functionalized mica. The labeled vesicles and their corresponding height traces are shown. In general, larger vesicles appear to flatten more than smaller vesicles. .... 142

Figure S5.75. Phase image of PO<sub>18</sub>C vesicles revealing the different deformation response between the sphere edge and sphere center. .... 143

Figure S5.76. AFM image of vesicles on a TEM grid after exposure to the high-vacuum TEM environment. Labeled vesicles and their corresponding height traces reveal a height of approximately 30 nm. A majority of the vesicles appear to flatten completely, except for a few that retained more of its shape (e.g., spheres 6 and 10). .... 144

Figure S5.77. PO<sub>18</sub>C length. The length of the extended 18mer oligonucleotide was reported to be 7.7 nm.<sup>170-171</sup> .... 145

Figure S5.78. Additional TEM images of gold nanoparticle-decorated PO<sub>18</sub>C vesicles after 2 hrs of incubation. .... 146

Figure S5.79. TEM image of 500 μM PO<sub>6</sub>C in 10 mM CaCl<sub>2</sub> after 15-20 hrs. Fibers, aggregates, and spherical assemblies were observed. .... 147

Figure S5.80. TEM image of 500 μM PO<sub>6</sub>C in 50 mM CaCl<sub>2</sub> after 15-20 hrs. Fibers were observed. .... 147

Figure S5.81. TEM image of 500 μM PO<sub>6</sub>C in 150 mM CaCl<sub>2</sub> after 15-20 hrs. Fibers and fiber networks were observed. .... 147

Figure S5.82. TEM image of 500 μM PO<sub>6</sub>C in 300 mM CaCl<sub>2</sub> after 15-20 hrs. Fibers and fiber networks were observed. .... 148

Figure S5.83. PO<sub>6</sub>C assemblies assembled in (a) 50 mM CaCl<sub>2</sub> and (b) 10 mM CaCl<sub>2</sub>. (c-e) Zoomed-in TEM images of the dashed boxes shown in b (the border colors correspond to the colors of the dashed boxes)..... 149

Figure S5.84. (a,b) TEM images 2 hrs. after addition of 5 nm gold nanoparticles (functionalized with complementary 6mer sequence) to a solution containing PO<sub>6</sub>C fibers in 50 mM CaCl<sub>2</sub>. (c) UV-Vis spectrum of free 5 nm gold nanoparticles functionalized with complementary 6mer sequence (black line) and 2 hrs. after addition to PO<sub>6</sub>C fibers (red line). The position of the LSPR band remains unchanged. The difference in signal intensity is due to different solution concentrations of gold nanoparticles. .... 150

Figure S5.85. PO<sub>18</sub>C (500 μM) assembled in the (a,b) absence of complement and in the (c,d) presence of complement. Both experiments were conducted in 150 mM CaCl<sub>2</sub>..... 151

## PREFACE

I am extremely grateful for the many individuals who have supported me throughout my PhD studies. Without their support, I would not be writing this dissertation today. I first want to extend my deepest thanks and gratitude to my advisor, Prof. Nathaniel L. Rosi, for giving me the opportunity to be a part of his research group. He has tirelessly supported me throughout my PhD studies and has been instrumental in my development as a scientist. I am grateful for the hard work that he has done on my behalf and for helping me navigate through my young career.

I also thank my committee members: Prof. Seth Horne (dissertation and proposal), Prof. Steve Weber (dissertation), Prof. Patrick van der Wel (dissertation), Prof. Seth Childers (proposal), and Prof. Haitao Liu (proposal). I thank them for their time and sacrifice in serving on my committee. I further want to highlight Prof. Seth Horne, Prof. Seth Childers, and Prof. van der Wel, who not only have supported my career here in Pittsburgh, but have helped me throughout the postdoctoral application process. I am thankful for their support of my future endeavors. In addition to these faculty members at Pitt, I thank all the current and past group members who supported me throughout my time in graduate school. In particular, I want to thank Dr. Chong Liu, Soumitra Mokashi Punekar, and Yicheng Zhou for their help with my research projects. They have been excellent collaborators and I am grateful for their help. Furthermore, I thank all the outside collaborators that have contributed their time and efforts towards my projects. These include Dr. Joe Slocik, Dr. Ryan Thaner, Prof. SonBinh Nguyen,

Jennifer Boatz, Dr. Abhishek Mandal, and Dr. Gongpu Zhao. I also want to thank Dr. Bhaskar Godugu, the mass spectroscopy facility director, for his help in determining the identity of  $C_{18}-(PEP_{Au}^{M-Ox})_2$ .

I also must thank my wonderful family and friends that have supported me since the very beginning. First and foremost, I acknowledge my deepest gratitude to my wife, Chelsea. She has been a constant source of light in my life. Through difficult moments of graduate school, she never wavered in her love and support of me, but has stood by me and encouraged me at every step. I am gratefully for her sacrificial love and support. I thank my father and mother, Mark and Keiko Merg, and my sister, Angelica, who have been instrumental in laying the foundation for me to be here today. I know that no matter what happens, I have a family that loves me. I also cannot forget the Church family that I have here in Pittsburgh. All the brothers and sisters in Christ at Renaissance Church have been a physical embodiment of God's love and care towards myself and Chelsea. I have grown immensely as a person through the deep friendships I have formed within the Church, and they have been influential for me throughout my PhD studies from the way that they have supported Chelsea and me. My journey with them in Pittsburgh will be a memory that I will cherish forever.

Lastly, I thank my Lord and Savior, Jesus Christ, and the good news of the Gospel. Though I see and feel the gravity of my own faults daily, I can live a life filled with joy and peace, because I have a Savior who saw fit to extend to me boundless grace and love that is mine forever. All this work I present in these pages, I humbly give to Him, who gives me more than I ever could give.

“The Kingdom of Heaven is like treasure hidden in a field. When a man found it, he hid it again, and then in his joy went and sold all he had and bought that field.” – Matthew 13:44



## **1.0 INTRODUCTION**

### **1.1 SELF-ASSEMBLY IN NATURE**

Humans have long been fascinated with and inspired by the natural world. The beauty and complexity found in nature have been resources mined throughout history for knowledge and understanding in every aspect of life and remain a source of inspiration for future transformative ideas and innovations. A variety of fields, such as the visual arts, architecture, engineering, and chemistry, would not be where they are today without their respective contributors seeking vision and insight from the natural world around them. Recently, within the realm of materials science and chemistry, the natural process of molecular self-assembly – ubiquitous in nature – has transformed how scientists in these fields contemplate the design and construction of new materials.

Molecular self-assembly is the spontaneous self-organization of individual molecules into hierarchical structures. These structures are assembled primarily through non-covalent interactions such as van der Waals forces, electrostatic interactions, and hydrogen-bonding. Nature provides countless examples of self-assembled systems that display exquisite properties and function. Amazingly, these complex structures are assembled using simple biomolecules. A prime example are proteins. Proteins are composed of amino acid residues connected via amide bond linkages (polypeptide chain). The amino acids that constitute the polypeptide chain encode

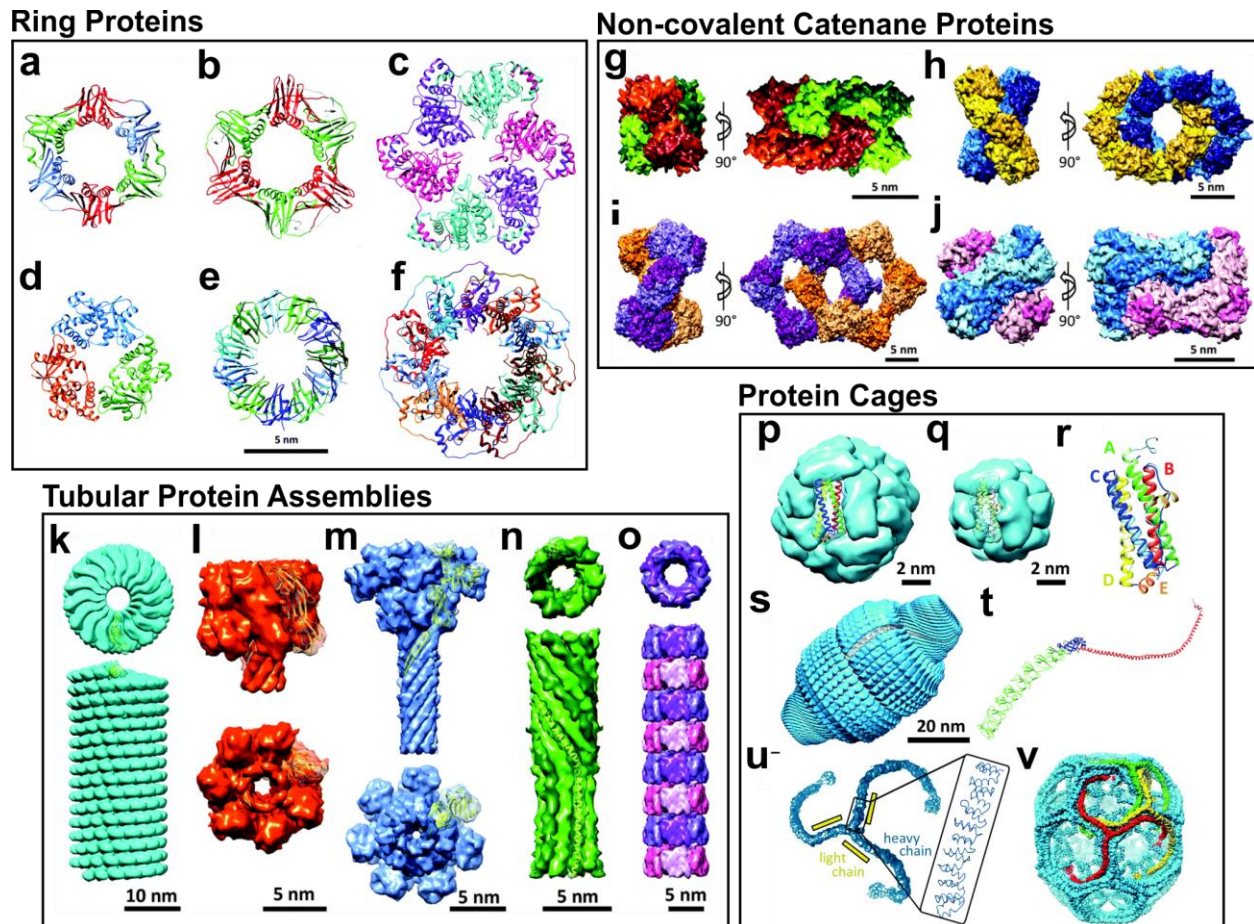


**Figure 1.1.** Several different natural supramolecular protein assemblies. Ring proteins: (a) the  $\beta$ -clamp of *E. coli* (PDB:2POL); (b) the proliferating cell nuclear antigen PCNA of *H. sapiens* (PDB:1AXC); (c) bacteriophage T7 gp4 helicase (PDB:1E0K); (d) bacteriophage  $\lambda$  exonuclease (PDB: 1AVQ); (e) TRAP (PDB: 1QAW); (f) RAD52 (PDB: 1KN0). Non-covalent catenane proteins: (a) RecR (PDB: 1VDD); (b) Cys168Ser variant of Prx III (PDB: 1ZYE); (c) class 1a RNR (PDB: 4ERP); (d) CS<sub>2</sub> hydrolase (PDB:3TEO). Tubular protein assemblies: (k) TMV (PDB: 4UDV). (l)  $\alpha$ -hemolysin pore complex (PDB: 7AHL); (m) anthrax protective antigen pore (PDB: 3J9C); (n) PhiX174 bacteriophage tail (PDB: 4JPP); (o) Hcp1 from *P. aeruginosa* (PDB: 1Y12). Protein cages: (a) maxi-ferritin (PDB: 1BFR); (q) mini-ferritin (PDB:1DPS); (r) superimposition of ribbon structures of mini-ferritin (light) and maxi-ferritin (dark); (s) a surface view of the rat vault shell (PDB: 4HL8); (t) ribbon structure of the major vault protein monomer, showing the structural repeat domains (green), the shoulder domain (blue), the cap-helix domain (red), and the cap-ring domain (magenta); (u) surface-structure of triskelion and zoom showing the  $\alpha$ -helical zigzags (PDB: 1XI4); (v) structure of hexagonal barrel. (All figures adapted from ref. 1)

the intricate folding information that directs their assembly into stable, functional 3D protein architectures. These defined protein architectures then serve to perform a variety of complex tasks, as observed in biology. **Figure 1.1** presents several diverse supramolecular protein assemblies found in nature, highlighting the immense potential of simple biomolecules (*e.g.*, amino acids) as building blocks for the design and construction of intricate, complex nanomaterials.<sup>1</sup>

## **1.2 SELF-ASSEMBLY OF METALLIC NANOPARTICLES**

Motivated by the complex and functional assemblies derived from biological building blocks, scientists have begun exploiting biomolecules for the design and fabrication of a diverse array of novel synthetic materials. In the context of this dissertation, I will focus on the assembly of metallic nanoparticles into hierarchical superstructures. These novel hybrid materials have received significant interest due to their unique and exceptional properties.

### **1.2.1 Properties of metallic nanoparticles and their assemblies**

Nanoparticles are classified as having at least one dimension between 1 and 100 nm. In this nanosized-regime, new properties emerge which are not observed for their bulk counterparts. This is especially evident with metallic nanoparticles. Metal nanoparticles exhibit unique size-, shape-, and composition-dependent properties which make them attractive candidates as building blocks for the fabrication of new materials. The optical properties of metal nanoparticles have been heavily studied and will be a focus of some of my work presented in this dissertation. Metal

nanoparticles, such as gold and silver nanoparticles, are characterized by their localized surface plasmon resonance (LSPR).<sup>2</sup> LSPR is the resonant oscillation of conduction band electrons of metal nanoparticles in the presence of an electromagnetic field. The frequency at which the electrons resonate can directly be observed by their absorption at that corresponding wavelength. This LSPR absorption band is highly dependent on the physical shape of the particle, their passivating ligands, and their composition. For example, the LSPR band of gold nanorods can be tuned from the visible to the near-infrared (NIR) simply by adjusting their aspect ratio (**Figure 1.2**).<sup>3</sup>

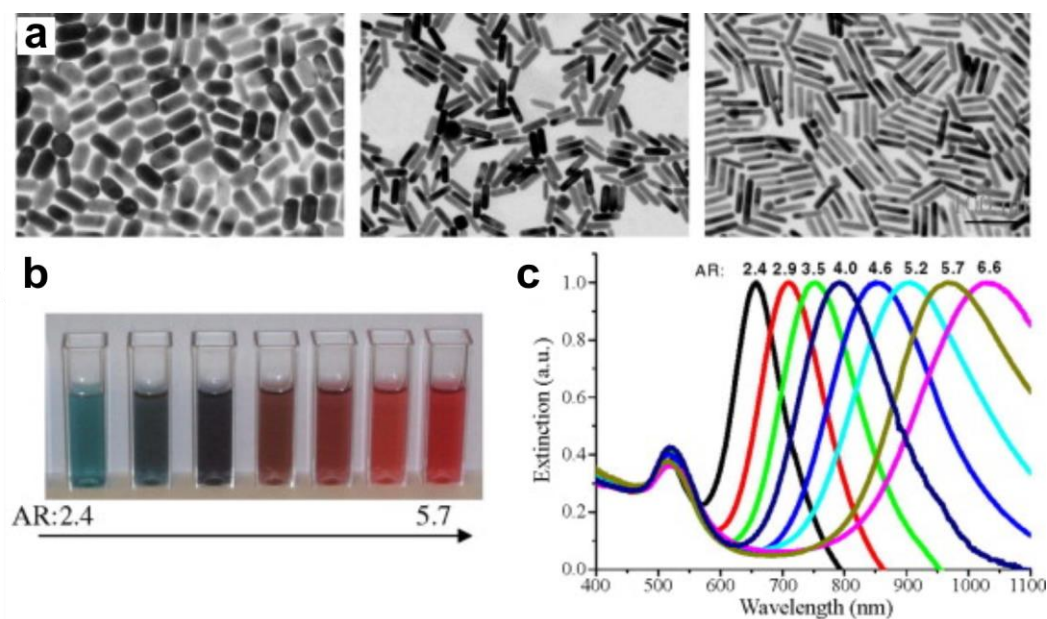


**Figure 1.2.** Tunable optical properties of gold nanorods by changing their aspect ratios. (a) Gold nanorods of different aspect ratios exhibit different dimensions as observed by TEM. (b) Different colors and (c) different LSPR wavelengths associated with colloidal solutions of nanorods of different aspect ratios. (Adapted from ref. 3)

In addition to their size-, shape-, and composition-dependent properties, metallic nanoparticles also exhibit ensemble properties when assembled together. For example, dispersed

and aggregated gold nanoparticles display different optical properties. 15 nm gold particles exhibit an LSPR band at approximately 520 nm. This absorption in the blue-green region of the visible spectrum gives rise to the deep red color that is observed when these particles are suspended in solution. However, under conditions that cause aggregation, a purple colored solution is observed, signifying a red-shift of the LSPR absorption band. This arises due to the plasmonic coupling between neighboring nanoparticles, where the conduction electrons of particles in close proximity oscillate in unison, thereby shifting the LSPR band to longer absorption wavelengths.

Based on the unique, tunable properties of metal nanoparticle-based assemblies, these materials have found applications as optical sensors,<sup>4-6</sup> surface-enhanced Raman spectroscopy (SERS) substrates,<sup>7-10</sup> heterogenous catalysts,<sup>11</sup> therapeutic agents,<sup>8, 12-13</sup> ‘plasmon rulers’,<sup>14-15</sup> and as components in optoelectronic and metamaterial devices.<sup>16-17</sup> Current work in this field is focused on developing methods to rationally arrange nanoparticles into desirable architectures to precisely engineer and optimize their properties.

### **1.2.2 Biomolecule-directed assembly of metallic nanoparticles**

Taking advantage of the intrinsic assembly properties of biomolecules, researchers have employed several different biomolecular building blocks, such as nucleic acids,<sup>16, 18-24</sup> peptides,<sup>25-30</sup> proteins,<sup>31-34</sup> and viruses,<sup>35-37</sup> for directing the ‘bottom-up’ construction of metallic nanoparticles. The unique programmability of biomolecules allows for rational design of assembly architectures and systematic construction of materials with tunable morphologies and properties.

A few examples of biomolecule-directed assembly of metallic nanoparticles are shown in **Figure 1.3**. Recently, the Mirkin group pioneered DNA-based assembly methods of metallic nanoparticles into 3D crystalline nanoparticle superlattices (**Figure 1.3a**).<sup>21-22</sup> Their method takes advantage of the programmable base-pairing interactions between complementary DNA-functionalized nanoparticles. Under thermodynamic control, they show that they can program the assembly of metallic nanoparticles into a variety of different periodic lattices.<sup>21-22</sup> In addition to DNA, viruses and proteins have also been utilized as assembly scaffolds and directing agents for assembling nanoparticles. (**Figure 1.3b,c**).

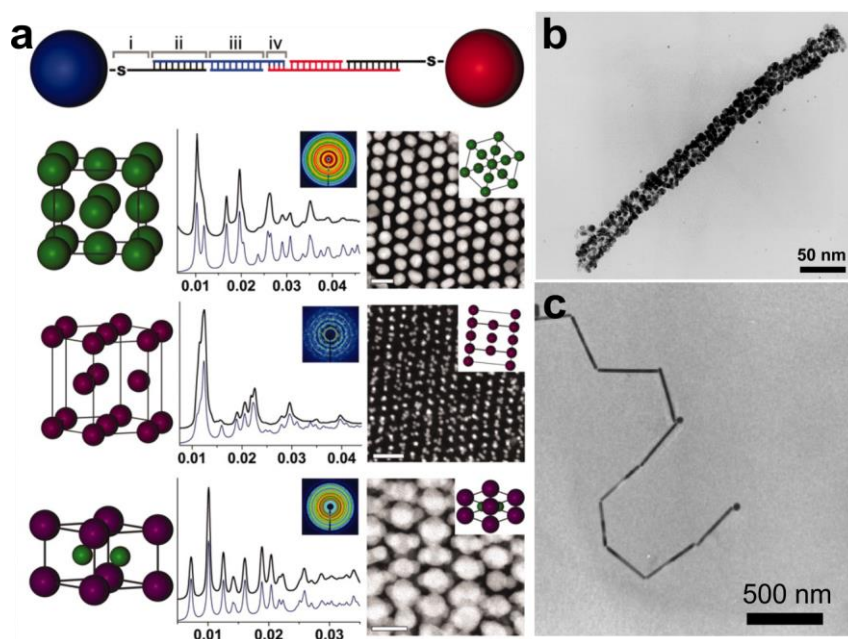


**Figure 1.3.** Examples of biomolecule-directed assemblies of metallic nanoparticles. (a) 3D crystalline nanoparticle superlattices assembled from DNA-functionalized nanoparticles (adapted from ref. 22). (b) Gold nanoparticles decorated onto a tobacco mosaic virus scaffold (adapted from ref. 36). (c) End-to-end assembly of gold nanorods using streptavidin/biotin linkages (adapted from ref. 34).

## 1.3 PEPTIDE-BASED METHOD FOR ASSEMBLING NANOPARTICLE SUPERSTRUCTURES

Over the past decade, the Rosi group has developed a peptide-based approach for assembling nanoparticles into complex and tunable architectures. The methodology centers around the distinctive capabilities of peptide-based molecules and provides a route for designing and assembling nanoparticles into intricate architectures.

### 1.3.1 Assembly and substrate-binding properties of peptides

Peptide self-assembly is promoted by a variety of non-covalent interactions including hydrogen bonding, electrostatics, van der Waals forces, hydrophobic interactions, and  $\pi$ - $\pi$  stacking. Based on the amino acid sequence of the polypeptide chain, these non-covalent interactions can drive the assembly of peptide molecules into various secondary structures such as  $\alpha$ -helices and  $\beta$ -sheets. In addition to the amino acid sequence itself, moieties that provide additional assembly properties can be attached to the N- and C-termini to generate ‘peptide conjugates’. Peptide conjugates often consist of a peptide linked to a hydrophobic group (*e.g.*, aliphatic chain); such peptide conjugates are designed to mimic the assembly properties of amphiphilic peptides. **Figure 1.4** shows several different peptide-based structures with different morphologies that were assembled using peptides and peptide conjugates including nanotubes,<sup>38-39</sup> helical fibers,<sup>40-41</sup> spherical structures,<sup>42-44</sup> and nanosheets.<sup>45-47</sup>



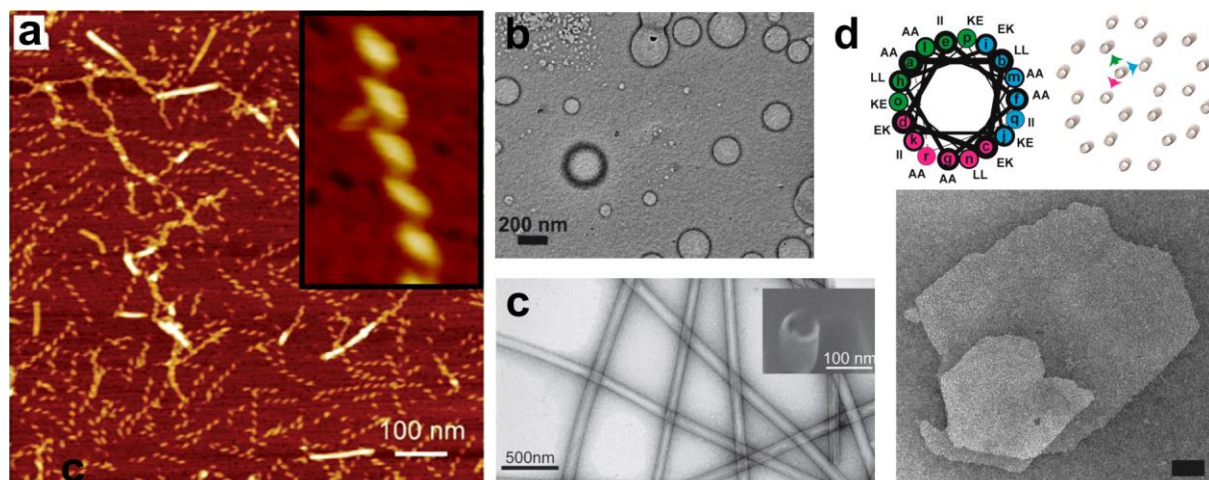


**Figure 1.4.** Various structures assembled from peptides and peptide conjugates. (a) AFM images of KFE8 helical assemblies in aqueous solution (adapted from ref. 41). (b) TEM image of vesicles assembled from BP-A<sub>2</sub>-PEP<sub>Au</sub> (BP = biphenyl, A = alanine) (adapted from ref. 59). (c) TEM and SEM (inset) image of nanotubes assembled from N-lauroyl-A $\beta$ (16-22) assembled in 40% CH<sub>3</sub>CN/water with 0.1% trifluoroacetic acid for 1-2 weeks (adapted from ref. 38). (d) Assembly scheme and TEM image of nanosheets assembled from alpha-helical peptides (scale bar = 200 nm; adapted from ref. 45).

An important feature of peptide-based materials is the ability to tune their morphology and assembly metrics by manipulating their primary sequence. Drawing from the chemically diverse set of amino acid residues, researchers can rationally assemble peptide constructs into materials with programmable physical, mechanical, and chemical properties. Cui *et al.* recently demonstrated the effect of amino acid sequence on the assembly of 1D nanostructures of four constitutionally isomeric tetrapeptide amphiphiles (**Figure 1.5a**).<sup>48</sup> They showed that they could tune the morphology and mechanical properties of 1D assemblies by changing the placement of E and V residues within the tetrapeptide (**Figure 1.5b-d**). For example, they determined that VVEE peptide conjugates assemble into rigid cylindrical fibers, whereas EVEV peptide conjugates assemble into flexible twisted nanoribbons (**Figure 1.5c,d**, respectively). Their results highlight the sequence-dependent properties of peptide-based materials and how simple



modifications to the peptide sequence can have a profound impact on their morphology and mechanical properties.

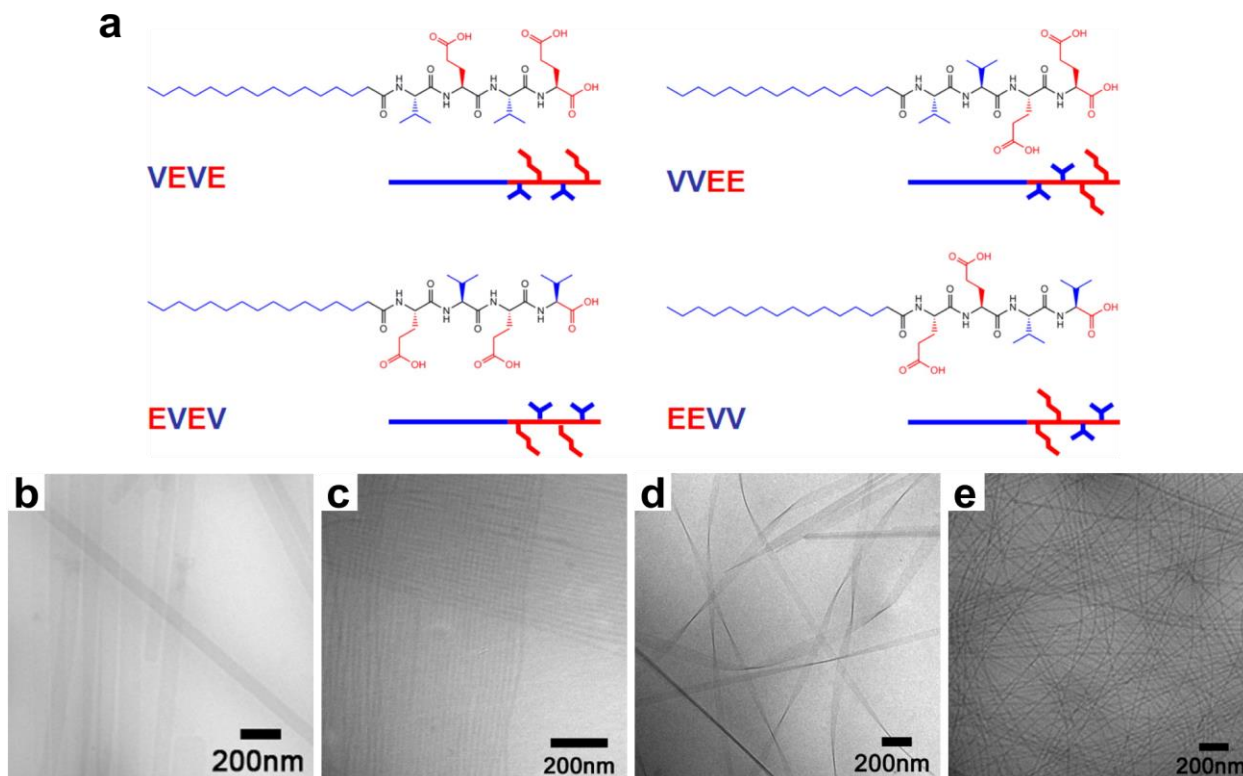


**Figure 1.5.** (a) Molecular structures and schematic representation of isomeric peptide amphiphiles. (b-e) Cryo-TEM images of a variety of 1D nanostructures formed by the designed peptides in water after 2 weeks of incubation at room temperature: (b) nanobelts of VEVE; (c) rigid cylindrical nanofibers of VVEE; (d) twisted nanoribbons of EVEV; and (e) flexible and entangled nanofibers of EEVV. (Adapted from ref. 48)

In addition to their intrinsic self-assembly capabilities, peptides also exhibit substrate recognition capabilities. Synthetic peptides can selectively recognize and bind biological substrates,<sup>49-51</sup> graphene,<sup>52-53</sup> and inorganic surfaces.<sup>54-56</sup> Chiu and co-workers elegantly demonstrated the binding capabilities of two platinum-binding peptides, T7 (TLTTLTN) and S7 (SSFPGPN), for directing the shape-controlled nanocrystal synthesis of platinum nanoparticles

(Figure 1.6).<sup>56</sup> Using phage display, T7 and S7 were identified for their preferential binding onto the [100] and [111] facets of platinum, respectively. They then showed that reduction of platinum in the presence of T7 or S7 directed the growth of nanocrystals into Pt nanocubes or Pt tetrahedra, respectively.

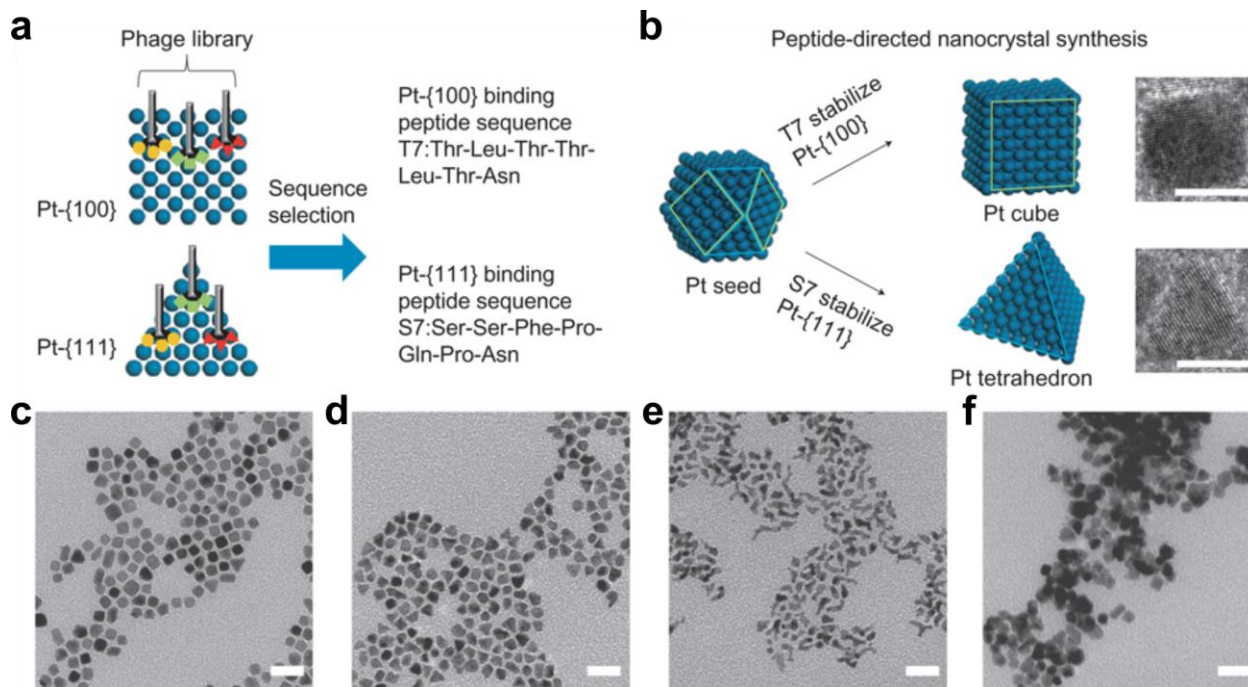


**Figure 1.6.** Biomimetic approach to the predictable synthesis of shaped nanocrystals. (a) Schematic illustration of face-specific peptide sequence selection and nanocrystal synthesis: Pt-[100] binding peptide sequence T7 and Pt-[111] binding peptide sequence S7 are selected against [100] faceted and [111] faceted substrates; (b) facet-specific peptides are used to direct the synthesis of platinum nanocrystal cubes and tetrahedra, respectively. (c) TEM images (scale bar = 20 nm) of platinum nanocrystals obtained in the presence of (c) T7, (d) S7, and (e) BP7A (a peptide previously selected against bulk platinum polycrystalline surfaces). (f) TEM image (scale bar = 20 nm) of platinum nanocrystals obtained in the absence of peptides. All samples were conducted under the same conditions and collected after reacting for 10 min. (Adapted from ref. 56)

### 1.3.2 Methodology background

Exploiting both the self-assembling and inorganic-binding properties of peptides, the Rosi group has developed peptide-based methods for constructing ordered nanoparticle superstructures having tunable structures and properties.<sup>11, 25, 57-65</sup> This method was first successfully realized in 2008, when Chen *et al.* employed a gold-binding peptide conjugate, C<sub>12</sub>-PEP<sub>Au</sub> (C<sub>12</sub> = 12-carbon aliphatic group, PEP<sub>Au</sub> = AYSSGAPPMPF<sup>55</sup>), to direct the assembly of gold nanoparticles.<sup>25</sup> They demonstrated that in the presence of a gold precursor (chloroauric acid, HAuCl<sub>4</sub>) and 4-(2-hydroxyethyl)-1-piperazineethanesulfonic acid (HEPES) buffer, C<sub>12</sub>-PEP<sub>Au</sub> both binds to and directs the assembly of gold nanoparticles into pristine double-helical superstructures (**Figure 1.7**). Since this work, the Rosi group has continued to develop their methodology with emphasis on: 1) exploring the construction of new nanoparticle assembly architectures, 2) controlling the structure metrics of nanoparticle assemblies, and 3) studying their structure-dependent properties.

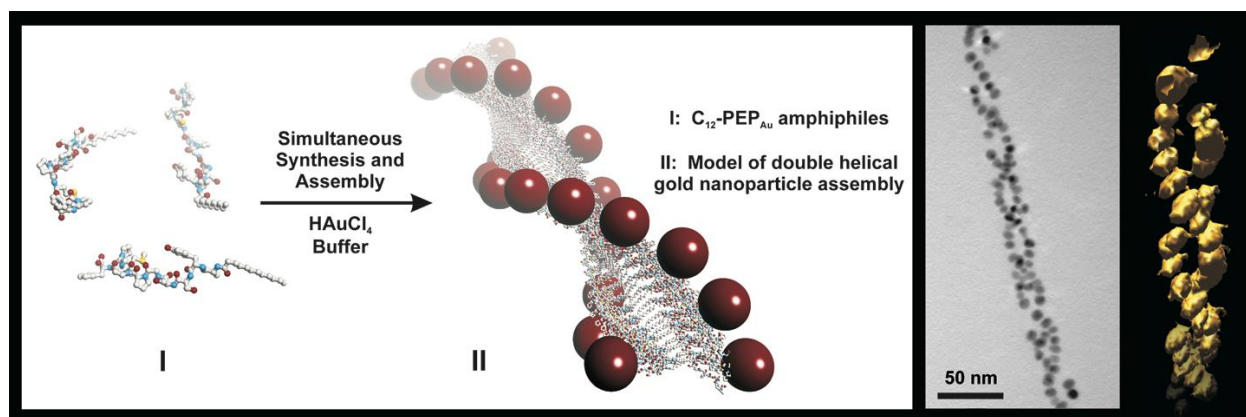


**Figure 1.7.** Left-handed gold nanoparticle double helices are synthesized and assembled directly in a reaction containing HEPES buffer solutions of chloroauric acid and C<sub>12</sub>-PEP<sub>Au</sub>. TEM image and electron tomography data of the double-helical gold nanoparticle superstructure are shown. (Adapted from ref. 25)

The central component of the peptide-based nanoparticle assembly methodology is the peptide conjugate (**Figure 1.8**). As mentioned above, the peptide conjugate plays a dual role in that it functions both as the molecular self-assembling building block *and* as a nanoparticle binding agent. Therefore, in order to target new assembly architectures and control their structure metrics (emphasis 1 and 2), new peptide conjugate molecules must be employed. To address this, several past and ongoing studies have focused on modifying the peptide conjugate. These modifications include: varying the R-group,<sup>62</sup> incorporating additional residues to the N- and C-termini,<sup>65</sup> controlling amino acid chirality,<sup>61</sup> varying the peptide valency,<sup>62</sup> modifying the chemical oxidation state of residues,<sup>63</sup> and utilizing different peptide sequences to bind particles of different compositions (**Figure 1.8**).<sup>11</sup>

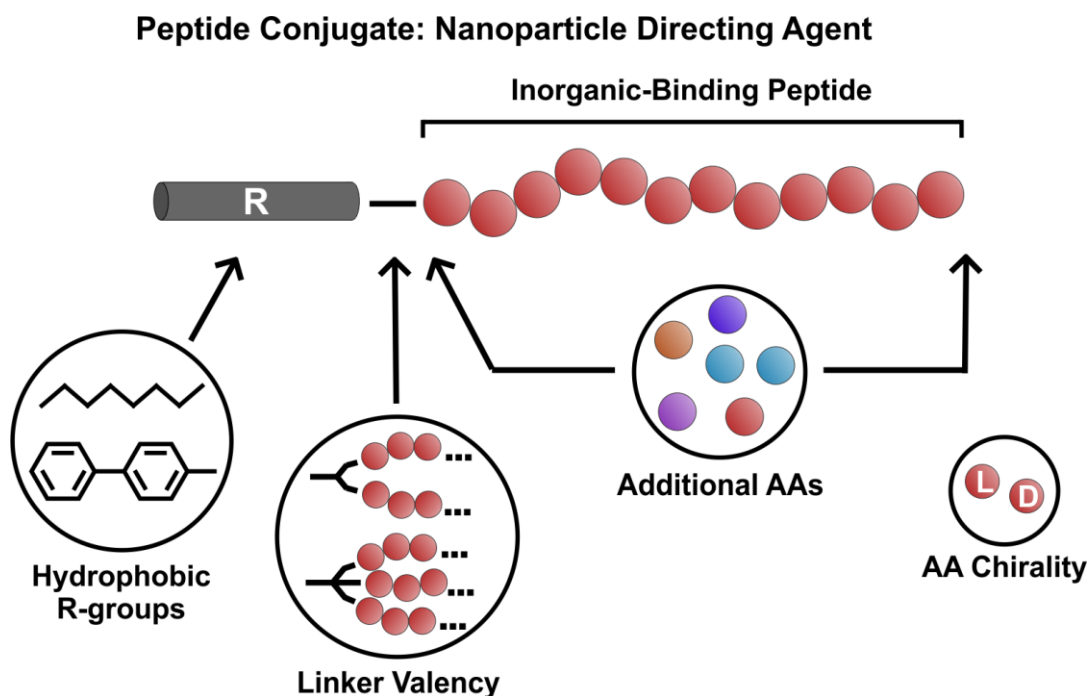


**Figure 1.8.** The peptide conjugate and the various modifications for tuning its assembly.

### 1.3.3 Chiroptical properties of helical nanoparticle superstructures

In addition to assembling nanoparticle superstructures, the Rosi group has also investigated the properties and applications of these hybrid structures (emphasis 3). As mentioned in Section 1.2.1, the optical properties of metal nanoparticles are dependent not only on their size, shape, and composition, but also on their spatial arrangement with respect to one another. This was clearly evidenced by the interesting chiroptical properties of the aforementioned double-helical gold nanoparticle superstructures (**Figure 1.9**). Song *et. al.* showed that gold nanoparticles arranged into a chiral superstructure give rise to a circular dichroism response at the plasmonic wavelength of the nanoparticle assembly.<sup>61</sup> This chiroptical property has sparked interest because of their potential applications as chiroptical sensors,<sup>66-68</sup> circular polarizers,<sup>69-70</sup> and metamaterials.<sup>17, 69-70</sup>

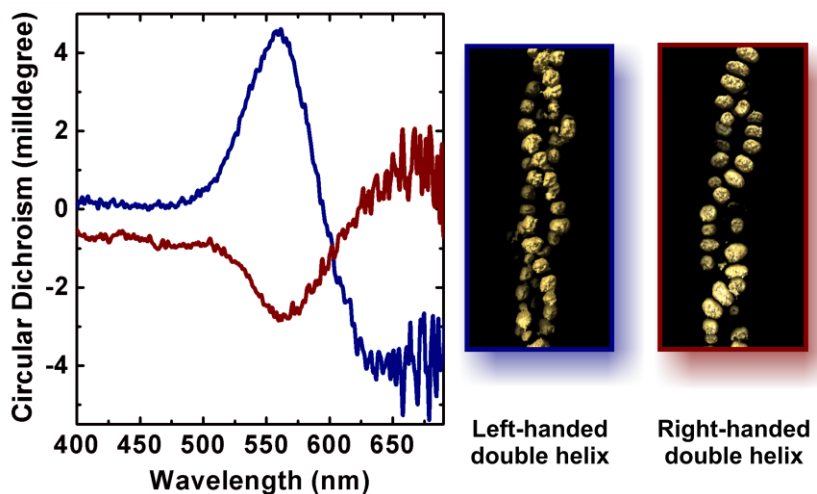


**Figure 1.9.** Circular dichroism spectra for left- and right-handed gold nanoparticle double helices (blue and red line, respectively) and the 3D surface rendering of the tomographic volumes revealing the left- and right-handed nature of the double helices are shown. (Adapted from ref. 61)

## 1.4 OBJECTIVES AND OUTLINES

Before I joined the lab in 2012, much of the research conducted in the group centered around exploring new nanoparticle superstructures through manipulation of the peptide conjugate building block as described in Section 1.3.2. This work provided a foundation for my dissertation studies aimed at i) rationally controlling and tuning nanoparticle assembly architectures, ii) systematically modifying the surface chemistry of nanoparticle superstructures, and iii) developing a more complete understanding of the peptide assembly scaffold underlying the nanoparticle superstructure. In addition, prior peptide conjugates explored in the Rosi group incorporated only simple R-groups (aliphatic carbons or biphenyl molecules). While these proved useful in assembling many interesting and previously unobserved nanoparticle superstructures, these moieties are limited as they carry no encoded information that could be used, for example, to build responsive or dynamic assemblies. As a last aim, I explored the assembly of peptide conjugates having functional, responsive R-groups.

Throughout my PhD work, I specifically addressed these areas of opportunity. In Chapter 2, I describe the use of multivalent peptide conjugates to control the structure metrics of double-helical gold nanoparticle superstructures, such as their pitch (*Langmuir* **2015**, *31*, 9492-9501). In Chapter 3, I describe the construction of chiral single-helical nanoparticle superstructures that exhibit intense chiroptical activity, and I develop a comprehensive peptide assembly model that accounts for their assembly (*J. Am. Chem. Soc.* **2016**, *138*, 13655-13663). Chapter 4 describes new methods for tuning the structures of hollow spherical gold nanoparticle superstructures including nanoparticle coverage density and sphere diameters. I also determine routes to stabilize their assembly and tune their surface chemistry (*manuscript in preparation*). Finally, in Chapter 5, I describe a new research direction that involves the design, synthesis, and assembly of

peptide-oligonucleotide chimeras (POCs) (*manuscript submitted*). I develop design rules that govern their assembly and show that one can logically alter and predict their morphology.

## **2.0 ADJUSTING THE METRICS OF 1D HELICAL GOLD NANOPARTICLE SUPERSTRUCTURES USING MULTIVALENT PEPTIDE CONJUGATES**

This work, written in collaboration with Joseph Slocik, Martin G. Blaber, George C. Schatz, Rajesh Naik, and Nathaniel L. Rosi\*, is reprinted with permission from *Langmuir* **2015**, *31*, 9492-9501. Copyright 2015, American Chemical Society. The supporting information is found in Appendix A.

Dr. Joseph Slocik performed the QCM binding studies. Dr. Martin G. Blaber conducted the computational modeling studies of the effect of pitch on CD intensity.

### **2.1 INTRODUCTION**

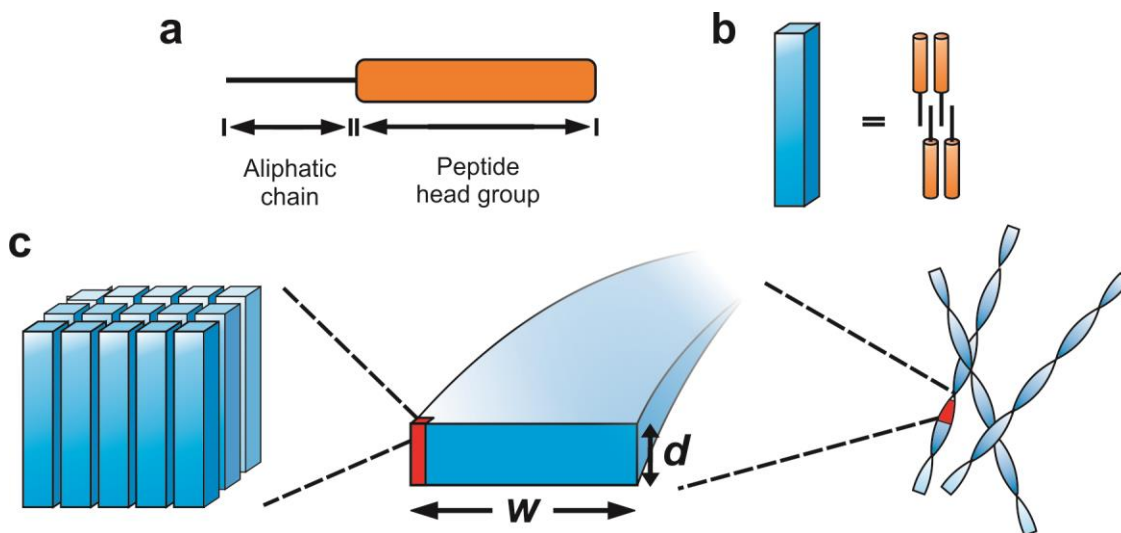
As mentioned in Chapter 1, nanoparticle superstructures exhibit collective properties that are dependent on their morphology and structure.<sup>71-75</sup> Therefore, methods that allow one to tune and optimize these collective properties are important for proposed applications. There are numerous studies that explore soft assembly structure as a function of peptide sequence and peptide terminus modification,<sup>48, 76-78</sup> however, few accounts exploit these highly tunable nanoscale soft assemblies as a means for designing programmable, precisely ordered nanoparticle superstructures.<sup>58, 61, 65</sup>



Previously, we used a peptide conjugate, C<sub>12</sub>-PEP<sub>Au</sub> to direct the assembly of chiral gold nanoparticle double helices.<sup>25</sup> These assemblies exhibit a collective plasmonic circular dichroism (CD) signal arising from the chiral arrangement of discrete achiral nanoparticles.<sup>61</sup> Chiral nanoparticles and chiral nanoparticle assemblies are receiving significant interest, and tuning their chiroptical properties is important for potential applications.<sup>17, 66-68</sup> However, adjusting the structure of helical nanoparticle assemblies has not been extensively explored experimentally. Govorov and co-workers computationally investigated the chiroptical signal of “ideal” nanoparticle helices as a function of defects and helical structure parameters.<sup>79</sup> They showed that adjusting the pitch and other metrics of the helix modulates the strength of the CD signal. Moreover, computational modeling of the CD behavior of double-helical gold nanoparticle superstructures prepared by our group indicates that the CD signal strength is dependent on structural parameters including helix pitch (**Figure S2.37**) and nanoparticle size.<sup>61</sup> Motivated by these computational studies that illustrate the need for fine-tuning helical nanoparticle superstructures, we aimed to use peptides to systematically control the structural parameters of double-helical gold nanoparticle assemblies via simple synthetic modifications to the peptide conjugate. Specifically, we address two important design factors of acylated peptide conjugates on their peptide assembly: (i) the length of the aliphatic tail and (ii) the steric requirements of the peptide. We present a study that explores the effect of these two factors on various structural metrics of assembled fibers and helical gold nanoparticle superstructures.

## 2.2 RESULTS AND DISCUSSION

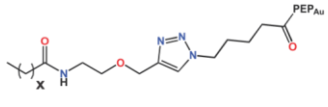
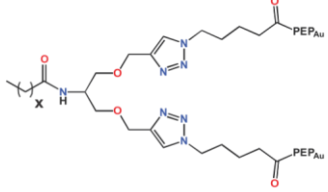
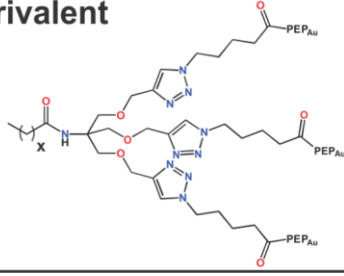
In previous research, C<sub>12</sub>-PEP<sub>Au</sub> conjugates assemble into 1D twisted fibers.<sup>25</sup> From structure and spectroscopy studies, it was determined that the handedness of the fibers derives from the chirality of the peptides,<sup>61</sup> which pack laterally perpendicular to the fiber axis. A reported assembly model that is consistent with these observations is illustrated in **Figure 2.10**.<sup>76</sup> In this model, the peptide conjugates associate in an end-to-end fashion through hydrophobic interactions between aliphatic tails and amino acid side chain interactions between the peptide head groups to form layers with a certain width ( $w$ ) that span the width of the fiber. Of course, this ignores restructuring that likely occurs because the structural model allows for direct exposure of the aliphatic tails to water. The fiber thickness,  $d$ , is determined by the length of the peptide bilayer and should remain relatively constant.



**Figure 2.10.** (a) Peptide conjugate consisting of a peptide headgroup and an aliphatic chain; (b) peptide conjugates associate in an end-to-end fashion via hydrophobic interactions between aliphatic tails and amino acid side chain interactions between peptide headgroups; (c) assembly scheme illustrating the assembly of twisted fibers from peptide conjugate building blocks (fiber width,  $w$ , and fiber thickness,  $d$ , are indicated).

With this model as the assembly basis, we designed a series of peptide conjugates in which we varied the number of peptide head groups to systematically control the sterics of the peptide portion. Within this series, we also adjusted the length of the aliphatic tail. In total, we prepared a new family of 12 peptide conjugate molecules containing either 1, 2, or 3 peptide head groups and having either 12-, 14-, 16-, or 18-carbon aliphatic chains attached to their N-termini: monovalent conjugates C<sub>12</sub>-(PEP<sub>Au</sub>)<sub>1</sub>, C<sub>14</sub>-(PEP<sub>Au</sub>)<sub>1</sub>, C<sub>16</sub>-(PEP<sub>Au</sub>)<sub>1</sub>, C<sub>18</sub>-(PEP<sub>Au</sub>)<sub>1</sub>; divalent conjugates C<sub>12</sub>-(PEP<sub>Au</sub>)<sub>2</sub>, C<sub>14</sub>-(PEP<sub>Au</sub>)<sub>2</sub>, C<sub>16</sub>-(PEP<sub>Au</sub>)<sub>2</sub>, C<sub>18</sub>-(PEP<sub>Au</sub>)<sub>2</sub>; and trivalent conjugates C<sub>12</sub>-(PEP<sub>Au</sub>)<sub>3</sub>, C<sub>14</sub>-(PEP<sub>Au</sub>)<sub>3</sub>, C<sub>16</sub>-(PEP<sub>Au</sub>)<sub>3</sub>, C<sub>18</sub>-(PEP<sub>Au</sub>)<sub>3</sub> (**Table 1.1**). We used Cu(I)-catalyzed azide-alkyne cycloaddition “click” chemistry to efficiently synthesize the conjugates.<sup>80-81</sup> The conjugates were prepared by reacting N-terminal azido-modified PEP<sub>Au</sub> (N<sub>3</sub>-PEP<sub>Au</sub> = N<sub>3</sub>-C<sub>4</sub>H<sub>8</sub>CO-AYSSGAPPMPPF, **Figure S2.38**) with aliphatic tails (C<sub>12</sub>, C<sub>14</sub>, C<sub>16</sub>, or C<sub>18</sub>) functionalized with 1, 2, or 3 alkyne groups (**Figure S2.39**). The identity of the alkyne substrates was confirmed using <sup>1</sup>H NMR spectroscopy. The peptide conjugates were purified using reverse-phase high-performance liquid chromatography (HPLC), and their composition was confirmed using mass spectrometry (**Figure S2.40**, **Figure S2.41**).

**Table 1.1.** Family of 12 peptide conjugate molecules with varying number of peptide head groups and varying aliphatic tail lengths

Monovalent											
	<table border="1"> <thead> <tr> <th>X</th> <th>Conjugate</th> </tr> </thead> <tbody> <tr> <td>10</td> <td><math>C_{12}-(PEP_{Au})_1</math></td> </tr> <tr> <td>12</td> <td><math>C_{14}-(PEP_{Au})_1</math></td> </tr> <tr> <td>14</td> <td><math>C_{16}-(PEP_{Au})_1</math></td> </tr> <tr> <td>16</td> <td><math>C_{18}-(PEP_{Au})_1</math></td> </tr> </tbody> </table>	X	Conjugate	10	$C_{12}-(PEP_{Au})_1$	12	$C_{14}-(PEP_{Au})_1$	14	$C_{16}-(PEP_{Au})_1$	16	$C_{18}-(PEP_{Au})_1$
	X	Conjugate									
	10	$C_{12}-(PEP_{Au})_1$									
	12	$C_{14}-(PEP_{Au})_1$									
14	$C_{16}-(PEP_{Au})_1$										
16	$C_{18}-(PEP_{Au})_1$										
Divalent											
	<table border="1"> <thead> <tr> <th>X</th> <th>Conjugate</th> </tr> </thead> <tbody> <tr> <td>10</td> <td><math>C_{12}-(PEP_{Au})_2</math></td> </tr> <tr> <td>12</td> <td><math>C_{14}-(PEP_{Au})_2</math></td> </tr> <tr> <td>14</td> <td><math>C_{16}-(PEP_{Au})_2</math></td> </tr> <tr> <td>16</td> <td><math>C_{18}-(PEP_{Au})_2</math></td> </tr> </tbody> </table>	X	Conjugate	10	$C_{12}-(PEP_{Au})_2$	12	$C_{14}-(PEP_{Au})_2$	14	$C_{16}-(PEP_{Au})_2$	16	$C_{18}-(PEP_{Au})_2$
	X	Conjugate									
	10	$C_{12}-(PEP_{Au})_2$									
	12	$C_{14}-(PEP_{Au})_2$									
14	$C_{16}-(PEP_{Au})_2$										
16	$C_{18}-(PEP_{Au})_2$										
Trivalent											
	<table border="1"> <thead> <tr> <th>X</th> <th>Conjugate</th> </tr> </thead> <tbody> <tr> <td>10</td> <td><math>C_{12}-(PEP_{Au})_3</math></td> </tr> <tr> <td>12</td> <td><math>C_{14}-(PEP_{Au})_3</math></td> </tr> <tr> <td>14</td> <td><math>C_{16}-(PEP_{Au})_3</math></td> </tr> <tr> <td>16</td> <td><math>C_{18}-(PEP_{Au})_3</math></td> </tr> </tbody> </table>	X	Conjugate	10	$C_{12}-(PEP_{Au})_3$	12	$C_{14}-(PEP_{Au})_3$	14	$C_{16}-(PEP_{Au})_3$	16	$C_{18}-(PEP_{Au})_3$
	X	Conjugate									
	10	$C_{12}-(PEP_{Au})_3$									
	12	$C_{14}-(PEP_{Au})_3$									
14	$C_{16}-(PEP_{Au})_3$										
16	$C_{18}-(PEP_{Au})_3$										

### 2.2.1 Soft assembly of peptide conjugates

Soft assembly studies were performed to determine how the conjugates assemble in aqueous buffer. Each conjugate was dissolved in a mixture of HEPES buffer (pH 7.3) and citrate. These conditions were chosen because they are used for the nanoparticle synthesis and assembly experiments (*vide infra*). The  $-COOH$  at the C-termini of the peptides are deprotonated at pH 7.3, so  $CaCl_2$  was added to the solutions to provide  $Ca^{2+}$  ions that could shield the negatively charged carboxylates and promote assembly of the conjugates.<sup>82</sup> After each solution was allowed to sit at room temperature for 1 day, TEM was used to observe and characterize the soft

assemblies (**Figure 2.11**). Depending on the conjugate, either 1D fibers or small spheres/aggregate structures were observed. Fibers were the predominant product for all the monovalent and divalent conjugates, except for  $C_{12}-(PEP_{Au})_2$ , for which no clear assembled structures were observed. Twisted ribbon fiber morphologies were clearly observed for the monovalent conjugates. In addition, some spherical structures were observed for  $C_{12}-(PEP_{Au})_1$  and  $C_{14}-(PEP_{Au})_2$ . Generally, more fibers were observed under TEM as the length of the aliphatic tail increases. Only small spherical assemblies/aggregate structures were observed for the trivalent conjugates. We concluded from these assembly studies that the propensity for a conjugate to assemble into fibers is dictated by the relative ratio of its hydrophobic (aliphatic tail) and hydrophilic (peptide) components. As the length of the hydrophobic tail increases, the likelihood of forming fibers increases. If the aliphatic tail is too short relative to the size of the peptide head group, the conjugates do not assemble into fibers. In these cases, to maximize the interactions between the hydrophobic tails, the peptide conjugates assemble into spherical/aggregate structures. The relative solubilities of the conjugates are also important. The peptide head group is relatively soluble due to numerous hydrogen bonding sites along the peptide; therefore, increasing the peptide valency would decrease the overall hydrophobicity of the conjugate and lower the driving force for assembly.

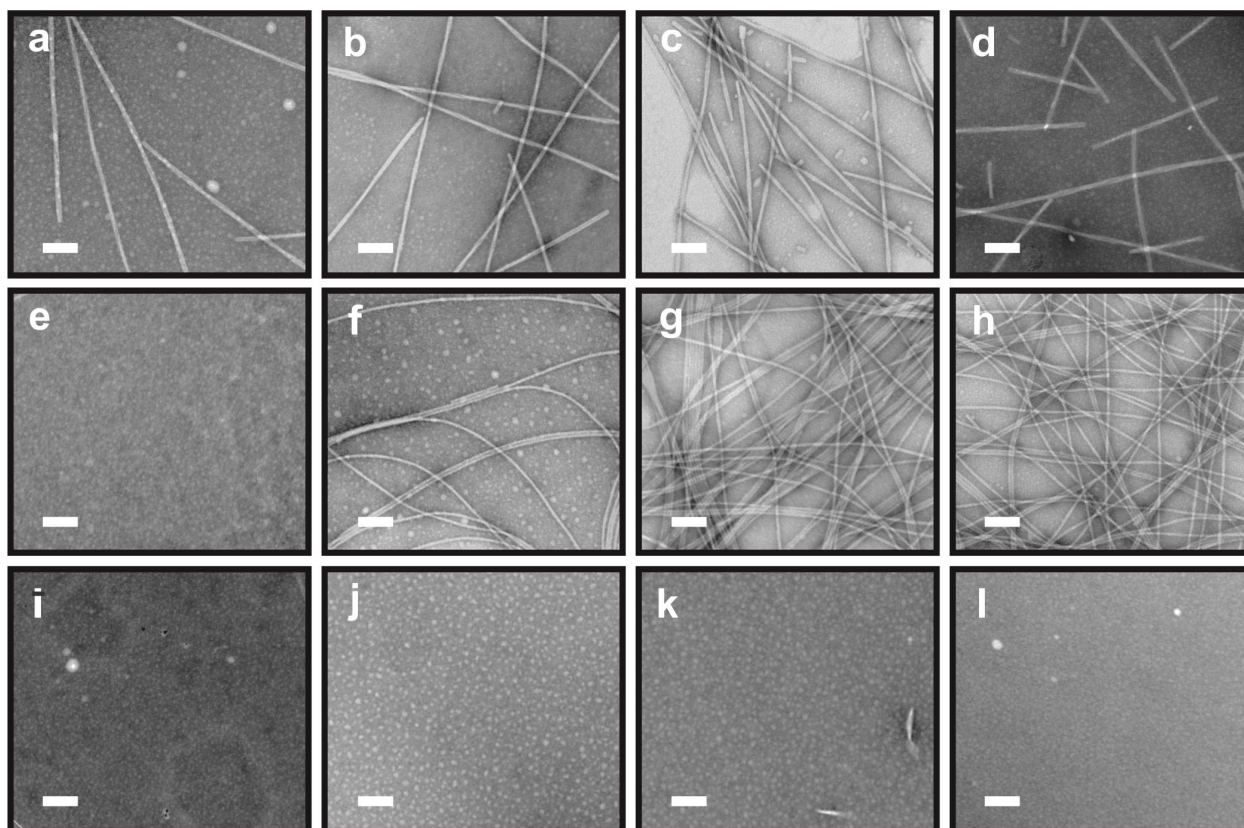


**Figure 2.11.** Negatively stained TEM images of the peptide conjugate soft assemblies as a function of peptide valency and aliphatic chain length (scale bar = 100 nm): (a)  $C_{12}$ -(PEP<sub>Au</sub>)<sub>1</sub>, (b)  $C_{14}$ -(PEP<sub>Au</sub>)<sub>1</sub>, (c)  $C_{16}$ -(PEP<sub>Au</sub>)<sub>1</sub>, (d)  $C_{18}$ -(PEP<sub>Au</sub>)<sub>1</sub>, (e)  $C_{12}$ -(PEP<sub>Au</sub>)<sub>2</sub>, (f)  $C_{14}$ -(PEP<sub>Au</sub>)<sub>2</sub>, (g)  $C_{16}$ -(PEP<sub>Au</sub>)<sub>2</sub>, (h)  $C_{18}$ -(PEP<sub>Au</sub>)<sub>2</sub>, (i)  $C_{12}$ -(PEP<sub>Au</sub>)<sub>3</sub>, (j)  $C_{14}$ -(PEP<sub>Au</sub>)<sub>3</sub>, (k)  $C_{16}$ -(PEP<sub>Au</sub>)<sub>3</sub>, and (l)  $C_{18}$ -(PEP<sub>Au</sub>)<sub>3</sub>.

Having established that the monovalent and divalent conjugates assemble into fibers, we next examined how valency and aliphatic tail length affect fiber width, thickness, and pitch. Fiber widths were measured from the TEM images (**Figure 2.12**). Fibers assembled from divalent conjugates had narrower widths than those assembled from monovalent conjugates, and in both cases the aliphatic tail length does not significantly affect the fiber width. This observation is consistent with the reported model (**Figure 2.10**). The fiber width correlates with the extent of lateral packing, and the monovalent conjugates can presumably assemble more easily laterally (**Figure 2.13a**) compared to the divalent conjugates (**Figure 2.13b**) because their

peptide head group has a smaller steric requirement. This allows for more favorable side-by-side packing for the monovalent conjugates and greater hydrophobic interactions between the aliphatic tails compared to the divalent conjugates. Peptide conjugate packing within the assemblies was studied using attenuated total reflectance Fourier-transform infrared (ATR-FTIR) spectroscopy. IR spectroscopy can provide information about the internal structure of the fibers.<sup>83</sup> Briefly, C<sub>18</sub>-(PEP<sub>Au</sub>)<sub>1</sub>, C<sub>18</sub>-(PEP<sub>Au</sub>)<sub>2</sub>, and C<sub>18</sub>-(PEP<sub>Au</sub>)<sub>3</sub> were dissolved in a 1:1 mixture of CH<sub>3</sub>CN and Nanopure water (NP H<sub>2</sub>O), and the solution was directly drop-cast onto the ATR-FTIR substrate. The solution was allowed to slowly evaporate to induce assembly. Both C<sub>18</sub>-(PEP<sub>Au</sub>)<sub>1</sub> and C<sub>18</sub>-(PEP<sub>Au</sub>)<sub>2</sub> formed fibers, while C<sub>18</sub>-(PEP<sub>Au</sub>)<sub>3</sub> formed spherical structures (**Figure S2.42**). The signals observed at 2920, 2924, and 2925 cm<sup>-1</sup> for C<sub>18</sub>-(PEP<sub>Au</sub>)<sub>1</sub>, C<sub>18</sub>-(PEP<sub>Au</sub>)<sub>2</sub>, C<sub>18</sub>-(PEP<sub>Au</sub>)<sub>3</sub>, respectively, correspond to C-H vibrations (**Figure 2.13d**). The signal for C<sub>18</sub>-(PEP<sub>Au</sub>)<sub>1</sub>

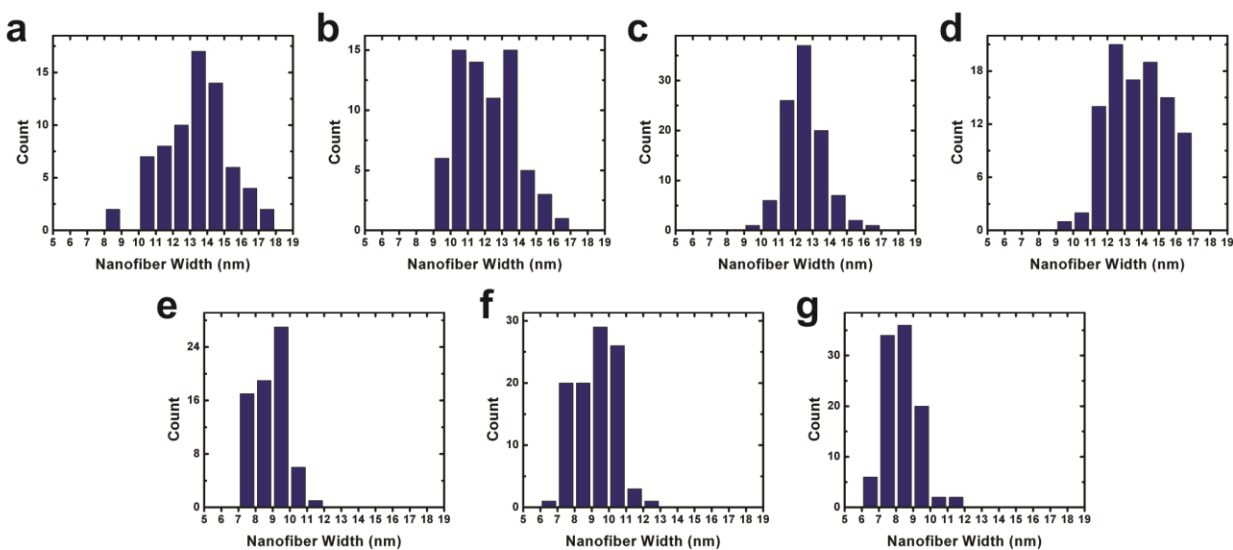


**Figure 2.12.** Nanofiber width distribution for (a) C<sub>12</sub>-(PEP<sub>Au</sub>)<sub>1</sub>, 12.6 ± 1.3 nm based on 60 counts; (b) C<sub>14</sub>-(PEP<sub>Au</sub>)<sub>1</sub>, 12.1 ± 1.7 nm based on 70 counts; (c) C<sub>16</sub>-(PEP<sub>Au</sub>)<sub>1</sub>, 12.6 ± 1.1 nm based on 100 counts; (d) C<sub>18</sub>-(PEP<sub>Au</sub>)<sub>1</sub>, 13.8 ± 1.1 nm based on 100 counts; (e) C<sub>14</sub>-(PEP<sub>Au</sub>)<sub>2</sub>, 8.9 ± 0.9 nm based on 70 counts; (f) C<sub>16</sub>-(PEP<sub>Au</sub>)<sub>2</sub>, 9.3 ± 1.2 nm based on 100 counts; and (g) C<sub>18</sub>-(PEP<sub>Au</sub>)<sub>2</sub>, 8.3 ± 0.9 nm based on 100 counts.

is the same for what is observed for crystalline polymethylene chains ( $\nu \sim 2920 \text{ cm}^{-1}$ ), and the signals for  $\text{C}_{18}\text{-(PEP}_{\text{Au}})_2$  and  $\text{C}_{18}\text{-(PEP}_{\text{Au}})_3$  are closer to what is observed for the liquid state ( $\nu \sim 2928 \text{ cm}^{-1}$ ).<sup>84-85</sup> These data suggest a greater amount of disorder within the aliphatic core of the divalent and trivalent peptide conjugate assemblies in comparison to the monovalent peptide conjugate assemblies, which is consistent with the assembly model and our fiber width measurements. Specifically, we expect greater order in the monovalent conjugate assemblies because the conjugates can more effectively pack together (**Figure 2.13a**) than the divalent (**Figure 2.13b**) or trivalent conjugates (**Figure 2.13c**). This efficient packing leads to better lateral assembly and larger fiber widths.

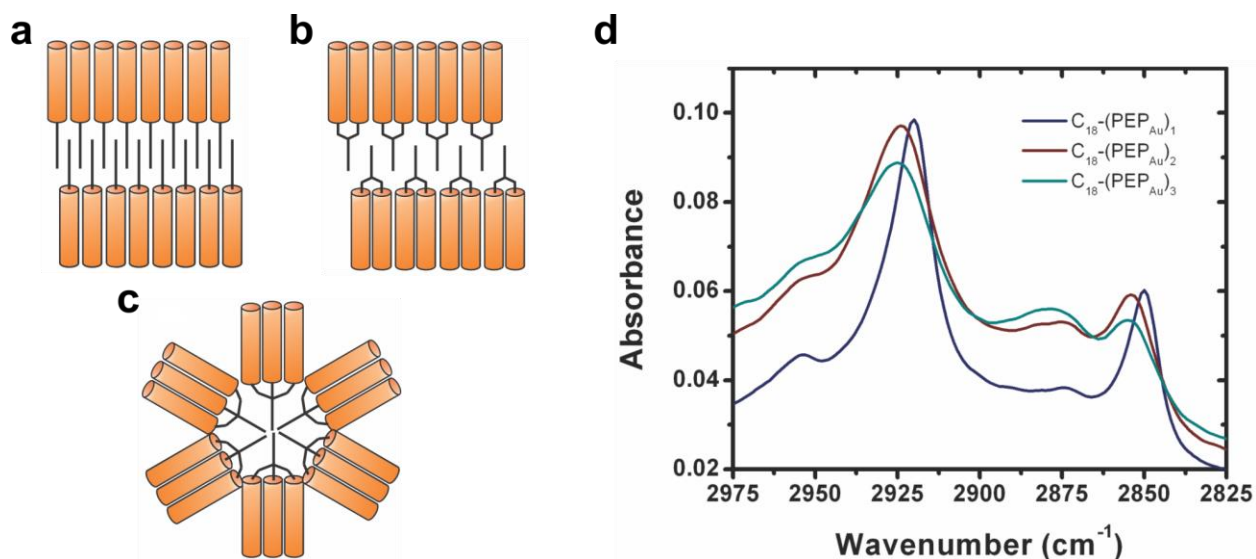


**Figure 2.13.** Packing model of (a)  $\text{C}_{18}\text{-(PEP}_{\text{Au}})_1$ , (b)  $\text{C}_{18}\text{-(PEP}_{\text{Au}})_2$ , and  $\text{C}_{18}\text{-(PEP}_{\text{Au}})_3$  assemblies. (d) C-H vibration bands in the IR spectra of  $\text{C}_{18}\text{-(PEP}_{\text{Au}})_1$  (blue line),  $\text{C}_{18}\text{-(PEP}_{\text{Au}})_2$  (red line), and  $\text{C}_{18}\text{-(PEP}_{\text{Au}})_3$  (green line) assemblies.

From the TEM images the monovalent conjugates clearly assemble into twisted fibers. In these cases, the fiber thickness ( $d$  in **Figure 2.10**) could be measured at the twist point where the



width of the fiber is aligned perpendicular to the surface of the TEM grid (**Figure 2.14a**). The fiber thicknesses were  $\sim 9$  nm and remained relatively consistent between assemblies, regardless of aliphatic tail length (**Figure 2.14b-e**). However, because the AFM data indicate that the divalent fibers are twisted (*vide infra*), we speculate that the thickness ( $d$ ) and the width ( $w$ ) are nearly the same ( $\sim 9$  nm).

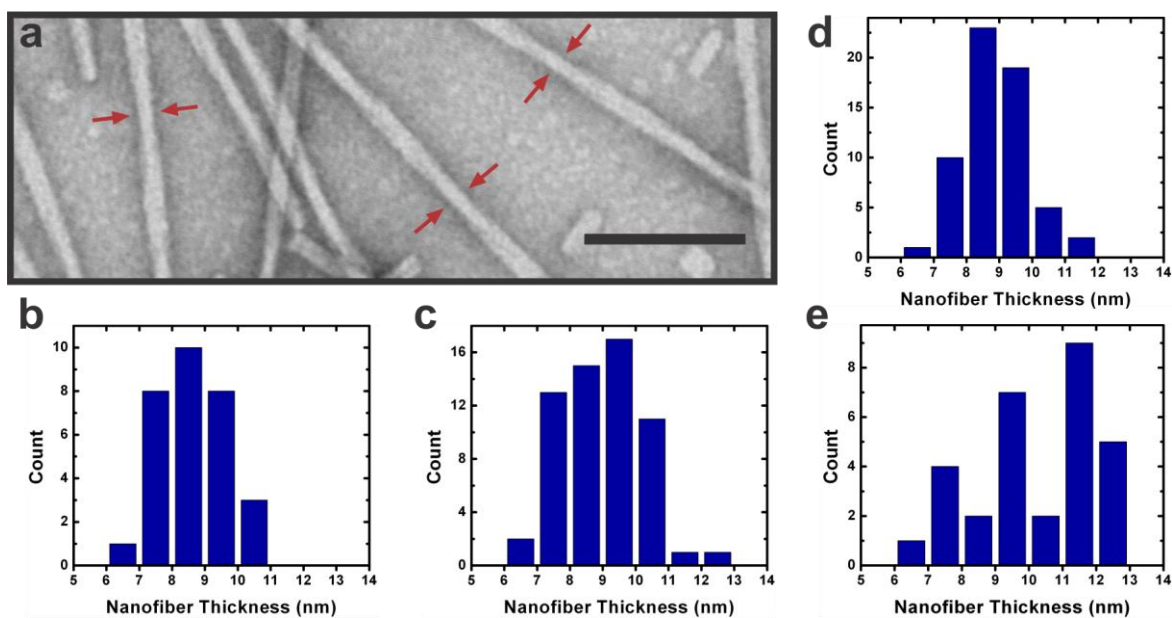


**Figure 2.14.** (a) TEM image showing the twist points used to measure the fiber thickness (scale bar = 100 nm). Fiber thickness distribution of (b) C<sub>12</sub>-(PEPAu)<sub>1</sub>:  $8.7 \pm 1.0$  based on 30 counts; (c) C<sub>14</sub>-(PEPAu)<sub>1</sub>:  $8.9 \pm 1.2$  based on 60 counts; (d) C<sub>16</sub>-(PEPAu)<sub>1</sub>:  $8.8 \pm 0.9$  based on 60 counts; (e) C<sub>18</sub>-(PEPAu)<sub>1</sub>:  $10.3 \pm 1.9$  based on 30 counts.

TEM and AFM were used to study the fiber helicity (**Figure S2.43-S2.50**). From AFM, helical segments of the fibers were analyzed to determine their pitch. The fibers assembled from C<sub>12</sub>-(PEPAu)<sub>1</sub>, C<sub>14</sub>-(PEPAu)<sub>1</sub>, C<sub>16</sub>-(PEPAu)<sub>1</sub>, and C<sub>18</sub>-(PEPAu)<sub>1</sub> had average pitch values of  $186 \pm 13$  nm,  $196 \pm 11$  nm,  $214 \pm 7$  nm, and  $238 \pm 30$  nm, respectively (**Figure S2.44-S2.47**). Because these twisted fibers were sufficiently wide, TEM could also be used to measure their pitch

(**Figure S2.43**). For the divalent conjugates,  $C_{16}-(PEP_{Au})_2$  and  $C_{18}-(PEP_{Au})_2$ , the average pitch measured from AFM was  $178 \pm 20$  nm and  $184 \pm 15$  nm, respectively (**Figure S2.49** and **Figure S2.50**). We were not able to observe fibers for  $C_{14}-(PEP_{Au})_2$  (**Figure S2.48**); instead, spherical structures were observed. We attribute this to the low yield of fibers formed for this conjugate compared to  $C_{16}-(PEP_{Au})_2$  and  $C_{18}-(PEP_{Au})_2$ , based on the TEM data. From these data, it was determined that the pitch i) increases with increasing aliphatic chain length; and ii) decreases with increasing peptide valency. These results are consistent with previous reports where larger fiber width leads to twisted fibers having longer pitch.<sup>40, 76</sup> To summarize, monovalent conjugates, which have larger fiber widths (more lateral packing) are less prone to twisting than their divalent counterparts, which have narrower widths.

### 2.2.2 Nanoparticle assembly studies

After studying the soft assembly behavior of the fibers, we proceeded to prepare nanoparticle assemblies using the peptide conjugates. The peptide conjugates were dissolved in a mixture of HEPES buffer and citrate. HEPES functions as the primary reducing agent for the gold ions and assists in dissolving the peptide conjugates.<sup>55, 86</sup> An aliquot of a solution of  $HAuCl_4$  in 1.0 M TEAA buffer was added and the resulting solution was vortexed and then left undisturbed at room temperature for several hours. Nanoparticle assemblies were observed by TEM (**Figure 2.15**). The morphology of the nanoparticle assemblies formed from the different peptide conjugates corresponds to the morphology of the respective soft assembly structures. 1D nanoparticle assemblies were observed for the conjugates that assembled into 1D fibers; randomly distributed nanoparticles were observed for the conjugates that did not assemble into fibers. In previous work, we found that conjugates that assemble rapidly into fibers tend to yield

poorly-formed nanoparticle superstructures with irregular particle shapes and diameters.<sup>58</sup> On the other hand, conjugates that assemble more slowly tend to yield more well-defined superstructures with clear morphological features and regular particle diameters.<sup>25</sup> In cases where conjugates assemble very slowly, either no nanoparticle assemblies or rather ill-formed assemblies are observed. A preponderance of evidence, both published and unpublished, suggests that the peptide conjugates must first associate with small gold particles prior to assembly in order to form a well-defined superstructure.<sup>58</sup> Thus, there exists a delicate balance between particle growth, particle-peptide conjugate binding, and peptide conjugate assembly that must be realized to produce well-defined nanoparticle superstructures. In this study, the conjugate that assembles most rapidly into fibers, C<sub>18</sub>-(PEP<sub>Au</sub>)<sub>1</sub>, and the one that assembles most slowly into fibers, C<sub>12</sub>-(PEP<sub>Au</sub>)<sub>1</sub>, form poorly defined linear superstructures with many overlapping nanoparticles. Conjugates having intermediate assembly rates (*e.g.*, C<sub>14</sub>-(PEP<sub>Au</sub>)<sub>1</sub>, C<sub>16</sub>-(PEP<sub>Au</sub>)<sub>1</sub>, C<sub>16</sub>-(PEP<sub>Au</sub>)<sub>2</sub>, and C<sub>18</sub>-(PEP<sub>Au</sub>)<sub>2</sub>) tend to form more well-defined nanoparticle superstructures consisting of co-linear chains of nanoparticles; in each of these cases, the nanoparticle superstructures exhibit regions of helicity (*vide infra*).

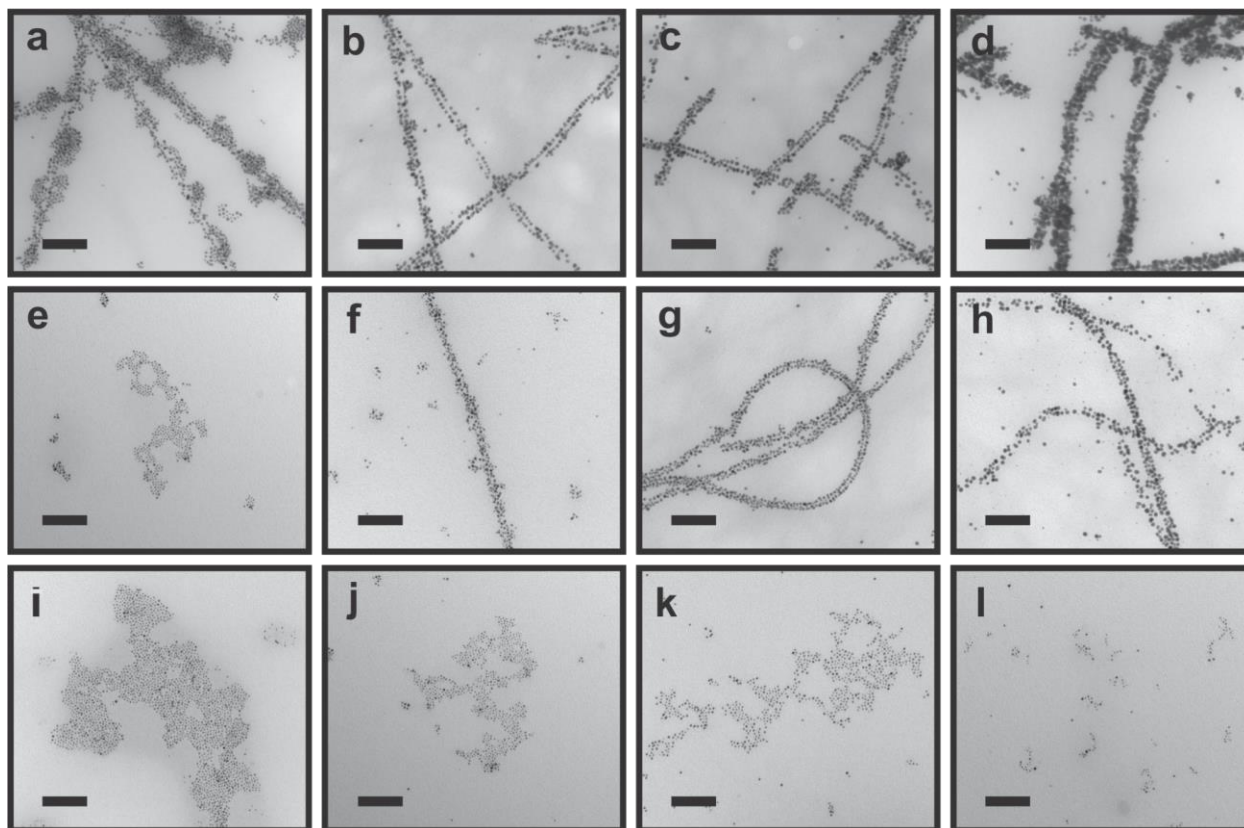


**Figure 2.15.** TEM images of the nanoparticle assemblies as a function of peptide valency and aliphatic chain length (scale bar = 100 nm): (a) C<sub>12</sub>-(PEP<sub>Au</sub>)<sub>1</sub>, (b) C<sub>14</sub>-(PEP<sub>Au</sub>)<sub>1</sub>, (c) C<sub>16</sub>-(PEP<sub>Au</sub>)<sub>1</sub>, (d) C<sub>18</sub>-(PEP<sub>Au</sub>)<sub>1</sub>, (e) C<sub>12</sub>-(PEP<sub>Au</sub>)<sub>2</sub>, (f) C<sub>14</sub>-(PEP<sub>Au</sub>)<sub>2</sub>, (g) C<sub>16</sub>-(PEP<sub>Au</sub>)<sub>2</sub>, (h) C<sub>18</sub>-(PEP<sub>Au</sub>)<sub>2</sub>, (i) C<sub>12</sub>-(PEP<sub>Au</sub>)<sub>3</sub>, (j) C<sub>14</sub>-(PEP<sub>Au</sub>)<sub>3</sub>, (k) C<sub>16</sub>-(PEP<sub>Au</sub>)<sub>3</sub>, and (l) C<sub>18</sub>-(PEP<sub>Au</sub>)<sub>3</sub>.

Several structural parameters of the nanoparticle superstructures could potentially affect their properties.<sup>87-88</sup> We first considered nanoparticle size within the assembled superstructures. Nanoparticle diameters were measured from the TEM images (**Figure 2.16**). The data indicate that nanoparticle diameter within the 1D nanoparticle assemblies is dependent on both the aliphatic tail length and the valency of the peptide conjugate. Nanoparticle diameter increases with increasing aliphatic chain length and decreases with increasing valency. These observations led us to hypothesize that the decrease in particle size with increased valency may be due to increased binding affinity associated with multivalency.<sup>89-91</sup> An increased binding affinity could

limit the growth of the nanoparticles. To test this hypothesis, we measured the equilibrium binding constants for mono- and divalent peptide conjugates using data from a quartz crystal microbalance (QCM) analysis (**Figure 2.17**). For this experiment, it was important to use mono- and divalent conjugates without aliphatic tails in order to prevent assembly before binding to the substrate (**Figure S2.51**). The equilibrium binding constant,  $K_{eq}$ , ( $K_{eq} = K_a/K_d$ , where  $K_a$  is the association constant and  $K_d$  is the dissociation constant) of the monovalent conjugate was slightly higher than that of the divalent conjugate, although the values were very similar. By comparison, these are consistent to the binding constants of multivalent dendrons with metal oxides and repeating gold-binding peptides.<sup>92-93</sup> One possible explanation for the statistically similar  $K_{eq}$  values is that the proximity of the two peptides in the divalent conjugate prevents favorable peptide interaction with the substrate. It is known that AYSSGAPPMPPF adopts a specific conformation for optimal binding; a second peptide in close proximity may hinder this conformation.<sup>89, 94</sup>

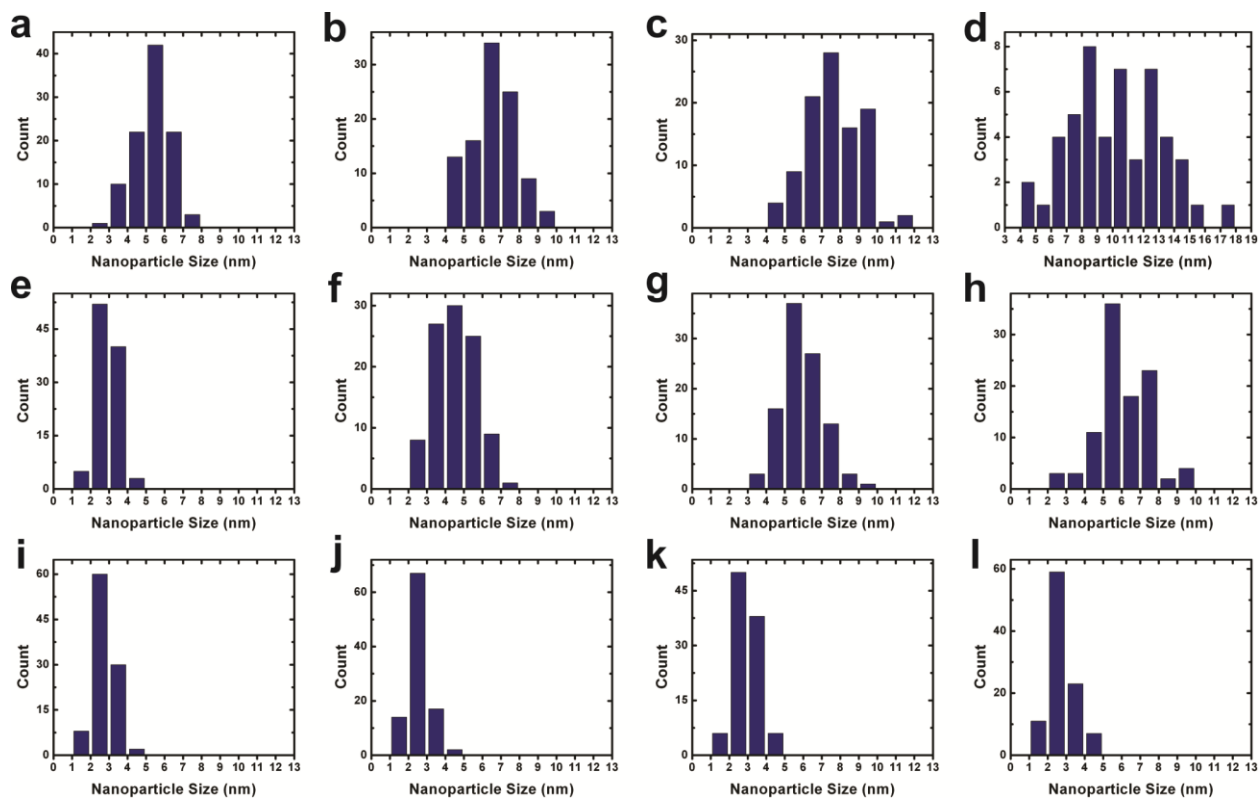


**Figure 2.16.** Nanoparticle diameters measured from TEM images: (a)  $C_{12}$ -(PEPAu)<sub>1</sub>:  $5.3 \pm 0.9$  nm based on 100 counts; (b)  $C_{14}$ -(PEPAu)<sub>1</sub>:  $6.6 \pm 1.2$  nm based on 100 counts; (c)  $C_{16}$ -(PEPAu)<sub>1</sub>:  $7.6 \pm 1.5$  nm based on 100 counts; (d)  $C_{18}$ -(PEPAu)<sub>1</sub>:  $10.2 \pm 2.9$  nm based on 50 counts; (e)  $C_{12}$ -(PEPAu)<sub>2</sub>:  $2.9 \pm 0.6$  nm based on 100 counts; (f)  $C_{14}$ -(PEPAu)<sub>2</sub>:  $4.5 \pm 1.1$  nm based on 100 counts; (g)  $C_{16}$ -(PEPAu)<sub>2</sub>:  $5.9 \pm 1.1$  nm based on 100 counts; (h)  $C_{18}$ -(PEPAu)<sub>2</sub>:  $6.1 \pm 1.4$  nm based on 100 counts; (i)  $C_{12}$ -(PEPAu)<sub>3</sub>:  $2.8 \pm 0.6$  nm based on 50 counts; (j)  $C_{14}$ -(PEPAu)<sub>3</sub>:  $2.6 \pm 0.5$  nm based on 100 counts; (k)  $C_{16}$ -(PEPAu)<sub>3</sub>:  $3.0 \pm 0.6$  nm based on 50 counts; (a)  $C_{18}$ -(PEPAu)<sub>3</sub>:  $2.8 \pm 0.7$  nm based on 100 counts.

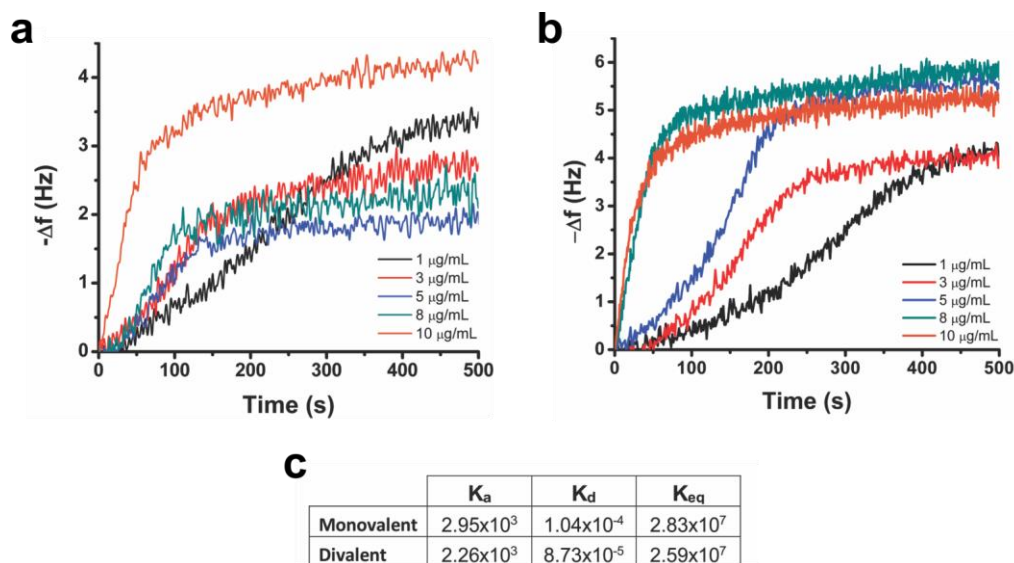


**Figure 2.17.** QCM binding data for the (a) monovalent and (b) divalent peptide conjugates. (c) The association binding constant,  $K_a$ , dissociation binding constant,  $K_d$ , and equilibrium binding constant,  $K_{eq}$ , were calculated from the QCM experiments.

The variation in particle diameter within the nanoparticle superstructures, however, may be explained by the interplay between fiber formation and nanoparticle binding (*vide supra*). For the conjugates that assemble into fibers, the nanoparticle diameter increases as the propensity to form fibers increases, as illustrated in going from  $C_{12}-(PEP_{Au})_1$  to  $C_{18}-(PEP_{Au})_1$  (**Figure 2.16a-d**) and in going from  $C_{14}-(PEP_{Au})_2$  to  $C_{18}-(PEP_{Au})_2$  (**Figure 2.16f-h**). If the peptide conjugate monomers rapidly assemble into fibers, they have less time free in solution to cap the growth of the growing nanoparticles. This leads to larger particle diameters. Conversely, if the peptide conjugate monomers slowly assemble into fibers, they will have more time free in solution to cap the growth of the nanoparticles, leading to smaller nanoparticle diameters. When nanoparticle assembly was not observed ( $C_{12}-(PEP_{Au})_2$ ,  $C_{12}-(PEP_{Au})_3$ ,  $C_{14}-(PEP_{Au})_3$ ,  $C_{16}-(PEP_{Au})_3$ , and  $C_{18}-(PEP_{Au})_3$ ), the particles are uniformly small ( $\sim 3$  nm), independent of valency

and tail length (**Figure 2.16e,i-l**). In these cases, the peptide conjugates remain in solution and have adequate time to bind to the growing nanoparticles to cap their growth.

We next considered structural metrics of the linear nanoparticle superstructures, including the distance between the co-linear nanoparticle chains as well as the helical pitch. The interchain distances of the nanoparticle superstructures constructed using  $C_{14}-(PEP_{Au})_1$ ,  $C_{16}-(PEP_{Au})_1$ ,  $C_{16}-(PEP_{Au})_2$ , and  $C_{18}-(PEP_{Au})_2$  were measured via TEM (**Figure S2.52**). These conjugates were chosen because they yielded the most well-defined superstructures in which two co-linear chains can clearly be identified. The interchain distances for the  $C_{14}-(PEP_{Au})_1$  and  $C_{16}-(PEP_{Au})_1$  superstructures were  $5.9 \pm 1.2$  nm and  $5.6 \pm 1.2$  nm, respectively, while those for the  $C_{16}-(PEP_{Au})_2$  and  $C_{18}-(PEP_{Au})_2$  superstructures were  $4.6 \pm 1.2$  and  $5.0 \pm 1.4$  nm, respectively. Although we cannot determine whether the particles are bound to the edge or the face of the fibers (**Figure S2.53**), the similar interchain distances suggests that the particles are bound to the fiber faces, because the fiber thicknesses are approximately the same, whereas the fiber widths for the monovalent and divalent are different.

Nanoparticle superstructures formed using  $C_{14}-(PEP_{Au})_1$ ,  $C_{16}-(PEP_{Au})_1$ ,  $C_{16}-(PEP_{Au})_2$ , and  $C_{18}-(PEP_{Au})_2$  each exhibit regions of helicity (**Figure 2.18 and Figure S2.54**). The helicity is most clearly defined in the  $C_{16}-(PEP_{Au})_1$ - and  $C_{18}-(PEP_{Au})_2$ -based nanoparticle superstructures (**Figure 2.18**). The average pitch for  $C_{16}-(PEP_{Au})_1$  and  $C_{18}-(PEP_{Au})_2$ ,  $\sim 204$  and  $\sim 173$  nm, respectively, are similar to the average pitch values of the  $C_{16}-(PEP_{Au})_1$  and  $C_{18}-(PEP_{Au})_2$  nanofibers as determined by AFM ( $214 \pm 7$  and  $184 \pm 15$  nm, respectively). These measurements suggest that the peptide conjugate assembly directs the structure of the nanoparticle assembly. Moreover, these results, when taken together with our reported results on  $C_{12}-PEP_{Au}$  double-helical gold nanoparticle superstructures (pitch  $\sim 85$  nm),<sup>25</sup> indicate that modifications to the



peptide conjugate can allow one to adjust the pitch of double-helical nanoparticle superstructures.

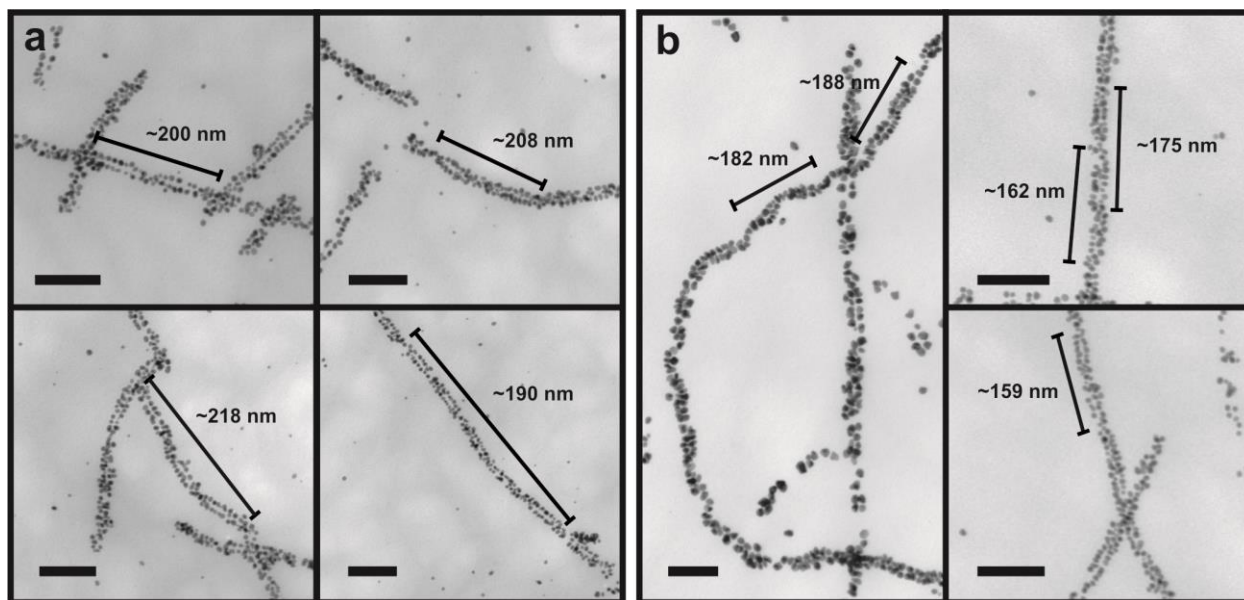


**Figure 2.18.** TEM images of nanoparticle assemblies showing regions of helicity and pitch measurements from (a) C<sub>16</sub>-(PEP<sub>Au</sub>)<sub>1</sub> and (b) C<sub>18</sub>-(PEP<sub>Au</sub>)<sub>2</sub> (scale bar = 100 nm).

### 2.3 CONCLUSION

We have prepared a family of peptide conjugate molecules in which the aliphatic tail length and peptide valency were systematically varied. The conjugates have an increased propensity to form twisted 1D fibers as the tail length increases and the valency decreases. In cases where twisted 1D fibers formed, we found that the pitch of the fibers was inversely proportional to valency and proportional to tail length while the width of the fibers decreased with increasing valency. The peptide conjugates were used to direct the assembly of nanoparticle superstructures, whose morphology and structural parameters correspond to those of the soft assemblies. The metrics of

the nanoparticle superstructures, including interchain distance and helical pitch correspond closely to the metrics of the conjugate soft assemblies. These results illustrate the ability to control and tailor the metrics of 1D helical nanoparticle superstructures through synthesis and assembly of peptide conjugate molecules, and they represent an important step forward in our ability to prepare programmable nanoparticle superstructures by design.

## 2.4 EXPERIMENTAL SECTION

### 2.4.1 General methods and instrumentations

All chemicals were purchased from either Aldrich or Fisher and used without further purification.  $N_3$ -C<sub>4</sub>H<sub>8</sub>CO-AYSSGAPPMPPF ( $N_3$ -PEP<sub>Au</sub>, **Figure S2.38**) was synthesized by the University of Pittsburgh Peptide Synthesis Facility or New England Peptide. Triethylammonium acetate buffer (TEAA) was purchased from Aldrich (catalog number: 90358) and 4-(2-hydroxyethyl)-1-piperazineethanesulfonic acid (pH = 7.3) (HEPES) buffer was purchased from Fisher (catalog number: BP299-100). Chloroauric acid (HAuCl<sub>4</sub>) was purchased from Aldrich (catalog number: 520918). 0.1 M citrate (pH 7.4) was prepared by dissolving citric acid in Nanopure water and adjusting the pH to 7.4 using NaOH. Peptide conjugates were purified using an Agilent 1200 Series reverse-phase high-pressure liquid chromatography (HPLC) instrument equipped with an Agilent Zorbax 300SB-C<sub>18</sub> column. Peptide conjugates were quantified based on their absorbance at 280 nm and using the extinction coefficient for tyrosine (1280 M<sup>-1</sup>cm<sup>-1</sup>). Spectra were collected using an Agilent 8453 UV-Vis spectrometer equipped with deuterium and tungsten lamps. Transmission electron microscopy (TEM) samples were prepared by drop-

casting 6  $\mu\text{L}$  of solution onto a 3-mm-diameter copper grid. TEM images were collected with a FEI Morgagni 268 (80 kV) equipped with an AMT side mount CCD camera system. Phosphotungstic acid (pH 7.4) was used to stain TEM sample grids for soft assembly studies. All proton nuclear magnetic resonance ( $^1\text{H}$  NMR) data were collected using a Bruker Avance III 300 MHz spectrometer. All liquid chromatography mass spectrometry (LC-MS) data were collected using a Shimadzu LC-MS 2020. Matrix assisted laser desorption ionization time-of-flight mass spectrometry (MALDI-TOF MS) data were collected using an Applied Biosystem Voyager System 6174 MALDI-TOF mass spectrometer (positive reflector mode; accelerating voltage: 20kV) and using  $\alpha$ -cyano-4-hydroxycinnamic acid (CHCA) as the ionization matrix. Atomic force microscopy (AFM) samples were prepared on freshly cleaved mica (sample incubated for 5 min. and washed twice with Nanopure water) and analyzed in tapping-mode using an Asylum MFP-3D atomic force microscope. Attenuated total reflectance Fourier-transform infrared (ATR-FTIR) spectra were collected on a Perkin Elmer Spectrum 100 FTIR with a universal attenuated total reflectance sampling accessory coupled to a computer using Perkin Elmer Spectrum Express software; the peptide conjugates were dissolved in a solution of acetonitrile/Nanopure water (1:1) and drop-casted onto the sample stage. A Q-Sense E4 quartz crystal microbalance with dissipation (QCM-D) was used to measure peptide conjugate binding on gold. Gold-coated QCM sensors (Q-Sense) were cleaned via UV-ozone treatment for 10 minutes, followed by heating in a 7.5:1:1 solution of double deionized water/ $30\%$   $\text{H}_2\text{O}_2/\text{NH}_4\text{OH}$  at  $80^\circ\text{C}$  for 10 minutes. The sensors were thoroughly rinsed with double deionized water, and dried with  $\text{N}_2$ . The clean gold-coated sensors were mounted in a Q-Sense window flow cell module. For peptide conjugate binding, a flow rate of  $0.17\text{ mL/min.}$  was used at a constant temperature of  $23^\circ\text{C}$ , and the 3<sup>rd</sup> overtone resonance was monitored. Nanopure water (NP  $\text{H}_2\text{O}$ ,  $18.2\text{ M}\Omega$ ) was obtained

from a Barnstead Diamond™ water purification system. All TEM and AFM measurements were made using ImageJ software.

#### 2.4.2 Preparation of peptide conjugates

Alkyne-terminated aliphatic substrates were prepared according to protocols detailed in Appendix A. The peptide conjugates were prepared using copper(I)-catalyzed azide-alkyne cycloaddition (CuAAC) in which N<sub>3</sub>-PEP<sub>Au</sub> was reacted with particular alkyne-terminated aliphatic substrates. A representative protocol for the preparation of C<sub>16</sub>-(PEP<sub>Au</sub>)<sub>2</sub> is detailed here. The following stock solutions were prepared: **A**, 24.7 mM divalent alkyne in tetrahydrofuran (THF); **B**, 198.3 mM CuSO<sub>4</sub> in NP H<sub>2</sub>O; **C**, 37.3 mM tris(3-hydroxypropyltriazolylmethyl)amine (THPTA) in NP H<sub>2</sub>O; and **D**, 101.0 mM sodium ascorbate in NP H<sub>2</sub>O. In a 2 mL glass vial, N<sub>3</sub>-PEP<sub>Au</sub> (3 mg, 2.23 μmol) was dissolved in 462.3 μL of THF and 337.5 μL of NP H<sub>2</sub>O. To this vial were added 37.7 μL **A**, a mixture of **B** and **C** (14.1 μL **B** mixed with 74.8 μL **C**), and 73.6 μL **D**. The vial was capped, wrapped in aluminum foil, and stirred for at least 4 hrs. at room temperature. Dimethylformamide (100 μL) was added to the product solution. The resulting solution was passed through a 0.2 μm syringe filter (Whatman, catalog number 6789-1302). The reaction vial was washed with 400 μL of a 1:1 mixture of NP H<sub>2</sub>O and acetonitrile (CH<sub>3</sub>CN), and this wash was passed through the same 0.2 μm syringe filter and mixed with the DMF/product solution. This final solution containing the product peptide conjugate was purified using reverse-phase HPLC eluting with a linear gradient of 0.05% formic acid in CH<sub>3</sub>CN and 0.1% formic acid in NP H<sub>2</sub>O (5/95 to 95/5 over 30 min.).

### **2.4.3 Preparation of soft assemblies**

In a plastic vial, lyophilized peptide conjugates ( $\sim 3.75 \times 10^{-8}$  mol) were dissolved in 250  $\mu\text{L}$  of a 1:4 mixture of 0.1 M citrate and 0.1 M HEPES buffer. 2  $\mu\text{L}$  of a 0.1 M  $\text{CaCl}_2$  solution in NP  $\text{H}_2\text{O}$  was added to the peptide conjugate solution. The resulting solution was vortexed briefly and then allowed to sit undisturbed at room temperature. TEM and/or AFM samples were prepared after 1 day of incubation at room temperature.

### **2.4.4 Preparation of nanoparticle assemblies**

In a plastic vial, lyophilized peptide conjugates ( $\sim 1.87 \times 10^{-8}$  mol to  $\sim 7.49 \times 10^{-8}$  mol) were completely dissolved in 250  $\mu\text{L}$  of a 1:4 mixture of 0.1 M citrate and 0.1 M HEPES buffer and allowed to sit at room temperature for 30 min. A fresh stock solution of  $\text{HAuCl}_4$  in TEAA buffer was prepared by mixing 100  $\mu\text{L}$  of 0.1 M  $\text{HAuCl}_4$  in NP  $\text{H}_2\text{O}$  with 100  $\mu\text{L}$  of 1.0 M TEAA buffer. The resulting mixture was vortexed for 1 minute. After sitting 30 min. at room temperature, 2  $\mu\text{L}$  of the freshly prepared  $\text{HAuCl}_4/\text{TEAA}$  solution was added to the peptide conjugate solution. A dark precipitate appeared 2-4 seconds after the addition of the  $\text{HAuCl}_4/\text{TEAA}$  solution; at this time, the vial was briefly vortexed and then left undisturbed at room temperature. TEM samples were prepared after 4 hrs. of incubation at room temperature.

### 3.0 PEPTIDE-DIRECTED ASSEMBLY OF SINGLE-HELICAL GOLD NANOPARTICLE SUPERSTRUCTURES EXHIBITING INTENSE CHIROPTICAL ACTIVITY

This work, written in collaboration with Jennifer C. Boatz, Abhishek Mandal, Gongpu Zhao, Soumitra Mokashi Punekar, Chong Liu, Xianting Wang, Peijun Zhang, Patrick C. A. van der Wel\*, and Nathaniel L. Rosi\*, is reprinted with permission from the *Journal of the American Chemical Society* **2016**, *138*, 13655-13663. Copyright 2016, American Chemical Society. The supporting information is found in Appendix B.

Jennifer C. Boatz and Abhishek Mandal conducted and processed the MAS solid-state spectroscopy experiments. Dr. Gongpu Zhao and Xianting Wang performed and analyzed the cryo-electron tomography data. Soumitra Mokashi Punekar assisted with synthesizing the single helices. Dr. Chong Liu collected the powder XRD data.

#### 3.1 INTRODUCTION

As described in Chapter 1, chiral nanoparticle assemblies are an emerging class of materials, which have the potential to serve as nanoscale circular polarizers<sup>69-70</sup> and chiroptical sensors,<sup>66-68</sup> and they represent an interesting new entry into the metamaterials catalogue.<sup>17, 69-70</sup> Peptides, which can assemble into chiral architectures, are attractive molecular building blocks that can be

used to direct the assembly of nanoparticles into chiral superstructures. Previously our group has constructed chiral double-helical gold nanoparticle superstructures and characterized their unique chiroptical properties.<sup>61</sup> While significant progress has been made toward (i) understanding how PEP<sub>Au</sub> associates with gold nanoparticle surfaces<sup>26, 55, 94-97</sup> and (ii) understanding how both R-groups and intrinsic secondary structure influence R-PEP<sub>Au</sub> assembly,<sup>25, 60, 62</sup> we have yet to establish a molecular-level understanding that accounts for the dual role that R-PEP<sub>Au</sub> conjugates play in the context of constructing nanoparticle superstructures. Significant questions remain unanswered: How does PEP<sub>Au</sub> associate to nanoparticles within an assembled nanoparticle superstructure? How do R-PEP<sub>Au</sub> conjugates pack and assemble within a nanoparticle superstructure? How do these conjugates simultaneously self-assemble *and* bind to gold nanoparticle surfaces? Uncovering answers to these questions is paramount to advancing peptide-based methods for assembling nanoparticle superstructures.

Here, we report the preparation of unique gold nanoparticle single helices that exhibit exceptionally strong plasmonic chiroptical activity. Motivated by these results, we rigorously examine the underlying molecular basis of these superstructures and ultimately arrive at a structural model that thoroughly accounts for their assembly. Through these studies, we make considerable progress toward answering the fundamental questions listed above, and we ultimately arrive at a new understanding of this methodology that will motivate future peptide design strategies for the rational construction and optimization of chiral nanoparticle superstructures.

## 3.2 RESULTS AND DISCUSSION

### 3.2.1 Single helix synthesis and chiroptical properties

I reported in Chapter 2 that the divalent peptide conjugate,  $C_{18}-(PEP_{Au})_2$ , directs the assembly of double-helical gold nanoparticle superstructures when mixed with gold salts, assembly buffers, and reducing agents (**Figure 3.19a**). In subsequent studies, single-helical gold nanoparticle superstructures, rather than double helices, were, at times, observed as the sole product. These confounding results prompted us to investigate the origin of the single helix architecture. Since the synthetic procedures used to prepare the double and single helices were virtually indistinguishable (*e.g.*, identical gold salt, identical buffer, and identical reagent concentrations), we carefully characterized the  $C_{18}-(PEP_{Au})_2$  used in each synthesis, reasoning that a small impurity or chemical change to the conjugate may have led to the observed results. High resolution liquid chromatography mass spectrometry (HR-LCMS) revealed that the molecular weight of the conjugates that directed the formation of the single helices was 16 m/z larger than expected ( $z = 2$ ), corresponding to a 32 au increase in the molecular weight. The thioether functional group of methionine can undergo oxidation to the sulfoxide; a 16 m/z increase would result if both methionine residues of  $C_{18}-(PEP_{Au})_2$  were oxidized (**Figure S3.55b**). Therefore, we hypothesized that oxidation of  $C_{18}-(PEP_{Au})_2$  to  $C_{18}-(PEP_{Au}^{M-ox})_2$  ( $PEP_{Au}^{M-ox} = AYSSGAPPM^{ox}PPF$ ) results in the formation of single-helical superstructures. To test this hypothesis, we chemically oxidized  $C_{18}-(PEP_{Au})_2$ ; LCMS data for these oxidized conjugates confirmed the increase in molecular weight associated with the addition of two oxygens (**Figure S3.56**). The oxidized conjugates exclusively directed the assembly of single-helical gold nanoparticle superstructures (**Figure 3.19b**).



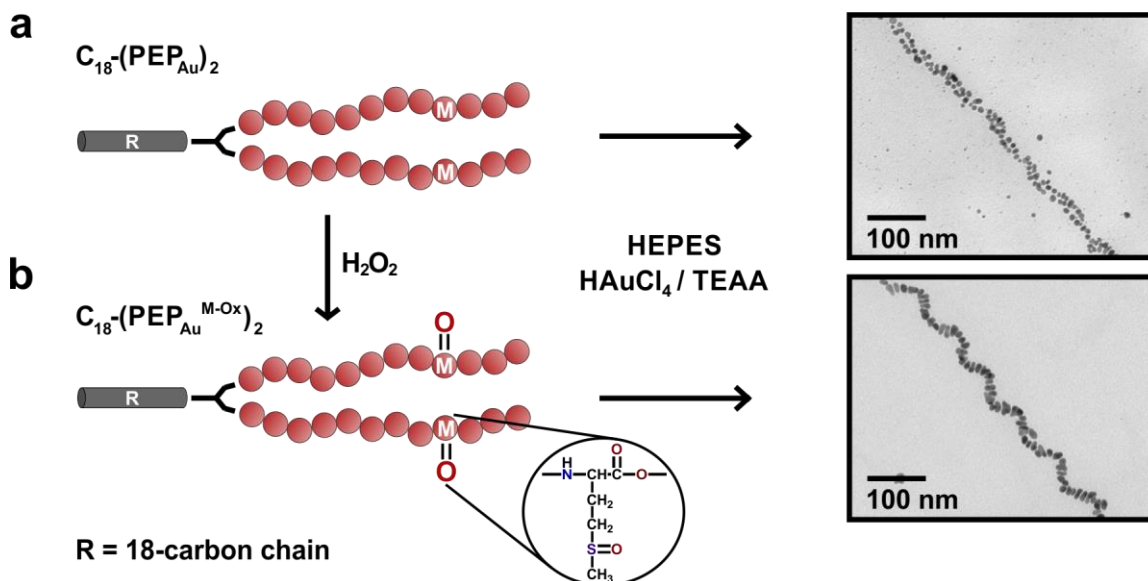


**Figure 3.19.** Preparation of (a) double- and (b) single-helical nanoparticle superstructures from  $C_{18}-(PEP_{Au})_2$  and  $C_{18}-(PEP_{Au}^{M-Ox})_2$ , respectively, under identical reaction conditions.  $C_{18}-(PEP_{Au}^{M-Ox})_2$  was prepared via oxidation using  $H_2O_2$ .

We next characterized the single-helical gold nanoparticle assemblies. Transmission electron microscopy (TEM) images (**Figure 3.20a-c** and **Figure S3.57**) reveal that the single helices have an average pitch of  $94.4 \pm 6.6$  nm (**Figure 3.20d**) and are composed of individual rod-like nanoparticles with lengths of  $16.6 \pm 3.0$  nm and widths of  $9.6 \pm 1.9$  nm (**Figure S3.58**). At the early stages of the synthesis and assembly process, the nanoparticles are spherical and bound to the 1D  $C_{18}-(PEP_{Au}^{M-Ox})_2$ -based fibers (**Figure 3.20c** and **Figure S3.59**), but over time they grow into oblong rod-like nanoparticles (**Figure S3.59**). Throughout the nanoparticle growth process, the nanoparticles remain bound to the fibers (**Figure S3.59**). These observations are consistent with our previously reported studies.<sup>25, 58</sup> We note that, in this method, *in situ* nanoparticle growth in the presence of the peptide conjugates is required to achieve ordered nanoparticle assemblies. Cryogenic electron tomography (cryo-ET) was employed to determine

the 3D architecture of the single helices (**Figure 3.20e,f**). The reconstructed tomographic volume confirms that the helices are left-handed, which can be attributed to L amino acid residues comprising the peptides. Structural parameters were also gathered from the 3D reconstruction of the helices. The pitch is  $102.0 \pm 2.5$  nm, within error of the measured data from 2D TEM images, and the rotation angle per particle is  $34.3 \pm 4.9$  degrees, corresponding to approximately 10-11 nanoparticles per pitch length (**Figure S3.60a,b**). The inner diameter of the helical superstructure is  $10.1 \pm 0.6$  nm (**Figure 3.20f and Figure S3.60c**). This distance corresponds to the measured width of the fibers (*vide infra*).

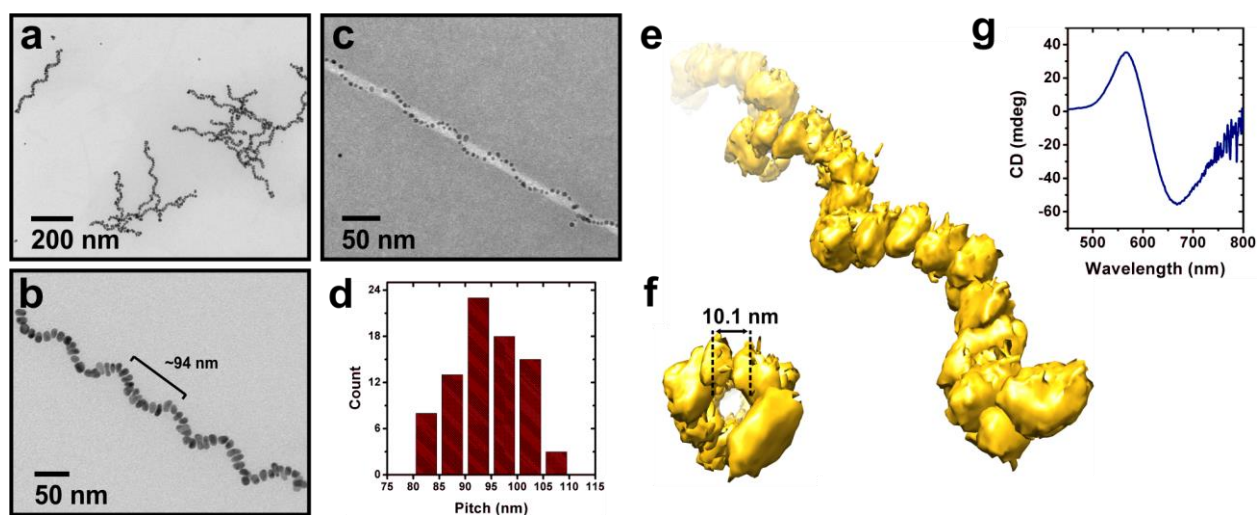


**Figure 3.20.** Single helix characterization. (a,b) TEM images of single-helical gold nanoparticle superstructures after 15 h of reaction and (c) negative-stained TEM image after 30 min. of reaction. (d) Pitch of the helices, measured from TEM ( $94.4 \pm 6.6$  nm; based on 80 counts). The cryo-ET 3D reconstruction of the single helices reveals their (e) left-handed helicity and, when viewed along the helix axis, their (f) core diameter where the fiber resides. (g) CD spectrum of the single-helical superstructures.

Circular dichroism (CD) spectroscopy was used to characterize the chiroptical activity of the single helices. The single helices exhibit a strong bisignate peak centered at approximately

600 nm, near the collective plasmonic extinction band for the assemblies (**Figure 3.20g**). Others have reported a visible plasmonic CD peak for peptide-capped gold nanoparticles.<sup>98</sup> However, gold nanoparticles capped with  $\text{PEP}_{\text{Au}}^{\text{M-ox}}$ , showed only a weak CD signal (**Figure S3.61**). Therefore, we can reasonably conclude that the strong plasmonic CD signal for the single helices originates from the chiral helical arrangement of gold particles; indeed, the observed signal is consistent with previous theoretical predictions.<sup>61, 88</sup> It is important to compare the chiroptical activity of the single helices to other reported chiral nanoparticle assemblies. The anisotropy factor,  $g$ , is typically used as a benchmark value for determining the intensity of the chiroptical signal. Optimized assemblies (**Figure S3.62a,b**), for which synthetic conditions were tuned to increase particle dimensions, have an absolute  $g$ -factor up to  $\sim 0.04$  (**Figure S3.62e**), which, to our knowledge, is one of the highest reported to date for comparable nanoparticle assemblies.<sup>99-</sup>

102

### 3.2.2 Peptide conjugate assembly studies

The intense chiroptical activity of single helices prompted us to examine the assembly and structure of  $\text{C}_{18}\text{-(PEP}_{\text{Au}}^{\text{M-ox}})_2$ . Understanding the underlying molecular structure of the fibers and how it correlates to the final nanoparticle assembly will allow for rational design of peptide conjugate building blocks and precise control over nanoparticle superstructure assembly and properties.

We first studied the morphology of the  $\text{C}_{18}\text{-(PEP}_{\text{Au}}^{\text{M-ox}})_2$  fibers in the absence of gold nanoparticles. Acylated peptide amphiphiles are known to assemble into two principal helical morphologies: twisted ribbons and helical ribbons (**Figure 3.21a,b**).<sup>48, 103-107</sup> Both assemblies are defined by a cross- $\beta$  amyloid-like structure. Twisted ribbons are characterized by their saddle-

like curvature with a C2 symmetry axis and both ribbon faces equally exposed. Helical ribbons, on the other hand, have cylindrical curvature and one face of the ribbon is directed toward the interior of the helical coil and the other is directed to the exterior. In both cases, the helicity originates from the chirality of the peptide-based molecular building blocks.<sup>40</sup> The observed single helix architecture suggests that  $C_{18}$ -(PEP<sub>Au</sub><sup>M-ox</sup>)<sub>2</sub> fibers assemble into helical ribbons, and the gold nanoparticles decorate the exterior face of the helical ribbon. Evidence from previous studies suggests that the twisted ribbon morphology favors the formation of a double-helical nanoparticle superstructure, where the particles associate to either both edges or both faces of the ribbon.<sup>25, 62</sup>

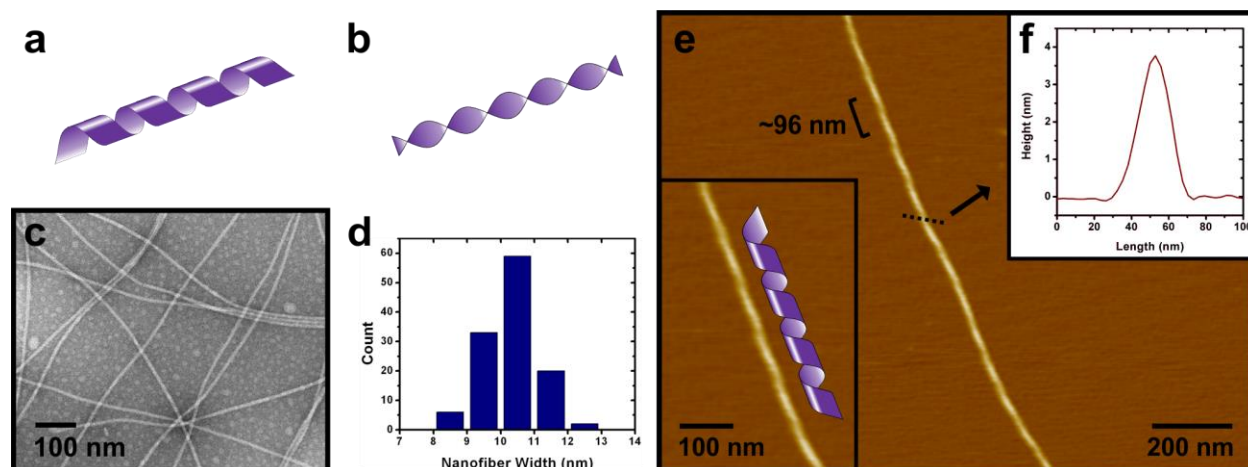


**Figure 3.21.**  $C_{18}$ -(PEP<sub>Au</sub><sup>M-ox</sup>)<sub>2</sub> fiber morphology studies. Helical peptide amphiphile fibers typically exhibit either (a) helical ribbon or (b) twisted ribbon morphology. (c) Negative-stained TEM image of  $C_{18}$ -(PEP<sub>Au</sub><sup>M-ox</sup>)<sub>2</sub> fibers. (d) Fiber widths were  $10.2 \pm 0.8$  nm. (e) AFM reveals the helical ribbon morphology of  $C_{18}$ -(PEP<sub>Au</sub><sup>M-ox</sup>)<sub>2</sub> fibers with a pitch of  $96.2 \pm 4.8$  nm and (f) a ribbon height of approximately 4 nm (height trace measured along the dashed line).

To precisely determine the fiber morphology, samples were analyzed using numerous microscopy techniques. TEM verifies the presence of 1D fibers (**Figure 3.21c**), in addition to small pseudospherical aggregates, which are always present in varying amounts, depending on

the length of time allowed for the assembly process. The fiber widths, measured via TEM, are  $10.2 \pm 0.8$  nm, which is consistent with the cryo-ET data that defined the inner diameter of the nanoparticle superstructure to be approximately 10.1 nm (*vide supra*) (**Figure 3.21d**). Distinct morphological features of the fibers, such as their helicity, were indistinguishable using traditional TEM imaging. Tapping-mode atomic force microscopy (AFM) images clearly reveal that the fibers adopt the helical ribbon morphology (**Figure 3.21e and Figure S3.63**). The pitch, measured via AFM, is  $96.2 \pm 4.8$  nm, consistent with the pitch of the gold nanoparticle single helices. The vertical thickness of the ribbon is  $\sim 4$  nm (**Figure 3.21f**). Height traces along the fiber axis suggest that the coiled helical ribbon compresses onto the mica substrate (**Figure S3.63e**), which is not surprising as such compression/collapse is common for soft assemblies having a hollow interior.<sup>108-109</sup> The morphological similarities between the helical ribbons and the gold nanoparticle single helices imply similarities between  $C_{18}-(PEP_{Au}^{M-ox})_2$  assembly in both the presence and absence of gold nanoparticles. Consistent with our previous reports, these observations suggest that the geometry and structure of the peptide conjugate assembly defines the nanoparticle assembly architecture. Studying and understanding the underlying molecular structure of the  $C_{18}-(PEP_{Au}^{M-ox})_2$  helical ribbons provides insights into the nature of the nanoparticle assembly and provides a basis for future studies aimed at modifying the single-helical structure.

We therefore next proceeded to examine the internal structure within the  $C_{18}-(PEP_{Au}^{M-ox})_2$  fibers. An amide I absorption peak at  $1630\text{ cm}^{-1}$ , characteristic of parallel  $\beta$ -sheet secondary structure,<sup>110-111</sup> was observed in the Fourier transform infrared (FTIR) spectrum (**Figure 3.22a**). In addition, a peak at  $2922\text{ cm}^{-1}$  corresponding to C-H stretches was observed, signifying relatively ordered packing of the alkyl chains within the assembly (**Figure 3.22a**).<sup>83</sup> CD spectra

for  $C_{18}$ -(PEP<sub>Au</sub><sup>M-ox</sup>)<sub>2</sub> were collected under conditions that promote fiber assembly.<sup>82</sup> A prominent negative band centered at ~211 nm and a positive band centered at ~238 nm (**Figure 3.22b**) were observed. Negative peaks corresponding to the presence of  $\beta$ -sheet structure are typically observed around 215-220 nm for peptide amphiphile assemblies.<sup>76, 112</sup> We speculate that the blue-shifted negative peak could be due to the presence of multiple secondary structures within the assembly. Molecular simulation studies of PEP<sub>Au</sub> predict that the proline residues near the C-terminus adopt a polyproline II (PPII) conformation when free in solution.<sup>94</sup> PPII helices typically display a strong negative CD band at ~205 nm.<sup>113-114</sup> We observe a negative band at 205 nm for  $C_{18}$ -(PEP<sub>Au</sub><sup>M-ox</sup>)<sub>2</sub> under conditions that do not promote fiber assembly (*i.e.* no  $\beta$ -sheet formation; **Figure S3.64**). Therefore, we conclude that the observed signal in the CD spectrum of  $C_{18}$ -(PEP<sub>Au</sub><sup>M-ox</sup>)<sub>2</sub> fibers is a superposition of bands deriving from both  $\beta$ -sheet and PPII secondary structure in the assembled fibers.

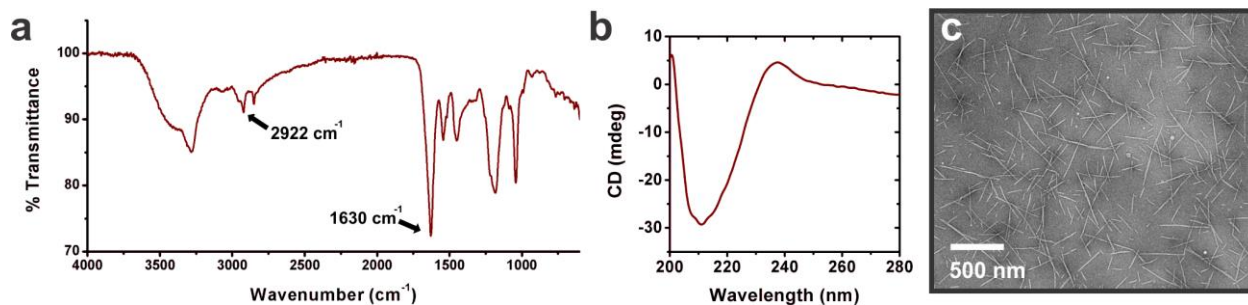


**Figure 3.22.** Spectroscopy studies. (a) FTIR spectrum of  $C_{18}$ -(PEP<sub>Au</sub><sup>M-ox</sup>)<sub>2</sub> fibers. Peaks at 1630 cm<sup>-1</sup> and 2922 cm<sup>-1</sup> correspond to the amide I band and C-H stretch, respectively. (b) CD spectrum of  $C_{18}$ -(PEP<sub>Au</sub><sup>M-ox</sup>)<sub>2</sub> in 10 mM HEPES and 1 mM CaCl<sub>2</sub> after one day, and (c) corresponding negative-stained TEM image of the  $C_{18}$ -(PEP<sub>Au</sub><sup>M-ox</sup>)<sub>2</sub> fibers.

While CD and FTIR spectroscopy provided information about the secondary structure, X-ray diffraction (XRD) experiments were conducted to probe the molecular-level packing of  $C_{18}$ -

(PEP<sub>Au</sub><sup>M-ox</sup>)<sub>2</sub> within the fibers. XRD patterns of aligned C<sub>18</sub>-(PEP<sub>Au</sub><sup>M-ox</sup>)<sub>2</sub> fibers displayed the prototypical pattern observed for cross-β amyloid-like structure (**Figure 3.23a**).<sup>115-116</sup> An intense meridional reflection corresponding to a d-spacing of 4.6 angstroms is attributed to the H-bonding distances between peptide backbones. Equatorial peaks with d-spacings of ~6.5, ~9, and ~18 angstroms correspond to repeat distances between β-sheets (**Figure 3.23b,c**). The off-meridian reflections corresponding to a d-spacing of ~4.2 may be attributed to the distance between hkl planes diagonal to the planes containing the β-sheets.<sup>117</sup>

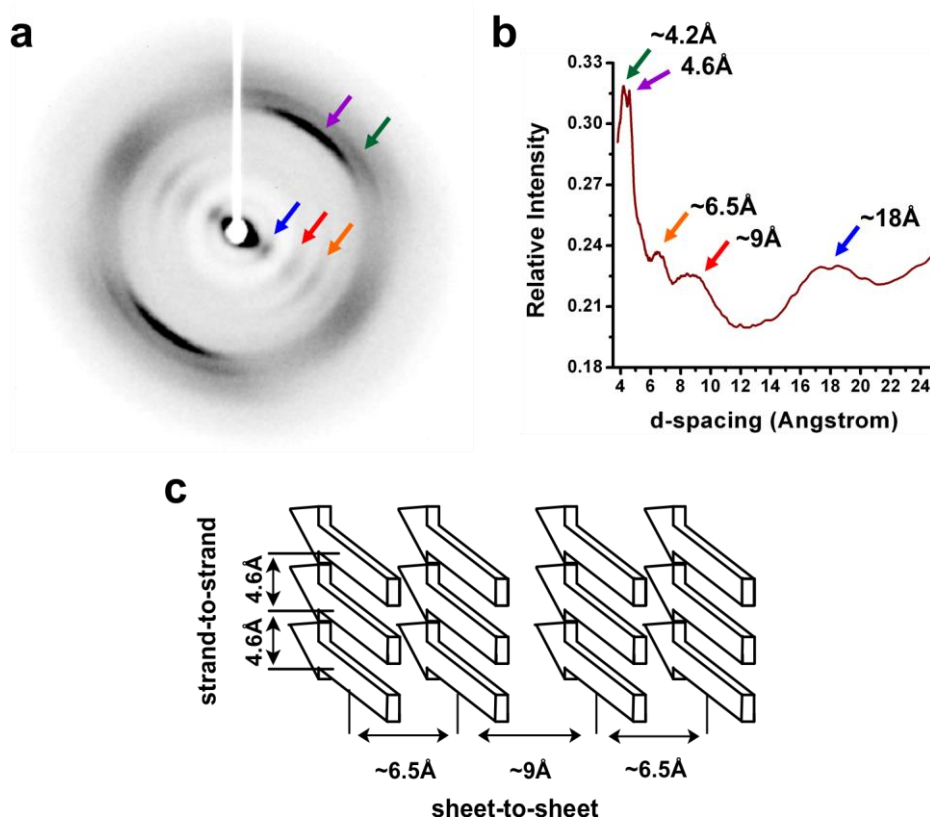


**Figure 3.23.** X-ray data. 2D x-ray diffraction pattern of aligned C<sub>18</sub>-(PEP<sub>Au</sub><sup>M-ox</sup>)<sub>2</sub> fibers reveals a cross-β architecture. The colored arrows correlate with the (c) integrated d-spacings of the XRD diffractogram. (c) Figure showing the strand-to-strand and sheet-to-sheet distances as revealed via XRD.

The CD, FTIR, and XRD data revealed that the peptide-based core of the assemblies is stabilized by substantial  $\beta$ -strand formation, but the location of the  $\beta$ -strand within the peptide is uncertain. To address this, we applied ssNMR to site-specifically labeled  $C_{18}$ -(PEP<sub>Au</sub><sup>M-ox</sup>)<sub>2</sub> assemblies. To probe the very N-terminal end of the peptide, we applied <sup>13</sup>C, <sup>15</sup>N-labeling to the A1 residue. To probe the Pro-rich C-terminal half of the peptide, we also included in the same peptide a <sup>13</sup>C, <sup>15</sup>N-labeled P10 (**Figure 3.24a**). **Figure 3.24b** shows a 2D magic-angle spinning (MAS) ssNMR spectrum obtained for labeled  $C_{18}$ -(PEP<sub>Au</sub><sup>M-ox</sup>)<sub>2</sub> assemblies. The off-diagonal cross-peaks provide residue-specific assignments of each labeled residue. The P10 peaks (black dashed lines) have chemical shifts indicative of a PPII helix structure (**Figure S3.65a**).<sup>118-119</sup> The observation of a single set of peaks shows that P10 has the same PPII structure in all the  $C_{18}$ -(PEP<sub>Au</sub><sup>M-ox</sup>)<sub>2</sub> in the sample. In contrast, A1 features multiple sets of peaks, indicating the presence of multiple structures. The dominant A1 peaks (A1a and A1b), accounting for ~90% of the signal, have chemical shifts that indicate A1 to be part of the  $\beta$ -sheet structure (**Figure 3.24c**). The A1c conformer is present at much lower intensity (~10% of the total signal), lacks  $\beta$ -sheet shifts, and presumably reflects peptide that failed to incorporate into the amyloid-like core (*e.g.*, the pseudospherical aggregates observed in TEM images). In long-mixing ssNMR data these three conformers show no sign of dynamics- or proximity-enabled polarization exchange (**Figure S3.65b**). Motion-sensitive ssNMR experiments (not shown) indicate that all sites are relatively rigid and immobilized in the peptide assemblies. Therefore, two structurally different peptide conformers, present at a 1:1 ratio, make up ~90% of the sample (**Figure 3.24d**). The ssNMR shows that the  $\beta$ -sheet structure extends to the very N-terminal residue A1. At the other end, P10 is outside the  $\beta$ -sheet, forming instead part of a PPII helix that presumably involves much of the Pro-rich C-terminal peptide end. We note a strong analogy to our studies of fibrillar



huntingtin exon1, which also has a peak-doubled amyloid core followed by a PPII-helical Pro-rich domain.<sup>119</sup> In that system the transition from  $\beta$ - to PPII-structure occurs over a single residue, making it reasonable that a similarly compact  $\beta$ -sheet/PPII-helix interface may occur here.

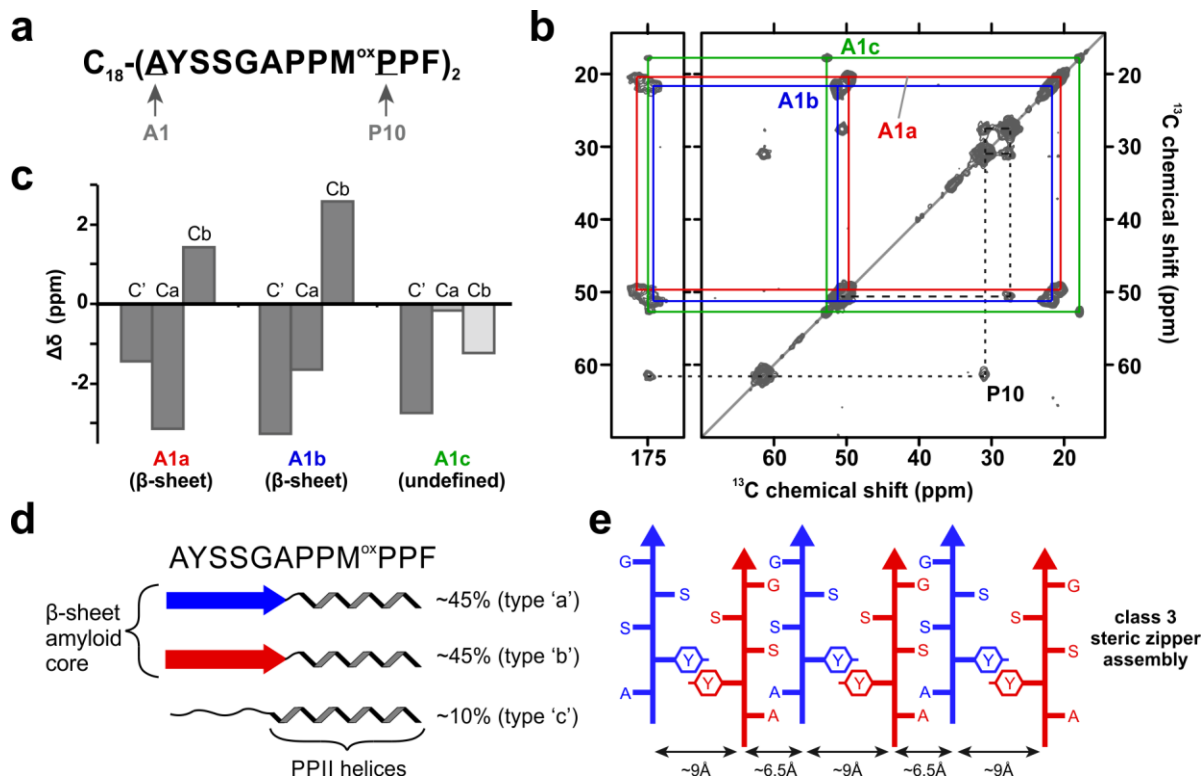


**Figure 3.24.** MAS ssNMR results. (a) Position of residue-specific  $^{13}\text{C}$ -,  $^{15}\text{N}$ -labeling (arrows). (b) 2D  $^{13}\text{C}$ - $^{13}\text{C}$  MAS ssNMR of labeled  $\text{C}_{18}$ -(PEP<sub>Au</sub><sup>M-ox</sup>)<sub>2</sub> assemblies. Dashed and colored lines connect sets of peaks from labeled P10 (black dashed line) and A1 residues (solid lines). Three A1 conformations are marked with red (A1a), blue (A1b), and green (A1c) lines. (c) Secondary structure analysis of A1 ssNMR signals, showing A1a and A1b to be part of the  $\beta$ -sheet core. (d) Secondary structure distribution in the three peptide conformers observed by ssNMR, along with their relative ssNMR peak intensities (right). (e) Amyloid core model based on a class 3 steric zipper architecture. The compact Ala/Ser/Gly interface and the aromatic interface present intersheet distances of  $\sim 6.5$  and  $\sim 9$  Å, respectively. Alternating peptides have distinct structures (blue/red coloring) that explain the observed peak doubling in the A1  $\beta$ -sheet peaks.

How do two equally populated  $\beta$ -sheet/PPII peptide building blocks (**Figure 3.24d**) co-assemble into the  $\beta$ -sheet-based core of our assemblies? The X-ray cross- $\beta$  pattern showed  $\sim 6.5$  and  $\sim 9$  Å inter-sheet distances between  $\beta$ -sheets. Sheet-to-sheet interfaces in amyloid structures have been characterized as ‘steric-zippers’ classified into distinct symmetry classes.<sup>120-121</sup> The structural data, self-assembly behavior, and chemical nature of  $C_{18}$ -(PEP<sub>Au</sub><sup>M-ox</sup>)<sub>2</sub> point to a likely architecture of the assemblies. The  $C_{18}$  acyl tails work to bring the peptides conjugates together to form micellar structures early in the assembly process. Clustering of the  $C_{18}$  tails dictates a parallel alignment of the self-assembling peptides and thus facilitates the formation of  $\beta$ -sheets that are co-aligned and parallel in nature. This fits well with our FTIR data and ssNMR results. Thus, these considerations restrict us to class 2 or class 3 type zipper motifs.<sup>120</sup> Of these, only a class 3 zipper explains the doubled  $\beta$ -sheet ssNMR peaks and their 1:1 intensity ratio as it predicts structural differences between two types of co-assembling  $\beta$ -sheets. In addition, class 3 zippers also predict the presence of two types of inter-sheet interfaces, which feature either the odd-numbered or the even-numbered residues (**Figure 3.24e**). The odd-residue interface features only small side chains (Ala/Ser/Gly), which enable the formation of a tight inter-sheet interface that places the sheets  $\sim 6.5$  Å apart (**Figure S3.65c**). The even-numbered interface includes the large aromatic Tyr. In amyloid-like crystal structures with parallel  $\beta$ -sheets, such Tyr rings adopt a characteristic ring-stacked orientation, as shown in **Figure S3.65d**. The bulkiness of the aromatic rings causes notably wide sheet-to-sheet interfaces that are  $\sim 9$ -10 Å apart (*e.g.*, **Figure S3.65e**), in line with the peptide assemblies’ X-ray pattern. Thus, this kind of assembly provides an elegant rationale for the ssNMR, FTIR, as well as X-ray results, and strongly argues for a

peptide core structure that combines packed PPII helical C-termini with a class 3 amyloid-like assembly.

### 3.2.3 Single helix assembly model

Taking into account the accumulated data on the  $C_{18}-(PEP_{Au}^{M-ox})_2$  assemblies, we propose a molecular packing model for the helical ribbon (**Figure 3.25a**). The ribbon consists of a monolayer of  $C_{18}-(PEP_{Au}^{M-ox})_2$  arranged perpendicular to the faces in a cross- $\beta$  architecture. This allows the PPII helix and negatively charged carboxylates (at pH  $\sim 7$ ) to be exposed on the outer surface of the helical ribbon. The model adheres to the ribbon vertical thickness constraint of  $\sim 4$  nm (labeled  $h$  in **Figure 3.25a**), as measured by AFM (*vide supra*); we estimate that the peptide length is  $\sim 3.8$  nm (**Figure S3.66**). Since the extended length of  $C_{18}-(PEP_{Au}^{M-ox})_2$  is estimated to be  $\sim 7.5$  nm (**Figure S3.66**), a bilayer structure where the alkyl chains are interdigitated in the core of the ribbon would not be possible. We speculate that the aliphatic chains, which are relatively ordered (*vide supra*), aggregate with one another at the inner surface of the helical ribbon or possibly fold inward with one another in-between  $\beta$ -sheets and therefore make only a small contribution to the measured ribbon thickness.<sup>38</sup> In either case, the helical ribbon architecture segregates the relatively hydrophobic N-terminus from the aqueous buffer while exposing the hydrophilic C-terminus.<sup>122</sup> This is in contrast to a twisted ribbon structure where both sides of the tape would be equally exposed. The ribbon width,  $w$ , is determined by the number of  $\beta$ -sheets stacked side-by-side with regular  $\sim 6.5$  and  $\sim 9$  Å distances.

Based on this assembly model and the structural parameters of both the single helices and  $C_{18}-(PEP_{Au}^{M-ox})_2$  fibers, we conclude that the gold nanoparticles decorate the outer face of the helical ribbon (**Figure 3.25b-d**). Careful inspection of the nanoparticle orientation within the

superstructures (**Figure 3.25c**) indicates that the rod-like particles align in parallel along the width of the ribbons, which supports a model where particle growth proceeds in one direction (**Figure 3.25d**) and could be limited by the width of the helical ribbon. The regular distances between the particles could be due to electrostatic repulsion between particles.<sup>28</sup>

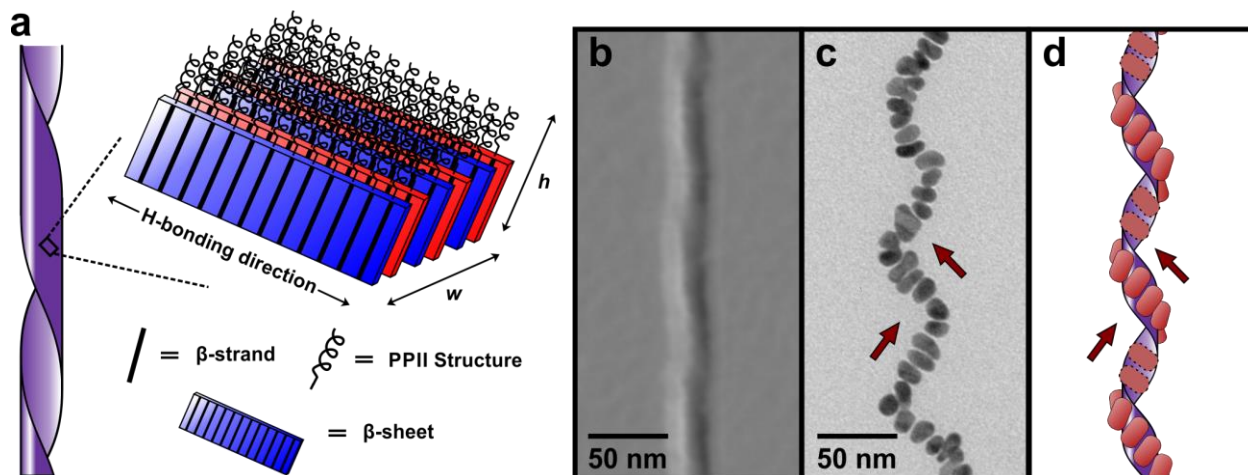


**Figure 3.25.** Single helix assembly model. (a) Proposed assembly model of  $C_{18}-(PEP_{Au}^{M-ox})_2$  helical ribbons.  $\beta$ -sheets run along the length of the fiber (interstrand distance = 4.6 Å). The width of the ribbon,  $w$ , is determined by the number of stacked  $\beta$ -sheets with lamination spacings of  $\sim 6.5$  and  $\sim 9$  Å. PPII helices are exposed at the outer surface of the helical ribbon. The blue and red layers correspond to the type ‘a’ and type ‘b’  $\beta$ -sheets, respectively, shown in Figure 3.24. The aliphatic tails have been omitted for clarity. (b) AFM (amplitude image) and (c) TEM image aligned to highlight the structural similarity between the fiber assembly and nanoparticle assembly, alongside (d) the proposed single helix assembly model with gold nanoparticles bound to the outer face of the helical ribbon. The arrows show directionality similarities of the nanoparticle orientation.

Since we propose that the C-termini of  $C_{18}-(PEP_{Au}^{M-ox})_2$  are exposed at the outer face of the helical ribbon, we reason then that the particles must be bound to the residues that make up the PPII helix. Previous reports on  $PEP_{Au}$  binding onto gold surfaces conclude that Y2 and F12 bind most strongly to the 111 facets of gold nanoparticles due to their aromatic side chains.<sup>94-96</sup>

Since the Y2 molecules are integral to the parallel  $\beta$ -sheet structure within the core of the peptide ribbon, the exposed phenylalanine at the C-terminus must account for much of the binding between the gold particles and the peptide assembly. In addition, methionine residues, which also bind strongly, could contribute to the overall binding interaction.<sup>96</sup> The inner surface of the helical ribbon is sterically hindered, which prevents particle binding.

### 3.3 CONCLUSION

We have demonstrated that  $C_{18}(PEP_{Au}^{M-Ox})_2$  directs the formation of well-defined single-helical gold nanoparticle assemblies having strong plasmonic chiroptical activity that ranks among the highest observed for comparable systems. In addition, we proposed a molecular assembly model based on data acquired from several characterization techniques that is consistent with the structural parameters of the single helices. This model provides foundational information for understanding how peptide conjugate molecules constructed from inorganic-binding peptides can simultaneously self-assemble and bind to inorganic nanoparticles, thus enabling the assembly of nanoparticles into intricate superstructures. Moreover, this model serves as a launching point for rigorous rational design of new peptide conjugates for directing and precisely controlling nanoparticle assembly structures and metrics. Collectively, the results presented herein underline the utility of peptide constructs as building blocks for directing the assembly of nanoparticles into highly complex and well-defined nanoscale superstructures. Finally, they point toward future studies aimed at incorporating specific chemical modifications to the peptide side chains (*e.g.*, oxidation, hydroxylation, phosphorylation, and glycosylation) and understanding how and why these modifications lead to morphological changes to a nanoparticle superstructure.

## 3.4 EXPERIMENTAL SECTION

### 3.4.1 General materials and methods

All chemicals were purchased from either Aldrich or Fisher and used without further purification.  $N_3\text{-C}_4\text{H}_8\text{CO-AYSSGAPPMPFF}$  ( $N_3\text{-PEP}_{\text{Au}}$ ) was synthesized by Pierce Biotechnology, Inc. Triethylammonium acetate buffer (TEAA) was purchased from Aldrich (catalog number 90358) and 4-(2-hydroxyethyl)-1-piperazineethanesulfonic acid (pH 7.3) (HEPES) buffer was purchased from Fisher (catalog number BP 299-100). Chloroauric acid ( $\text{HAuCl}_4$ ) was purchased from Aldrich (catalog number 520918). Peptide conjugates were purified using an Agilent 1200 series reverse-phase high-pressure liquid chromatography (HPLC) instrument equipped with an Agilent Zorbax 300SB- $\text{C}_{18}$  column. Peptide conjugates were quantified based on their absorbance at 280 nm and using the extinction coefficient for tyrosine ( $1280 \text{ M}^{-1}\text{cm}^{-1}$ ). UV-vis spectra were collected using an Agilent 8453 UV-vis spectrometer equipped with deuterium and tungsten lamps. Matrix-assisted laser desorption ionization time-of-flight mass spectrometry (MALDI-TOF MS) data were collected using an Applied Biosystem Voyager System 6174 MALDI-TOF mass spectrometer (positive reflector mode; accelerating voltage: 20 kV) and using  $\alpha$ -cyano-4-hydroxycinnamic acid (CHCA) as the ionization matrix. TEM images were collected with a FEI Morgagni 268 (80 kV) with an AMT side mount CCD camera system. Phosphotungstic acid (pH 7.4) was used to stain TEM sample grids for the peptide assembly studies. TEM samples were prepared by drop-casting 6  $\mu\text{L}$  of solution onto a 3 mm diameter copper grid coated with formvar. After 5 min., the excess solution was wicked away. The grid was washed with NP  $\text{H}_2\text{O}$  (6  $\mu\text{L}$ ) and wicked away after 1 min. Attenuated total reflectance Fourier transform infrared (ATR-FTIR) spectroscopy data were

collected on a PerkinElmer Spectrum 100 FTIR instrument with a universal attenuated total reflectance sampling accessory coupled to a computer using PerkinElmer Spectrum Express software. The sample was background-corrected in air.  $C_{18}-(PEP_{Au}^{M-ox})_2$  was dissolved and sonicated in 0.1 M HEPES (75 $\mu$ M). After 1 day, the assembled fibers were dialyzed three times in nanopure water using d-tube dialyzers (Millipore, catalog number 71505-3) to remove the buffer, and the fibers were concentrated. The concentrated solution containing the fibers were then drop-cast onto the ATF-FTIR substrate and allowed to air-dry. Nanopure water (NP H<sub>2</sub>O, 18.1 M $\Omega$ ) was obtained from a Barnstead Diamond<sup>TM</sup> water purification system.

### **3.4.2 Preparation of $N_3-PEP_{Au}^{M-ox}$**

$N_3-PEP_{Au}$  (3 mg, 2.23  $\mu$ mol) was dissolved in a 1:1 mixture of CH<sub>3</sub>CN/NP H<sub>2</sub>O. To this solution was added concentrated H<sub>2</sub>O<sub>2</sub> to bring the final H<sub>2</sub>O<sub>2</sub> concentration to 100 mM. The solution was vortexed and left undisturbed for 8-15 h. This final solution was purified using reverse-phase HPLC eluting with a linear gradient of 0.05% formic acid in CH<sub>3</sub>CN and 0.1% formic acid in NP H<sub>2</sub>O (5/95 to 95/5 over 30 min.).

### **3.4.3 Preparation of $C_{18}-(PEP_{Au}^{M-ox})_2$**

Alkyne-terminated aliphatic substrates and peptide conjugates were prepared according to protocols detailed in a previous report.<sup>62</sup>

#### 3.4.4 Preparation of single helices

In a plastic vial,  $C_{18}-(PEP_{Au}^{M-ox})_2$  (~18.7 nmol) was dissolved in 250  $\mu$ L of 0.1 M HEPES buffer and sonicated for 5 min. After sonication, the solution was allowed to sit at room temperature for 25 min. A fresh stock solution of  $HAuCl_4$  in TEAA buffer was prepared by mixing 100  $\mu$ L of 0.1 M  $HAuCl_4$  in NP  $H_2O$  with 100  $\mu$ L of 1 M TEAA buffer. The resulting mixture was vortexed for 1 min. To the  $C_{18}-(PEP_{Au}^{M-ox})_2$  solution was added 2  $\mu$ L of the freshly prepared  $HAuCl_4$ /TEAA solution. A “dark cloud” appeared 2-4 s after the addition of the  $HAuCl_4$ /TEAA solution; at this point, the vial was briefly vortexed and then left undisturbed at room temperature.

#### 3.4.5 Preparation of $C_{18}-(PEP_{Au}^{M-ox})_2$ fibers

75  $\mu$ M solutions of  $C_{18}-(PEP_{Au}^{M-ox})_2$  fibers were prepared in 0.1 M HEPES buffer. For CD spectroscopy studies, 10 mM HEPES buffer was used. After 1 day of sitting at room temperature, the solutions were analyzed. For some CD and TEM experiments,  $CaCl_2$  was added (1 mM final concentration) to accelerate fiber formation.

#### 3.4.6 Cryogenic electron tomography and 3D reconstruction

For the single-helical gold nanoparticle superstructure, 4  $\mu$ L of solution was applied to the carbon side of glow discharged perforated R2/2 Quantifoil grids (Quantifoil Micro Tools, Jena, Germany) before plunge-freezing using a manual gravity plunger. A series of images were recorded by tilting the specimen from  $-60$  to  $70^\circ$  in increments of  $3^\circ$  ( $<45^\circ$ ) and  $2^\circ$  ( $>45^\circ$ ). Images were recorded on a FEI Falcon II direct electron detector camera at a nominal



magnification of 39 000x. Altogether, 51 images were collected in one tilt series with a total dose of  $\sim 50 \text{ e}^-/\text{\AA}^2$ . Images were recorded at a defocus value of  $\sim 0.5 \text{ }\mu\text{m}$  using FEI batch tomography software. The IMOD package<sup>123</sup> was used to align tilted projection images and reconstruct the final 3D density map from the aligned image stack. For surface rendering, the tomogram was filtered to 20  $\text{\AA}$  resolution and displayed using the program UCSF CHIMERA.<sup>124</sup>

### 3.4.7 Atomic force microscopy

AFM images were collected with an Asylum MFP-3D atomic force microscope using tapping-mode. Images were obtained using ultrasharp AFM tips (NanoandMore, SHR-150), with a 1 Hz scanning rate. The APTES-mica was prepared by drop-casting a 0.1% APTES solution in NP H<sub>2</sub>O onto freshly cleaved mica, and after 10 min., the mica was rinsed with NP H<sub>2</sub>O. C<sub>18</sub>-(PEP<sub>Au</sub><sup>M-ox</sup>)<sub>2</sub> was dissolved in 0.1 M HEPES (75  $\mu\text{M}$ ) and allowed to sit at room temperature overnight. After 1 day of incubation, 20  $\mu\text{L}$  of the solution was drop-cast onto the APTES-functionalized mica. After 1 min., the sample was rinsed with NP H<sub>2</sub>O and allowed to air-dry overnight.

### 3.4.8 Circular dichroism spectroscopy

CD measurements were conducted on an Olis DSM 17 CD spectrometer. The scan rate was 8 nm/min., and the bandwidth was 2 nm. All CD experiments were carried out in 10 mM HEPES (peptide assembly; 200 -280 nm) or 0.1 M HEPES (nanoparticle assembly; 450-800 nm) with a 1 mm path length quartz cuvette at 25°C.

### 3.4.9 Powder X-ray diffraction

Powder X-ray diffraction was performed on a Bruker X8 Prospector Ultra diffractometer equipped with an APEX II CCD detector and an I $\mu$ S microfocus Cu K $\alpha$  source ( $\lambda = 1.54178 \text{ \AA}$ ). The diffractograms were recorded at a distance of 15 cm at room temperature. Raw data were retrieved using the PILOT plug-in in the Bruker APEX II software package and further processed in Match! software to obtain  $d$  and intensity values. The sample was prepared by dissolving  $\sim 1.5 \text{ mg}$  of C<sub>18</sub>-(PEP<sub>Au</sub><sup>M-ox</sup>)<sub>2</sub> in 1 mL of 0.1 M HEPES and sonicating for 5 min. The sample was left to sit overnight. After 24 h, the solution was ultracentrifuged ( $r_{\text{max}} = 213\,000g$ ) for 1 h. The supernatant was removed and NP H<sub>2</sub>O (1 mL) was added, and the sample was ultracentrifuged again at the same speed. After centrifugation, the supernatant was removed, leaving behind a clear gel. The peptide gel was loaded into a glass capillary ( $\varphi = 0.7 \text{ mm}$ ) and air-dried.

### 3.4.10 MAS solid-state NMR spectroscopy

Labeled N<sub>3</sub>-PEP<sub>Au</sub> was purchased from Pierce Custom Peptides, and labeled C<sub>18</sub>-(PEP<sub>Au</sub><sup>M-ox</sup>)<sub>2</sub> was synthesized according to the protocols detailed above. Labeled C<sub>18</sub>-(PEP<sub>Au</sub><sup>M-ox</sup>)<sub>2</sub> fibers ( $\sim 2 \text{ mg}$ ) were packed into thin-wall 3.2 mm zirconia MAS rotors (Bruker Biospin, Billerica, MA) by ultracentrifugation at  $\sim 175\,000g$  in a home-built sample packing tool spun in a Beckman Coulter Optima L-100 XP ultracentrifuge equipped with a SW-32 Ti rotor. MAS ssNMR spectra were obtained with a widebore Bruker Avance I NMR spectrometer operating at a <sup>1</sup>H Larmor frequency of 600 MHz (14.1 T) using a 3.2 mm HCN MAS ssNMR probe equipped with a “EFree” reduced electric field coil (Bruker Biospin). Sample temperature was maintained at 277

K using a constant flow (800 L/h) of cooled gas. Bruker Topspin software was used to acquire the spectra. Spectra were processed using NMRPipe software and analyzed with CCPNMR/Analysis.<sup>125-126</sup> The <sup>13</sup>C signals of adamantane were used to externally reference chemical shifts to 4,4-dimethyl-4-silapentane-1-1 sulfonic acid (DSS).<sup>127</sup> 1D and 2D ssNMR spectra were acquired at 10 kHz MAS, using ramped <sup>1</sup>H, <sup>13</sup>C cross polarization (CP) with a 2.0 ms CP contact time, a 3 s recycle delay, and 83 kHz two-pulse phase-modulated (TPPM) decoupling.<sup>128</sup> A total of 1024 scans were obtained for the 1D Cp Experiment. The short-mixing <sup>13</sup>C-<sup>13</sup>C 2D spectrum was obtained with 20 ms of dipolar assisted rotational resonance (DARR) <sup>13</sup>C-<sup>13</sup>C mixing. The 2D spectrum in Appendix B (**Figure S3.65b**) feature 500 ms of <sup>13</sup>C-<sup>13</sup>C proton-driven spin diffusion (PDSD), which is expected to allow longer-range signal transfer over up to 6-7 Å.<sup>129</sup> Additional experimental details are summarized in **Table S3.2** of Appendix B.

## **4.0 POST-SYNTHETIC SURFACE MODIFICATION OF HOLLOW SPHERICAL GOLD NANOPARTICLE SUPERSTRUCTURES WITH TUNABLE ASSEMBLY METRICS**

This work is a *manuscript in preparation*. The supporting information for this chapter is found in Appendix C.

### **4.1 INTRODUCTION**

As mentioned in Chapter 1, metallic nanoparticles and their assemblies have attracted significant attention due to their myriad properties and applications. An important component of metallic nanoparticles is the ligand that is adsorbed to the nanoparticle surface. They serve a variety of important roles: i) they passivate the nanoparticle surface, preventing aggregation; ii) they can impart functionality to the nanoparticle; iii) they serve as the interface between the nanoparticle and its environment; and iv) they can significantly affect the physical properties of the nanoparticle core. To date, hundreds of ligands have been successfully employed to introduce new properties and functions to nanoparticles, giving rise to a plethora of applications.<sup>130</sup> For example, gold nanoparticles that have a shell of oligonucleotide ligands anchored onto their surface exhibit unique cellular uptake properties, which make them attractive therapeutic candidates.<sup>131</sup> Motivated by the important role that ligand chemistry plays in nanoparticle-based

systems, we aimed to explore methods to modify the surfaces of pre-fabricated nanoparticle superstructures. To our knowledge, post-synthetic modification of nanoparticle assemblies has been relatively unexplored. Most nanoparticle self-assembly methods use nanoparticles anchored with thiolated ligands (*e.g.*, thiolated oligonucleotides, thiolated amphiphilic block copolymers) to direct their assembly,<sup>13, 21-22, 132-137</sup> which make them poor candidates for post-synthetic modification (via ligand exchange) due to the relatively strong gold-thiol bond.

In contrast to other nanoparticle assembly methods, the Rosi group has developed a peptide-based route for assembling gold nanoparticle superstructures.<sup>25</sup> In this method, a gold-binding peptide conjugate, R-PEP<sub>Au</sub> (where R = hydrophobic organic group, and PEP<sub>Au</sub> = AYSSGAPPMPPF<sup>55</sup>), both caps and directs the assembly of gold nanoparticles.<sup>25</sup> The peptide assembly serves as the underlying scaffold that supports the nanoparticle superstructure.<sup>25, 62-63</sup> We propose that the amino acid residues near the C-terminus of PEP<sub>Au</sub> are responsible for much of the binding between the particle and the peptide assembly,<sup>63</sup> which is in agreement with computational studies.<sup>96</sup> We postulate that the peptides that incorporate into the peptide assembly scaffold bind to part of the gold nanoparticles, anchoring them to the structure,<sup>63</sup> while a combination of free, unincorporated peptide conjugate molecules and buffer constituent molecules (*e.g.*, HEPES, which is a weak binding agent<sup>138</sup>) in solution help stabilize the solvent-exposed nanoparticle surface. We reason then that the portion of the nanoparticles making up the superstructure that are exposed to solution could be replaced by more strongly binding surface capping ligands via ligand exchange and that such ligand exchange methods may provide a means of tailoring the properties of the superstructure. As a proof-of-concept, we chose to conduct these post-synthetic modification studies on hollow spherical gold nanoparticle (HSAuNP) superstructures that were previously assembled and studied by our group.<sup>60, 64, 139</sup>

These superstructures were chosen because i) they have a propensity to aggregate, which limits their potential utility in various applications; ii) they are spherical and we envision that they can ultimately be used as a ‘supernanoparticle’ which could constitute a complex building block for extended periodic lattices; and iii) they have properties that make them attractive as therapeutics agents<sup>8, 12-13, 134, 140-141</sup> and metamaterials.<sup>142-144</sup> Herein, we describe post-synthetic methods to functionalize the surfaces of HSAuNP superstructures. We show that the superstructures can be stabilized and their surface properties manipulated. These results offer a glimpse of the potential of using these methods to modify the surface properties of a variety of different nanoparticle superstructures.

## **4.2 RESULTS AND DISCUSSION**

### **4.2.1 Monitoring the assembly formation of HSAuNP superstructures**

As opposed to other methods where particles are pre-fabricated prior to assembly, our assembly methodology is unique in that the gold nanoparticles are synthesized *and* directed into the nanoparticle superstructure in one concerted step.<sup>25</sup> This process is highly dynamic in that the structural features of the superstructure evolve throughout the assembly process. Therefore, we first began by studying the formation of HSAuNP superstructures over time with varying amounts of gold precursor solution added to the assembly solution. We hypothesized that varying the amount of gold precursor solution to the assembly medium would be a straightforward approach to adjust the density of nanoparticles bound to the peptide surface and therefore would serve as a means to control their optical properties. We used a modified version

of a protocol developed in our lab (see experimental section for details).<sup>60, 64</sup> Briefly, 0.7, 0.9, and 1.1  $\mu\text{L}$  of a mixture of chloroauric acid ( $\text{HAuCl}_4$ ) and triethylammonium acetate (TEAA) (0.1 M  $\text{HAuCl}_4$  in 1 M TEAA), which serves as the gold precursor solution, was added to solutions of  $\text{C}_6\text{-AA-PEP}_{\text{Au}}$  in 0.1 M 4-(2-hydroxyethyl)-1-piperazineethanesulfonic acid (HEPES) buffer (150  $\mu\text{M}$ ). In this method, HEPES functions as the primary reducing agent for the  $\text{HAuCl}_4/\text{TEAA}$  mixture, promoting the *in situ* synthesis of gold nanoparticles, and  $\text{C}_6\text{-AA-PEP}_{\text{Au}}$  functions as the directing agent for nanoparticle assembly. The resulting assemblies were monitored via transmission electron microscopy (TEM) at multiple different time points (10 min., 30 min., 1 hr., 3 hrs., and 1 day).

From TEM, HSAuNP superstructures were observed after 10 min. for all samples (**Figure S4.67**). The superstructures were well-dispersed with few small particles bound to the peptide assembly surface. Samples prepared after 30 min. revealed structures with a greater number of particles adhered to the spherical peptide assembly (**Figure 4.26a,e,i**). After 1 hr., more particles attach to the peptide assembly but to a varying extent depending on the amount of  $\text{HAuCl}_4/\text{TEAA}$  introduced (**Figure 4.26b,f,j**). HSAuNP superstructures with the highest density of nanoparticles were observed for samples injected with 1.1  $\mu\text{L}$  of gold precursor solution (**Figure 4.26j**), whereas decreasing nanoparticle coverage was observed for the solutions injected with 0.9 and 0.7  $\mu\text{L}$  of the gold precursor solution, respectively. (**Figure 4.26f,b**). These results confirm our hypothesis that the nanoparticle density of the HSAuNP superstructures can indeed be tuned simply by adjusting the amount of gold precursor solution added to the assembly mixture. Well-dispersed HSAuNP superstructures were observed after 3 hrs. of assembly (**Figure 4.26c,g,k**). At this point, however, we noticed few small clusters of assemblies,

suggesting the onset of aggregation between the nanoparticle superstructures (**Figure 4.26c,g,k**). Extensive aggregation was observed after 24 hrs. (**Figure 4.26d,h,l**).

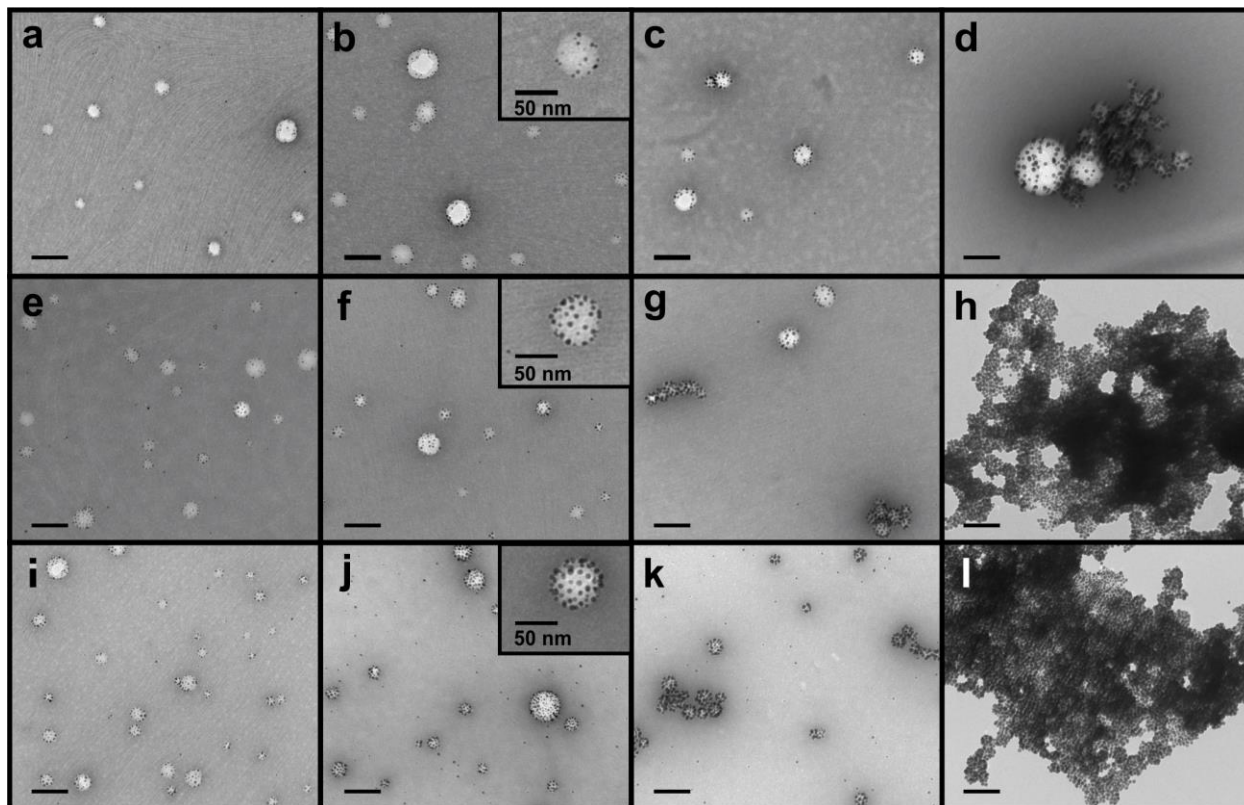


**Figure 4.26.** TEM images of HSAuNP superstructures assembled with 0.7  $\mu\text{L}$   $\text{HAuCl}_4/\text{TEAA}$  after (a) 30 min., (b) 1 hr., (c) 3 hrs., and (d) 24 hrs. TEM images of HSAuNP superstructures assembled with 0.9  $\mu\text{L}$   $\text{HAuCl}_4/\text{TEAA}$  after (e) 30 min., (f) 1 hr., (g) 3 hrs., and (h) 24 hrs. TEM images of HSAuNP nanoparticle superstructures assembled with 1.1  $\mu\text{L}$   $\text{HAuCl}_4/\text{TEAA}$  after (i) 30 min., (j) 1 hr., (k) 3 hrs., and (l) 24 hrs. (scale bars = 100 nm)

The propensity for aggregation at later time points could be due to the absence of capping ligands, which are necessary for passivating the gold nanoparticle surface. At initial time points, unincorporated  $\text{C}_6\text{-AA-PEP}_{\text{Au}}$  monomers in solution may serve to temporarily cap the nanoparticle superstructures; however, as the assembly progresses,  $\text{C}_6\text{-AA-PEP}_{\text{Au}}$  monomers incorporate into the spherical peptide assemblies, thus depleting the population of  $\text{C}_6\text{-AA-PEP}_{\text{Au}}$



monomers in the assembly medium. This depletion may initiate the aggregation of the nanoparticle superstructures. In fact, the average HSAuNP superstructure diameter, measured via TEM, increases during the assembly process (**Figure 4.27a**). This could be due to an Ostwald ripening-like effect, where larger, more stable HSAuNP superstructures continue to grow at the expense of smaller ones. Interestingly, collected data on the diameters of HSAuNP superstructures formed with 0.7, 0.9, or 1.1  $\mu\text{L}$  revealed a distinctive trend: smaller diameters are observed when larger amounts of  $\text{HAuCl}_4/\text{TEAA}$  is introduced to the assembly solution (**Figure 4.27b**). We attribute this trend to the amount of cationic gold ions present in the assembly solution. These ions can initiate peptide nucleation events that lead to peptide assembly.<sup>82</sup> Therefore, we reason that larger concentrations of gold ions lead to more nucleation events, which results in smaller HSAuNP superstructures on average.<sup>145</sup> These results show that one can tune the superstructure size by adjusting the amount of gold precursor solution added to the assembly mixture.

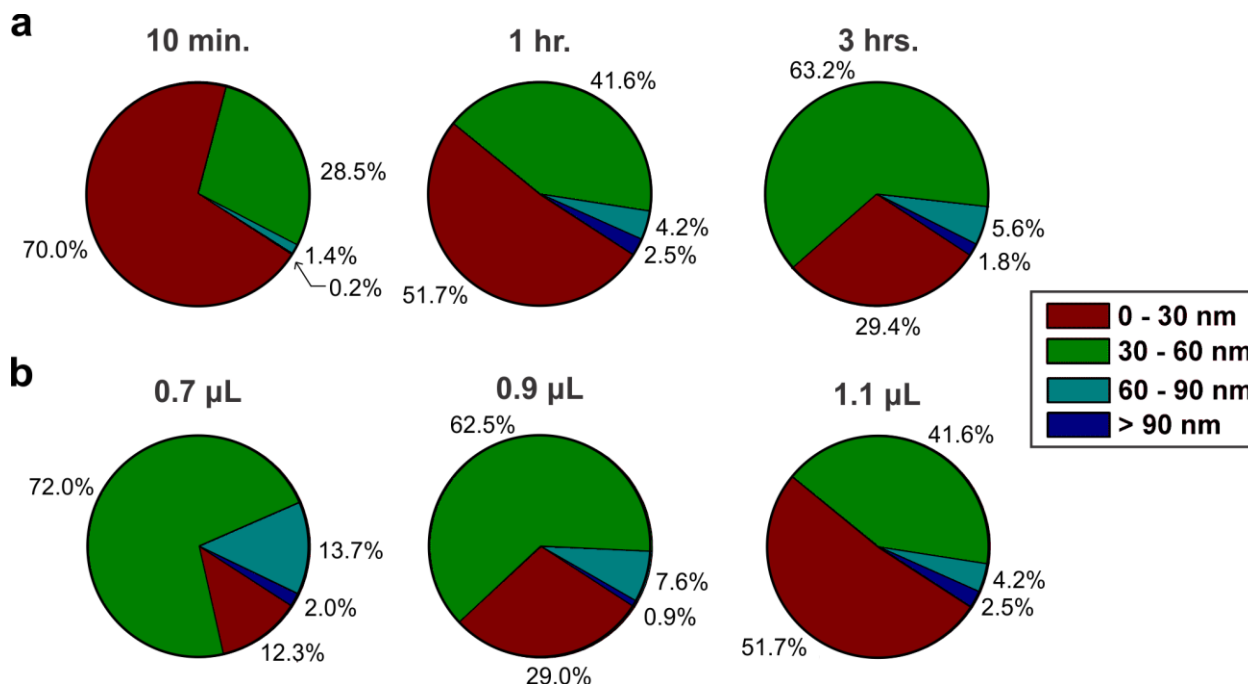


**Figure 4.27.** (a) Distribution of sphere diameters of HSAuNP superstructures after 10 min., 1 hr. and 3 hrs. for samples assembled with 1.1  $\mu\text{L}$  of  $\text{HAuCl}_4/\text{TEAA}$ . (b) Distribution of sphere diameters (collected after 1 hr. of assembly time) as a function of the amount of  $\text{HAuCl}_4/\text{TEAA}$  added to the  $\text{C}_6\text{-AA-PEP}_{\text{Au}}$  solution in HEPES.

#### 4.2.2 Ligand-capped nanoparticle superstructures

Based on the assembly formation studies, we hypothesized that introduction of capping ligands immediately before the onset of aggregation could stabilize the HSAuNP superstructures, thus preventing their aggregation. Since prior work has shown that  $\text{PEP}_{\text{Au}}$  can effectively cap the surface of gold nanoparticles,<sup>55</sup> we introduced an excess amount of  $\text{PEP}_{\text{Au}}$  (4.7 nmol) to HSAuNP superstructures formed after 1 hr. of assembly with 0.7  $\mu\text{L}$  and 1.1  $\mu\text{L}$  of  $\text{HAuCl}_4/\text{TEAA}$  added. After 24 hrs., well-dispersed HSAuNP superstructures were observed, indicating that  $\text{PEP}_{\text{Au}}$  successfully passivated the nanoparticle superstructure surface (**Figure 4.28a,b**). UV-Vis spectra of these superstructures revealed a LSPR band at  $\sim 540$  nm for both assemblies, which is consistent with particles that are in close proximity with one another

(Figure 4.28c,d). We also note that the nanoparticle coverage density between the superstructures formed with 0.7 and 1.1  $\mu\text{L}$   $\text{HAuCl}_4/\text{TEAA}$  remained consistent with our prior results in that the former had lower coverage of nanoparticles compared to the latter. As expected, the diameters of the individual gold nanoparticles increased, indicating that excess gold ions in solution continue to reduce onto the nanoparticles.

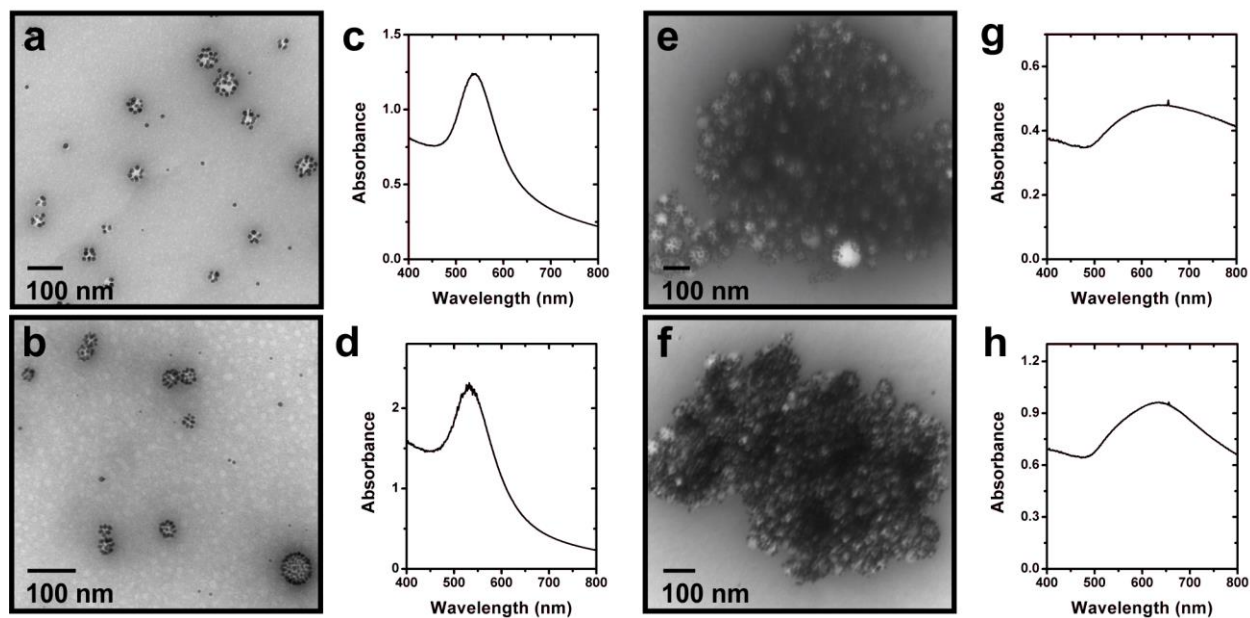


**Figure 4.28.** TEM images of HSAuNP superstructures formed with (a) 0.7  $\mu\text{L}$  and (b) 1.1  $\mu\text{L}$  of  $\text{HAuCl}_4/\text{TEAA}$ , after 1 day of incubation with  $\text{PEP}_{\text{Au}}$ , and (c,d) their corresponding UV-Vis absorption spectra, respectively. TEM images of HSAuNP superstructures formed with (e) 0.7  $\mu\text{L}$  and (f) 1.1  $\mu\text{L}$  of  $\text{HAuCl}_4/\text{TEAA}$  after 1 day of incubation with proteinase K, and (g,h) their corresponding UV-Vis absorption spectra, respectively.

While  $\text{PEP}_{\text{Au}}$  served to maintain the dispersion of the HSAuNP superstructures, upon centrifugation, the superstructures aggregated (not shown). This is not surprising considering the relatively weak peptide-nanoparticle binding interaction. Furthermore, incubation of  $\text{PEP}_{\text{Au}}$ -capped spheres in the presence of proteinase K, a non-specific peptidase, led to aggregation, but

in agreement with a prior study, the HSAuNP superstructure themselves remained intact (**Figure 4.28e,f**).<sup>139</sup> UV-Vis spectra showed a sizeable red-shift confirming the aggregated product (**Figure 4.28g,h**). We conclude that the PEP<sub>Au</sub> capping layer used to prevent aggregation was digested by the peptidase, but the C<sub>6</sub>-AA-PEP<sub>Au</sub> molecules that make up the peptide-gold nanoparticle superstructure remain intact, suggesting that the peptides within the structure are highly compact and resistant to proteinase K digestion. These studies suggest that one can exploit the different binding properties between “core” peptide molecules (*i.e.*, C<sub>6</sub>-AA-PEP<sub>Au</sub> molecules that make up the peptide assembly scaffold) and “surface” peptide molecules (*i.e.*, PEP<sub>Au</sub> molecules that passivate the solvent-exposed nanoparticle surface), as hypothesized.

Motivated by the promising results of PEP<sub>Au</sub>-capped nanoparticles superstructures and the stability exhibited by C<sub>6</sub>-AA-PEP<sub>Au</sub> molecules that make up the spherical peptide assembly scaffold, we began to explore the possibility of functionalizing the surfaces of HSAuNP superstructures. We first employed thiolated ligands. Two common thiolated ligands used for functionalizing gold nanoparticles, mercaptohexanoic acid (MHA) and poly(ethylene glycol) methyl ether thiol (PEG-SH; M<sub>n</sub> = 1000 Da), were chosen. Since thiols form a strong bond with gold, we predicted that the presence of thiolated capping ligands may affect the structural integrity of the HSAuNP superstructures; therefore, we investigated how varying amounts of added ligand affects the nanoparticle superstructure integrity. After 30 min. of assembly, stock solutions of MHA and PEG-SH were added directly to solutions of HSAuNP superstructures (formed using 1.1 μL HAuCl<sub>4</sub>/TEAA) to give final thiol concentrations of 2, 20, and 200 μM. TEM samples were prepared after 24 hrs. of incubation (**Figure 4.29**).

Well-dispersed HSAuNP superstructures were observed only under certain conditions. At very low MHA concentrations (2 μM), aggregated superstructures were the dominant product

(**Figure 4.29a**). However, at intermediate MHA concentrations (20  $\mu\text{M}$ ), the superstructures remained dispersed (**Figure 4.29b**). At higher MHA concentration (200  $\mu\text{M}$ ), only a few dispersed superstructures were observed indicating that a majority of the HSAuNP superstructures degraded (**Figure 4.29c**). Based on this data set, we conclude that there is a minimum threshold thiol concentration that is needed to disperse the spheres, but there is also a maximum amount of added thiol that the spheres can tolerate, beyond which they deconstruct. For HSAuNP superstructures incubated with PEG-SH, we observed dispersed superstructures for spheres incubated in 2 and 20  $\mu\text{M}$  PEG-SH solutions (**Figure 4.29d,e**), but degraded superstructure and free nanoparticles were observed in 200  $\mu\text{M}$  PEG-SH (**Figure 4.29f**). The discrepancy between MHA and PEG-SH at low concentration (2  $\mu\text{M}$ ) is most likely due to the steric difference between the two molecules. PEG-SH, which is much more sterically bulky than MHA, would have less ligand density than MHA on the nanoparticle surface, and therefore can stabilize the nanoparticle superstructure at lower thiol concentrations.<sup>146</sup> In addition to dispersed HSAuNP superstructures, there appeared to be a greater concentration of free nanoparticles with increasing amount of added thiol. This may be attributed to i) the reduction of free gold ions in solution by the thiol ligands or ii) possibly the deconstruction of some HSAuNP superstructures. Based on these studies we conclude that thiolated ligands can indeed be used to effectively cap the surface of pre-fabricated nanoparticle superstructures, assembled using our peptide-based method, provided that certain controlled amounts of thiolated ligands are added. Beyond a certain threshold amount, the thiolated ligands can displace/disrupt the peptide assembly-gold nanoparticle ‘bonds’, and thus promote the assembly deconstruction (**Figure 4.29c,f**).

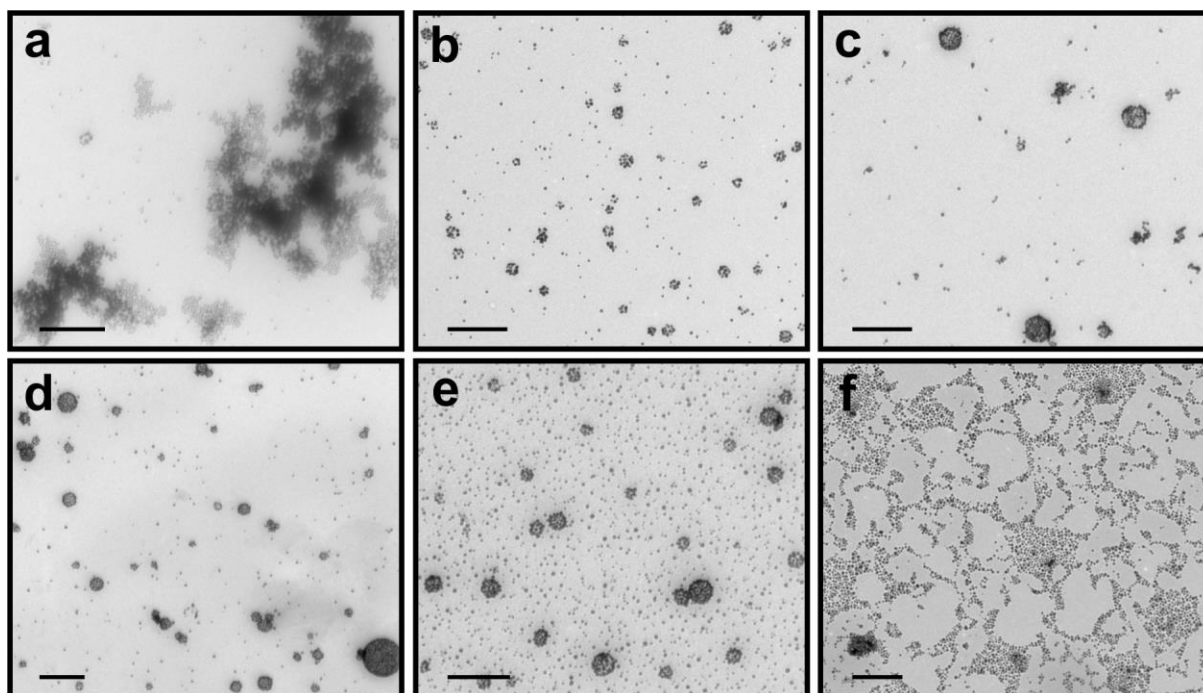


**Figure 4.29.** TEM images of HSAuNP superstructures after 1 day of incubation in (a) 2  $\mu\text{M}$ , (b) 20  $\mu\text{M}$ , and (c) 200  $\mu\text{M}$  MHA. TEM images of HSAuNP superstructures after 1 day of incubation in (d) 2  $\mu\text{M}$ , (e) 20  $\mu\text{M}$ , and (f) 200  $\mu\text{M}$  PEG-SH (MW = 1000). (scale bars = 200 nm)

### 4.3 CONCLUSION AND FUTURE WORK

In conclusion, we demonstrate that the surface of HSAuNP superstructures can be modified through addition of capping ligands during the nanoparticle assembly process. We show that for thiolated ligands, there is an optimum concentration needed to disperse the assemblies and prevent degradation of the superstructures. These studies show that the peptide assembly-gold nanoparticle ‘bonds’ are robust and ligand exchange can take place only on the surface-exposed portion of the nanoparticles. These results highlight a powerful and versatile post-synthetic approach for tuning the surface chemistry and properties of nanoparticle superstructures. We also show that the assembly metrics, such as nanoparticle coverage density and size, can be tuned by

simply adjusting the amount of gold precursor mixture introduced into the assembly solution. Future work will be directed toward extending these methods by expanding the repertoire of ligands attached to the nanoparticle superstructure (*e.g.*, thiolated oligonucleotides), as well as translating this post-synthetic modification method to other peptide-based nanoparticle superstructures that have been developed by our group, such as optically active single helices.

## 4.4 EXPERIMENTAL SECTION

### 4.4.1 General materials and methods

N<sub>3</sub>-C<sub>4</sub>H<sub>8</sub>CO-AYSSGAPPMPPF (N<sub>3</sub>-PEP<sub>Au</sub>) was synthesized and purified by Pierce Biotechnology, Inc. AYSSGAPPMPPF was synthesized and purified by New England Peptide Inc. Triethylammonium acetate buffer (TEAA) was purchased from Aldrich (catalog number 90358) and 4-(2-hydroxyethyl)-1-piperazineethanesulfonic acid (pH 7.3) (HEPES) buffer was purchased from Fisher (catalog number, BP 299-100). Chloroauric acid (HAuCl<sub>4</sub>) was purchased from Aldrich (catalog number, 520918). Poly(ethylene glycol) methyl ether thiol (PEG-SH, average M<sub>n</sub> = 1000 Da) was obtained from Laysan Bio, Inc. 6-Mercaptohexanoic acid (MHA) was obtained from Aldrich (catalog number, 674974). Peptide conjugates were purified using an Agilent 1200 series reverse-phase high-pressure liquid chromatography (HPLC) instrument equipped with an Agilent Zorbax 300SB-C<sub>18</sub> column. Peptide conjugates were quantified based on their absorbance at 280 nm and using the extinction coefficient for tyrosine (1280 M<sup>-1</sup>cm<sup>-1</sup>). UV-Vis spectra were collected using an Agilent 8453 UV-vis spectrometer equipped with deuterium and tungsten lamps. TEM images were collected with a FEI Morgagni 268 (80 kV)

with an AMT side mount CCD camera system. TEM samples were prepared by drop-casting 5  $\mu\text{L}$  of solution onto a 3 mm diameter copper grid coated with formvar. After 4 min., the excess solution was wicked away. The grid was stained with phosphotungstic acid solution (pH = 7.4, 5  $\mu\text{L}$ ) and wicked away after 1 min. Nanopure water (NP H<sub>2</sub>O, 18.2 M $\Omega$ ) was obtained from a Barnstead Diamond<sup>TM</sup> water purification system.

#### **4.4.2 Assembly of HSAuNP superstructures**

We use a protocol that is similar to the protocols used previously within the group.<sup>60, 64</sup> In a plastic vial, lyophilized C<sub>6</sub>-AA-PEP<sub>Au</sub> (~18.7 nmol) was dissolved in 125  $\mu\text{L}$  of 0.1 M HEPES buffer and sonicated for 5 min. After sonication, the solution was allowed to sit at room temperature for 30 min. During the 30 min. incubation time, a fresh gold precursor solution was prepared: a mixture of 0.1 M chloroauric acid (HAuCl<sub>4</sub>) in 1 M triethylammonium acetate (TEAA; pH = 7.0) buffer was vortexed for 1 min. and incubated for 10 min. at room temperature. Thereafter, the supernatant of the mixture was centrifuged for 10 min. at 5k rpm. After the 30 min. 0.7-1.1  $\mu\text{L}$  of the freshly prepared HAuCl<sub>4</sub>/TEAA solution was added to the peptide solution. A “dark cloud” appeared 2-4 s after the addition of the HAuCl<sub>4</sub>/TEAA solution; at this point, the vial was briefly vortexed and then left undisturbed.

#### **4.4.3 PEP<sub>Au</sub>-capped HSAuNP superstructures**

125  $\mu\text{L}$  solutions of HSAuNP superstructures (formed using 0.7  $\mu\text{L}$ , and 1.1  $\mu\text{L}$  HAuCl<sub>4</sub>/TEAA) were synthesized according to the protocol detailed above. After 1 hr. of assembly time, the



solution was transferred to a vial containing lyophilized PEP<sub>Au</sub> (4.7 nmol). The solution was mixed briefly and left undisturbed at room temperature.

#### **4.4.4 Proteinase K stability studies**

The experimental protocol for the proteinase K stability studies was conducted previously in our group.<sup>139</sup> Briefly, 5  $\mu\text{L}$  of 20 mg/mL proteinase K was added to as-synthesized PEP<sub>Au</sub>-capped spherical gold nanoparticle superstructures. The mixtures were incubated at 37°C for up to 24 hrs.

#### **4.4.5 Thiol-capped HSAuNP superstructures**

To 125  $\mu\text{L}$  solutions of as-synthesized HSAuNP superstructures (after 20 min. of assembly time; formed using 1.1  $\mu\text{L}$  H<sub>2</sub>AuCl<sub>4</sub>/TEAA) was added 1  $\mu\text{L}$  of 0.1 mM MHA/PEG-SH, 1  $\mu\text{L}$  of 1 mM MHA/PEG-SH, or 10  $\mu\text{L}$  of 1 mM MHA/PEG-SH stock solutions to make a 2, 20, or 200  $\mu\text{M}$  solution concentration of MHA/PEG-SH, respectively. The solutions were vortexed briefly and allowed to sit at room temperature for 24 hrs.

## **5.0 PEPTIDE-OLIGONUCLEOTIDE CHIMERAS (POCS): PROGRAMMABLE BIOMOLECULAR CONSTRUCTS FOR THE ASSEMBLY OF MORPHOLOGICALLY-TUNABLE SOFT MATERIALS**

This work, written in collaboration with Ryan V. Thaner, Soumitra Mokashi Punekar, SonBinh T. Nguyen\*, and Nathaniel L. Rosi\*, is *under revision*. The supporting information for this chapter is found in Appendix D.

Dr. Ryan V. Thaner prepared the azido-functionalized oligonucleotide starting material. Soumitra Mokashi Punekar assisted with the synthesis and purification of POCs and the assembly experiments.

### **5.1 INTRODUCTION**

Few classes of material building blocks exhibit the programmability offered by nucleic acids and peptides, and from a material-assembly standpoint, each offers a distinct set of properties. Nucleic acids feature unrivalled site-specificity based on sequence-specific base-pairing interactions, which allows for the construction of highly intricate nanoscale architectures including DNA origami<sup>147-148</sup> and spherical nucleic acid assemblies.<sup>20-21</sup> Peptides have highly modular assembly and substrate-recognition capabilities, drawing from their rich diversity of amino acid sequences. For example, a 10-mer peptide built from natural amino acids can have

$20^{10}$  possible sequences. It stands to reason then that molecular building blocks composed of both nucleic acids and peptides could assemble into materials that exhibit heretofore unobserved features and properties.

Peptide-oligonucleotide chimeras (POCs), comprising interlinked peptides and oligonucleotides, represent a new, versatile class of building blocks having assembly characteristics and properties deriving from both biomolecular components. While biological applications of POCs have been explored,<sup>149-150</sup> few studies have examined their potential as programmable building blocks for the construction of soft materials.<sup>151-155</sup> Herein, we present a modular synthesis of POCs in which the peptide and oligonucleotide are attached to an organic-core molecule, resulting in a highly tunable assembly platform where both peptide and oligonucleotide “character” can be independently varied, akin to a block copolymer. The resulting POCs can assemble into either vesicles or 1D fibers, depending on the length of the oligonucleotide building block and the salt concentration. These results highlight the promise of POCs as a versatile class of soft material building blocks and point toward their use for the construction of responsive and dynamic functional materials.

## 5.2 RESULTS AND DISCUSSION

For this initial report, we focus our attention on a POC design that links a single peptide to a single oligonucleotide through a biphenyl organic core (**Figure 5.30**). The AAAYSSGAPPMPPF peptide sequence, was chosen based on its ability to assemble into various structures when conjugated to an organic molecule at its N-terminus.<sup>60</sup> A,4,4'-bisethynylbiphenyl organic core was used so that copper (I) catalyzed “click” chemistry could be

employed to covalently attach azido-modified peptides and oligonucleotides (**Figure 5.30**).<sup>80-81,</sup>  
<sup>156</sup> Conjugation was achieved in a stepwise fashion: 1) the oligonucleotide, an azido-modified 18- or 6-base sequence (**Figure S5.68**), was first attached to the biphenyl core using established solid-phase synthesis method;<sup>157</sup> and 2) the peptide, an N-terminal azido-modified peptide (N<sub>3</sub>-C<sub>4</sub>H<sub>8</sub>CO-AAAYSSGAPPMPPF) (**Figure S5.69**), was next attached in the solution phase to yield the POCs (**Figure 5.30**). Each PO<sub>n</sub>C (n = 18, 6) was purified via reverse-phase high-performance liquid chromatography (HPLC) and their compositions were confirmed by matrix-assisted laser desorption/ionization time-of-flight mass spectrometry (MALDI-TOF MS; **Figure S5.70**).

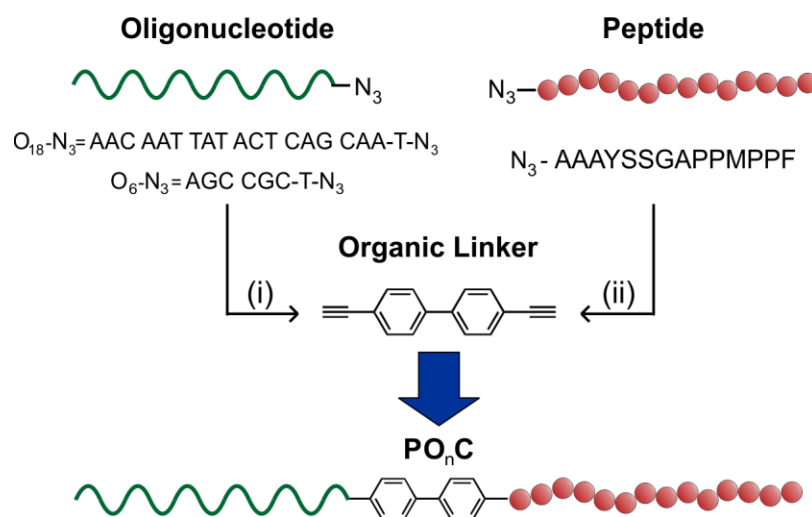


**Figure 5.30.** Modular synthesis of POCs: i) covalent attachment of an azido-modified oligonucleotide sequence to a biphenyl organic linker followed by ii) covalent attachment of an azido-modified peptide.

We first determined optimal conditions for PO<sub>18</sub>C assembly. In the absence of charge-shielding cations, POCs resisted assembling in aqueous media due to the oligonucleotide's negatively charged phosphate backbone. Countercation screening revealed that Ca<sup>+2</sup> promotes assembly of PO<sub>18</sub>Cs into well-defined structures, which prompted a systematic study of PO<sub>18</sub>C

assembly as a function of  $[\text{CaCl}_2]$ . 500  $\mu\text{M}$  solutions of desalted and lyophilized  $\text{PO}_{18}\text{C}$  (500  $\mu\text{M}$ ) were prepared in aqueous  $\text{CaCl}_2$  solutions (10, 50, 150, and 300 mM). These solutions were heated to  $80^\circ\text{C}$  to denature any non-specific  $\text{PO}_{18}\text{C}$  aggregation states and then cooled to room temperature to arrive at preferred assembled structures. Transmission electron microscopy (TEM) was used to image resulting assemblies. Defined circular structures were observed in 50 mM  $\text{CaCl}_2$  (**Figure 5.31b and Figure S5.71**), whereas fibers were exclusively observed in 300 mM  $\text{CaCl}_2$  (**Figure 5.31d and Figure S5.73**). In 150 mM  $\text{CaCl}_2$ , a mixture of products was observed including circular/pseudo circular structures and fibers (**Figure 5.31c and Figure S5.72**). Few amorphous assemblies were observed at 10 mM  $\text{CaCl}_2$ , indicating the existence of a threshold in salt concentration for assembly to occur (**Figure 5.31a**).

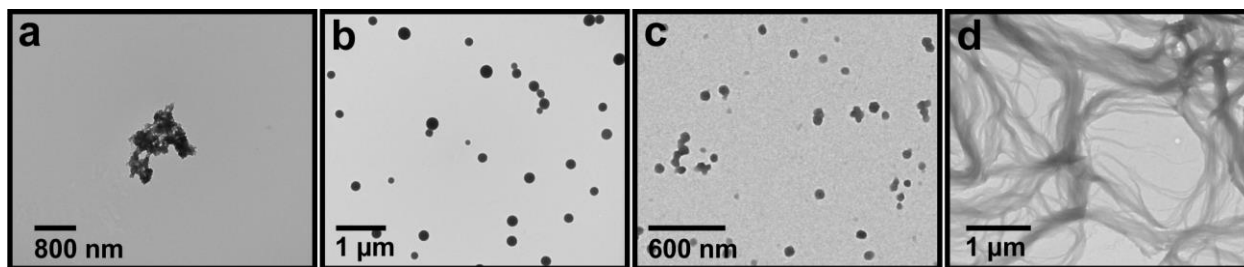


**Figure 5.31.**  $\text{PO}_{18}\text{C}$  assemblies at varying  $\text{CaCl}_2$  concentrations. TEM images of  $\text{PO}_{18}\text{C}$  assemblies formed in (a) 10 mM, (b) 50 mM, (c) 150 mM, and (d) 300 mM  $\text{CaCl}_2$ . TEM samples were prepared after 15-20 hrs. of assembly time.

Scanning electron microscopy (SEM) and tapping-mode atomic force microscopy (AFM) were employed to further investigate the morphology of the circular structures formed in 50 mM  $\text{CaCl}_2$ . SEM images suggest a spherical morphology, (**Figure 5.32a**) and AFM indicates vesicular structure, as the height profile traces are typical of collapsed hollow spheres (**Figure 5.32b-d and Figure S5.74**).<sup>108, 158</sup> In addition, phase images reveal different surface profiles

between the periphery and the interior (**Figure 5.32e** and **Figure S5.75**), which is likely due to the different deformation response of the sphere “center” and “edges”.<sup>108, 158</sup> The thickness, measured via AFM, of the fully collapsed spheres that were previously exposed to high-vacuum TEM environment, is approximately 30 nm (**Figure S5.76**), which is equal to twice the length of an extended PO<sub>18</sub>C (~15 nm; **Figure S5.77**). We therefore conclude that the sphere membrane consists of a single, flexible PO<sub>18</sub>C monolayer.

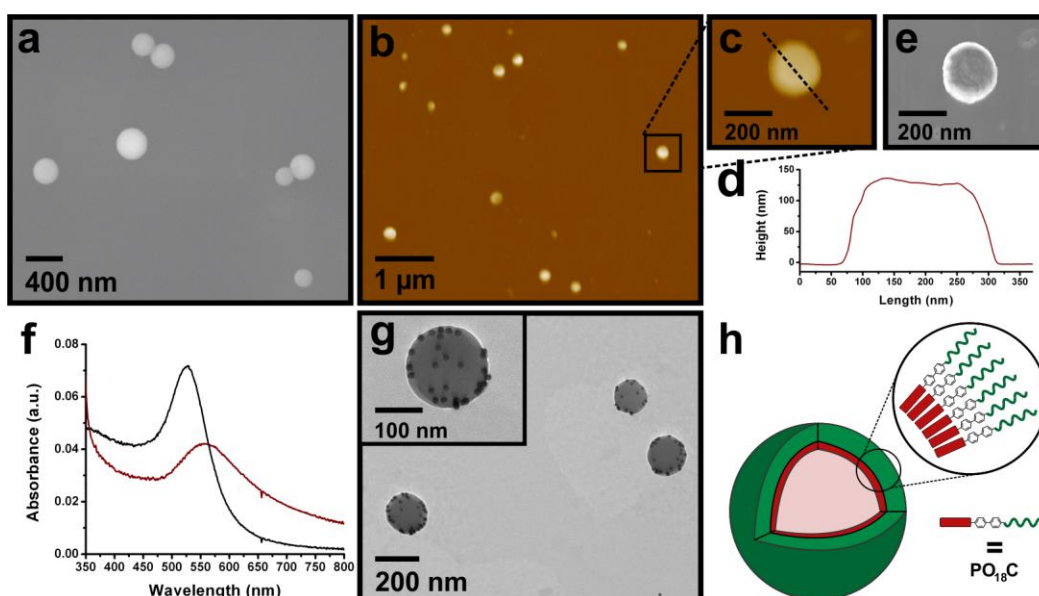


**Figure 5.32.** PO<sub>18</sub>C assembly characterization. (a) SEM images of PO<sub>18</sub>C vesicles assembled in 50 mM CaCl<sub>2</sub>. (b) AFM image of PO<sub>18</sub>C vesicles deposited on mica. (c) AFM image of a vesicle and (d) corresponding height profile along the dashed line shown in c. (e) Phase image of the vesicle shown in c. (f) UV-Vis spectrum of free 15 nm gold nanoparticle functionalized with complementary O<sub>18</sub> sequence (black line) and gold nanoparticle-decorated vesicles after addition of the complementary functionalized gold nanoparticles to a solution containing PO<sub>18</sub>C vesicles (red line). (g) TEM images of the gold nanoparticle-decorated vesicles after addition of 15 nm gold nanoparticles functionalized with complementary O<sub>18</sub> to a solution of PO<sub>18</sub>C vesicles. (h) Proposed assembly model of PO<sub>18</sub>C vesicles. The vesicles are composed of a PO<sub>18</sub>C monolayer, with the oligonucleotides exposed on the outer surface.

Because both the peptide and oligonucleotide are hydrophilic compared to the biphenyl organic core, either may be exposed at the outer surface of the PO<sub>18</sub>C spheres. To determine if the O<sub>18</sub> block is exposed, we mixed the spheres with 15 nm gold nanoparticles decorated with oligonucleotides complementary to O<sub>18</sub>. Under conditions that promote hybridization, localized surface plasmon resonance (LSPR) band of the particles red shifts, signifying particle aggregation and assembly (**Figure 5.32f**), and TEM images show the gold nanoparticles adhered to the sphere surface (**Figure 5.32g and Figure S5.78**). Collectively, the results lead us to propose that the spheres consist of a single PO<sub>18</sub>C monolayer, with the peptide directed inward and the highly-charged oligonucleotide projected outward to the aqueous salt solution (**Figure 5.32h**). These structures resemble ‘spherical nucleic acid’ (SNA) constructs, which have shown promise as therapeutic agents.<sup>131, 159-163</sup> Unlike reported SNAs, however, the PO<sub>18</sub>C assemblies feature a hollow interior enclosed by a pliable, asymmetric monolayer membrane. Their unique composition and structure will motivate future studies aimed at exploration of their therapeutic potential.

As noted earlier, PO<sub>18</sub>Cs assemble into fibers in 150 mM and 300 mM Ca<sup>+2</sup> solutions. These higher salt concentrations may facilitate tighter O<sub>18</sub> packing, resulting in parallel alignment of the PO<sub>18</sub>Cs into fibers (**Figure 5.33a**). In contrast, at lower salt concentrations (50 mM), repulsive interactions between phosphate backbones would drive the oligonucleotides apart from one another, resulting in spherical assemblies (**Figure 5.33b**). Based on this reasoning, tuning the length of the oligonucleotide should significantly affect the assembly morphology. PO<sub>6</sub>C with a much shorter oligonucleotide portion than PO<sub>18</sub>C, may assemble into fibers at salt concentrations below 150 mM.

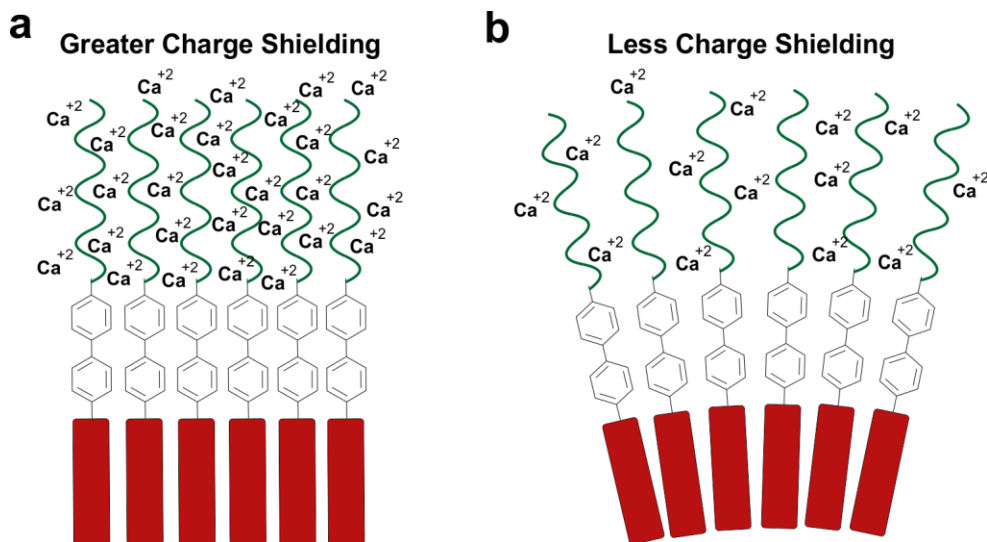


**Figure 5.33.** Role of charge shielding. (a) Greater charge shielding can allow for tighter packing of POCs, which can lead to fiber formation. (b) Greater repulsion due to less charge shielding favors the formation of vesicles.

Indeed, TEM images of PO<sub>6</sub>C assemblies show primarily twisted fibers and fiber aggregates at 50-300 mM CaCl<sub>2</sub> (**Figure 5.34b-d** and **Figure S5.80-S5.82**). A mixture of spherical and fiber assemblies was observed at 10 mM CaCl<sub>2</sub> concentration, which is also consistent with our hypothesis (**Figure 5.34a** and **Figure S5.79**). At higher ionic strengths (150 and 300 mM Ca<sup>+2</sup>), the fibers appear to consist of several bundled strands (**Figure 5.34c,d** and **Figure S5.81, Figure S5.82**); however, individual fibers can be observed at lower ionic strengths (10 and 50 mM Ca<sup>+2</sup>) (**Figure S5.83**). The fibers were exposed to a solution of 5 nm gold nanoparticles functionalized with the O<sub>6</sub>-complementary sequence. However, the particles did not adhere to the fibers and no shift in the LSPR band was observed (**Figure S5.84**); this implies that the O<sub>6</sub> within the fibers are packed tightly together and relatively inaccessible, which prevents duplex formation. Although we cannot propose a detailed model for POC assembly within the fibers at this stage, these results are not inconsistent with the highly-charged oligonucleotide block of the POC still being exposed to the aqueous assembly medium. In



summary, our results clearly demonstrate that both salt concentration and oligonucleotide length significantly affect the morphology of the POC assembly and that both can be independently tuned to promote either fiber or sphere assembly.

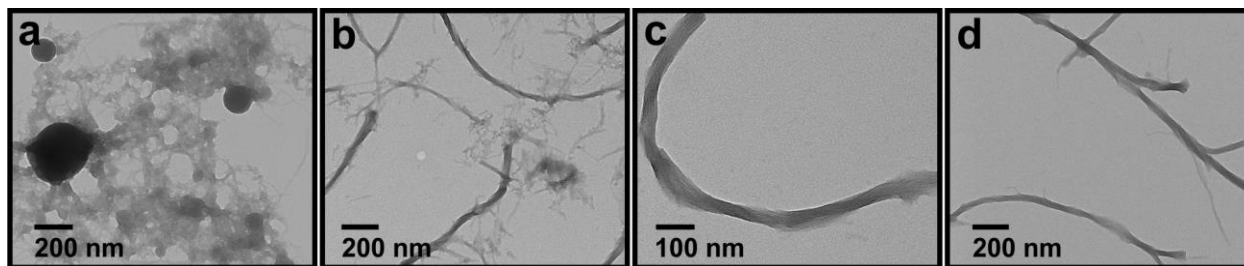


**Figure 5.34.** PO<sub>6</sub>C assemblies at varying CaCl<sub>2</sub> concentrations. TEM images of PO<sub>6</sub>C assemblies formed in (a) 10 mM, (b) 50 mM, (c) 150 mM, and (d) 300 mM CaCl<sub>2</sub>. TEM samples were prepared after 15-20 hrs.

We also considered whether interpeptide interactions affect assembly behavior and morphology. In previous studies, we determined that the N-terminal portion of AYSSGAPPMPFF can assemble into  $\beta$ -sheets if a hydrophobic R-group is attached to the alanine residue.<sup>25, 63</sup> We used Fourier-transformed infrared (FTIR) spectroscopy to determine if similar interpeptide interactions contribute to the assembly behavior of the POCs. An amide I band at 1642 cm<sup>-1</sup>, which indicates the absence of interpeptide secondary structure, was observed for PO<sub>18</sub>C spheres; in contrast, an amide I band at 1631 cm<sup>-1</sup>, characteristic of  $\beta$ -sheet structure, was observed for PO<sub>6</sub>C fibers, suggesting that  $\beta$ -sheets help stabilize and promote fiber formation (**Figure 5.35**).<sup>110-111</sup>

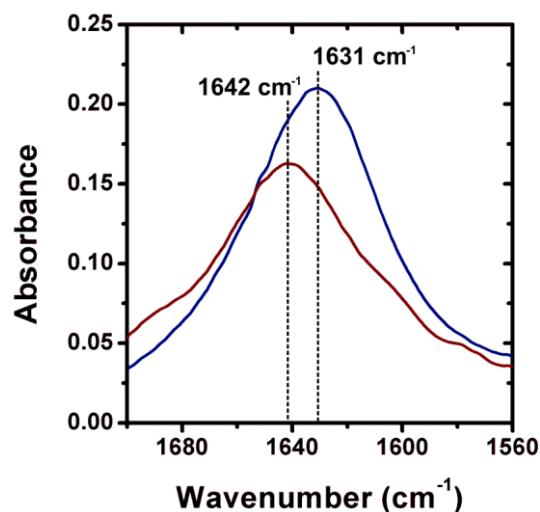


**Figure 5.35.** FTIR spectra of PO<sub>18</sub>C vesicles (red line) and PO<sub>6</sub>C fibers (blue line) assembled in 50 mM CaCl<sub>2</sub>.

Multiple interdependent factors influence the morphology of PO<sub>18</sub>C and PO<sub>6</sub>C assemblies, including salt concentration, oligonucleotide length, and the presence or absence of  $\beta$ -sheet structure. For PO<sub>18</sub>C, with a long oligonucleotide, fibers are not favored at low salt concentrations, presumably due to interstrand repulsive interactions between the phosphate backbones. However, at sufficiently high salt concentrations (*e.g.*, 300 mM CaCl<sub>2</sub>), enhanced charge-screening enables tighter packing of the oligonucleotides, allowing for the parallel alignment of PO<sub>18</sub>Cs into  $\beta$ -sheet networks that facilitate fiber formation (**Figure 5.33a**). For PO<sub>6</sub>C, with a much shorter oligonucleotide, tight parallel packing of the POCs can occur at lower salt concentrations, which enables  $\beta$ -sheet formation and the assembly of fibers. As the salt concentration is lowered, a threshold can be reached at which charge repulsions between the phosphate backbones becomes significant enough to favor sphere formation (**Figure 5.33b**).

Our data and observations point to the possibility of morphology prediction based on the ‘charge ratio,’ defined as the ratio of the total number of positive charges from the Ca<sup>+2</sup> in solution to the total number of negative charges on the POC (**Figure 5.36a**). As the charge ratio

increases, so does the propensity for fiber formation; as it decreases, the propensity for forming spheres increases (**Figure 5.36b**). Based on these trends, we explored the possibility of changing POC assembly morphology by changing the charge ratio of the assembly solution. PO<sub>18</sub>C vesicles were first assembled in 50 mM CaCl<sub>2</sub> (**Figure 5.36c**); thereafter, a small volume of concentrated CaCl<sub>2</sub> solution was added to increase the charge ratio of the assembly mixture from 10 to 67. After one day, fibers were observed (**Figure 5.36d**). This result confirms our hypothesis that altering the charge ratio should induce a morphological change, which can serve as a design rule for future exploration of POC-based assembly.

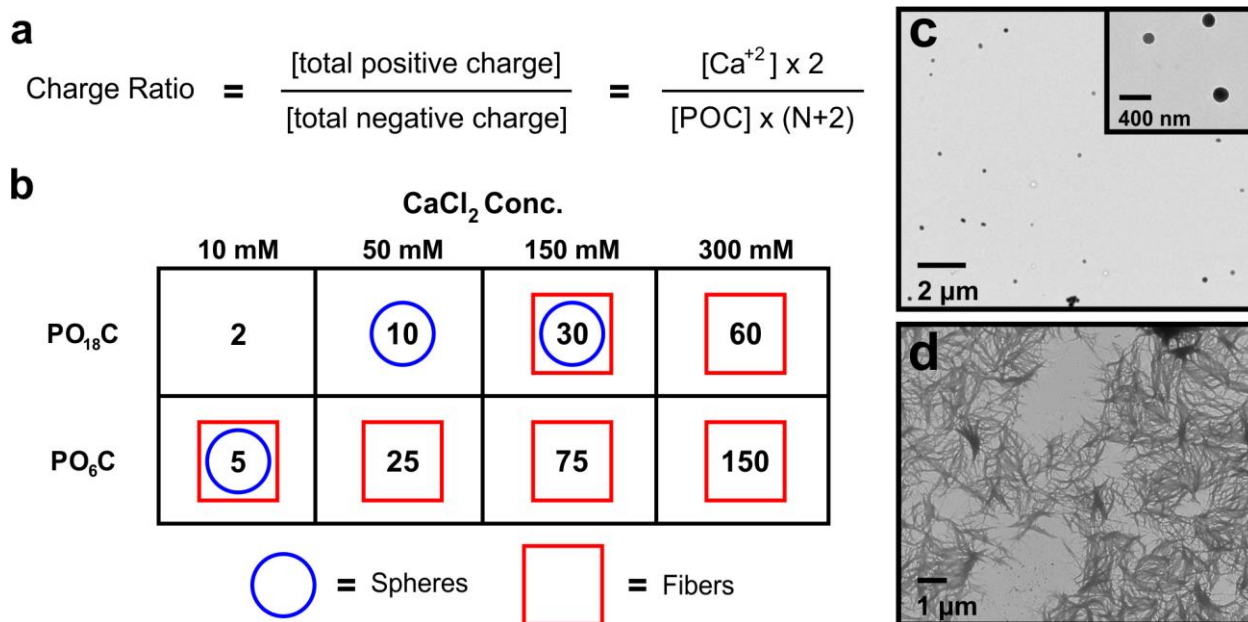


**Figure 5.36.** (a) The charge ratio value is the ratio of positive to negative charges of the assembly solution ( $N$  = number of oligonucleotide bases; the '+2' results from the azido-functionalized T residue, Figure S5.68, and the deprotonated COO<sup>-</sup> terminus of the peptide). (b) The charge ratio of the assembly solution as a function of CaCl<sub>2</sub> concentration and oligonucleotide length. TEM images of PO<sub>18</sub>C vesicles (c) before and (d) after conc. CaCl<sub>2</sub> addition.

One of the most powerful aspects of the POC design is the ability to introduce a highly specific chemical effector into the system in the form of a complementary oligonucleotide. In addition to changes in the rigidity of the oligonucleotide component, such a hybridization would also affect the assembly behavior by decreasing the charge ratio. To this end, subjecting a mixture of PO<sub>18</sub>C (500  $\mu$ M) and the O<sub>18</sub>-complementary oligonucleotide (500  $\mu$ M) in 150 mM CaCl<sub>2</sub> to our assembly conditions clearly revealed defined spherical structures as observed by TEM (**Figure S5.85c,d**). In contrast, the PO<sub>18</sub>C-alone control only showed ill-defined spherical structures or fibers at this salt concentration (**Figure S5.72 and Figure S5.85a,b**). While the enhanced rigidity upon duplex formation cannot be ignored, these preliminary data indicate that adjusting the charge ratio is a straightforward way to adjust the POC assembled structure.

### 5.3 CONCLUSION

In conclusion, we demonstrated that POCs are versatile building blocks for the programmable assembly of new soft materials. With oligonucleotide-biphenyl-peptide as the first POC prototype, assembly morphology can be readily controlled by adjusting the length of the oligonucleotide and the ionic strength of the assembly solution. These studies only scratch the surface of the rich assembly space and morphology control that can be enabled by designing new members of the POC family with variations in peptide sequence, cross linkers, conjugate valency, and oligonucleotide structure and sequence. Lastly, the observation that POCs can be induced to assemble into multiple structures heralds the prospect of using these building blocks to build materials that can undergo morphological changes in response to external conditions or stimuli.

## 5.4 EXPERIMENTAL SECTION

### 5.4.1 General materials and methods

All chemicals were purchased from either Aldrich or Fisher and used without further purification. N<sub>3</sub>-C<sub>4</sub>H<sub>8</sub>CO-AAAYSSGAPPMPPF (N<sub>3</sub>-A<sub>2</sub>PEP<sub>Au</sub>, **Figure S5.69**) was purchased from ThermoFisher Scientific. Gold nanoparticles were purchased from Ted Pella (#15702-20 and #15704-20 for 5 and 15 nm particles, respectively). Peptide oligonucleotide chimeras (POCs) were purified using an Agilent 1200 Series reverse-phase high-pressure liquid chromatography (HPLC) instrument equipped with an Agilent Zorbax 300SB-C<sub>18</sub> column. POCs were quantified based on their absorbance at 260 nm and using the total extinction coefficient of DNA (195,100 M<sup>-1</sup>cm<sup>-1</sup> and 62,800 M<sup>-1</sup>cm<sup>-1</sup> and PO<sub>18</sub>C and PO<sub>6</sub>C, respectively). Spectra were collected using an Agilent 8453 UV-Vis spectrometer equipped with deuterium and tungsten lamps. Transmission electron microscopy (TEM) samples were prepared by drop-casting 4 μL of solution onto a 3-mm-diameter copper grid coated with formvar. After 4 min., the excess solution was wicked away and the grid was washed with nanopure H<sub>2</sub>O (4 μL) and wicked away immediately. TEM images were collected with a FEI Morgagni 268 (80 kV) equipped with an AMT side mount CCD camera system. AFM samples were prepared by drop-casting 6 μL of solution onto freshly cleaved mica or mica functionalized with 3-aminopropyltriethoxysilane(APTES) and air dried. The samples were washed with 30 μL Nanopure H<sub>2</sub>O and wicked away (repeated once). The samples were allowed to dry overnight. AFM images were collected with an Asylum MFP-3D atomic force microscopy using tapping-mode. Images were obtained using ultra-sharp AFM tips (NanoandMore, SHR-150), with a 0.8 Hz scanning rate and 512 pixel resolution. Scanning electron microscopy (SEM) samples were

prepared by drop-casting 5  $\mu\text{L}$  of solution onto silicon wafers and allowed to dry. The samples were then washed with 5  $\mu\text{L}$  nanopure  $\text{H}_2\text{O}$  and wicked away and allowed to dry overnight. SEM images were collected using a ZEISS Sigma 500 VP SEM. Matrix-assisted laser desorption/ionization time-of-flight mass spectrometry (MALDI-TOF MS) data were collected using an Applied Biosystem Voyager System 6174 MALDI-TOF mass spectrometer (negative reflector mode; accelerating voltage: 20kV) with 3-hydroxypicolinic acid (3-HPA) as the ionization matrix. Nanopure water (NP  $\text{H}_2\text{O}$ , 18  $\text{M}\Omega$ ) was obtained from a Barnstead Diamond<sup>TM</sup> water purification system. All TEM measurements were made using ImageJ software.

#### 5.4.2 Preparation of $\text{O}_{18}\text{-N}_3$ and $\text{O}_6\text{-N}_3$

In a typical procedure, syntheses were carried out from the 3' direction using controlled pore glass (CPG) beads possessing 1  $\mu\text{mol}$  of adenine (Glen Research, dA-CPG #20-2001-10, (1000  $\text{\AA}$ , 38  $\mu\text{mol/g}$ ). The CPG beads were placed in a 1  $\mu\text{mol}$  synthesis column and Ultramild 3'-phosphoramidites (Glen Research, Pac-dA-CE phosphoramidite #10-1601-05, Ac-dC-CE phosphoramidite #10-1015-C5, iPr-Pac-dG-CE phosphoramidite #10-1621-05, dT-CE phosphoramidite #10-1030-C5) and 5'-Iodo-dT phosphoramidite (Glen Research, #10-1931-90) were then added using the standard 1  $\mu\text{mol}$  protocol on an Expedite 8909 synthesizer. Note, a mild Cap A Mix (Glen Research, 5% Phenoxyacetic anhydride in THF, #40-4212-52) was also used for synthesis to the lability of the Iodo moiety. At the end of the synthesis, the beads were dried overnight and kept in a tightly capped vial at ambient conditions.

The terminal Iodo groups were substituted for azides using an established procedure.<sup>164</sup> The CPG beads were kept in the columns while a saturated mixture of sodium azide in anhydrous dimethylformamide (DMF) was prepared (approximately 30 mg per 1 mL, per 1

μmol). Upon pulling up 1 mL of the mixture in a syringe, the column was firmly attached with an empty syringe on one end and the one containing the mixture in the other. The mixture was slowly passed over the CPG beads several times before either being left at ambient overnight or placed in a shaker at 60 °C for one hour. The beads were then washed thoroughly with DMF and acetone before drying with nitrogen. The solid-phase coupling reactions with the organic core were performed using these dry CPG beads.

### **5.4.3 Attachment of azido-modified oligonucleotide to diacetylene biphenyl organic core**

Dry CPG beads containing azide-modified DNA were placed in an Eppendorf tube. The biphenyl core (200 mM in DMF, 200 equivalents based on the azide-DNA strands on CPG beads, assuming a 100% yield in the oligonucleotide synthesis), tris(3-hydroxypropyltriazolylmethyl)amine (THPTA, 100 mM in DMF, 100 equivalents based on the azide-DNA strands on CPGs), CuSO<sub>4</sub>·5H<sub>2</sub>O (100 mM in DMF, 100 equivalents based on the azide-DNA strands on CPGs), and L-ascorbic acid (100 mM in DMF, 100 equivalents based on the azide-DNA strands on CPGs) were also added. The reaction mixture was then blanketed with nitrogen before capping and shook for 7 to 18 hours at 25 °C in an Eppendorf® Thermomixer® R (Eppendorf, #022670107) at 1000 rpm. It is important that the CPG beads are constantly agitated while mixing and not sitting at the bottom of the tube.

Once the reaction was complete, the CPG beads were filtered using a one-side fritted 1 μmol Expedite DNA synthesis column (Glen Research, #20-0021-01), then the beads were washed with DMF (5×1 mL) and acetone (5×1 mL) and dried with nitrogen. The beads were then placed in 1 mL of AMA (CAUTION: Only fresh AMA solutions that are not more than two weeks old and have been kept in the refrigerator below 0 °C should be used) at 65 °C for 15

minutes to cleave the conjugates from the solid supports. Afterwards, the ammonia and methyl amine were removed by passing a stream of nitrogen over the solution. To the remaining material was added ultrapure deionized H<sub>2</sub>O (affording roughly 1 mL at the end), and the resulting solution was filtered through 0.45 μm nylon syringe filter (Acrodisc® 13 mm syringe filter #PN 4426T). The filtered solution was purified using reverse-phase HPLC eluting with a linear gradient of CH<sub>3</sub>CN and 0.1 M TEAA (5/95 to 45/55 over 30 min.).

#### 5.4.4 Attachment of azido-modified peptide

The POCs were prepared using copper(I)-catalyzed azide-alkyne cycloaddition (CuAAC)<sup>80-81</sup> in which N<sub>3</sub>-A<sub>2</sub>PEP<sub>Au</sub> (**Figure S5.69**) was reacted with the azido-modified 18mer and 6mer conjugates (**Figure S5.68**). A representative protocol for PO<sub>18</sub>C is detailed here (the same procedure was used for synthesizing PO<sub>6</sub>C). The following stock solutions were prepared: **A**, 198.3 mM CuSO<sub>4</sub> in NP H<sub>2</sub>O; **B**, 37.3 mM THPTA in NP H<sub>2</sub>O; **C**, 2 M urea in NP H<sub>2</sub>O; and **D**, 60.6 mM sodium ascorbate in NP H<sub>2</sub>O. Lyophilized N<sub>3</sub>-A<sub>2</sub>PEP<sub>Au</sub> (125 nmol) was dissolved in 70 μL of DMF and 50 μL of NP H<sub>2</sub>O and the solution was transferred to a vial containing N<sub>3</sub>-BP-Oligo (100 nmol, Figure S1). To this vial were added a mixture of **A** and **B** (1.05 μL **A** mixed with 5.58 μL **B**), 1.5 μL of **C**, and 13.8 μL of **D**. The vial was parafilmmed and wrapped in aluminum foil, and stirred for at least 4 h at room temperature. DMF/NP H<sub>2</sub>O (1:1) was added to bring the total volume to 500 μL. The resulting solution was desalted using a NAP-5 desalting column (GE Healthcare Life Sciences, #17-0853-02). The eluted solution was purified using reverse-phase HPLC eluting with a linear gradient of CH<sub>3</sub>CN and 0.1 M TEAA (5/95 to 45/55 over 30 min.).



#### **5.4.5 POC assembly protocol**

In a 250  $\mu$ L plastic vial, lyophilized POCs (20 nmol) were dissolved in  $\text{CaCl}_2$  solution to yield the desired concentration. The solutions were sonicated for 2 minutes, and centrifuged briefly. The vials were placed in a 1.5 mL centrifuge tube containing water that was pre-heated at 80°C in an Eppendorf® Thermomixer® R (Eppendorf, # 022670107), and the POC solutions were allowed to incubate for 15 min. at 80°C. After incubation, the temperature setting was lowered 1°C every 5 min. until the temperature reached 25°C. It is important to note that at 70°C the samples were centrifuge very briefly to maintain POC concentration. After cooling to 25°C, the POC solutions were removed from the 1.5 mL centrifuge tube and allowed to sit overnight at room temperature. TEM samples were prepared after 15 to 20 hrs.

#### **5.4.6 Preparation of DNA-functionalized gold nanoparticles**

5 and 15 nm gold nanoparticles were functionalized using methods developed previously.<sup>165</sup> To lyophilized complementary oligonucleotides functionalized with thiol hexyl linker at the 5' (purchased from IDT, 10 OD) was added 200  $\mu$ L of freshly prepared dithiothreitol (DTT) and phosphate buffer (PB) solution (100 mM DTT in 170 mM PB). The solution was allowed to react for 1 hr. The cleaved oligonucleotides were purified using a NAP-5 column. The purified oligonucleotides (in 1 mL NP  $\text{H}_2\text{O}$ ) were then added to 10 mL of particles. The particle solution was allowed to sit overnight. The next morning, the concentrations of PB and sodium dodecyl sulfate (SDS) were brought to 0.01 M and 0.01%, respectively. The oligonucleotide/gold nanoparticle solution was allowed to incubate at room temperature for 30 min. The concentration of NaCl was increased slowly to 0.5 M (in 6 increments) using 2 M NaCl. After each addition of

NaCl, the solution was sonicated for 10 sec. and incubated for 30 min. before the next addition. After the salting procedure, excess oligonucleotides were removed via centrifugation (1 hr.; 16,100 x g for 15 nm particles and 10900 x g for 5 nm particles), and subsequent supernatant removal. The remaining pellets were combined and the washing process was repeated twice more. The final oligonucleotide/functionalized nanoparticle pellet was suspended in 100  $\mu$ L of NP H<sub>2</sub>O. The gold nanoparticle concentration was determined via UV-Vis spectroscopy using extinction coefficients of  $2.4 \times 10^8$  L/(mol·cm)<sup>165</sup> and  $9.696 \times 10^6$  L/(mol·cm)<sup>5</sup> for 15 and 5 nm particles, respectively. The concentrations of these stock solutions of nanoparticles were  $4.09 \times 10^{14}$  and  $2.17 \times 10^{13}$  particles in 100  $\mu$ L NP H<sub>2</sub>O, for the 5 nm and 15 nm stock solutions, respectively.

#### **5.4.7 Addition of DNA-functionalized gold nanoparticles to PO<sub>18</sub>C vesicles and PO<sub>6</sub>C fibers**

To a solution of PO<sub>18</sub>C vesicles (30  $\mu$ L) assembled in 50 mM CaCl<sub>2</sub> was added 1  $\mu$ L of a 25x diluted solution of the 15 nm stock solution prepared above. The mixture was mixed and vortexed briefly and allowed to sit at room temperature for 1 hr. TEM samples were prepared after 15 hrs.

To a solution of PO<sub>6</sub>C fibers (30  $\mu$ L) assembled in 50 mM CaCl<sub>2</sub> was added 1  $\mu$ L of a 10x diluted solution of the 5 nm stock solution prepared above. The mixture was mixed and vortexed briefly and allowed to sit at room temperature for 1 hr. TEM samples were prepared after 15 hrs.

## APPENDIX A

### SUPPORTING INFORMATION FOR CHAPTER 2: “ADJUSTING THE METRICS OF 1D HELICAL NANOPARTICLE SUPERSTRUCTURES USING MULTIVALENT PEPTIDE CONJUGATES”

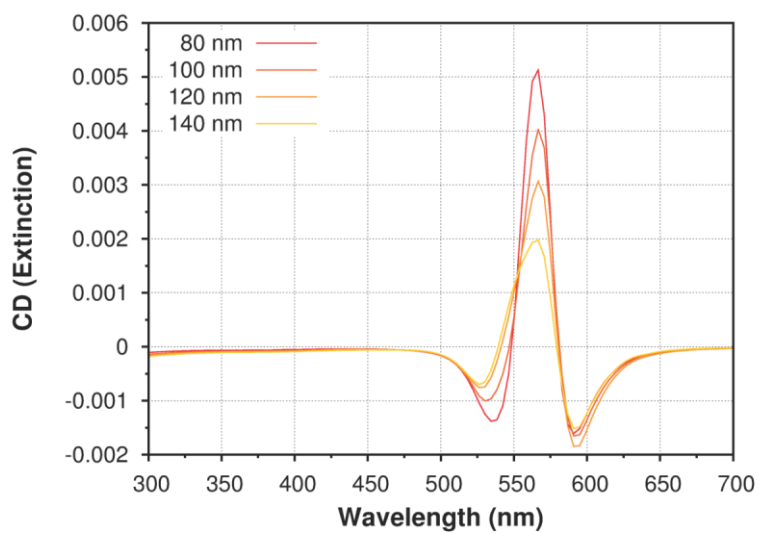


**Figure S2.37.** Plasmonic circular dichroism signal as a function of helical pitch, calculated according to reported methods.<sup>61</sup>

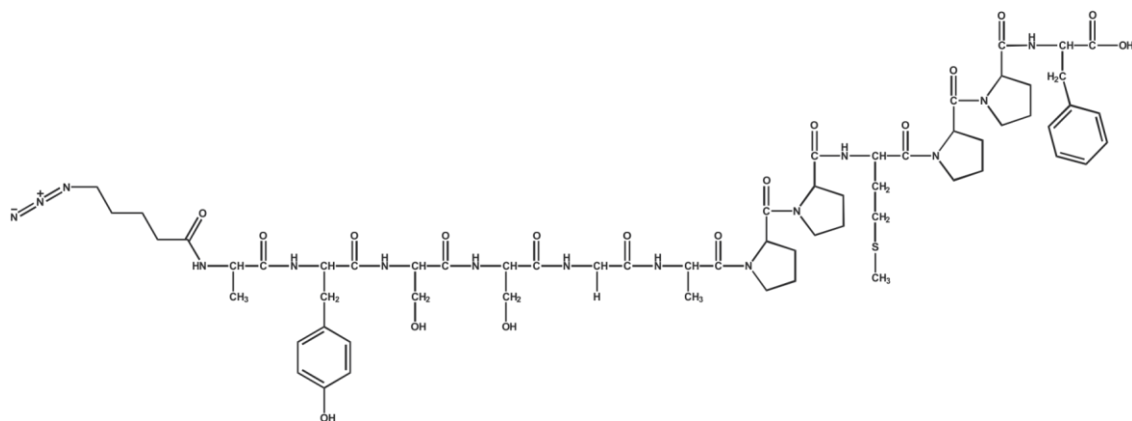


**Figure S2.38.** Chemical structure of N<sub>3</sub>-PEP<sub>Au</sub>

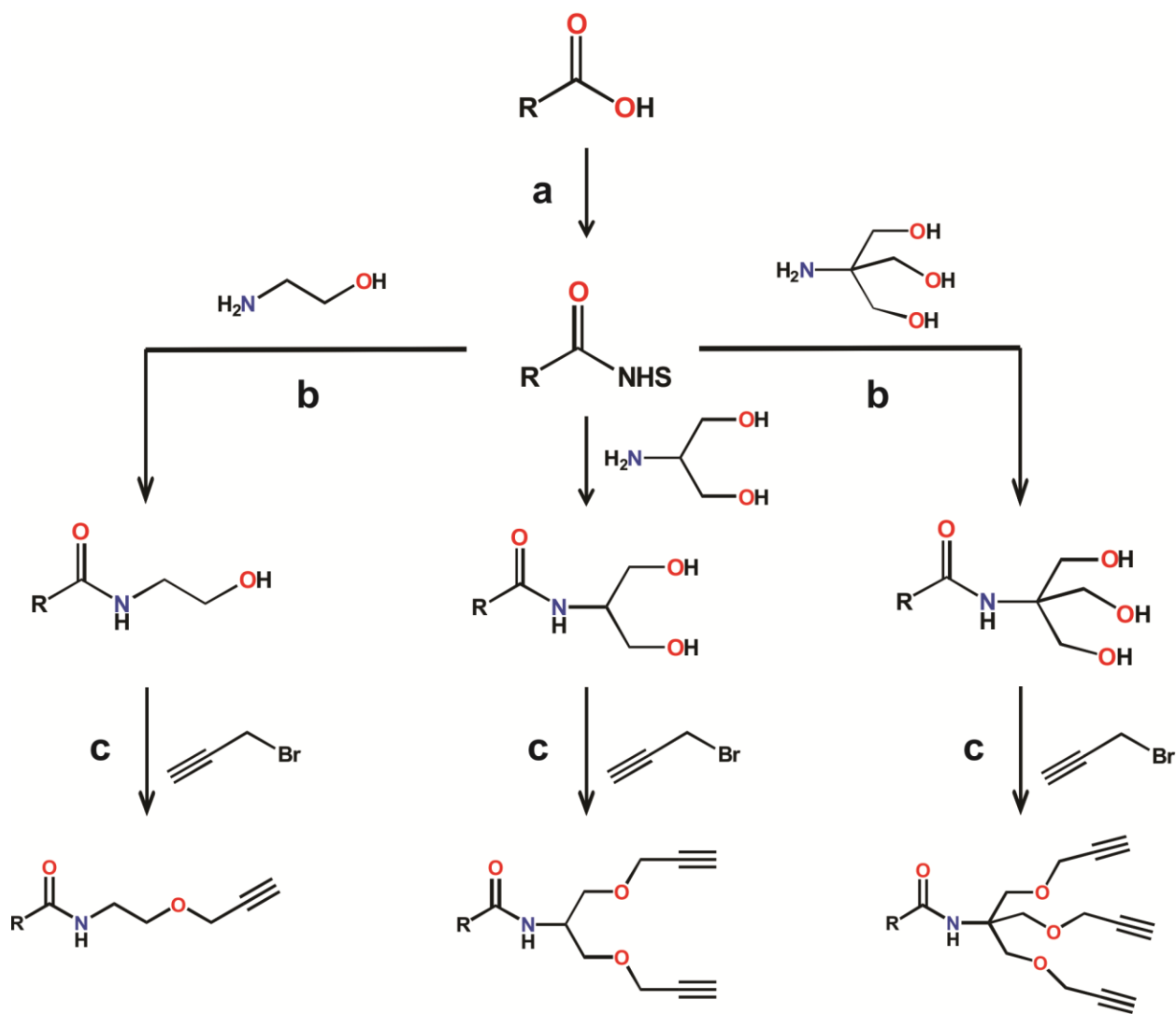


**Figure S2.39.** Scheme detailing the construction of the monovalent, divalent, and trivalent alkyne-modified aliphatic substrates. Briefly, the experimental details include: a) EDC-mediated NHS activation of the carboxylic acid, b) amide bond formation, and c) propargylation under basic conditions.

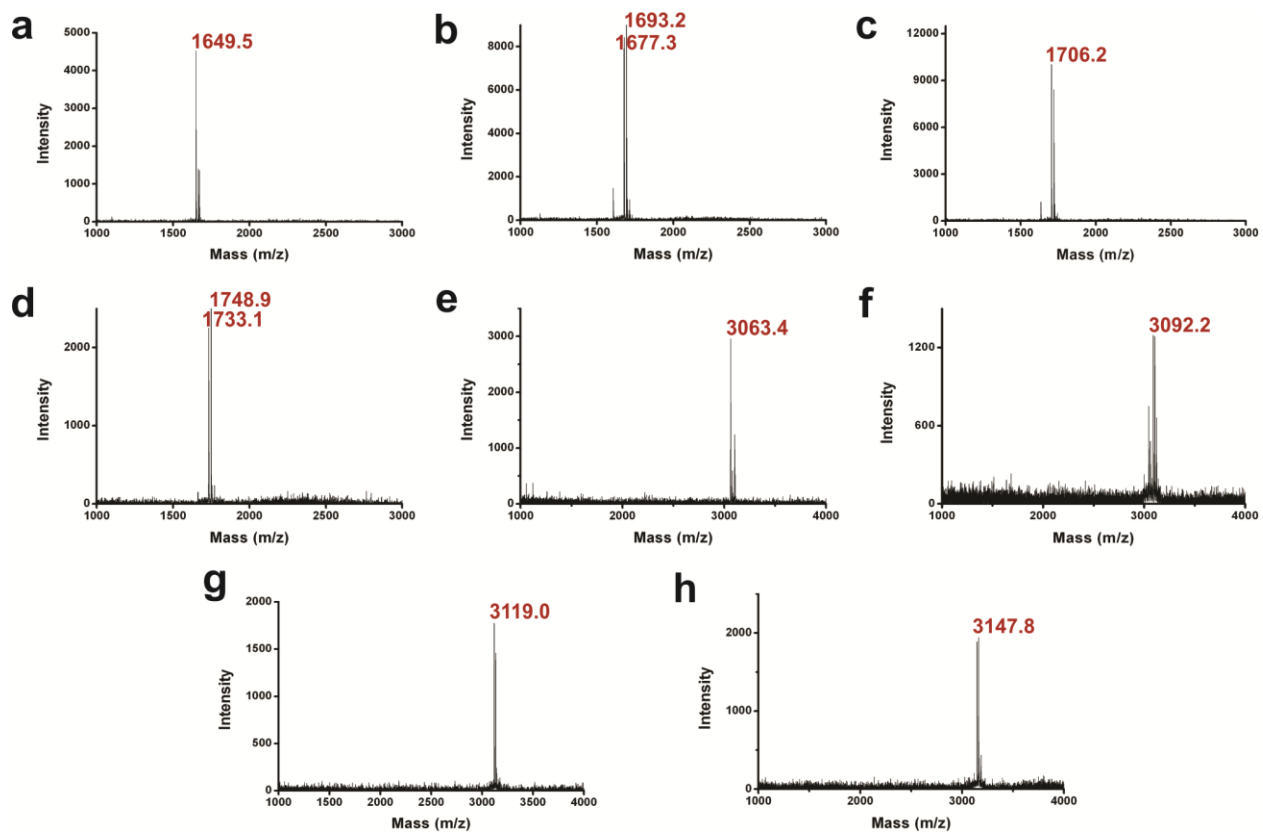


**Figure S2.40.** MALDI-TOF mass spectra of purified monovalent and divalent peptide conjugates: (a)  $C_{12}$ -(PEP<sub>Au</sub>)<sub>1</sub>,  $m/z = 1649.5$  ( $M + Na^+$ ); (b)  $C_{14}$ -(PEP<sub>Au</sub>)<sub>1</sub>,  $m/z = 1677.3$  ( $M + Na^+$ ); (c)  $C_{16}$ -(PEP<sub>Au</sub>)<sub>1</sub>,  $m/z = 1693.2$  ( $M + Na^+$ ); (d)  $C_{18}$ -(PEP<sub>Au</sub>)<sub>1</sub>,  $m/z = 1733.1$  ( $M + Na^+$ ),  $m/z = 1748.9$  ( $M + K^+$ ); (e)  $C_{12}$ -(PEP<sub>Au</sub>)<sub>2</sub>,  $m/z = 3063.4$  ( $M + Na^+$ ); (f)  $C_{14}$ -(PEP<sub>Au</sub>)<sub>2</sub>,  $m/z = 3092.2$  ( $M + Na^+$ ); (g)  $C_{16}$ -(PEP<sub>Au</sub>)<sub>2</sub>,  $m/z = 3119.0$  ( $M + Na^+$ ); (h)  $C_{18}$ -(PEP<sub>Au</sub>)<sub>2</sub>,  $m/z = 3147.8$  ( $M + Na^+$ ).

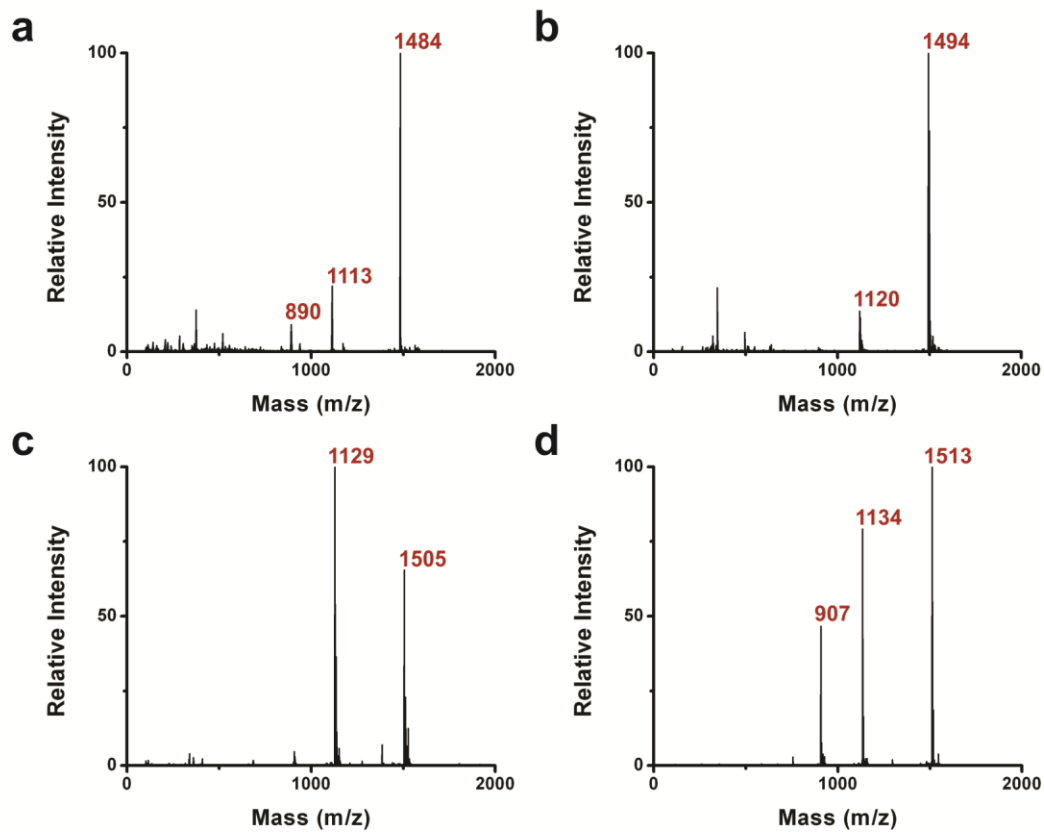


**Figure S2.41.** LCMS spectra of purified trivalent peptide conjugates: (a)  $C_{12}$ -(PEP<sub>Au</sub>)<sub>3</sub>, m/z = 1484 (m/3), m/z = 1113 (m/4), m/z = 890 (m/5); (b)  $C_{14}$ -(PEP<sub>Au</sub>)<sub>3</sub>, m/z = 1494 (m/3), m/z = 1120 (m/4); (c)  $C_{16}$ -(PEP<sub>Au</sub>)<sub>3</sub>, m/z = 1505 (m/3), m/z = 1129 (m/4); (d)  $C_{18}$ -(PEP<sub>Au</sub>)<sub>3</sub>, m/z = 1513 (m/3), m/z = 1134 (m/4), m/z = 907 (m/5).

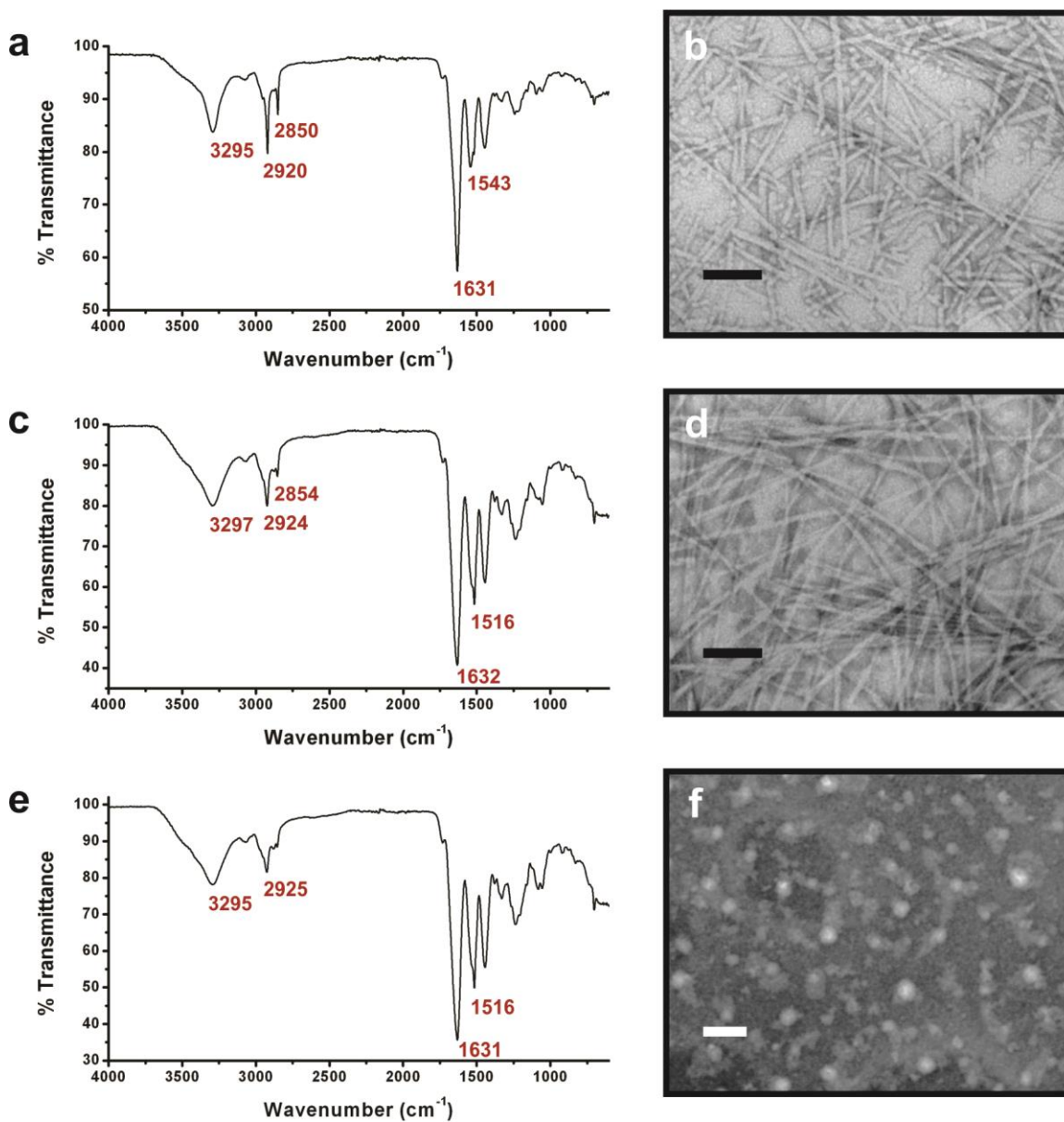


**Figure S2.42.** ATR-FTIR spectra of (a)  $C_{18}$ -(PEP<sub>Au</sub>)<sub>1</sub> and (b) its corresponding negatively stained TEM image of the soft assembly. ATR-FTIR spectra of (c)  $C_{18}$ -(PEP<sub>Au</sub>)<sub>2</sub> and (d) its corresponding negatively stained TEM image of the soft assembly. ATR-FTIR spectra of (e)  $C_{18}$ -(PEP<sub>Au</sub>)<sub>3</sub> and (f) its corresponding negatively stained TEM image of the soft assembly (scale bar = 100 nm)



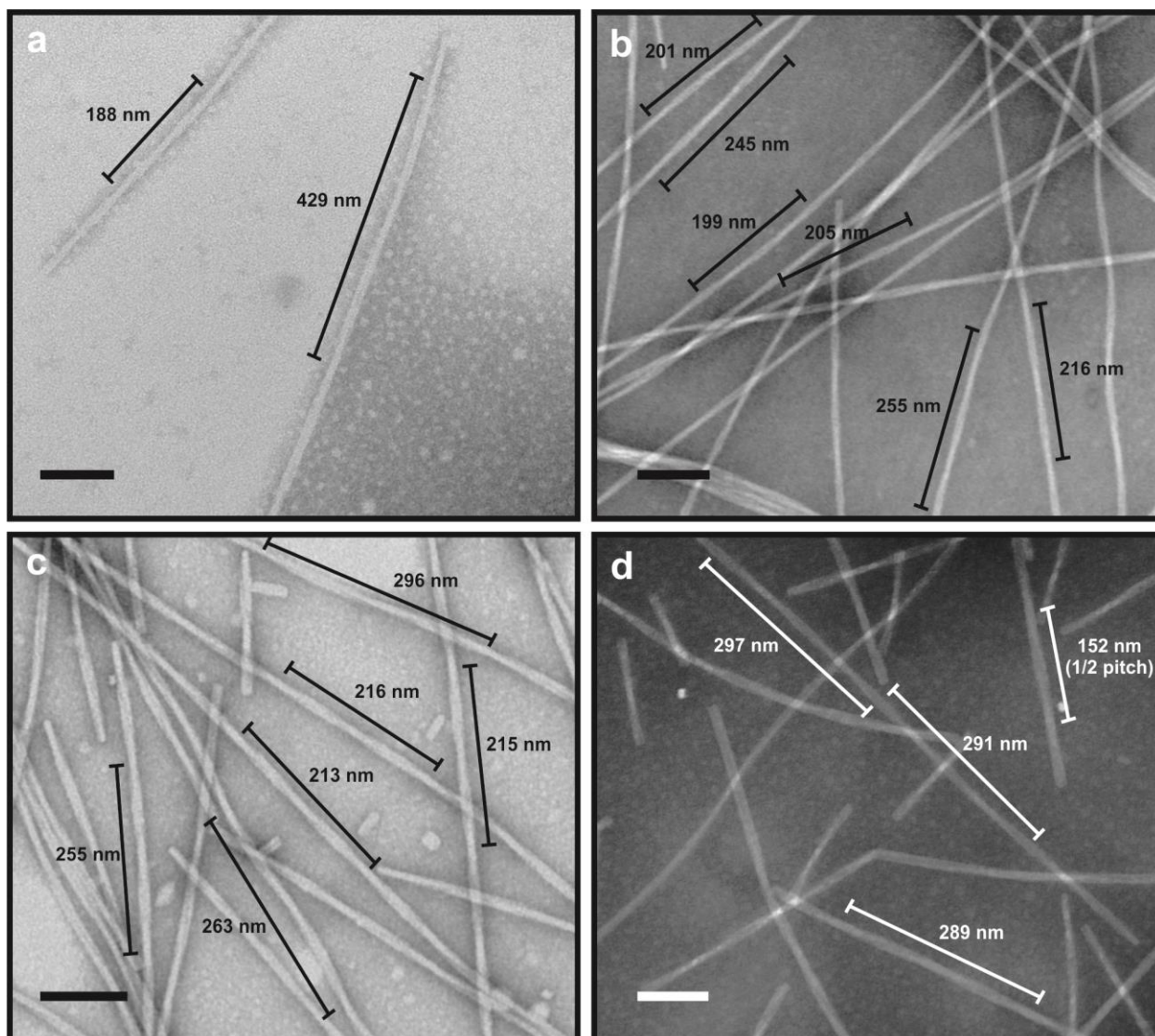


**Figure S2.43.** Pitch measurements of selected fibers from negatively stained TEM images of (a)  $C_{12}$ -(PEP<sub>Au</sub>)<sub>1</sub>; (b)  $C_{14}$ -(PEP<sub>Au</sub>)<sub>1</sub>; (c)  $C_{16}$ -(PEP<sub>Au</sub>)<sub>1</sub>; and (d)  $C_{18}$ -(PEP<sub>Au</sub>)<sub>1</sub> (scale bar = 100 nm). Note: in general, the measurements from TEM confirm the trend determined from the AFM data. However, the TEM pitch measurements can vary widely between different fibers, as is clear for the  $C_{12}$ -(PEP<sub>Au</sub>)<sub>1</sub> assemblies.

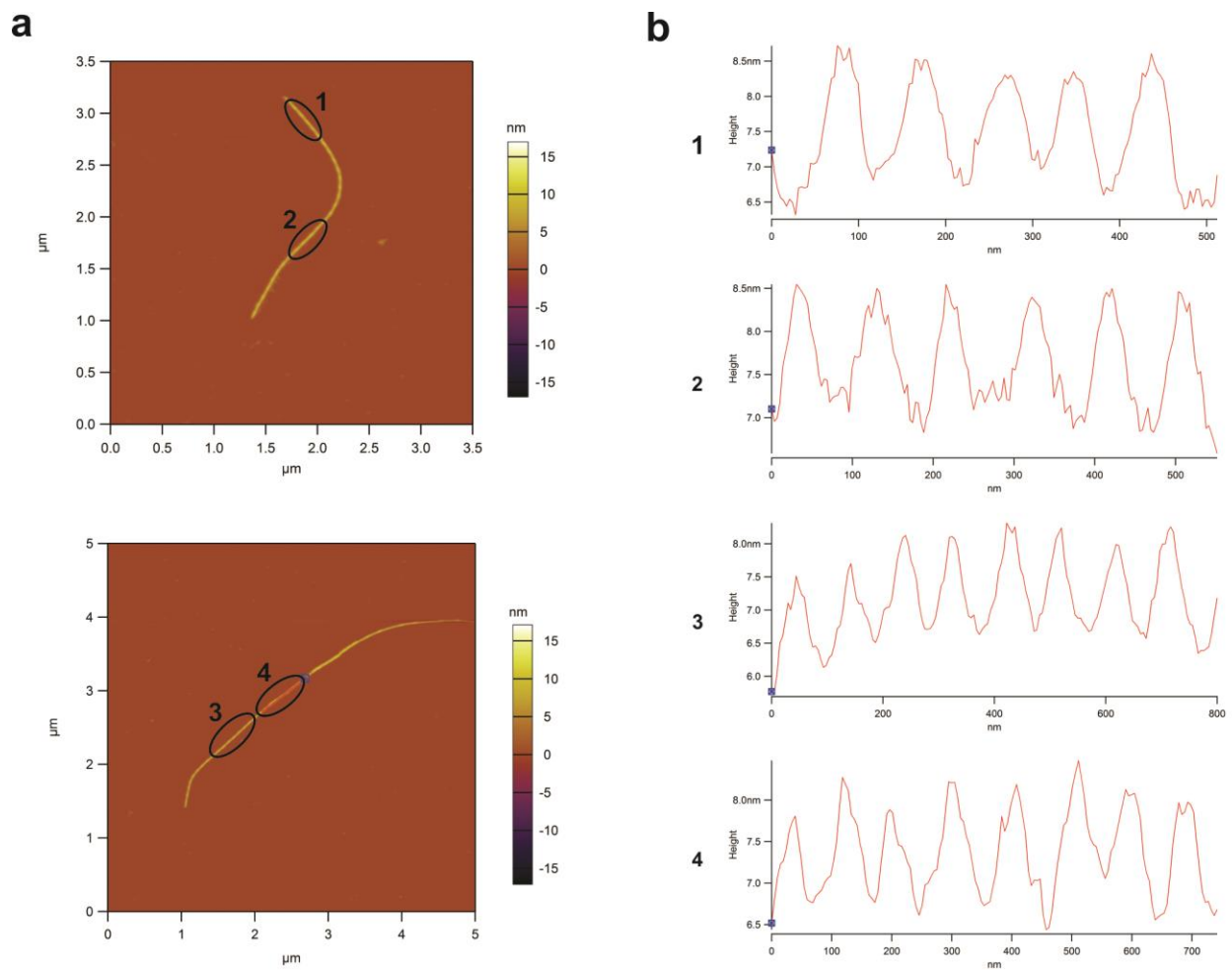


**Figure S2.44.** (a) AFM images of  $C_{12}$ -(PEP<sub>Au</sub>)<sub>1</sub> assemblies and (b) corresponding height traces. The pitch length was calculated by averaging the distances between every other peak in the height traces. Average pitch is  $186 \pm 13$  nm based on 18 counts.

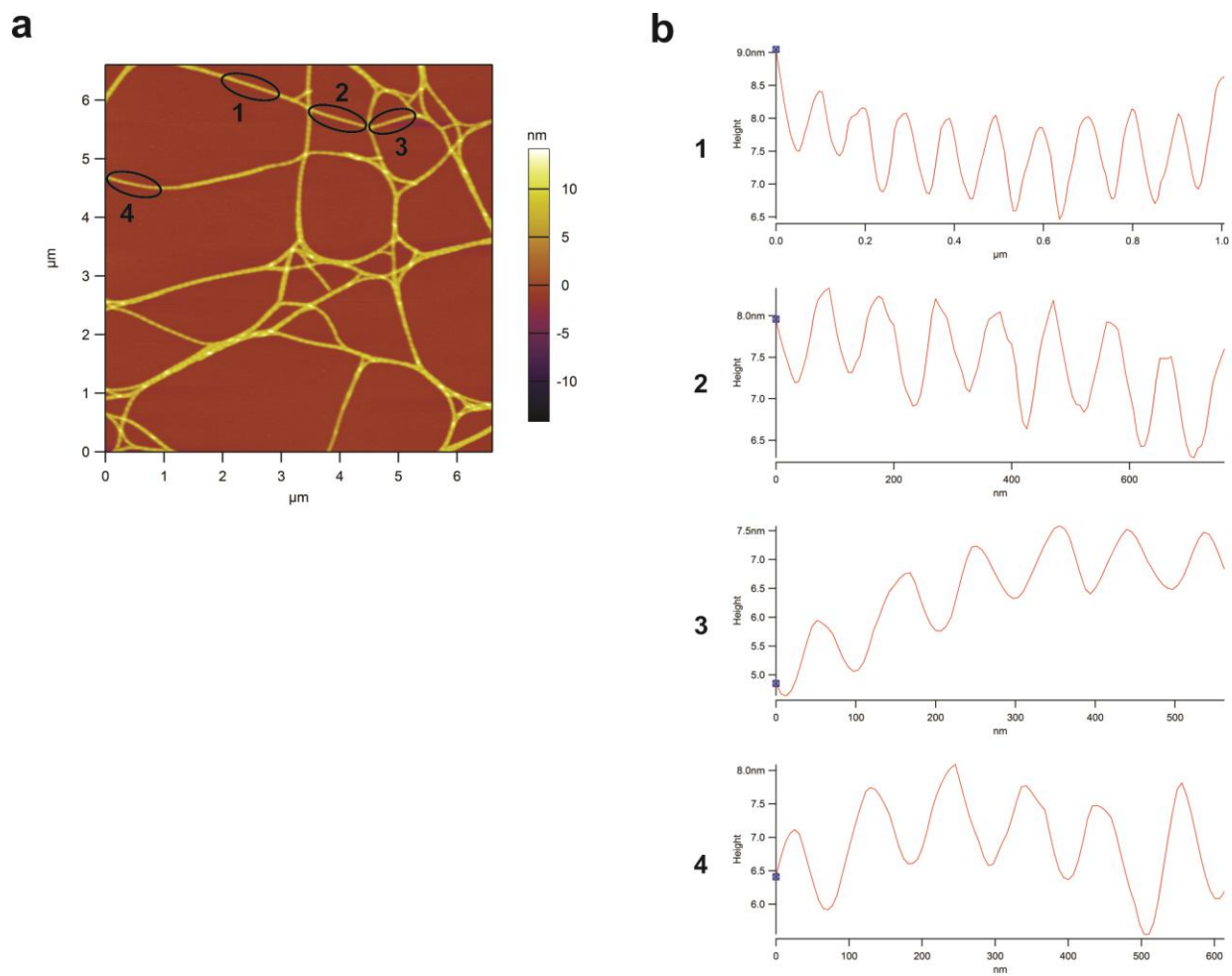


**Figure S2.45.** (a) AFM image of  $C_{14}$ -(PEP<sub>Au</sub>)<sub>1</sub> assemblies and (b) corresponding height traces. The pitch length was calculated by averaging the distances between every other peak in the height traces. Average pitch is  $196 \pm 11$  nm based on 20 counts. It is clear that some fibers intertwine, but the pitch measurements were only made on single fibers.

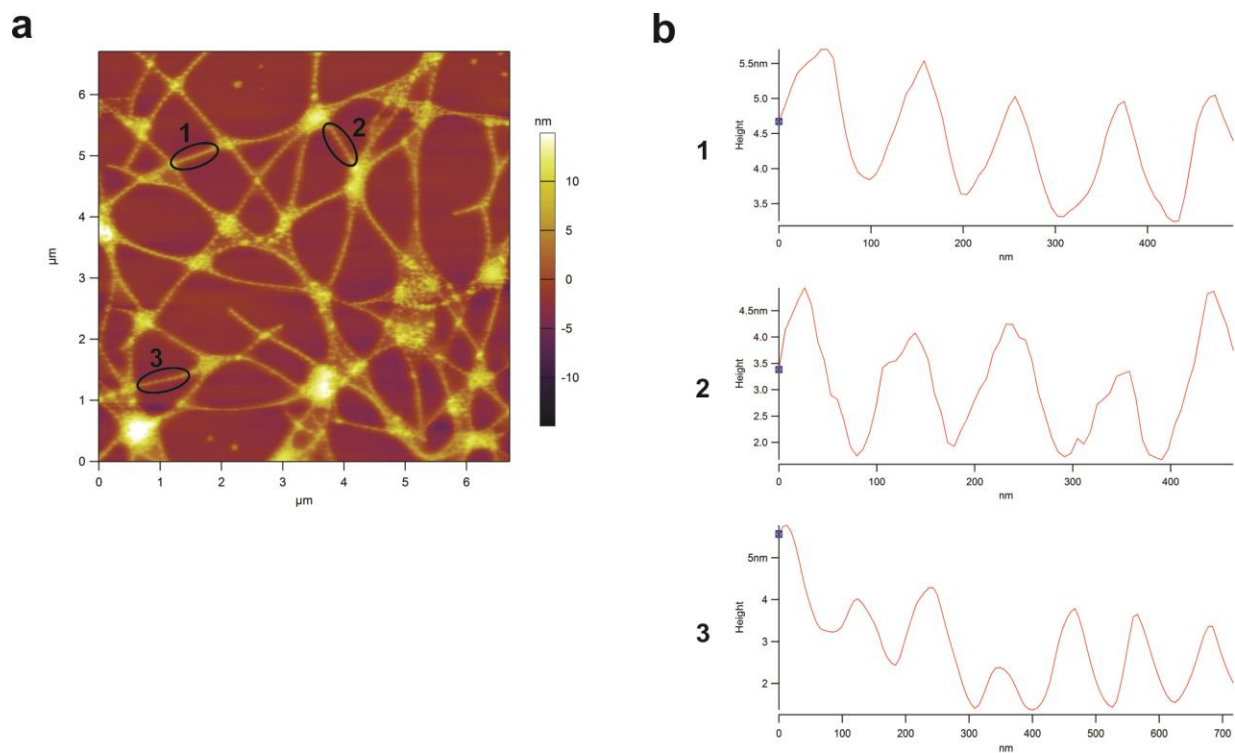


**Figure S2.46.** (a) AFM image of  $C_{16}$ -(PEP<sub>Au</sub>)<sub>1</sub> assemblies and (b) corresponding height traces. The pitch length was calculated by averaging the distances between every other peak in the height traces. Average pitch is  $214 \pm 7$  nm based on 10 counts. It is clear that some fibers intertwine, but the pitch measurements were only made on single fibers.

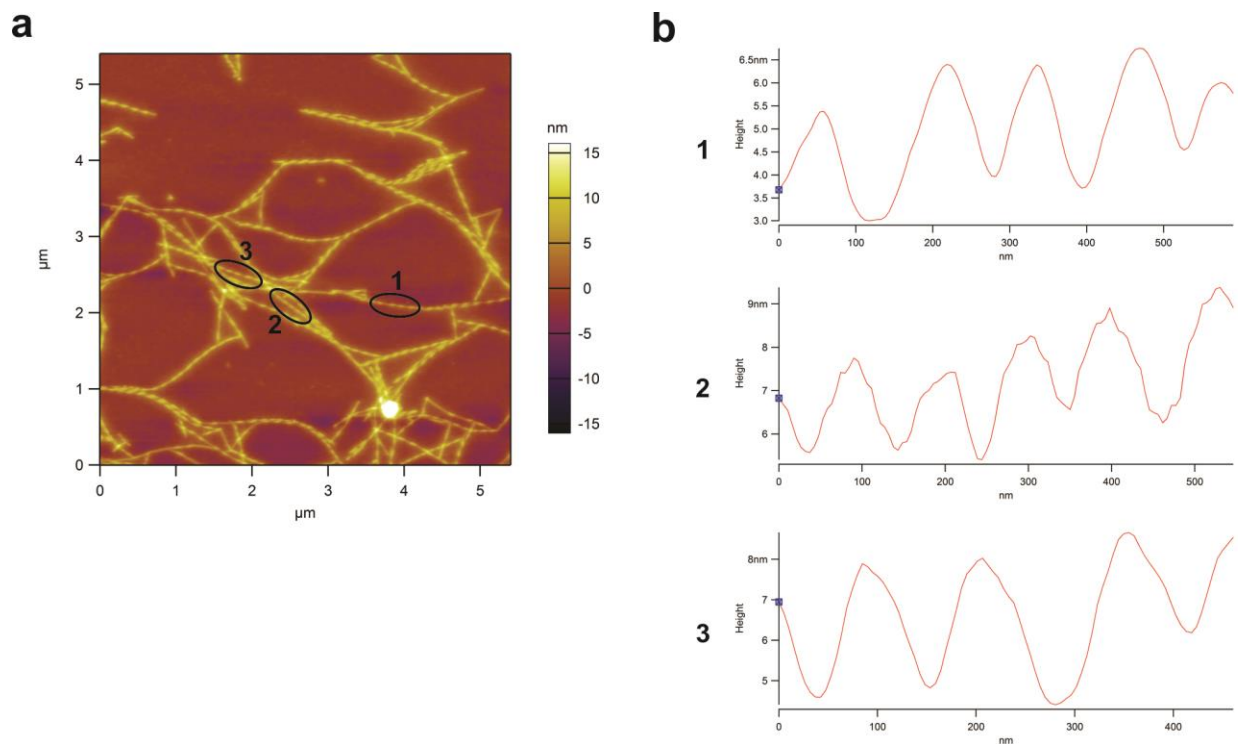


**Figure S2.47.** (a) AFM image of  $\text{C}_{18}\text{-(PEP}_{\text{Au}})_1$  assemblies and (b) corresponding height traces. The pitch length was calculated by averaging the distances between every other peak in the height traces. Average pitch is  $228 \pm 30$  nm based on 8 counts. It is clear that some fibers intertwine, but the pitch measurements were only made on single fibers.

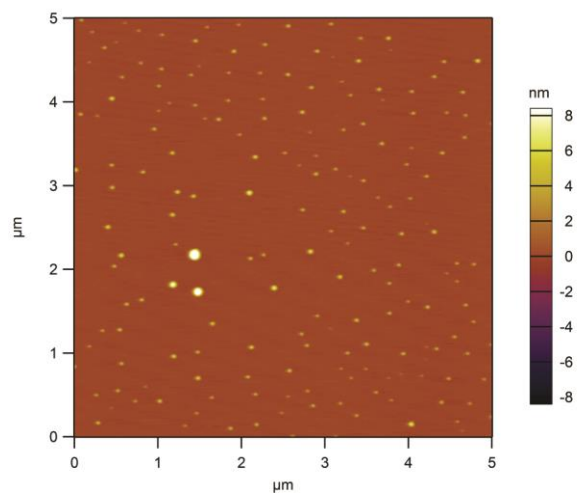


**Figure S2.48.** AFM image of  $C_{14}$ -(PEP<sub>Au</sub>)<sub>2</sub> assemblies. Only spherical assemblies/agggregates were observed.

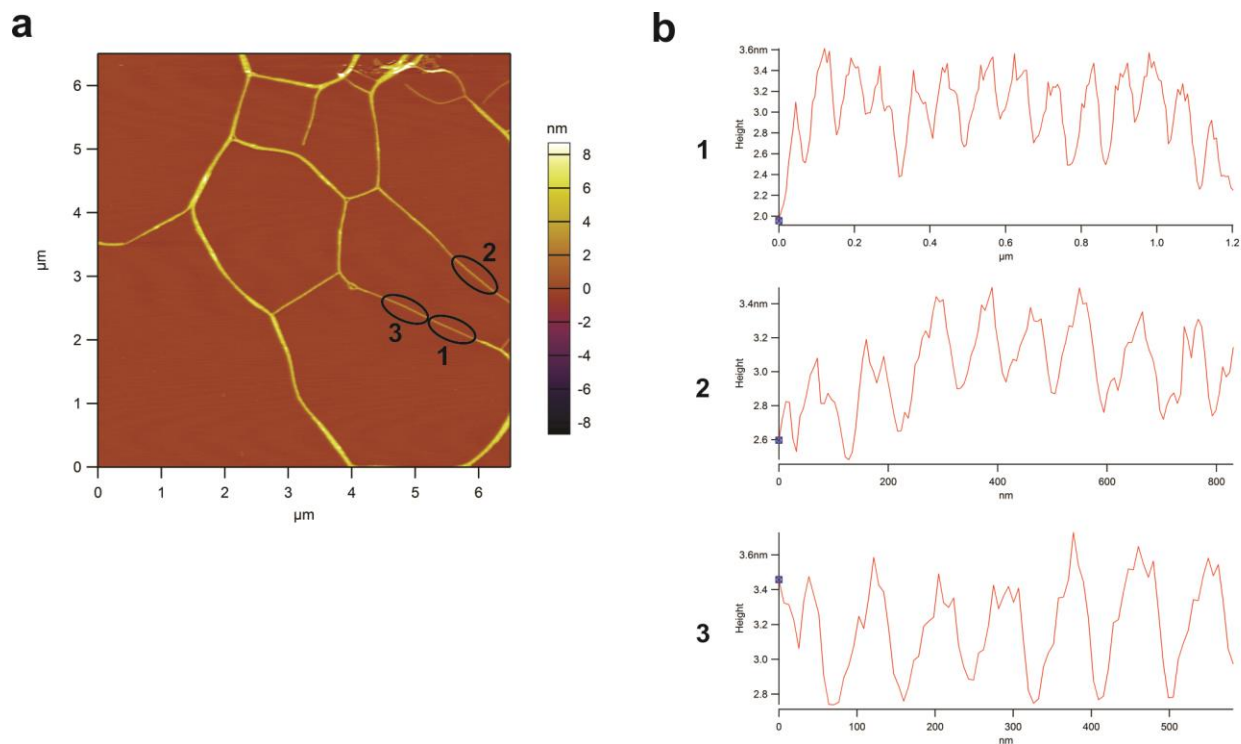


**Figure S2.49.** (a) AFM image of  $C_{16}$ -(PEP<sub>Au</sub>)<sub>2</sub> assemblies and (b) corresponding height traces. The pitch length was calculated by averaging the distances between every other peak in the height traces. Average pitch is  $178 \pm 20$  nm based on 20 counts. It is clear that some fibers intertwine, but the pitch measurements were only made on single fibers.



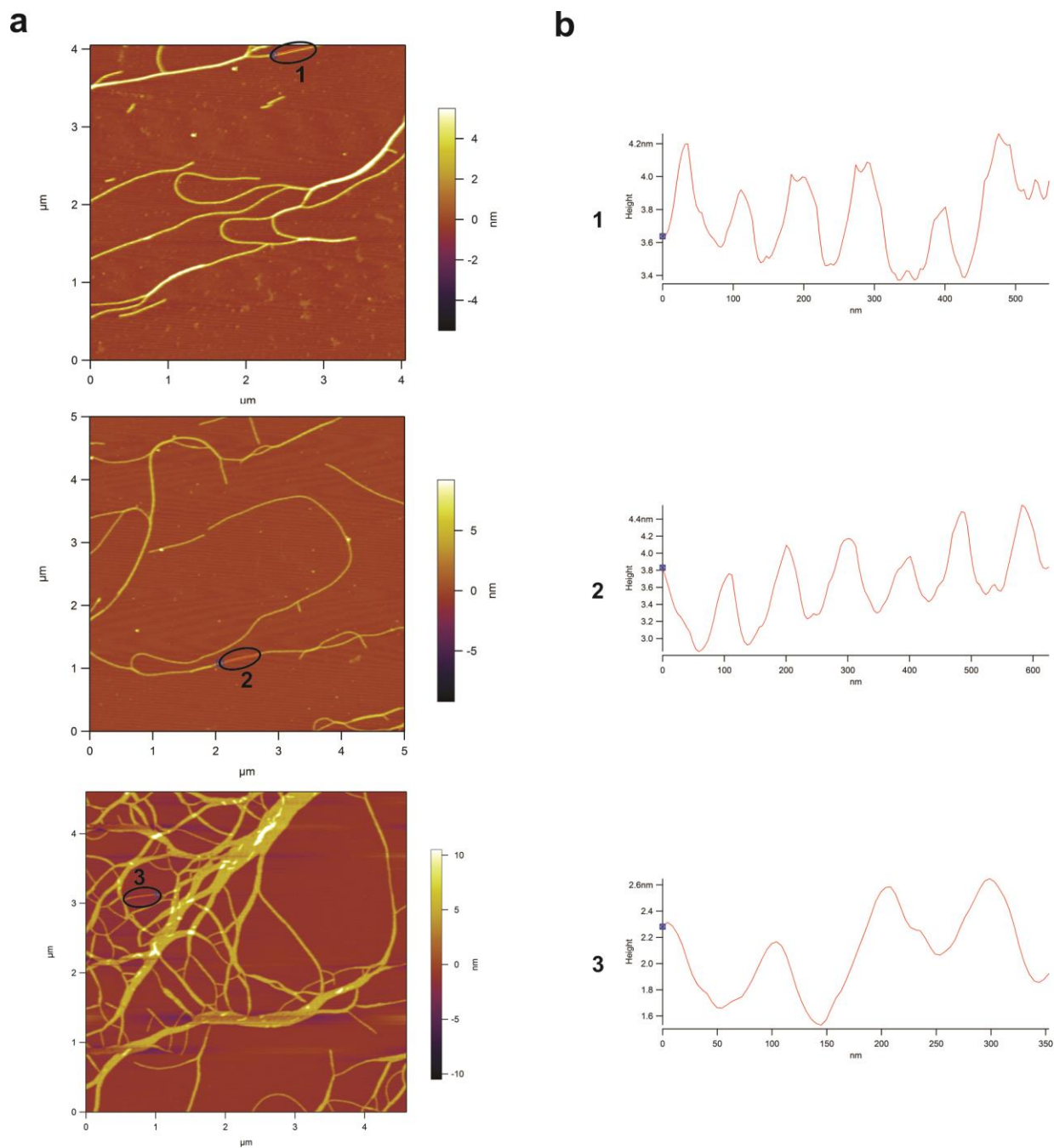


**Figure S2.50.** (a) AFM image of  $C_{18}$ -(PEP<sub>Au</sub>)<sub>2</sub> assemblies and (b) corresponding height traces. The pitch length was calculated by averaging the distances between every other peak in the height traces. Average pitch is  $184 \pm 15$  nm based on 9 counts. It is clear that some fibers intertwine, but the pitch measurements were only made on single fibers.



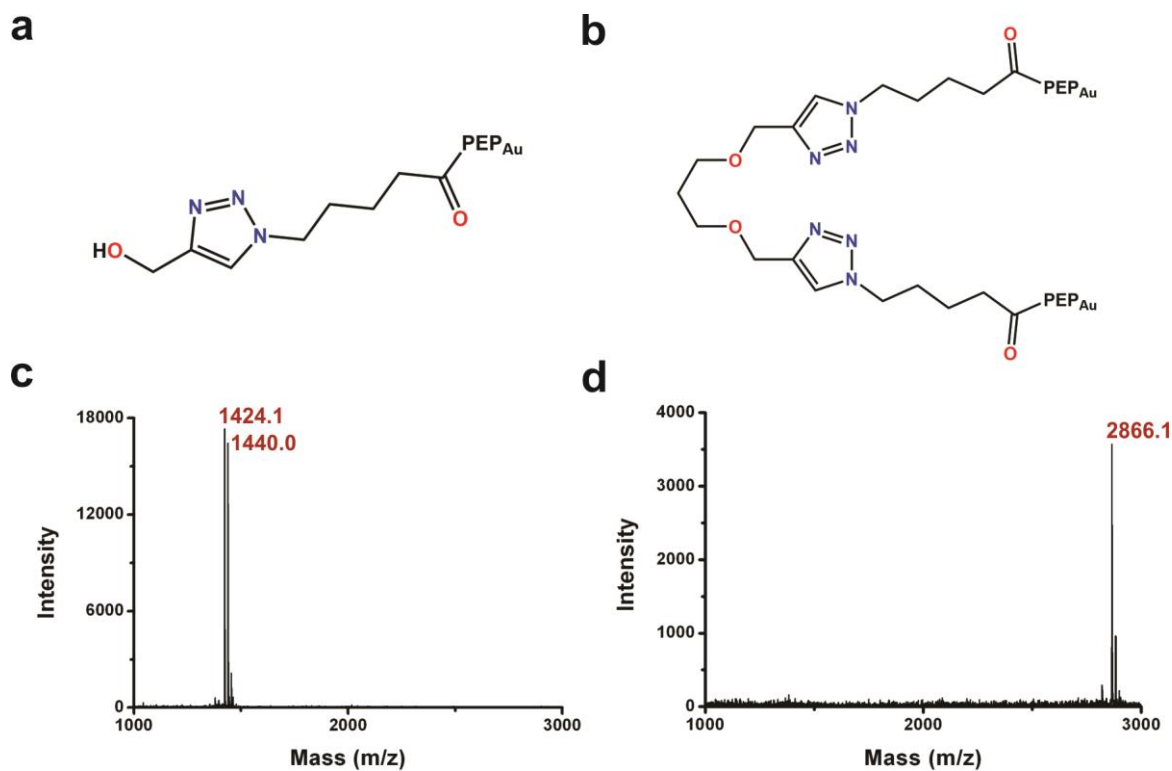


**Figure S2.51.** Molecular structure of the (a) mono- and (b) divalent peptide conjugates used for the QCM experiments. MALDI-TOF mass spectra of (c) monovalent peptide conjugate,  $m/z = 1424$  ( $M + \text{Na}^+$ ),  $m/z = 1440.0$  ( $M + \text{K}^+$ ) and (d) divalent peptide conjugate,  $m/z = 2866.1$  ( $M + \text{Na}^+$ ).

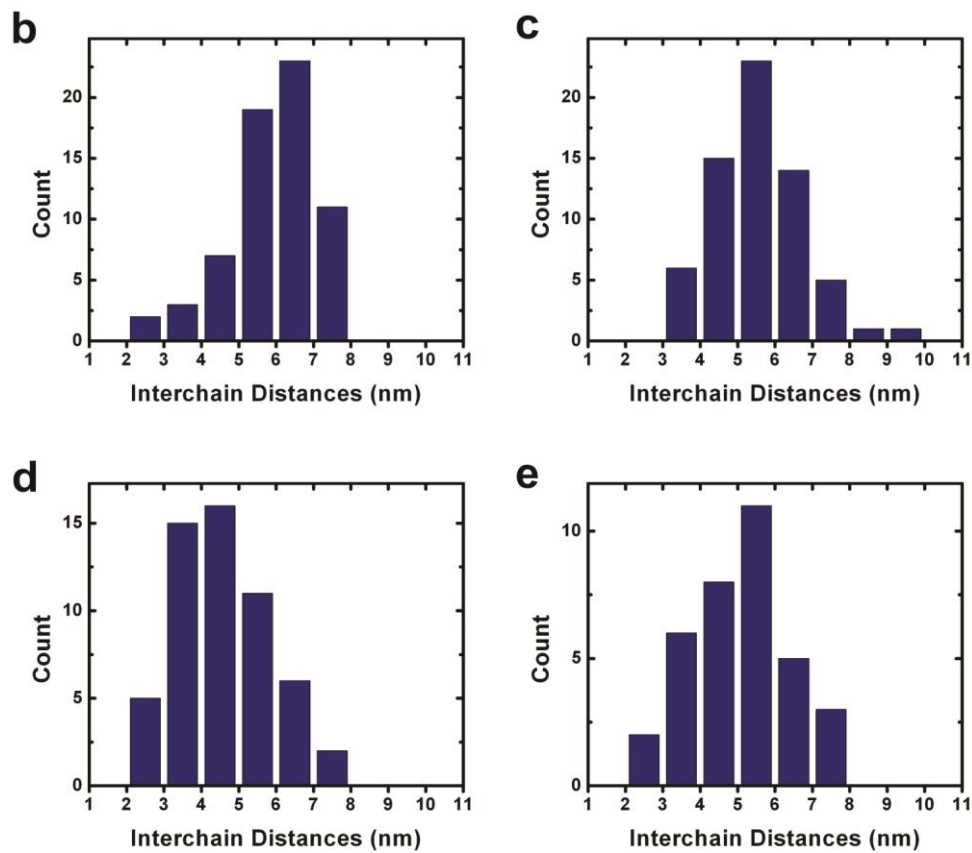
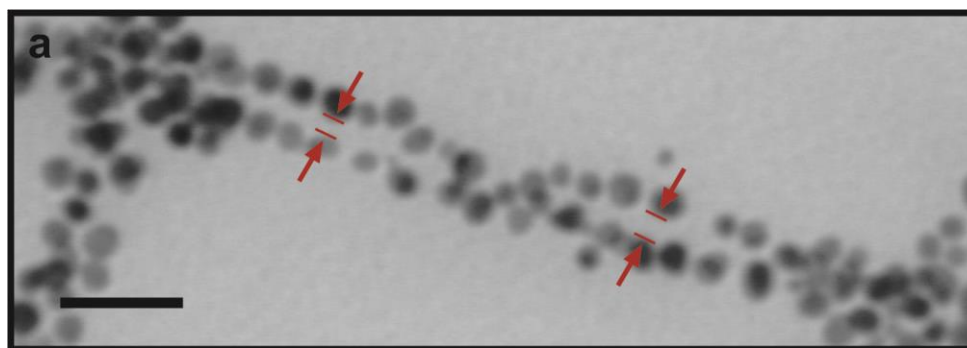


**Figure S2.52.** (a) TEM image showing the interchain distances (scale bar = 50 nm). Interchain distances of (b)  $C_{14}$ -(PEP<sub>Au</sub>)<sub>1</sub>:  $5.9 \pm 1.2$  nm based on 65 counts; (c)  $C_{16}$ -(PEP<sub>Au</sub>)<sub>1</sub>:  $5.6 \pm 1.2$  nm based on 65 counts; (d)  $C_{16}$ -(PEP<sub>Au</sub>)<sub>2</sub>:  $4.6 \pm 1.2$  nm based on 55 counts; (e)  $C_{18}$ -(PEP<sub>Au</sub>)<sub>2</sub>:  $5.0 \pm 1.4$  nm based on 35 counts.

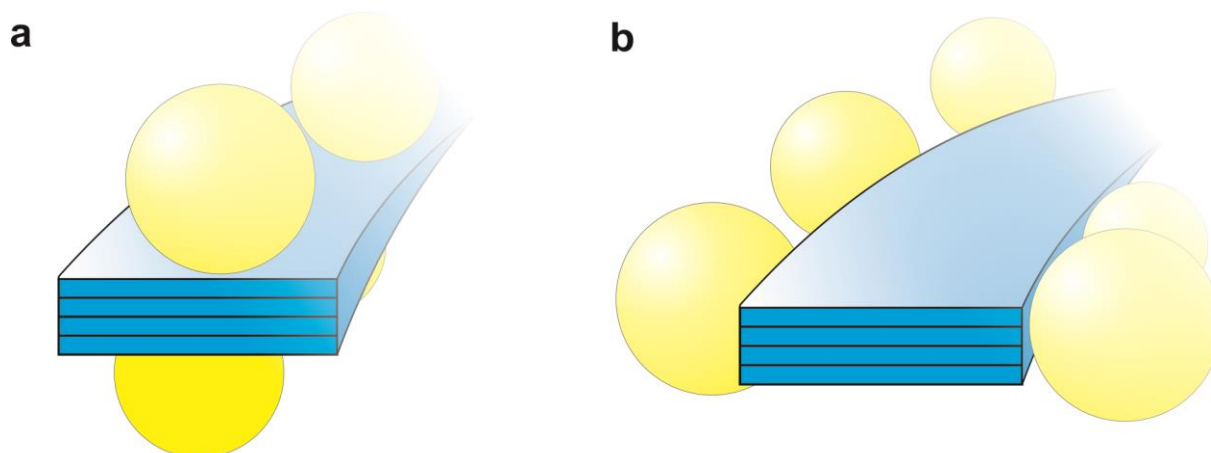


**Figure S2.53.** Possible locations for particle association to fibers: (a) fiber faces or (b) fiber edges.

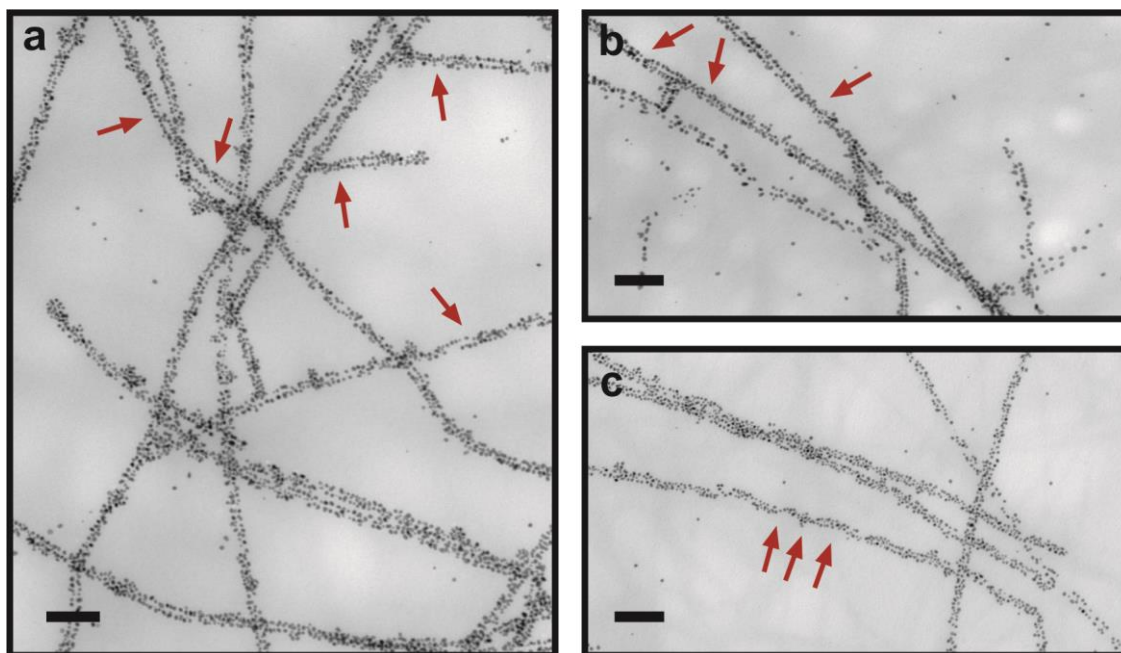
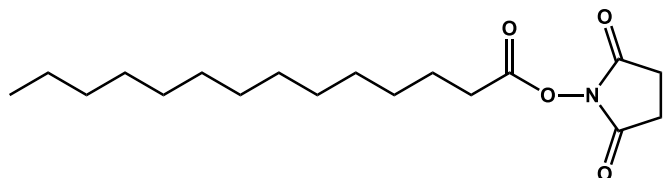


**Figure S2.54.** TEM images indicating helical segments of assemblies constructed from (a,b)  $C_{14}$ -(PEP<sub>Au</sub>)<sub>1</sub> and (c)  $C_{16}$ -(PEP<sub>Au</sub>)<sub>2</sub> (scale bar = 100 nm). The red arrows indicate points of helicity.

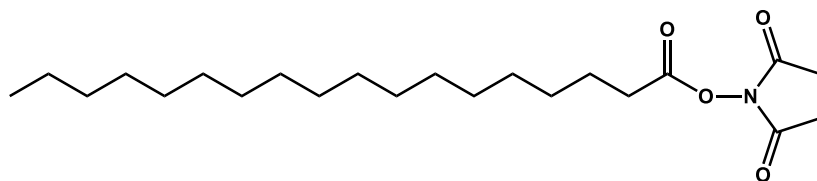
## Synthesis and Characterization of Alkyne-Modified Aliphatic Substrates

### Myristic N-hydroxyl-succinimide ester



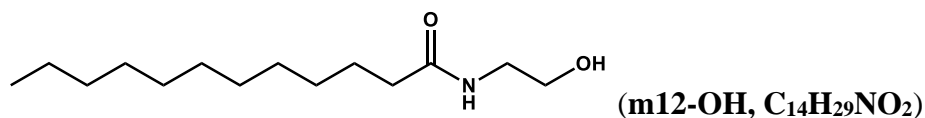
Myristic acid (268.5 mg, 1.18 mmol) was dissolved in 10 mL of dry dimethylformamide (DMF). N-hydroxysuccinimide (270.0 mg, 2.35 mmol) and 1-ethyl-3-(3-dimethylaminopropyl)carbodiimide (451.0 mg, 2.35 mmol) were added to the solution. While stirring, N,N-diisopropylethylamine (408  $\mu$ l, 2.35 mmol) was then added, and the reaction mixture was stirred at room temperature for 15 hours. After 15 hours, a white precipitate was observed. Acidified NP H<sub>2</sub>O (pH ~4) was added to the mixture and the white solid was collected by vacuum filtration. The collected solid was dried *in vacuo*. Yield: 304.1 mg, 79 %. <sup>1</sup>H NMR (300 MHz, CDCl<sub>3</sub>)  $\delta$  2.81 (s, 4H), 2.58 (t, 2H), 1.72 (m, 2H), 1.41 – 1.32 (m, 2H), 1.31 – 1.20 (m, 18H), 0.86 (t, 3H).

### Stearic N-hydroxyl-succinimide ester

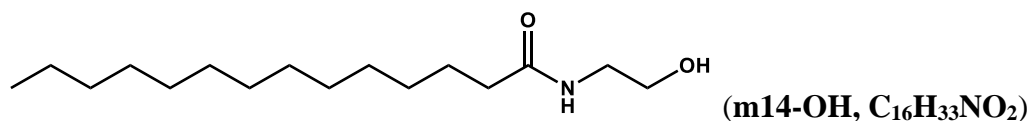


Stearic acid (479.0 mg, 1.68 mmol) was dissolved in 10 mL of dry DMF. N-hydroxysuccinimide (339.1 mg, 2.95 mmol) and 1-ethyl-3-(3-dimethylaminopropyl)carbodiimide (565.9 mg, 2.95 mmol) were added to the solution. While

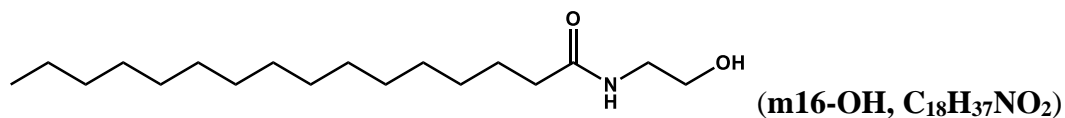
stirring, N,N-diisopropylethylamine (512  $\mu$ l, 2.95 mmol) was then added, and the reaction mixture was stirred at room temperature for 15 hours. After 15 hours, a white precipitate was observed. Acidified NP H<sub>2</sub>O (pH~4) was added to the mixture and the white solid was collected by vacuum filtration. The collected solid was dried *in vacuo*. Yield: 530.2 mg, 83 %. <sup>1</sup>H NMR (300 MHz, CDCl<sub>3</sub>)  $\delta$  2.83 (s, 4H), 2.60 (t, 2H), 1.74 (m, 2H), 1.43 – 1.32 (m, 2H), 1.32 – 1.20 (m, 26H), 0.88 (t, 3H).



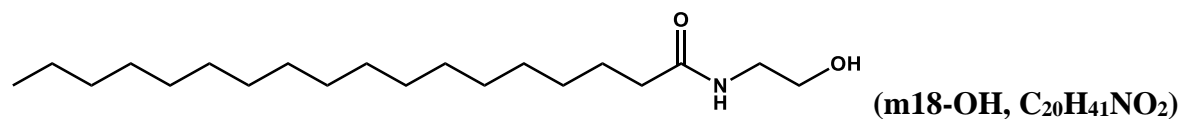
Lauric N-hydroxyl-succinimide ester (183.8 mg, 0.62 mmol) was dissolved in 4 mL of dichloromethane (DCM). Ethanolamine (74.4  $\mu$ L, 1.24 mmol) was added to the solution. While stirring, triethylamine (172  $\mu$ L, 1.24 mmol) was then added, and the reaction mixture was stirred at room temperature for 15 hours. The reaction mixture was transferred to a separatory funnel and washed with NP H<sub>2</sub>O (1x) and brine (2x). The organic layer was collected and dried over MgSO<sub>4</sub>. The mixture was filtered and the DCM was evaporated under air flow to yield product which was dried *in vacuo*. Yield: 104.9 mg, 70 %. <sup>1</sup>H NMR (300 MHz, CDCl<sub>3</sub>)  $\delta$  7.73 (t, 1H), 4.62 (t, 1H), 3.36 (q, 2H), 3.08 (q, 2H), 2.04 (t, 2H), 1.51 – 1.40 (m, 2H), 1.31 – 1.15 (m, 16H), 0.85 (t, 3H).



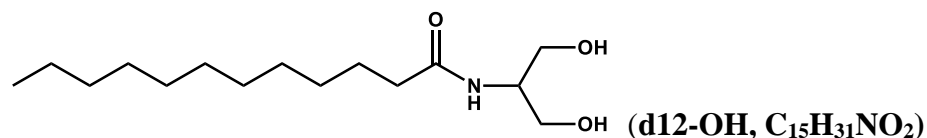
Myristic N-hydroxyl-succinimide ester (146.3 mg, 0.45 mmol) was dissolved in 8 mL of dry DMF. Ethanolamine (54.0  $\mu$ L, 0.90 mmol) was added to the solution. While stirring, triethylamine (93.1  $\mu$ L, 0.67 mmol) was then added, and the reaction mixture was stirred at room temperature for 15 hours. After reaction, a white precipitate was observed. The product was precipitated with NP H<sub>2</sub>O, recovered by vacuum filtration, and then dried *in vacuo*. Yield: 70.1 mg, 57 %. <sup>1</sup>H NMR (300 MHz, DMSO)  $\delta$  7.73 (t, 1H), 4.61 (t, 1H), 3.36 (q, 2H), 3.08 (q, 2H), 2.04 (t, 2H), 1.51 – 1.40 (m, 2H), 1.30 – 1.17 (m, 20H), 0.85 (t, 3H).



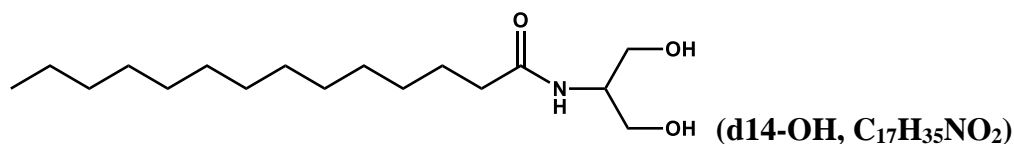
Palmitic N-hydroxyl-succinimide ester (144.5 mg, 0.41 mmol) was dissolved in 10 mL of dry DMF. Ethanolamine (49.1  $\mu$ L, 0.82 mmol) was added to the solution. While stirring, triethylamine (84.7  $\mu$ L, 0.61 mmol) was then added, and the reaction mixture was stirred at room temperature for 15 hours. The product was precipitated with NP H<sub>2</sub>O, recovered by vacuum filtration, and then dried *in vacuo*. Yield: 90.5 mg, 74 %. <sup>1</sup>H NMR (300 MHz, DMSO)  $\delta$  7.72 (t, 1H), 4.61 (t, 1H), 3.36 (q, 2H), 3.08 (q, 2H), 2.04 (t, 2H), 1.51 – 1.40 (m, 2H), 1.30 – 1.17 (m, 24H), 0.85 (t, 3H).



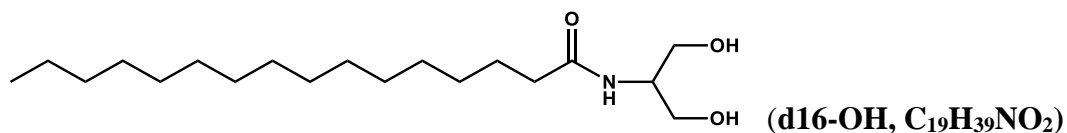
Stearic N-hydroxyl-succinimide ester (175.4, 0.46 mmol) was dissolved in 10 mL of dry DMF. Ethanolamine (55.3  $\mu$ L, 0.92 mmol) was added to the solution. While stirring, triethylamine (95.2  $\mu$ L) was then added, and the reaction mixture was stirred at room temperature for 15 hours. After reaction, a white precipitate was observed. The product was precipitated with NP H<sub>2</sub>O, recovered by vacuum filtration, and then dried *in vacuo*. Yield: 111.9 mg, 74 %. <sup>1</sup>H NMR (300 MHz, DMSO)  $\delta$  7.73 (t, 1H), 4.62 (t, 1H), 3.36 (q, 2H), 3.08 (q, 2H), 2.04 (t, 2H), 1.51 – 1.40 (m, 2H), 1.30 – 1.15 (m, 28H), 0.85 (t, 3H).



Lauric N-hydroxyl-succinimide ester (186.4 mg, 0.63 mmol) was dissolved in 5 mL of dry DMF. 2-amino-1,3-propanediol (~20 mg, ~1.2 mmol) was combined with 1 mL of dry DMF and then added to the solution. While stirring, triethylamine (132  $\mu$ L, 0.94 mmol) was then added, and the reaction mixture was stirred at room temperature for 15 hours. After reaction, a white precipitate was observed. The product was precipitated with acidified NP H<sub>2</sub>O (pH ~4). The gel-like precipitate was recovered by vacuum filtration and then dried *in vacuo*. Yield: 149.0 mg, 86 %. <sup>1</sup>H NMR (300 MHz, DMSO)  $\delta$  7.41 (d, 1H), 4.55 (t, 2H), 3.73 – 3.62 (m, 1H), 3.37 (t, 4H), 2.06 (t, 2H), 1.52 – 1.40 (m, 2H), 1.32 – 1.13 (m, 16H), 0.85 (t, 3H).

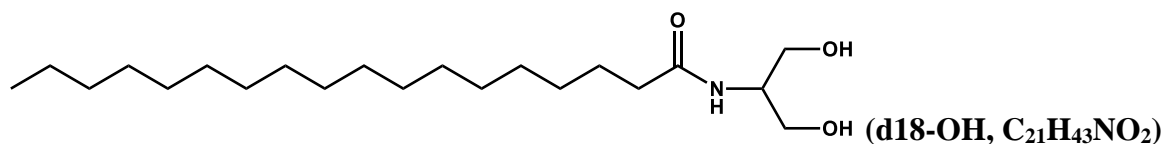


Myristic N-hydroxyl-succinimide ester (135.3 mg, 0.42 mmol) was dissolved in 4 mL of dry DMF. 2-amino-1,3-propanediol (~90 mg, ~1 mmol) was combined with 1 mL of dry DMF and then added to the solution. While stirring, triethylamine (86.3  $\mu$ L, 0.62 mmol) was then added, and the reaction mixture was stirred at room temperature for 15 hours. After reaction, a white precipitate was observed. The product was precipitated with acidified NP H<sub>2</sub>O (pH ~4). The gel-like precipitate was recovered by vacuum filtration and then dried *in vacuo*. Yield: 95.7 mg, 76 %. <sup>1</sup>H NMR (300 MHz, DMSO)  $\delta$  7.40 (d, 1H), 4.54 (t, 2H), 3.72 – 3.64 (m, 1H), 3.37 (t, 4H), 2.06 (t, 2H), 1.52 – 1.40 (m, 2H), 1.39 – 1.14 (m, 20H), 0.85 (t, 3H).

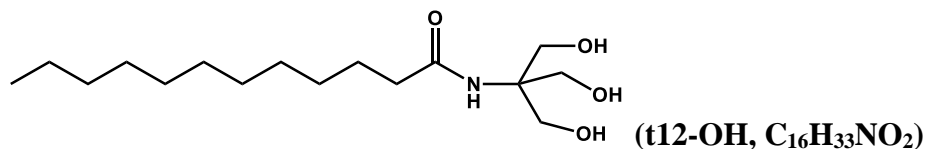


Palmitic N-hydroxyl-succinimide ester (133.4, 0.38 mmol) was dissolved in 7 mL of dry DMF. 2-amino-1,3-propanediol (~83 mg, ~0.8 mmol) was combined with 1 mL of dry DMF. While stirring, triethylamine (78.9  $\mu$ L, 0.57 mmol) was then added, and the reaction mixture was stirred at room temperature for 15 hours. After reaction, a white precipitate was observed. The product was precipitated with acidified NP H<sub>2</sub>O (pH ~4). The white solid was recovered by vacuum filtration and then dried *in vacuo*. Yield: 63.5 mg, 51 %. <sup>1</sup>H NMR (300 MHz, DMSO)  $\delta$  7.41 (d, 1H), 4.55 (s, 2H), 3.71 – 3.63 (m, 1H), 3.37 (t, 4H), 2.05 (t, 2H), 1.50 – 1.40 (m, 2H), 1.31 – 1.17 (m, 24H), 0.85 (t, 3H).



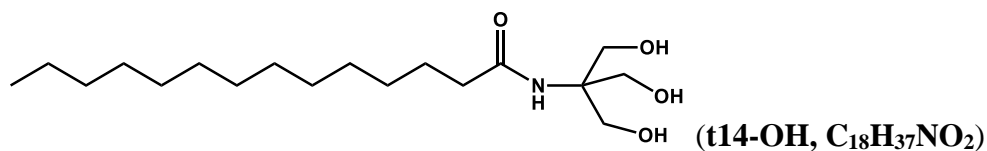


Stearic N-hydroxyl-succinimide ester (189.5 mg, 0.50 mmol) was dissolved in 13 mL of dry DMF. The solution remained a cloudy white due to incomplete dissolution. 2-amino-1,3-propanediol (~106 mg,  $\geq 1$  mmol) was combined with 1 mL of dry DMF. While stirring, triethylamine (104  $\mu$ L, 0.75 mmol) was then added, and the reaction mixture was stirred at room temperature for 15 hours. After reaction, a white precipitate was observed. The product was precipitated with acidified NP H<sub>2</sub>O (pH ~4). The white solid was recovered by vacuum filtration and then dried *in vacuo*. Yield: 125.2 mg, 70 %. <sup>1</sup>H NMR (300 MHz, DMSO)  $\delta$  7.41 (d, 1H), 4.55 (s, 2H), 3.72 – 3.65 (m, 1H), 3.37 (t, 4H), 2.05 (t, 2H), 1.50 – 1.40 (m, 2H), 1.30 – 1.17 (m, 28H), 0.85 (t, 3H).

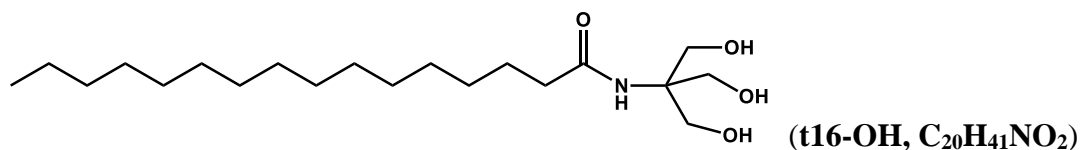


Lauric N-hydroxyl-succinimide ester (198.7 mg, 0.67 mmol) was dissolved in 10 mL of dry DMF. Tris(hydroxymethyl)aminomethane (202.3 mg, 1.67 mmol) was then added to the solution. The resulting solution was sonicated to ensure complete dissolution. While stirring, triethylamine (186  $\mu$ L, 1.34 mmol) was then added, and the reaction mixture was stirred at room temperature for 15 hours. After reaction, ~5 mL of NP H<sub>2</sub>O and ~3-4 mL of 1 M HCl were added to the product solution, bringing the pH to ~3-4. White precipitate was observed. The cloudy solution was then transferred to a 15 mL centrifuge tube. The solid product was collected via centrifugation; the supernatant was discarded. The product was rinsed with additional acidified

NP H<sub>2</sub>O (pH ~4) and collected via centrifugation. After decanting the supernatant, the white solid was collected via vacuum filtration and then dried *in vacuo*. Yield: 123.9 mg, 61 %. <sup>1</sup>H NMR (300 MHz, DMSO) δ 7.08 (s, 1H), 4.75 (t, 3H), 3.51 (d, 6H), 2.11 (t, 2H), 1.50 – 1.40 (m, 2H), 1.30 – 1.15 (m, 16H), 0.85 (t, 3H).

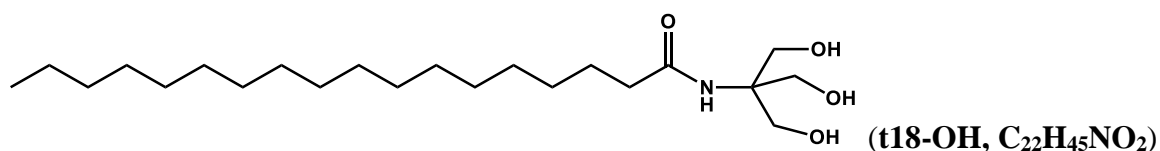


Myristic N-hydroxyl-succinimide ester (159.4 mg, 0.49 mmol) was dissolved in 10 mL of dry DMF. Tris(hydroxymethyl)aminomethane (119.0 mg, 0.98 mmol) was then added to the solution. The resulting solution was sonicated to ensure complete dissolution. While stirring, triethylamine (102 μL, 0.73 mmol) was then added, and the reaction mixture was stirred at room temperature for 15 hours. After reaction, ~5 mL of NP H<sub>2</sub>O and ~3-4 mL of 1 M HCl were added to the product solution, bringing the pH to ~3-4. White precipitate was observed. The cloudy solution was then transferred to a 15 mL centrifuge tube. The solid product was collected via centrifugation; the supernatant was discarded. The product was rinsed with additional acidified NP H<sub>2</sub>O (pH ~4) and collected via centrifugation. After decanting the supernatant, the white solid was collected via vacuum filtration and then dried *in vacuo*. Yield: 113.9 mg, 70 %. <sup>1</sup>H NMR (300 MHz, DMSO) δ 7.07 (s, 1H), 4.75 (t, 3H), 3.51 (d, 6H), 2.12 (t, 2H), 1.50 – 1.40 (m, 2H), 1.30 – 1.15 (m, 20H), 0.85 (t, 3H).



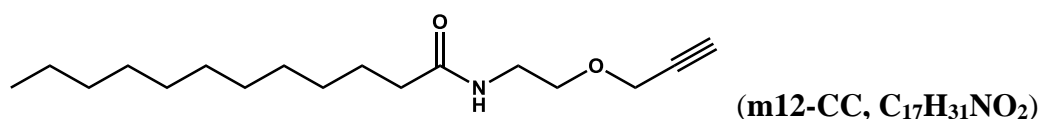
Palmitic N-hydroxyl-succinimide ester (175.2 mg, 0.50 mmol) was dissolved in 10 mL of dry DMF. Tris(hydroxymethyl)aminomethane (120.1 mg, 0.99 mmol). The resulting solution was sonicated to ensure complete dissolution. While stirring, triethylamine (103  $\mu$ L, 0.74 mmol) was then added, and the reaction mixture was stirred at room temperature for 15 hours. After reaction, 1.5 mL of 1 M HCl followed by 25 mL H<sub>2</sub>O were added to the reaction, and a white precipitate was observed. The cloudy solution was then transferred to a 15 mL centrifuge tube. The solid product was collected via centrifugation; the supernatant was discarded. The product was rinsed with NP H<sub>2</sub>O and collected via centrifugation. After decanting the supernatant, the white solid was collected via vacuum filtration and then dried *in vacuo*. Yield: 61.9 mg, 35 %.

<sup>1</sup>H NMR (300 MHz, DMSO)  $\delta$  7.07 (s, 1H), 4.74 (t, 3H), 3.51 (d, 6H), 2.12 (t, 2H), 1.50 – 1.40 (m, 2H), 1.30 – 1.15 (m, 24H), 0.85 (t, 3H).

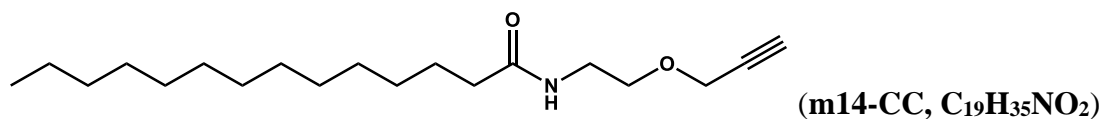


Stearic N-hydroxyl-succinimide ester (153.7 mg, 0.40 mmol) was dissolved in 10 mL of dry DMF. Tris(hydroxymethyl)aminomethane (97.6 mg, 0.80 mmol) was then added to the solution. The resulting solution was sonicated to ensure complete dissolution. While stirring, triethylamine (84.6  $\mu$ L, 1.34 mmol) was then added, and the reaction mixture was stirred at room temperature for 15 hours. After reaction, NP H<sub>2</sub>O was added to the flask and a white/clear gel was observed. The cloudy solution was then transferred to a 15 mL centrifuge tube and centrifuged. The solid

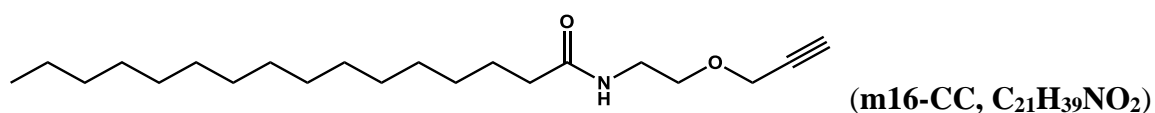
product was collected via centrifugation; the supernatant was discarded. The product was rinsed with NP H<sub>2</sub>O and collected via centrifugation. After decanting the supernatant, the white solid was collected via vacuum filtration and then dried *in vacuo*. Yield: 74.5 mg, 48 %. <sup>1</sup>H NMR (300 MHz, DMSO) δ 7.08 (s, 1H), 4.75 (t, 3H), 3.51 (d, 6H), 2.11 (t, 2H), 1.50 – 1.40 (m, 2H), 1.30 – 1.17 (m, 28H), 0.85 (t, 3H).



**m12-OH** (119.2 mg, 0.49 mmol) was dissolved in 6 mL of dry DMF. An 80% by mass solution of propargyl bromide in toluene (163 μL, 1.47 mmol) was added to the solution. The reaction flask was placed in an ice bath, and after cooling, 1 pellet of KOH, ground into a fine powder, was added over 5 min. The reaction flask was placed under argon, removed from the ice bath, warmed to room temperature, and stirred at room temperature for 2 days. After 2 days, the solvent was evaporated under reduced pressure, and the resulting product was extracted with DCM and washed with brine (3x) and H<sub>2</sub>O (1x). The organic layer was collected and dried over MgSO<sub>4</sub>. The MgSO<sub>4</sub> was removed by filtration and the solvent was removed via rotary evaporation. Any remaining DMF was removed *in vacuo* while heating at 50°C. The resulting crude product was purified by column chromatography on silica gel (230-400 Å mesh, 75% ethyl acetate in hexanes; R<sub>f</sub> = 0.55). Yield: 69.9 mg, 51 %. <sup>1</sup>H NMR (300 MHz, DMSO) δ 7.86 (t, 1H), 4.12 (d, 2H), 3.45 – 3.40 (t, t, 3H), 3.19 (q, 2H), 2.04 (t, 2H), 1.52 – 1.39 (m, 2H), 1.32 – 1.13 (m, 16H), 0.86 (t, 3H).

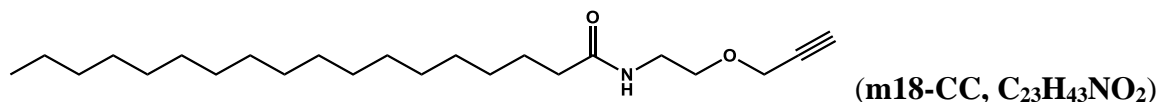


**m14-OH** (68.6 mg, 0.25 mmol) was dissolved in 7 mL of dry DMF. An 80% by mass solution of propargyl bromide in toluene (70.7  $\mu$ L; 0.63 mmol) was added to the solution. The reaction flask was placed in an ice bath, and after cooling, 1 pellet of KOH, ground into a fine powder, was added over 5 min. The reaction flask was placed under argon, removed from the ice bath, warmed to room temperature, and stirred at room temperature for 2 days. After 2 days, the solvent was evaporated under reduced pressure, and the resulting product was extracted with DCM and washed with brine (3x) and H<sub>2</sub>O (1x). The organic layer was collected and dried over MgSO<sub>4</sub>. The MgSO<sub>4</sub> was removed by filtration, the solvent was removed via rotary evaporation, and the crude product was dried *in vacuo*. The resulting crude product was purified by column chromatography on silica gel (230-400 Å mesh, 50% ethyl acetate in hexanes; R<sub>f</sub> = 0.45). Yield: 37.8 mg, 49 %. <sup>1</sup>H NMR (300 MHz, DMSO)  $\delta$  7.83 (t, 1H), 4.12 (d, 2H), 3.45 – 3.40 (t, t, 3H), 3.19 (q, 2H), 2.04 (t, 2H), 1.50 – 1.39 (m, 2H), 1.30 – 1.15 (m, 20H), 0.85 (t, 3H).



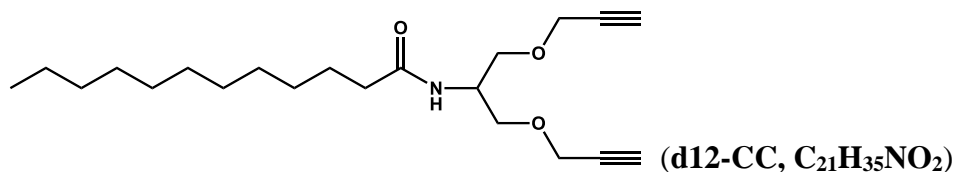
**m16-OH** (79.9 mg, 0.27 mmol) was dissolved in 4 mL of dry DMF and 2 mL of DCM. An 80% by mass solution of propargyl bromide in toluene (74.6  $\mu$ L, 0.67 mmol) was added to the solution. The reaction flask was placed in an ice bath, and after cooling, 1 pellet of KOH, ground into a fine powder, was added over 5 min. The reaction flask was placed under argon, removed from the ice bath, warmed to room temperature, and stirred at room temperature for 2

days. After 2 days, the solvent was evaporated under reduced pressure, and the resulting product was extracted with DCM and washed with brine (3x) and H<sub>2</sub>O (1x). The organic layer was collected and dried over MgSO<sub>4</sub>. The MgSO<sub>4</sub> was removed by filtration, the solvent was removed via rotary evaporation, and the crude product was dried *in vacuo*. The resulting crude product was purified by column chromatography on silica gel (230-400 Å mesh, 50% ethyl acetate in hexanes; R<sub>f</sub> = 0.5). Yield: 40.1 mg, 44 %. <sup>1</sup>H NMR (300 MHz, DMSO) δ 7.83 (t, 1H), 4.12 (d, 2H), 3.45 – 3.40 (t, t, 3H), 3.19 (q, 2H), 2.04 (t, 2H), 1.50 – 1.39 (m, 2H), 1.30 – 1.15 (m, 24H), 0.85 (t, 3H).

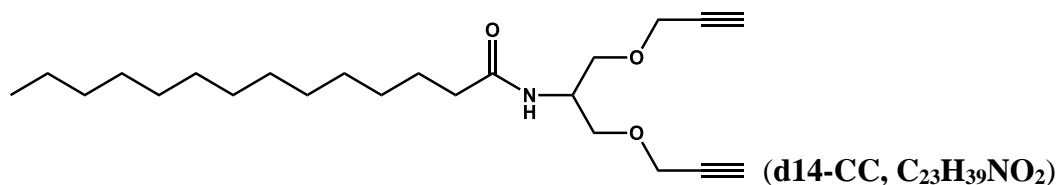


**m18-OH** (101.8 mg, 0.31 mmol) was dissolved in 5 mL of dry DMF and 7 mL of dry THF, resulting in a slightly cloudy solution. An 80% by mass solution of propargyl bromide in toluene (104 µL, 0.93 mmol) was added to the solution. The reaction flask was placed in an ice bath, and after cooling, 1 pellet of KOH, ground into a fine powder, were added over 5 min. The reaction flask was placed under argon, removed from the ice bath, warmed to room temperature, and stirred at room temperature for 2 days. After 2 days, the solvent was evaporated under reduced pressure, and the resulting product was extracted with DCM and washed with brine (3x) and H<sub>2</sub>O (1x). The organic layer was collected and dried over MgSO<sub>4</sub>. The MgSO<sub>4</sub> was removed by filtration, the solvent was removed via rotary evaporation, and the crude product was dried *in vacuo*. The resulting crude product was purified by column chromatography on silica gel (230-400 Å mesh, 50% ethyl acetate in hexanes; R<sub>f</sub> = 0.5). Yield: 43.0 mg, 38 %. <sup>1</sup>H NMR (300 MHz,

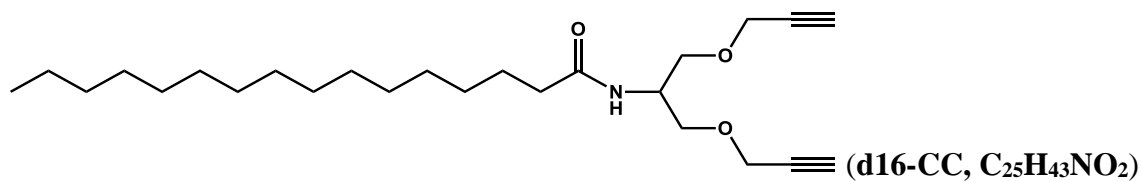
DMSO)  $\delta$  7.83 (t, 1H), 4.12 (d, 2H), 3.45 – 3.39 (t, t, 3H), 3.19 (q, 2H), 2.04 (t, 2H), 1.50 – 1.39 (m, 2H), 1.30 – 1.15 (m, 28H), 0.85 (t, 3H).



**d12-OH** (68.5 mg, 0.25 mmol) was dissolved in 3 mL of dry DMF. An 80% by mass solution of propargyl bromide in toluene (167  $\mu$ L, 1.50 mmol) was added to the solution. The reaction flask was placed in an ice bath, and after cooling, 1-1.5 pellets of KOH, ground into a fine powder, were added over 5 min. The reaction flask was placed under argon, removed from the ice bath, warmed to room temperature, and stirred at room temperature for 2 days. After 2 days, the solvent was evaporated under reduced pressure, and the resulting product was extracted with DCM and washed with brine (3x) and H<sub>2</sub>O (1x). The organic layer was collected and dried over MgSO<sub>4</sub>. The MgSO<sub>4</sub> was removed by filtration, the solvent was removed via rotary evaporation, and the crude product was dried *in vacuo*. The resulting crude product was purified by column chromatography on silica gel (230-400 Å mesh, 50% ethyl acetate in hexanes; R<sub>f</sub> = 0.5). Yield: 38.5 mg, 44 %. <sup>1</sup>H NMR (300 MHz, DMSO)  $\delta$  7.75 (d, 1H), 4.12 (d, 4H), 4.07 – 3.97 (m, 1H) 3.47 – 3.38 (t, d, 6H), 2.06 (t, 2H), 1.52 – 1.40 (m, 2H), 1.35 – 1.13 (m, 16H), 0.85 (t, 3H).



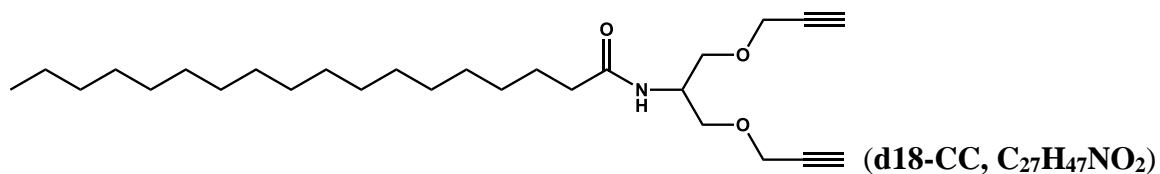
**d14-OH** (88.5 mg, 0.29 mmol) was dissolved in 4 mL of dry DMF. An 80% by mass solution of propargyl bromide in toluene (129  $\mu$ L, 1.17 mmol) was added to the solution. The reaction flask was placed in an ice bath, and after cooling, 1-1.5 pellets of KOH, ground into a fine powder, were added over 5 min. The reaction flask was placed under argon, removed from the ice bath, warmed to room temperature, and stirred at room temperature for 2 days. After 2 days, the solvent was evaporated under reduced pressure, and the resulting product was extracted with DCM and washed with brine (3x) and H<sub>2</sub>O (1x). The organic layer was collected and dried over MgSO<sub>4</sub>. The MgSO<sub>4</sub> was removed by filtration, the solvent was removed via rotary evaporation, and the crude product was dried *in vacuo*. The resulting crude product was purified by column chromatography on silica gel (230-400 Å mesh, 33% ethyl acetate in hexanes; R<sub>f</sub> = 0.3). Yield: 44.2 mg, 40 %. <sup>1</sup>H NMR (300 MHz, DMSO)  $\delta$  7.74 (d, 1H), 4.13 (d, 4H), 4.07 – 3.97 (m, 1H), 3.47 – 3.38 (t, d, 6H), 2.06 (t, 2H), 1.50 – 1.40 (m, 2H), 1.31 – 1.16 (m, 20H), 0.85 (t, 3H).



**d16-OH** (62.8 mg, 0.15 mmol) was dissolved in 8 mL of dry DMF. An 80% by mass solution of propargyl bromide in toluene (127  $\mu$ L, 1.14 mmol) was added to the solution. The reaction flask was placed in an ice bath, and after cooling, 1-1.5 pellets of KOH, ground into a fine powder, were added over 5 min. The reaction flask was placed under argon, removed from the ice bath,

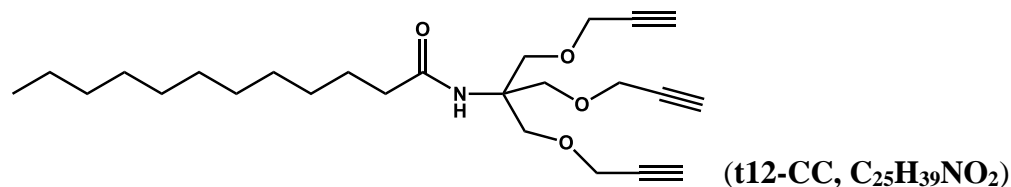


warmed to room temperature, and stirred at room temperature for 2 days. After 2 days, the solvent was evaporated under reduced pressure, and the resulting product was extracted with DCM and washed with brine (3x) and H<sub>2</sub>O (1x). The organic layer was collected and dried over MgSO<sub>4</sub>. The MgSO<sub>4</sub> was removed by filtration, the solvent was removed via rotary evaporation, and the crude product was dried *in vacuo*. The resulting crude product was purified by column chromatography on silica gel (230-400 Å mesh, 33% ethyl acetate in hexanes; R<sub>f</sub> = 0.35). Yield: 31.0 mg, 51 %. <sup>1</sup>H NMR (300 MHz, DMSO) δ 7.73 (d, 1H), 4.12 (d, 4H), 4.06 – 3.96 (m, 1H), 3.44 – 3.39 (t, d, 6H), 2.06 (t, 2H), 1.50 – 1.39 (m, 2H), 1.35 – 1.13 (m, 24H), 0.85 (t, 3H).

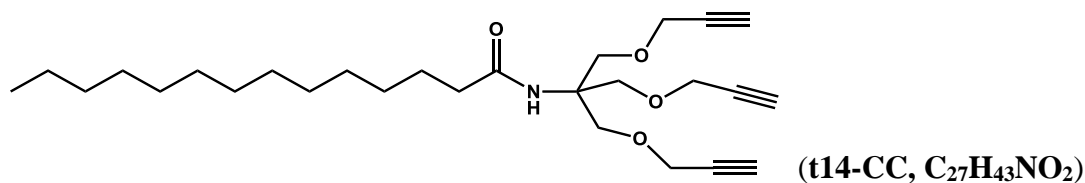


**d18-OH** (44.2 mg, 0.12 mmol) was dissolved in 2 mL of dry DMF and 1.5 mL of dry THF. An 80% by mass solution of propargyl bromide in toluene (110 µL, 0.99 mmol) was added to the solution. The reaction flask was placed in an ice bath, and after cooling, 1-1.5 pellets of KOH, ground into a fine powder, were added over 5 min. The reaction flask was placed under argon, removed from the ice bath, warmed to room temperature, and stirred at room temperature for 2 days. After 2 days, the solvent was evaporated under reduced pressure, and the resulting product was extracted with DCM and washed with brine (3x) and H<sub>2</sub>O (1x). The organic layer was collected and dried over MgSO<sub>4</sub>. The MgSO<sub>4</sub> was removed by filtration, the solvent was removed via rotary evaporation, and the crude product was dried *in vacuo*. The resulting crude product was purified by column chromatography on silica gel (230-400 Å mesh, 33% ethyl acetate in hexanes; R<sub>f</sub> = 0.45). Yield: 22.1 mg, 42 %. <sup>1</sup>H NMR (300 MHz, DMSO) δ 7.73 (d,

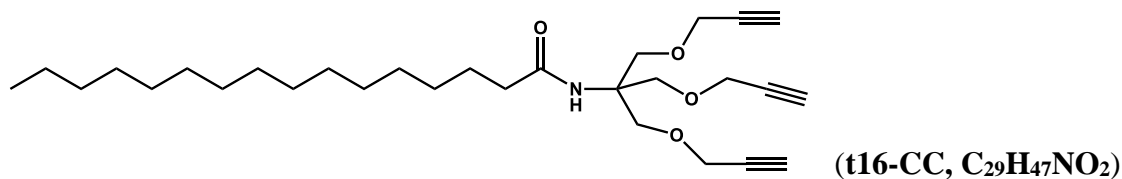
1H), 4.12 (d, 4H), 4.08 – 3.98 (m, 1H), 3.45 – 3.39 (t, d, 6H), 2.06 (t, 2H), 1.50 – 1.39 (m, 2H), 1.36 – 1.17 (m, 28H), 0.85 (t, 3H).



**t12-OH** (144.5 mg, 0.48 mmol) was dissolved in 6 mL of dry DMF. An 80% by mass solution of propargyl bromide in toluene (377  $\mu$ L, 3.40 mmol) was added to the solution. The reaction flask was placed in an ice bath, and after cooling, 2 pellets of KOH, ground into a fine powder, were added over 5 min. The reaction flask was placed under argon, removed from the ice bath, warmed to room temperature, and stirred at room temperature for 2 days. After 2 days, the solvent was evaporated under reduced pressure, and the resulting product was extracted with DCM and washed with brine (3x) and H<sub>2</sub>O (1x). The organic layer was collected and dried over MgSO<sub>4</sub>. The MgSO<sub>4</sub> was removed by filtration, the solvent was removed via rotary evaporation, and the crude product was dried *in vacuo*; any remaining DMF was removed *in vacuo* while heating at 50°C. The resulting crude product was purified by column chromatography on silica gel (230-400 Å mesh, 33% ethyl acetate in hexanes; R<sub>f</sub> = 0.6). Yield: 135.4 mg, 67 %. <sup>1</sup>H NMR (300 MHz, DMSO)  $\delta$  7.15 (s, 1H), 4.11 (d, 6H), 3.64 (s, 6H), 3.41 (t, 3H), 2.05 (t, 2H), 1.50 – 1.37 (m, 2H), 1.30 – 1.15 (m, 16H), 0.85 (t, 3H).

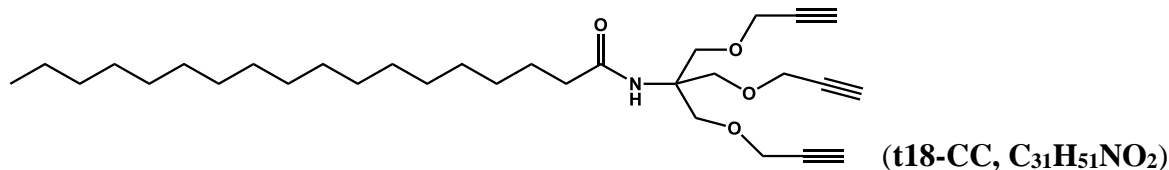


**t14-OH** (85.0 mg, 0.26 mmol) was dissolved in 5 mL of dry DMF. An 80% by mass solution of propargyl bromide in toluene (172  $\mu$ L, 1.54 mmol) was added to the solution. The reaction flask was placed in an ice bath, and after cooling, 2 pellets of KOH, ground into a fine powder, were added over 5 min. The reaction flask was placed under argon, removed from the ice bath, warmed to room temperature, and stirred at room temperature for 2 days. After 2 days, the solvent was evaporated under reduced pressure, and the resulting product was extracted with DCM and washed with brine (3x) and H<sub>2</sub>O (1x). The organic layer was collected and dried over MgSO<sub>4</sub>. The MgSO<sub>4</sub> was removed by filtration, the solvent was removed via rotary evaporation, and the crude product was dried *in vacuo*. The resulting crude product was purified by column chromatography on silica gel (230-400 Å mesh, 30% ethyl acetate in hexanes; R<sub>f</sub> = 0.5). Yield: 63.7 mg, 55 %. <sup>1</sup>H NMR (300 MHz, DMSO)  $\delta$  7.14 (s, 1H), 4.11 (d, 6H), 3.64 (s, 6H), 3.40 (t, 3H), 2.05 (t, 2H), 1.50 – 1.38 (m, 2H), 1.30 – 1.15 (m, 20H), 0.85 (t, 3H).



**t16-OH** (61.9 mg; 0.17 mmol) was dissolved in 4 mL of dry DMF. An 80% by mass solution of propargyl bromide in toluene (115  $\mu$ L, 1.03 mmol) was added to the solution. The reaction flask was placed in an ice bath, and after cooling, 2 pellets of KOH, ground into a fine powder, were added over 5 min. The reaction flask was placed under argon, removed from the ice bath,

warmed to room temperature, and stirred at room temperature for 2 days. After 2 days, the solvent was evaporated under reduced pressure, and the resulting product was extracted with DCM and washed with brine (3x) and H<sub>2</sub>O (1x). The organic layer was collected and dried over MgSO<sub>4</sub>. The MgSO<sub>4</sub> was removed by filtration, the solvent was removed via rotary evaporation, and the crude product was dried *in vacuo*. The resulting crude product was purified by column chromatography on silica gel (230-400 Å mesh, 30% ethyl acetate in hexanes; R<sub>f</sub> = 0.5). Yield: 42.6 mg, 53 %. <sup>1</sup>H NMR (300 MHz, DMSO) δ 7.16 (s, 1H), 4.11 (d, 6H), 3.64 (s, 6H), 3.41 (t, 3H), 2.05 (t, 2H), 1.50 – 1.37 (m, 2H), 1.30 – 1.16 (m, 24H), 0.85 (t, 3H).



**t18-OH** (72.2 mg; 0.19 mmol) was dissolved in 3 mL of dry DMF and 3 mL of dry THF. An 80% by mass solution of propargyl bromide in toluene (125 µL, 1.12 mmol) was added to the solution. The reaction flask was placed in an ice bath, and after cooling, 2 pellets of KOH, ground into a fine powder, were added over 5 min. The reaction flask was placed under argon, removed from the ice bath, warmed to room temperature, and stirred at room temperature for 2 days. After 2 days, the solvent was evaporated under reduced pressure, and the resulting product was extracted with DCM and washed with brine (3x) and H<sub>2</sub>O (1x). The organic layer was collected and dried over MgSO<sub>4</sub>. The MgSO<sub>4</sub> was removed by filtration, the solvent was removed via rotary evaporation, and the crude product was dried *in vacuo*. The resulting crude product was purified by column chromatography on silica gel (230-400 Å mesh, 30% ethyl acetate in hexanes; R<sub>f</sub> = 0.5). Yield: 41.2 mg, 43 %. <sup>1</sup>H NMR (300 MHz, DMSO) δ 7.16 (s, 1H),

4.10 (d, 6H), 3.64 (s, 6H), 3.41 (t, 3H), 2.04 (t, 2H), 1.49 – 1.38 (m, 2H), 1.30 – 1.15 (m, 28H),  
0.85 (t, 3H).

## APPENDIX B

### SUPPORTING INFORMATION FOR CHAPTER 3: “PEPTIDE-DIRECTED ASSEMBLY OF SINGLE-HELICAL GOLD NANOPARTICLE SUPERSTRUCTURES EXHIBITING INTENSE CHIROPTICAL ACTIVITY”

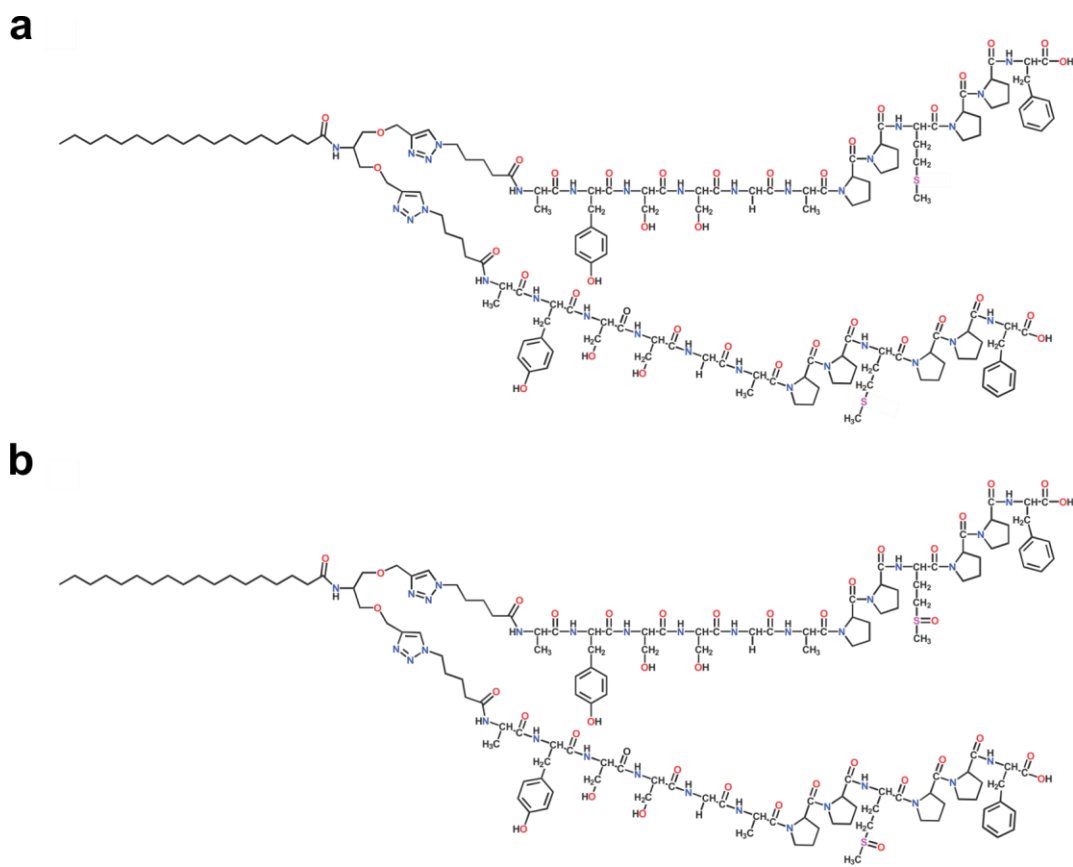


**Figure S3.55.** Chemical structure of (a)  $C_{18}$ -(PEPAu)<sub>2</sub> and (b)  $C_{18}$ -(PEPAu<sup>M-ox</sup>)<sub>2</sub>.

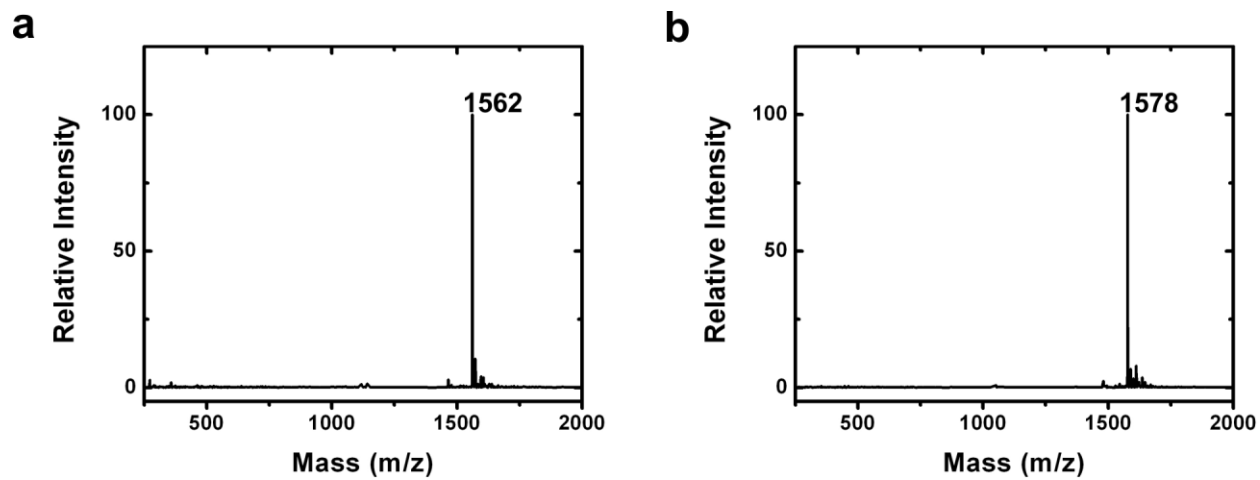
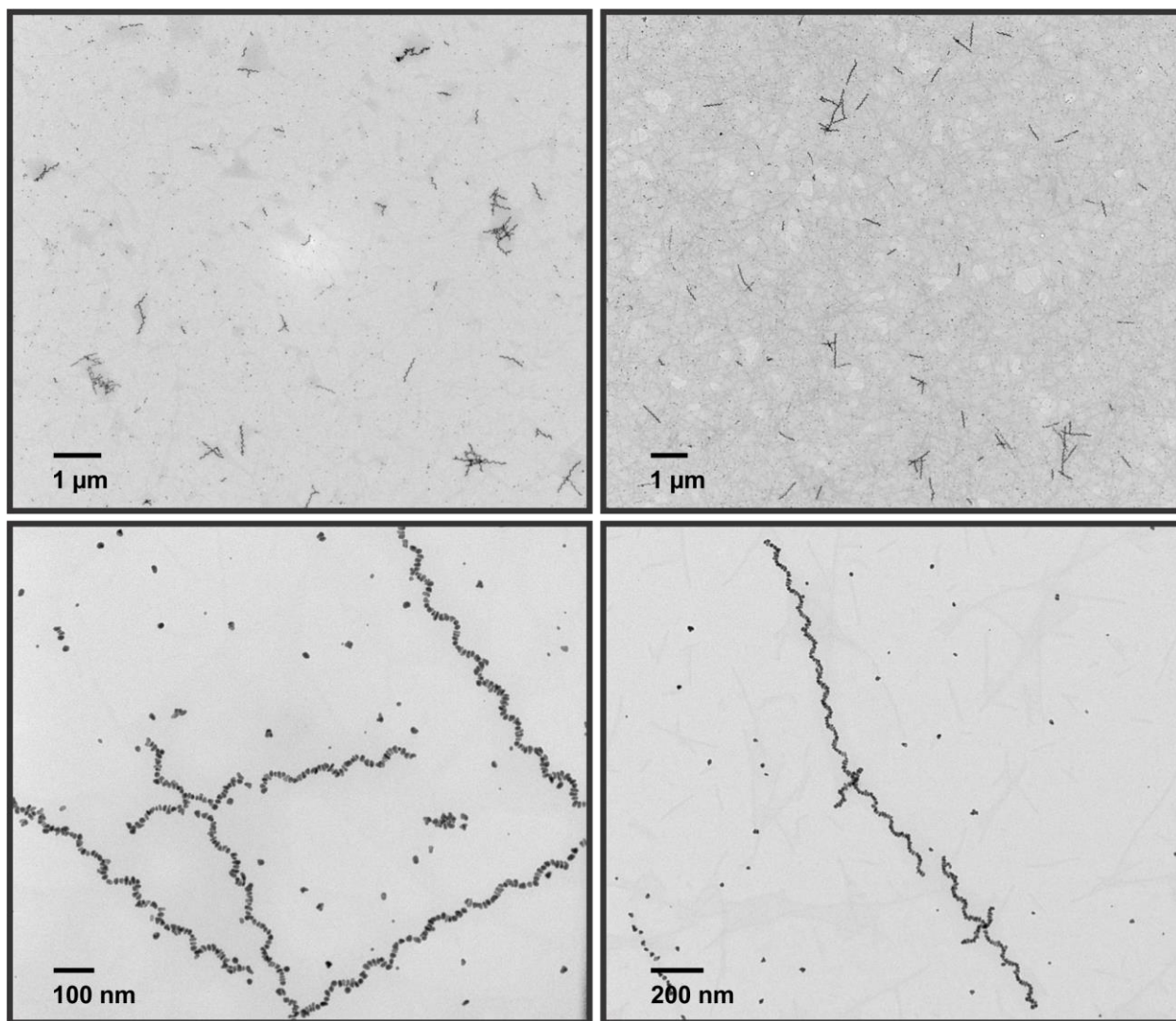
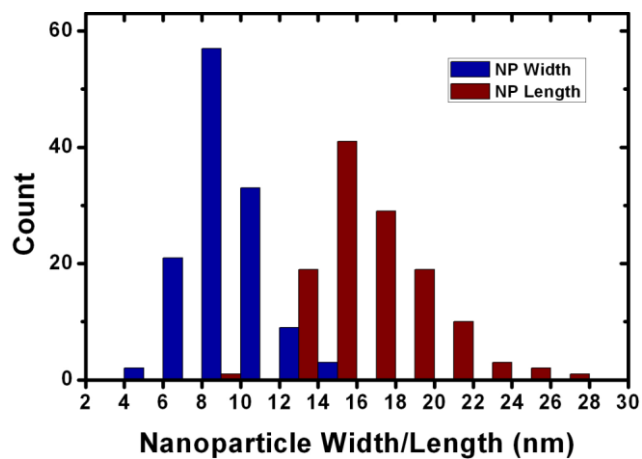


Figure S3.56. LCMS spectra of (a)  $C_{18}-(PEP_{Au})_2$ ,  $m/z = 1562$  ( $m/2$ ) and  $C_{18}-(PEP_{Au}^{M-ox})_2$ ,  $m/z = 1578$  ( $m/2$ ).



**Figure S3.57.** Additional TEM images of the single-helical superstructure at different magnifications.





**Figure S3.58.** The nanoparticle length and widths of the single-helical superstructure were  $16.6 \pm 3.0$  nm and  $9.6 \pm 1.9$  nm, respectively, after 15 hours of reaction (based on 125 counts each).

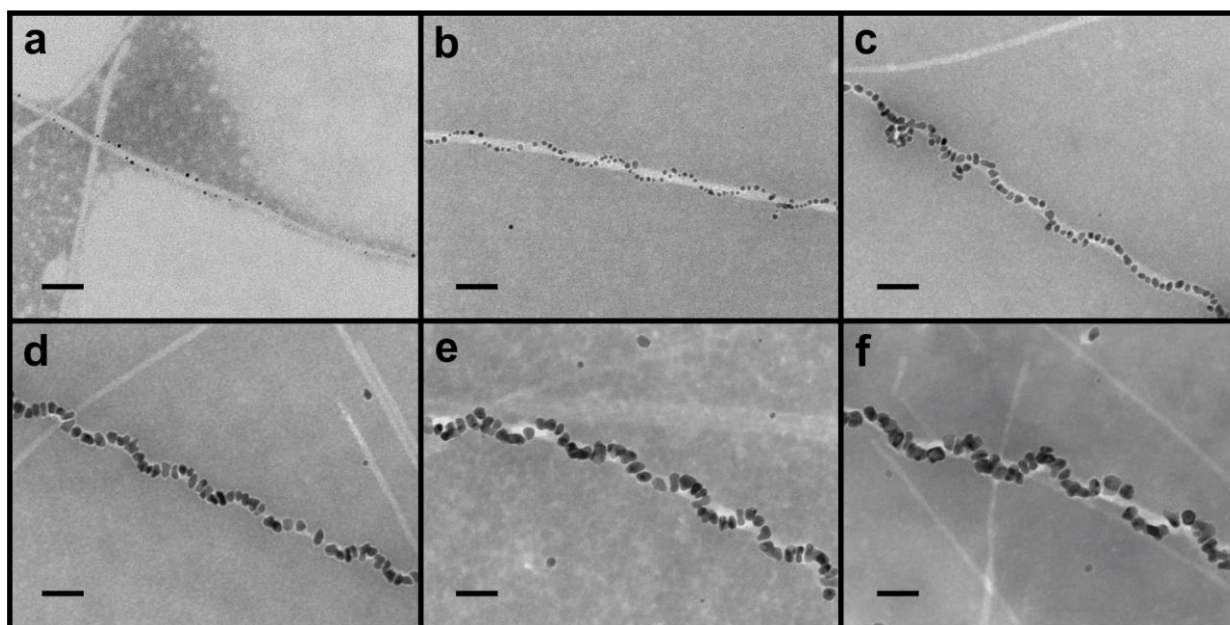


**Figure S3.59.** Negative-stained TEM images of the single helices after (a) 0 min., (b) 30 min., (c) 2 hrs., (d) 5 hrs., (e) 8 hrs., and (f) 2 days of reaction at room temperature (scale bars = 50 nm)

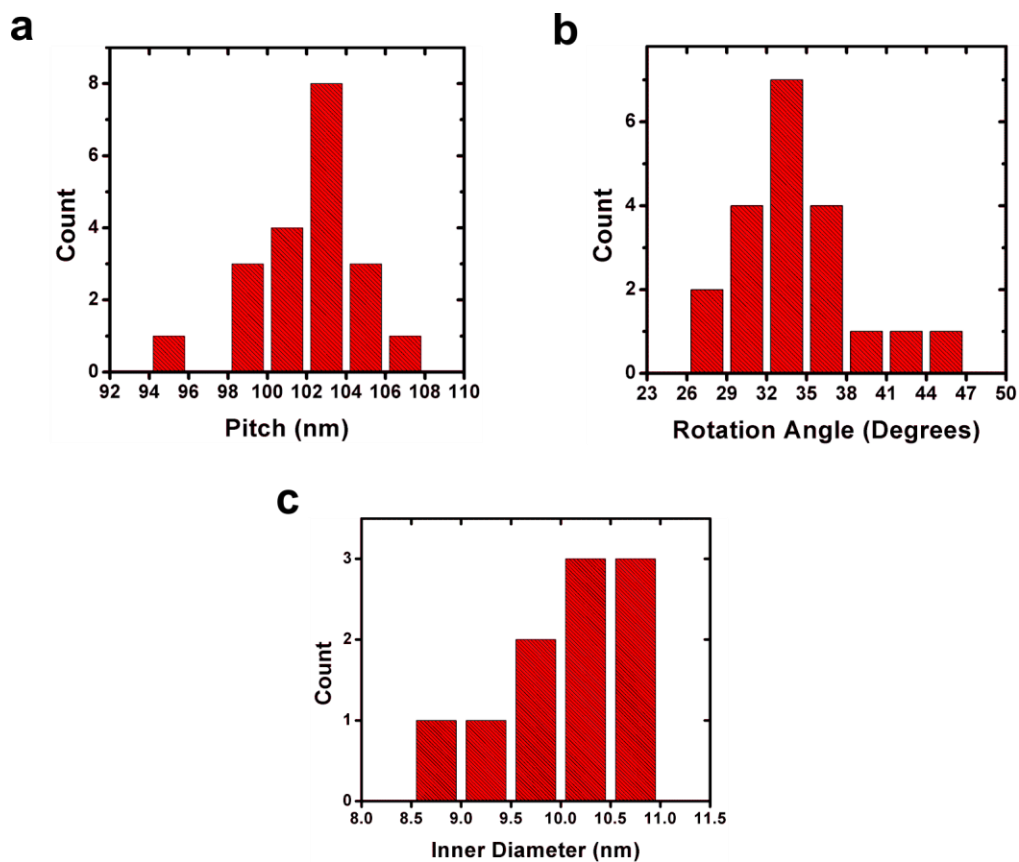


**Figure S3.60.** Structural parameters of single helices from cryo-ET: (a) the helical pitch was  $102.0 \pm 2.5$  nm, based on 20 counts; (b) rotation angle was  $34.3 \pm 4.9$  degrees, based on 20 counts; and (c) inner diameter was  $10.1 \pm 0.6$  nm, based on 10 counts.

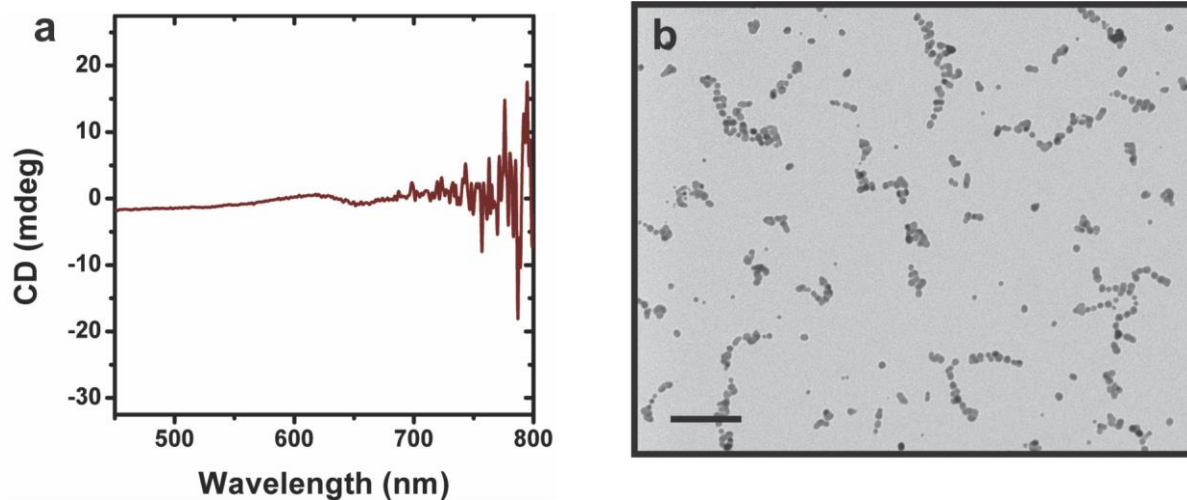


**Figure S3.61.** (a) CD spectrum of  $\text{PEP}_{\text{au}}^{\text{M-ox}}$  capped gold nanoparticles and (b) their corresponding TEM image (scale bar = 100 nm). Both single particles and particle aggregates are observed.

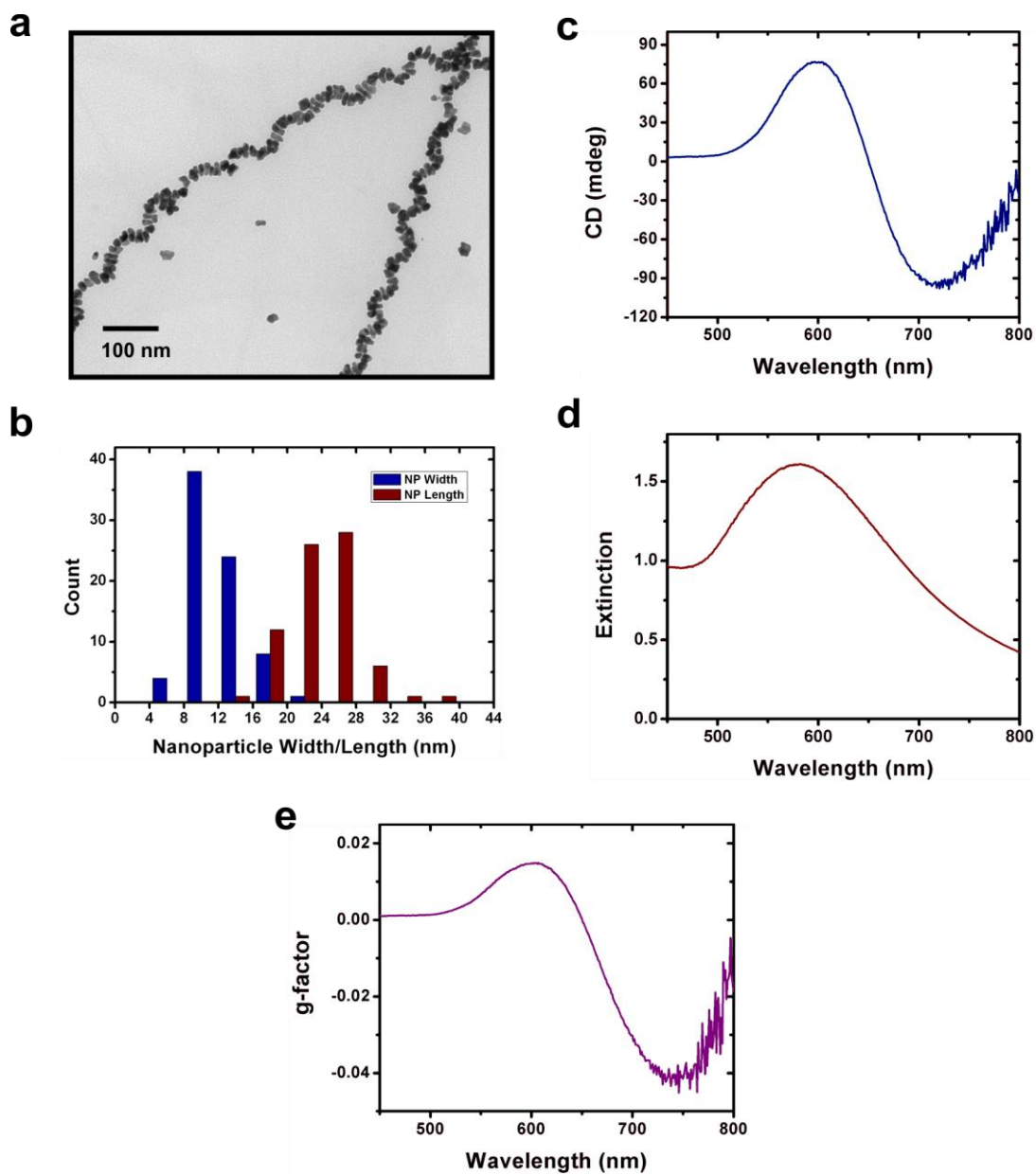


**Figure S3.62.** (a) TEM image of helices formed with 10 min. of sonication and 20 min. of incubation prior to  $\text{HAuCl}_4/\text{TEAA}$  addition. (b) The particle width and lengths were  $12.1 \pm 3.0$  nm and  $23.9 \pm 3.9$  nm, respectively (based on 75 counts each). (c) CD spectrum of the optimized single helices exhibit a very strong CD signal. (d) UV-Vis extinction spectrum, and (e)  $g$ -factor graph showing absolute  $g$ -factor values up to 0.04.  $g$ -factor =  $\Delta\epsilon/\epsilon$ , where  $\Delta\epsilon$  is the molar circular dichroism and  $\epsilon$  is the molar extinction.

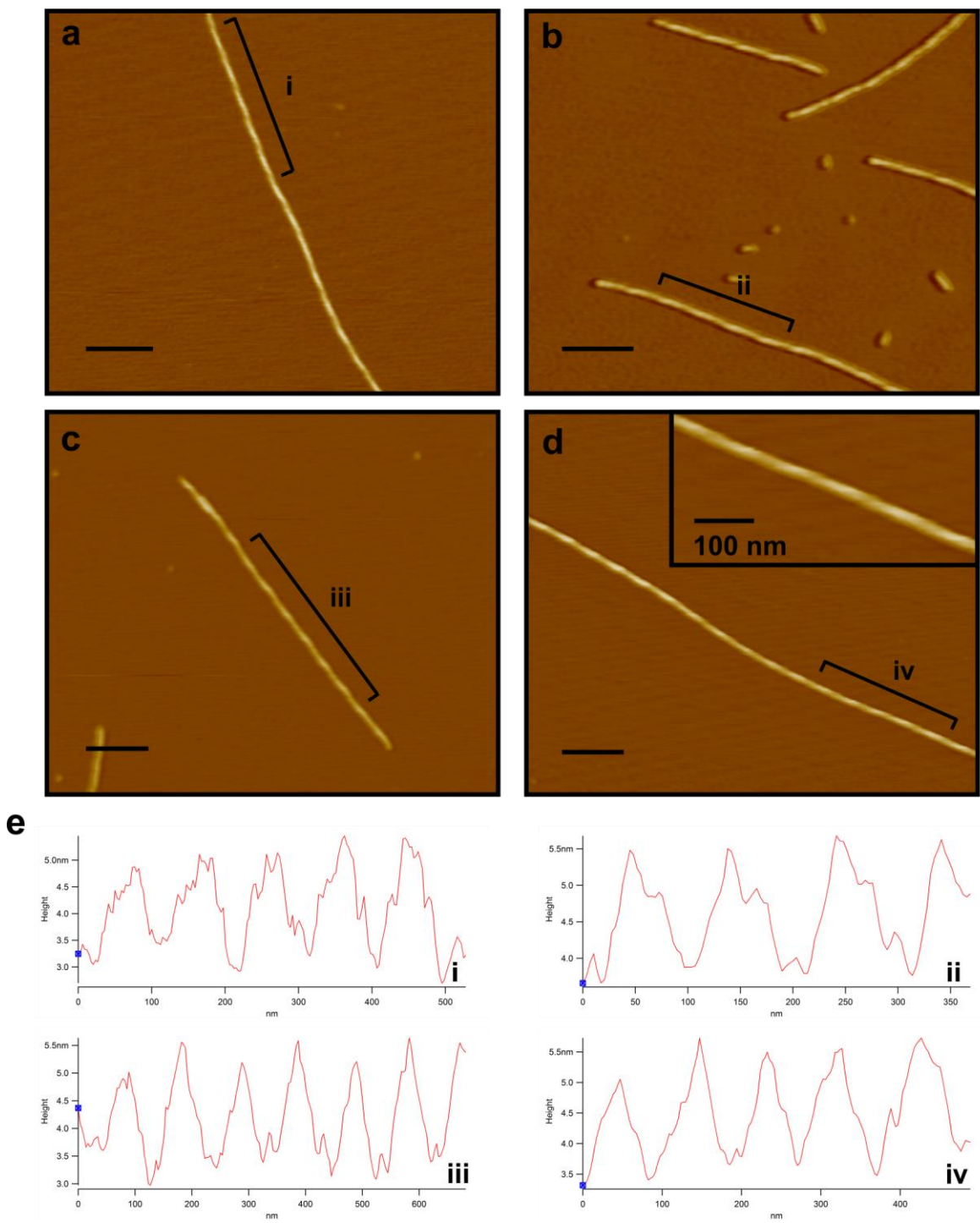


**Figure S3.63.** (a-d) AFM images of  $C_{18}$ -(PEPAu<sup>M-ox</sup>)<sub>2</sub> fibers dispersed on APTES-functionalized mica (scale bars = 200 nm) and (e) height traces of the labeled segments.

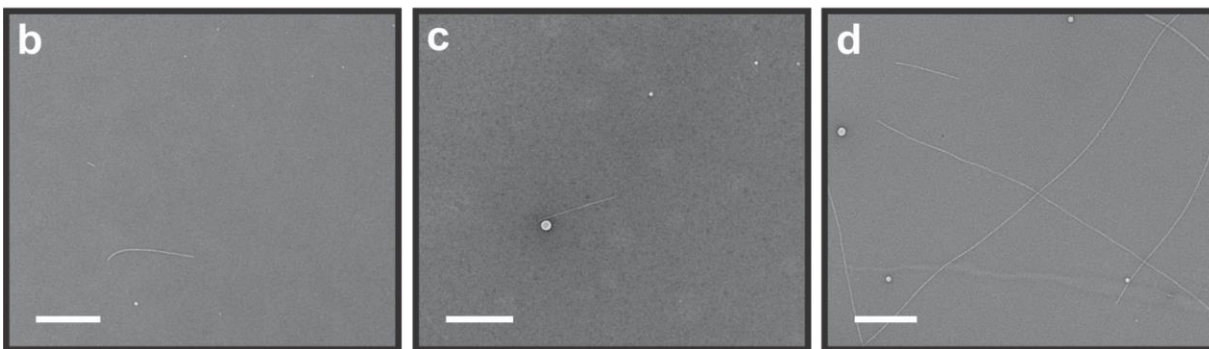
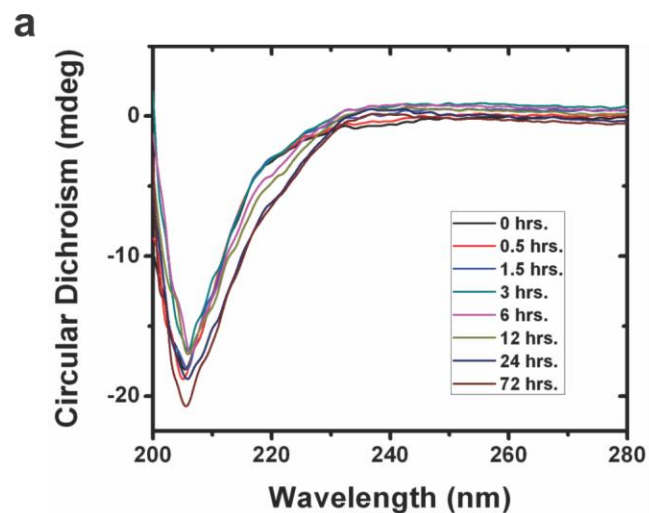


**Figure S3.64.** (a)  $C_{18}-(PEP_{Au}^{M-ox})_2$  in 10 mM HEPES as a function of time. Negative-stained TEM images after (b) 15 min., (c) 3 hrs., and (d) 72 hrs. are shown (scale bars = 500 nm). Under these conditions, fibers form very slowly, and very few fibers are observed at early time points.



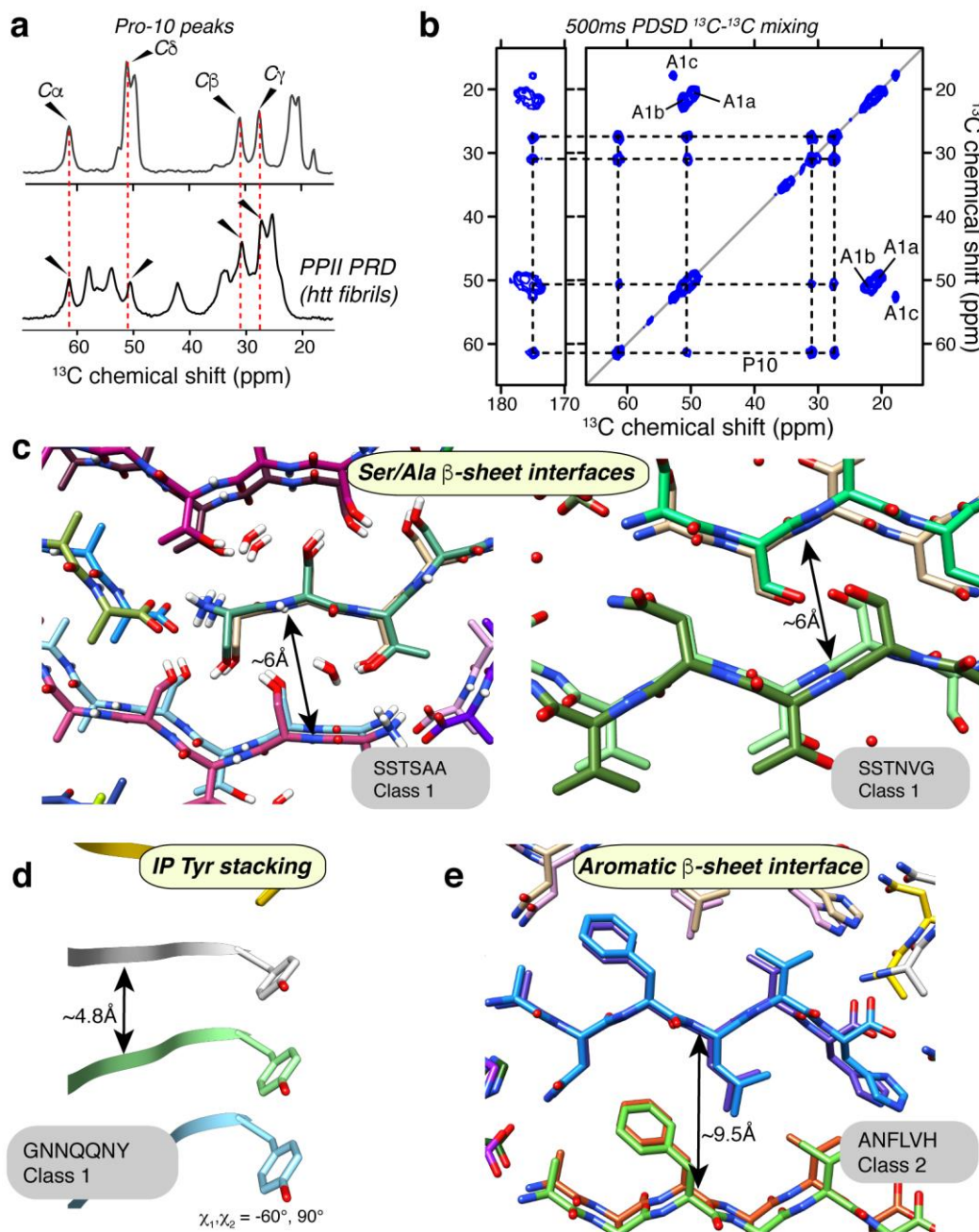


**Figure S3.65.** Additional ssNMR results and structural reference. (a) Aliphatic  $^{13}\text{C}$  1D MAS ssNMR spectrum of the site-specifically labeled  $\text{C}_{18}\text{-(PEP}_{\text{Au}}^{\text{M-ox}}\text{)}_2$  assemblies (top), with the P10 peaks indicated. Bottom: ssNMR spectrum of fibrillar huntingtin exon1-derived peptide  $\text{htt}^{\text{NT}}\text{Q}_{30}\text{P}_{10}\text{K}_2$ , with  $^{13}\text{C}$ -,  $^{15}\text{N}$ -labeled Pro P48 (adapted from ref. <sup>119</sup>). In both cases the labeled Pro is part of a PPII helix that flanks the  $\beta$ -sheet amyloid core. (b) Long-mixing 500ms PDSD 2D ssNMR spectrum on the labeled  $\text{C}_{18}\text{-(PEP}_{\text{Au}}^{\text{M-ox}}\text{)}_2$  assemblies. Compared to the short-mixing spectrum (**Figure 3.24b**) only new intra-residue P10 peaks are observed, with no contacts between the distinct A1

conformers. (c) Compact zipper interfaces mediated by Ser and other small amino acids in amyloid-like crystals of peptides SSTSAA and SSTNVG from RNase and IAPP.<sup>120</sup> The compact 6 Å inter-sheet distance is indicated. (d) Tyr ring stacking in GNNQQNY in-register parallel (IP)  $\beta$ -sheets.<sup>166</sup> (e) Amyloid interfaces featuring aromatic residues generate wider 9-10 Å inter-sheet distances. Illustrated for Phe in this Class-2 amyloid-like crystal of peptide ANFLVH.<sup>167</sup> The PDB entries for the four peptide crystal structures are 2ONW, 3DG1, 1YJP, and 5E5X.

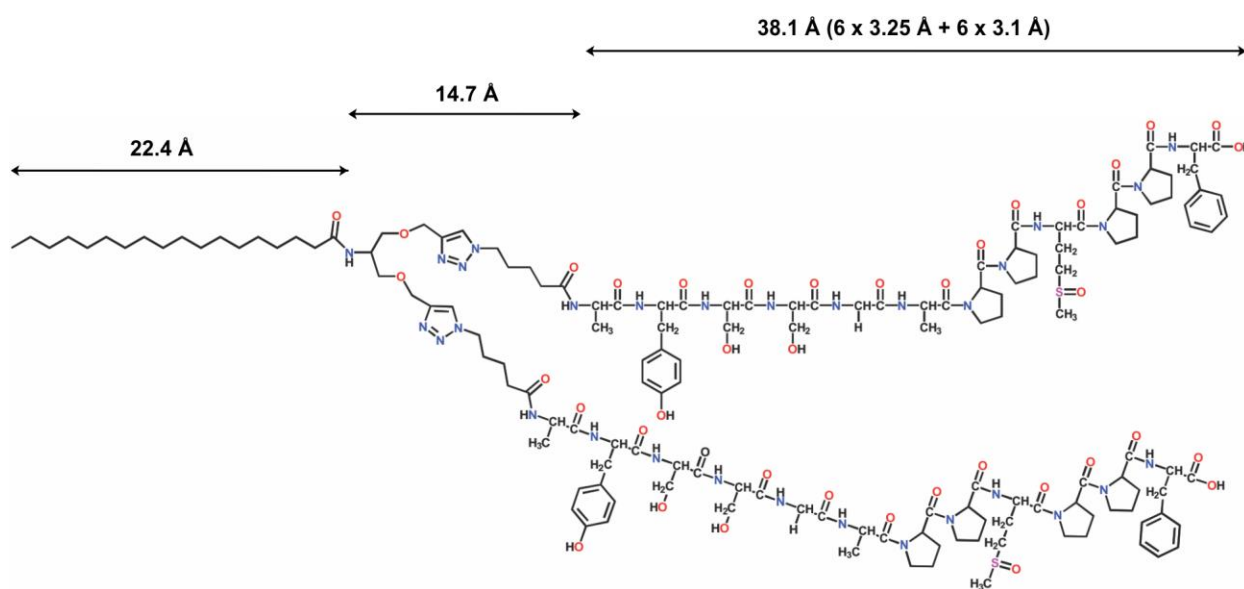


**Figure S3.66.** Length of the different extended segments of  $C_{18}-(PEP_{Au}^{M-ox})_2$ . The total length of the extended molecule is  $\sim 7.5$  nm. The length measurements of the peptide portion takes into account the average length spanned by one amino acid in both the parallel  $\beta$ -sheet (3.25 Å)<sup>168</sup> and the PPII (3.1 Å)<sup>169</sup> secondary structure.



**Table S3.2 Detailed experimental conditions of the MAS ssNMR experiments.** *Abbreviations: NS, number of scans; Set Temp, set temperature of cooling gas; MAS, magic angle spinning rate; RD, recycle delay; TPPM, two-pulse phase-modulated  $^1\text{H}$  decoupling power during evolution and acquisition.*

Figure	Expt.	NS	Set Temp (K)	MAS (kHz)	RD (s)	TPPM (kHz)	$t_1$ evol. ( $\mu\text{s}$ )	DARR mixing time (ms)	$^1\text{H}$ - $^{13}\text{C}$ Contact time (ms)
4b	2D $^{13}\text{C}$ - $^{13}\text{C}$ CP-DARR	64	277	10	3	83	562*35.6	20	2
S14-a	$^1\text{H}$ - $^{13}\text{C}$ CP	1024	277	10	3	83	NA	NA	2
S14-b	2D $^{13}\text{C}$ - $^{13}\text{C}$ PDSD	64	277	10	3	83	562*33.11	500	2

## APPENDIX C

### SUPPORTING INFORMATION FOR CHAPTER 4: “POST-SYNTHETIC SURFACE MODIFICATION OF HOLLOW SPHERICAL GOLD NANOPARTICLE SUPERSTRUCTURES WITH TUNABLE ASSEMBLY METRICS”

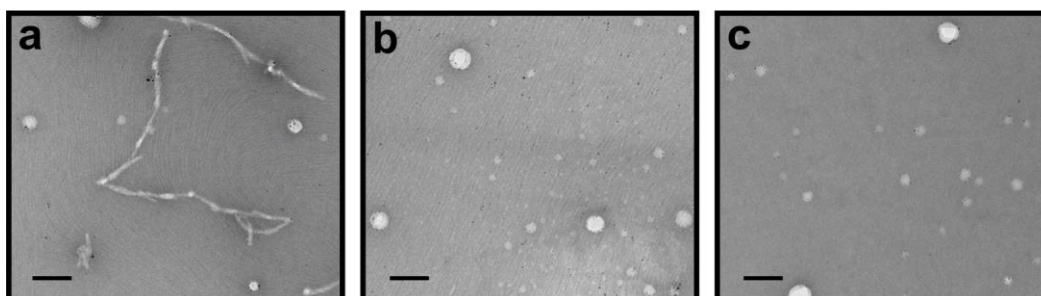


**Figure S4.67.** TEM images of HSAuNP superstructures assembled after 10 min. with (a) 0.7  $\mu\text{L}$   $\text{HAuCl}_4/\text{TEAA}$ , (b) 0.9  $\mu\text{L}$   $\text{HAuCl}_4/\text{TEAA}$ , and (c) 1.1  $\mu\text{L}$   $\text{HAuCl}_4/\text{TEAA}$  (scale bars = 100 nm).

## APPENDIX D

### SUPPORTING INFORMATION FOR CHAPTER 5: “PEPTIDE-OLIGONUCLEOTIDE CHIMERAS (POCS): PROGRAMMABLE BIOMOLECULAR CONSTRUCTS FOR THE ASSEMBLY OF MOPHOLOGICALLY-TUNABLE SOFT MATERIALS”

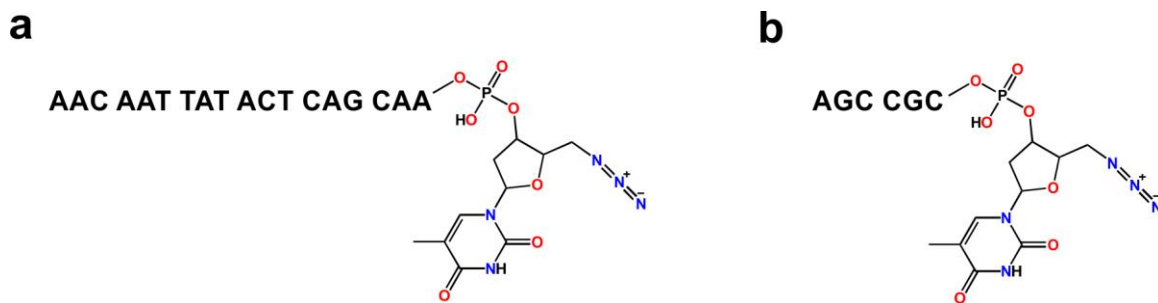


**Figure S5.68.** Structure of the (a) 18-base azido-modified oligonucleotide ( $O_{18}-N_3$ ) and (b) 6-base azido-modified oligonucleotide ( $O_6-N_3$ ).

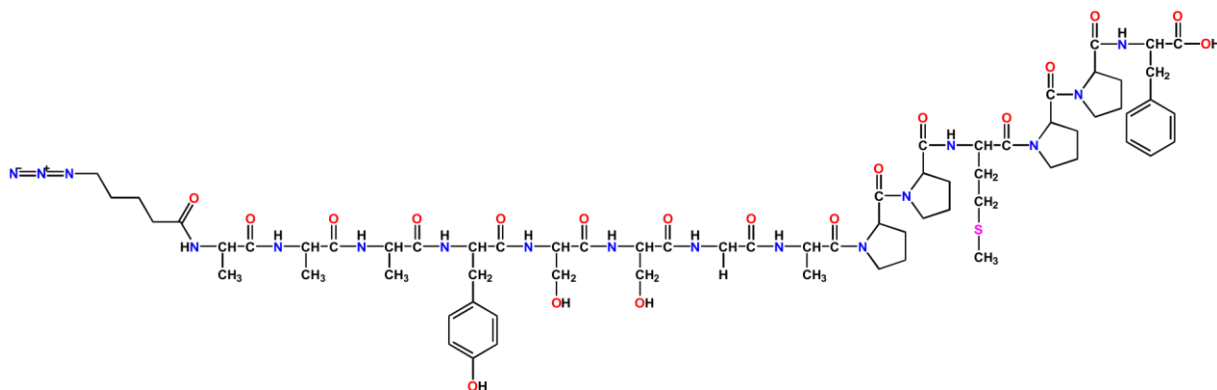


**Figure S5.69.** Chemical structure of the azido-modified peptide ( $N_3$ - $C_4H_8CO$ -AAAYSSGAPMPPF).

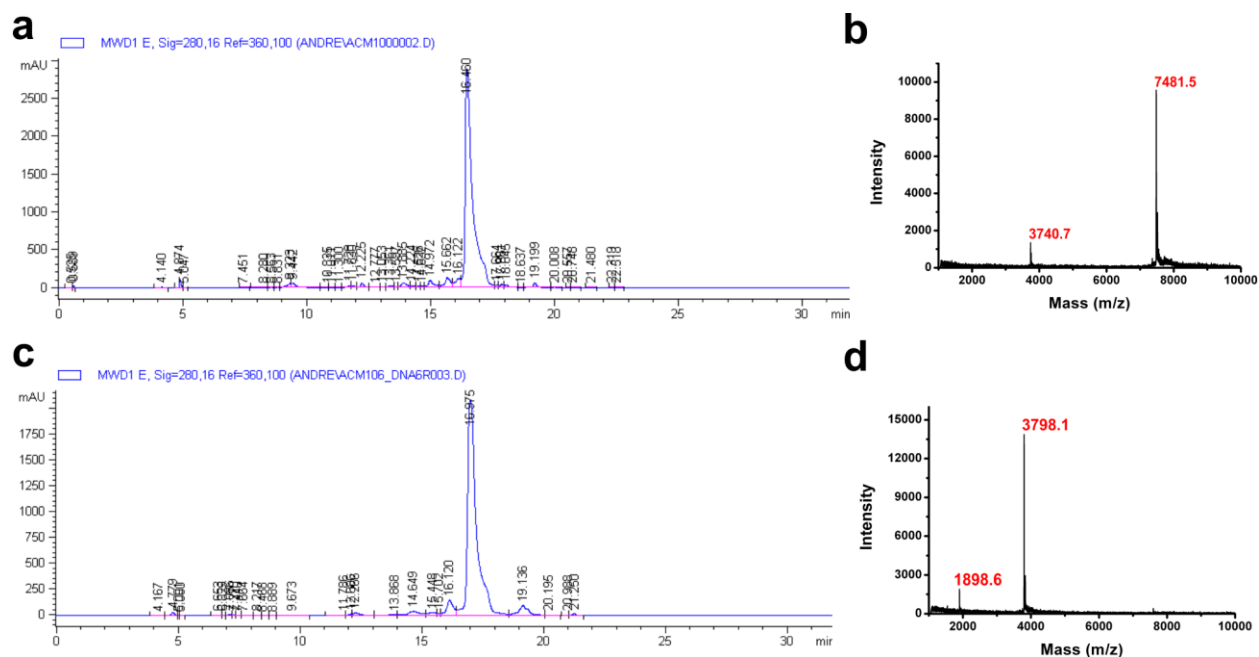


**Figure S5.70.** (a) Reverse-phase HPLC trace and (b) MALDI spectrum of  $PO_{18}C$ . (c) Reverse-phase HPLC trace and (d) MALDI spectrum of  $PO_6C$ . Note:  $m/1$  and  $m/2$  peaks were observed in the MALDI spectra.

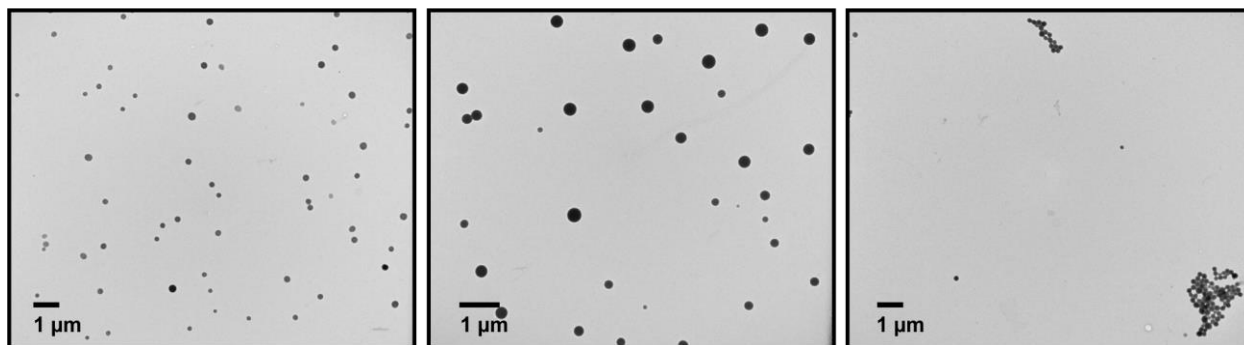


**Figure S5.71.** TEM images of 500 μM PO<sub>18</sub>C in 50 mM CaCl<sub>2</sub> after 15-20 hrs. Spherical assemblies were observed.

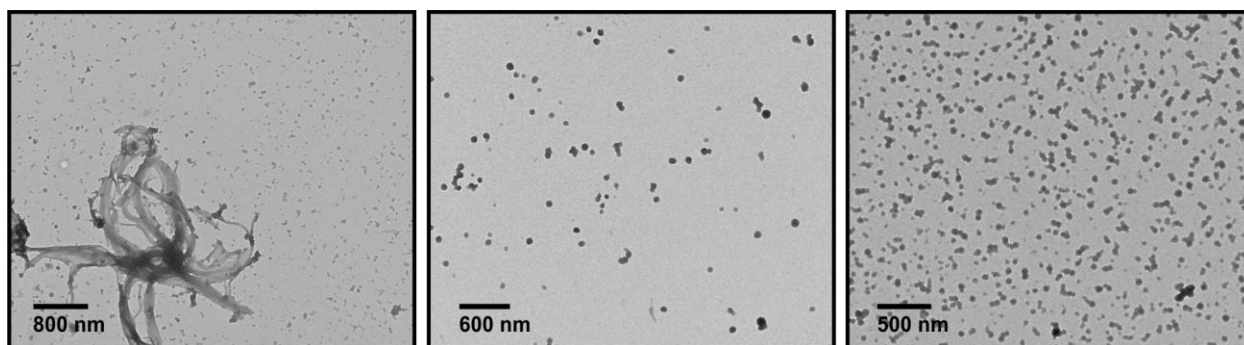


**Figure S5.72.** TEM images of 500 μM PO<sub>18</sub>C in 150 mM CaCl<sub>2</sub> after 15-20 hrs. Spherical/pseudo-spherical assemblies were the major products. Few fiber assemblies were also observed.

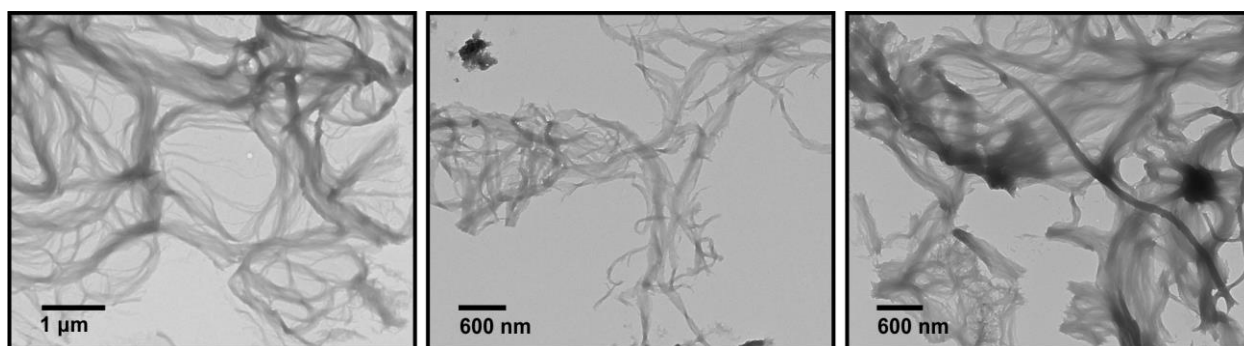


**Figure S5.73.** TEM images of 500 μM PO<sub>18</sub>C in 300 mM CaCl<sub>2</sub> after 15-20 hrs. Fibers were observed.

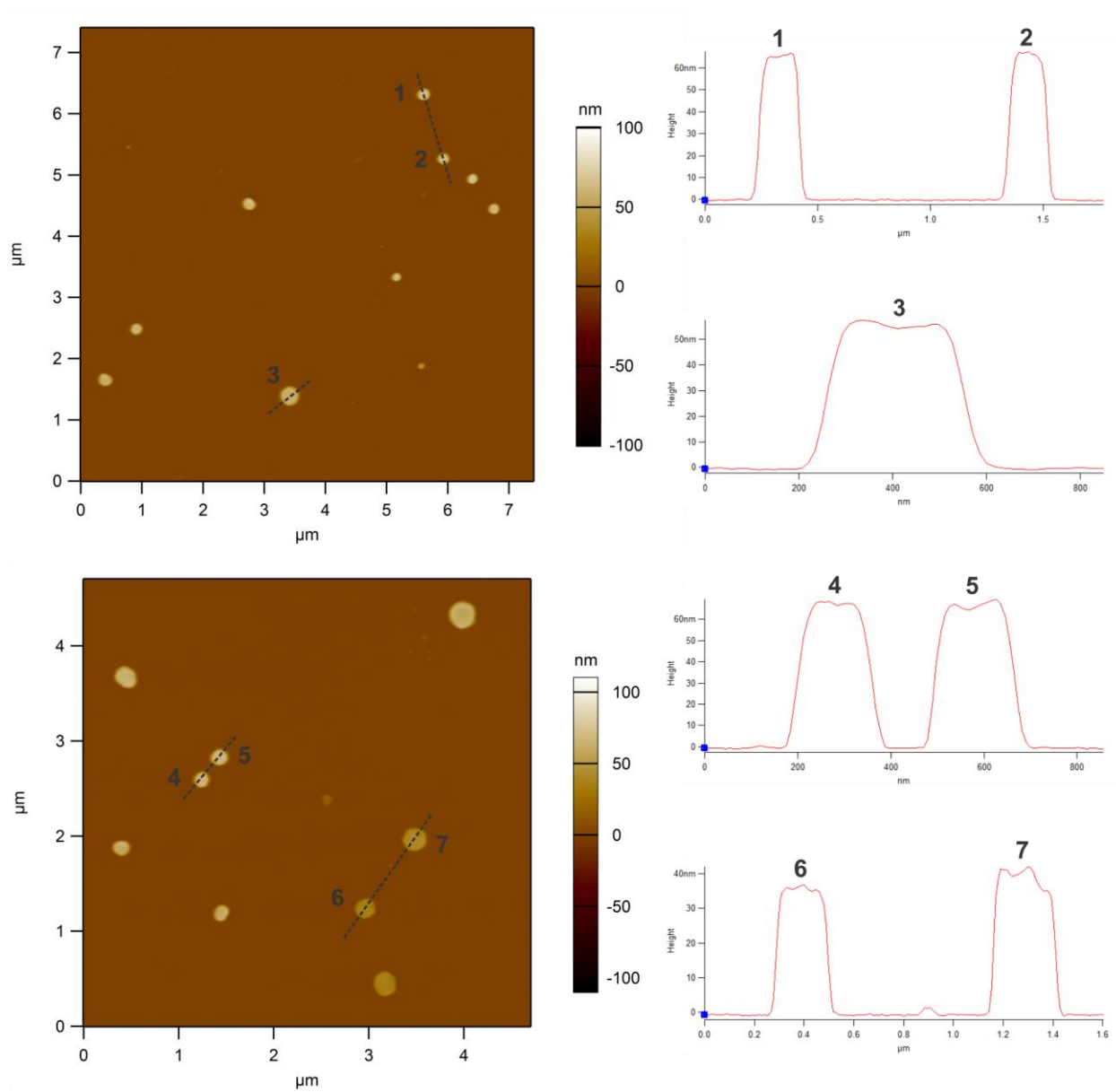


**Figure S5.74.** AFM images of  $\text{PO}_{18}\text{C}$  vesicles deposited on APTES-functionalized mica. The labeled vesicles and their corresponding height traces are shown. In general, larger vesicles appear to flatten more than smaller vesicles.

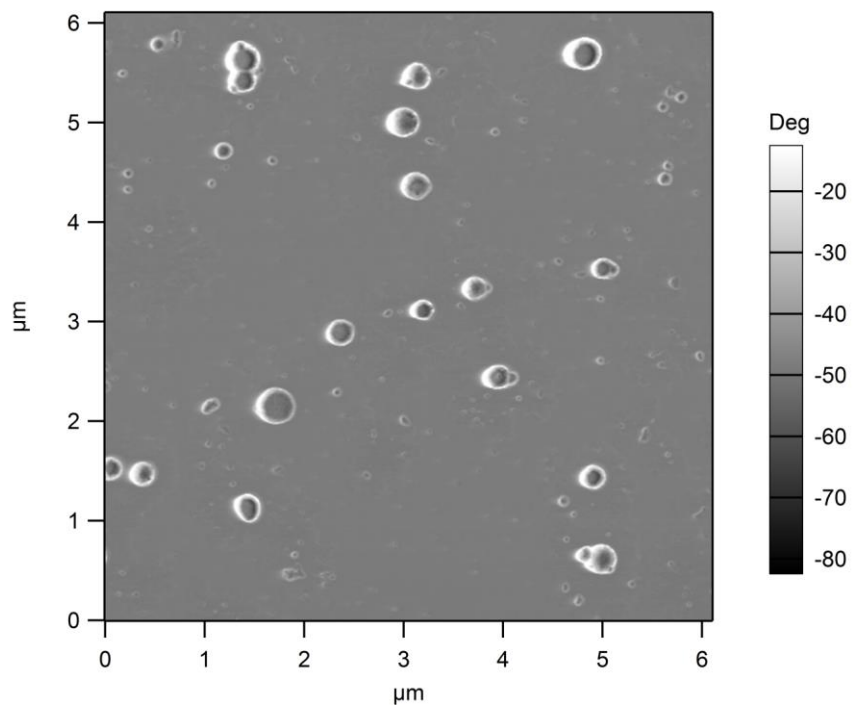


**Figure S5.75.** Phase image of PO<sub>18</sub>C vesicles revealing the different deformation response between the sphere edge and sphere center.

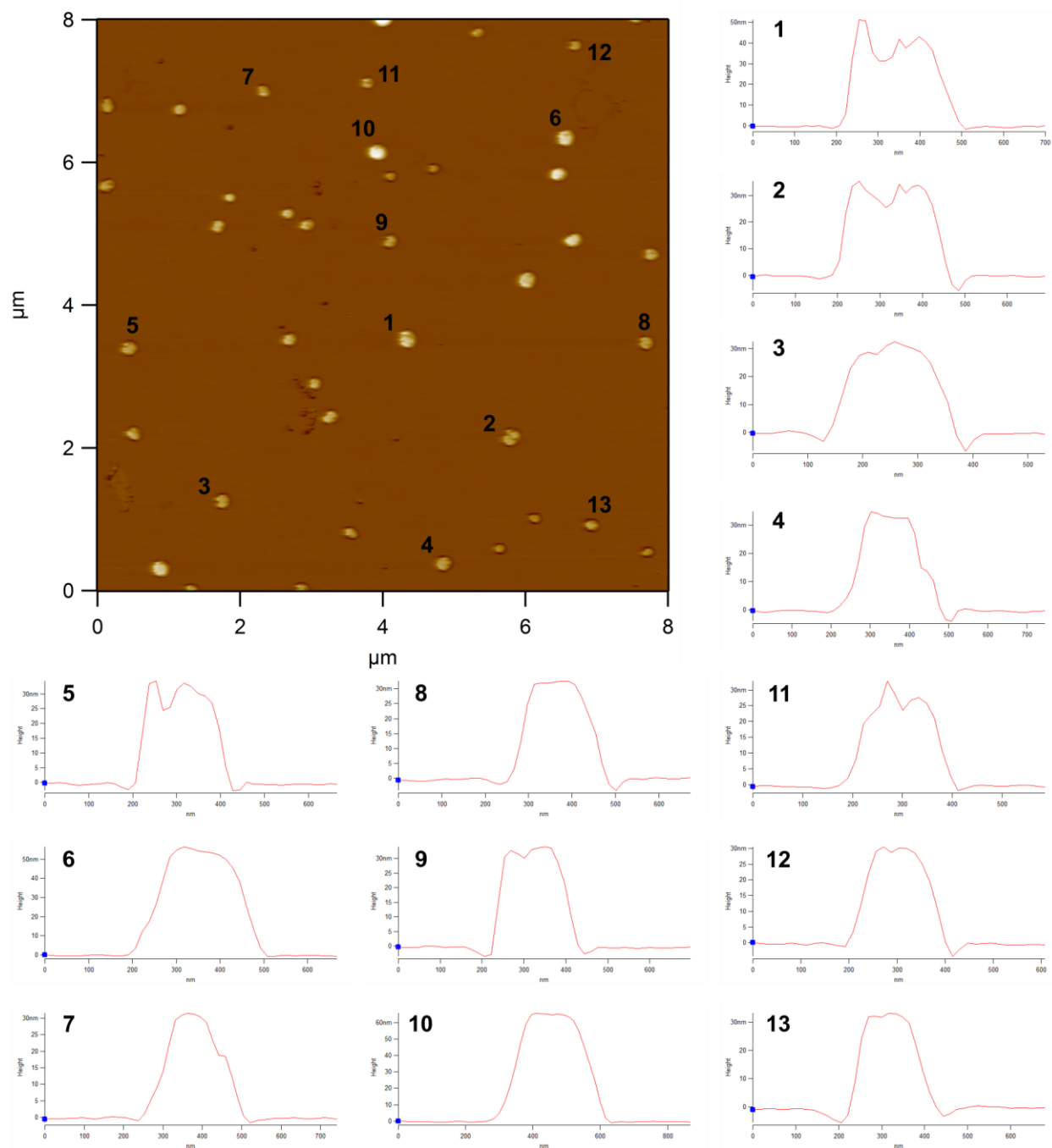
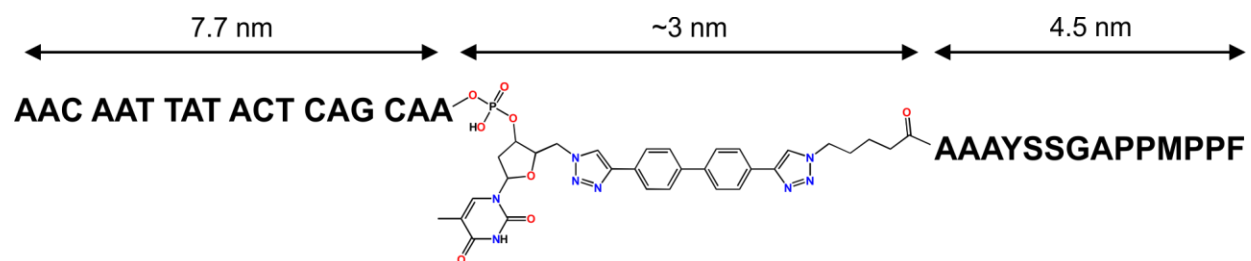


**Figure S5.76.** AFM image of vesicles on a TEM grid after exposure to the high-vacuum TEM environment. Labeled vesicles and their corresponding height traces reveal a height of approximately 30 nm. A majority of the vesicles appear to flatten completely, except for a few that retained more of its shape (*e.g.*, spheres 6 and 10).





**Extended PO<sub>18</sub>C length = ~15 nm**

**Figure S5.77.** PO<sub>18</sub>C length. The length of the extended 18mer oligonucleotide was reported to be 7.7 nm.<sup>170-171</sup>

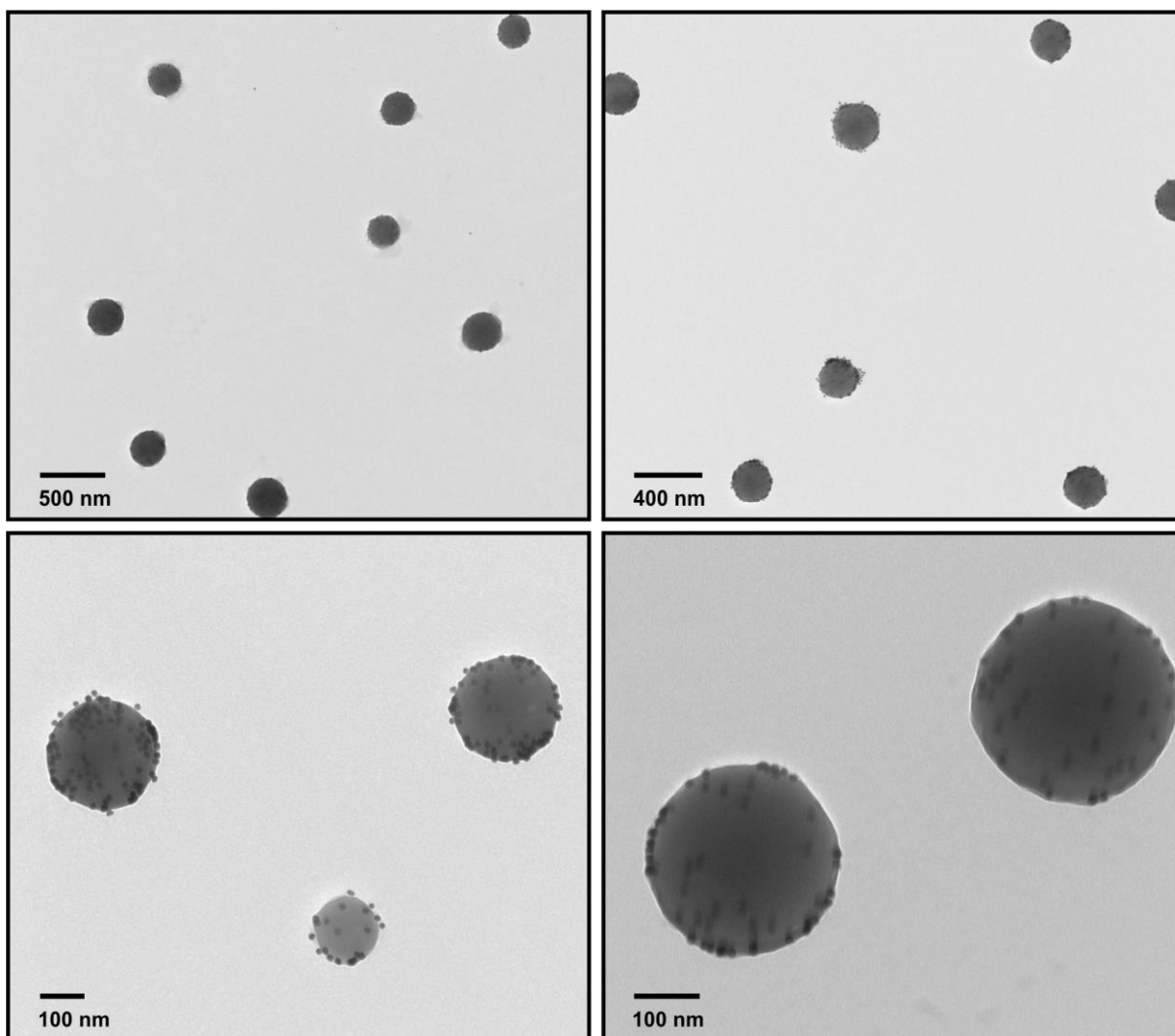


**Figure S5.78.** Additional TEM images of gold nanoparticle-decorated PO<sub>18</sub>C vesicles after 2 hrs of incubation.

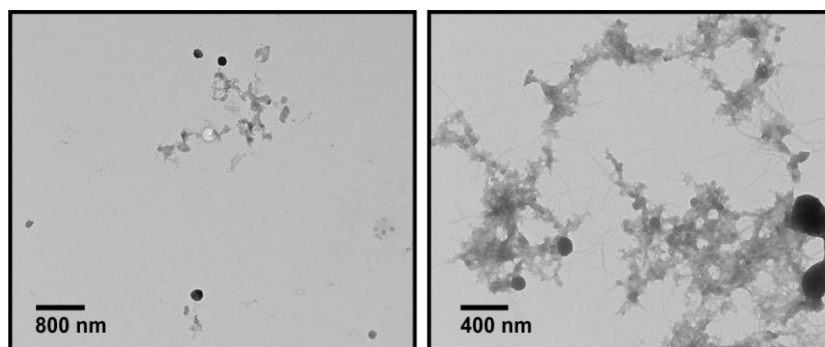


**Figure S5.79.** TEM image of 500  $\mu\text{M}$   $\text{PO}_6\text{C}$  in 10 mM  $\text{CaCl}_2$  after 15-20 hrs. Fibers, aggregates, and spherical assemblies were observed.

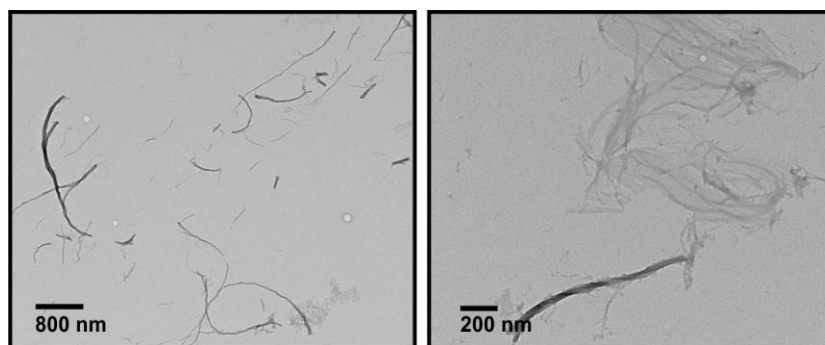


**Figure S5.80.** TEM image of 500  $\mu\text{M}$   $\text{PO}_6\text{C}$  in 50 mM  $\text{CaCl}_2$  after 15-20 hrs. Fibers were observed.

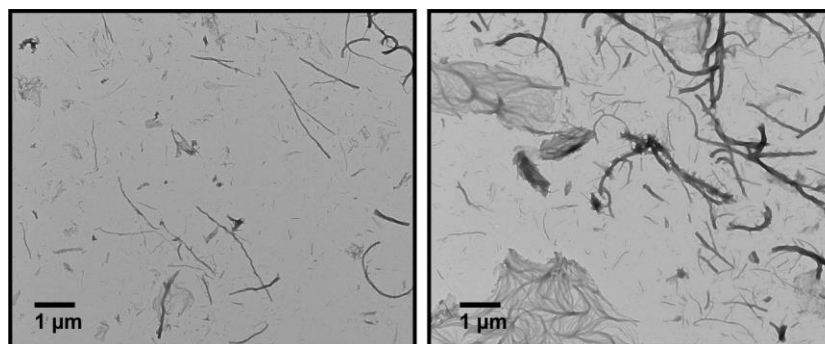


**Figure S5.81.** TEM image of 500  $\mu\text{M}$   $\text{PO}_6\text{C}$  in 150 mM  $\text{CaCl}_2$  after 15-20 hrs. Fibers and fiber networks were observed.

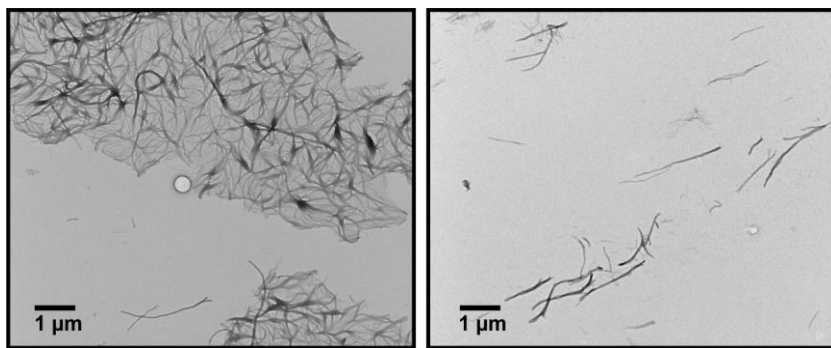


**Figure S5.82.** TEM image of 500  $\mu\text{M}$   $\text{PO}_6\text{C}$  in 300 mM  $\text{CaCl}_2$  after 15-20 hrs. Fibers and fiber networks were observed.

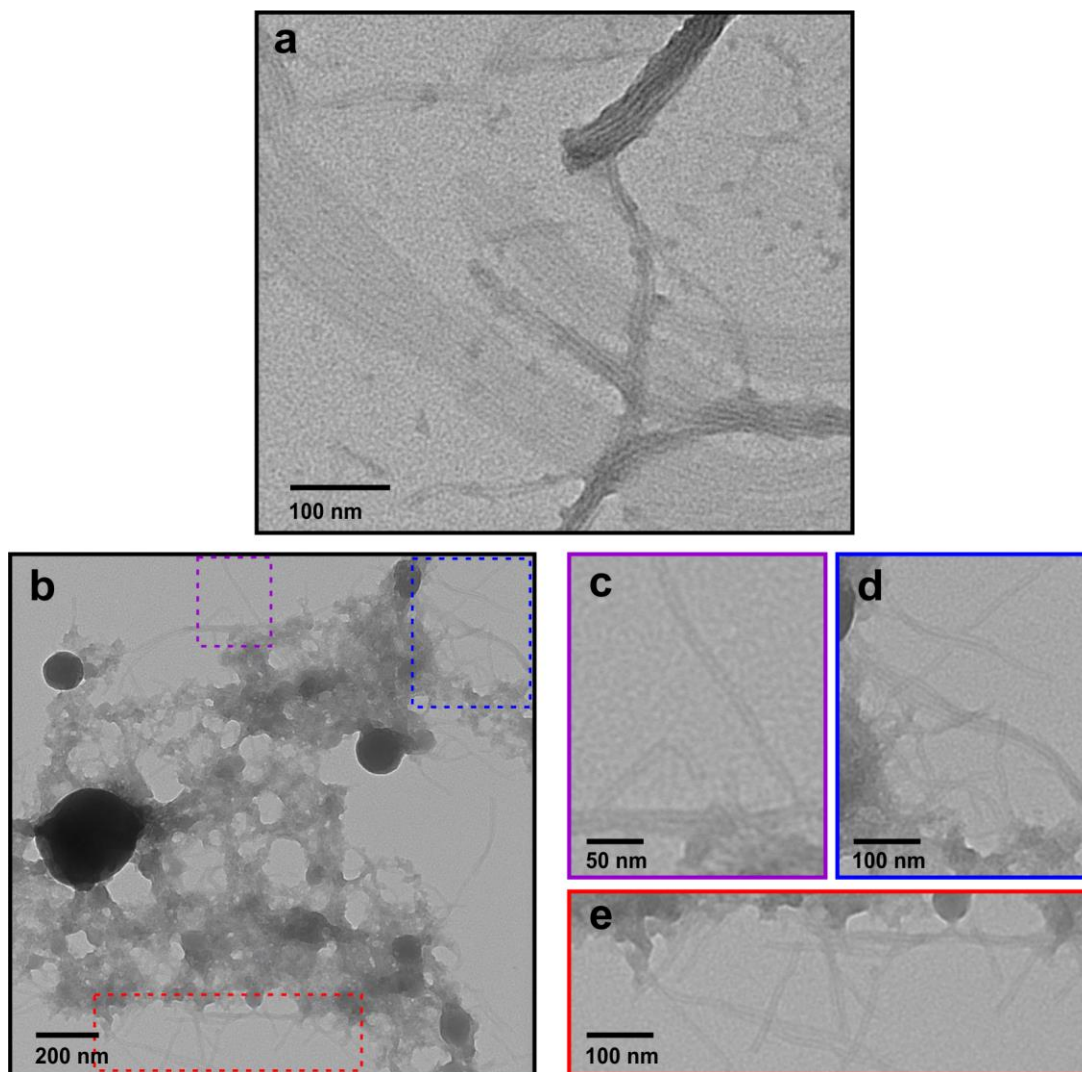


**Figure S5.83.** PO<sub>6</sub>C assemblies assembled in (a) 50 mM CaCl<sub>2</sub> and (b) 10 mM CaCl<sub>2</sub>. (c-e) Zoomed-in TEM images of the dashed boxes shown in b (the border colors correspond to the colors of the dashed boxes).

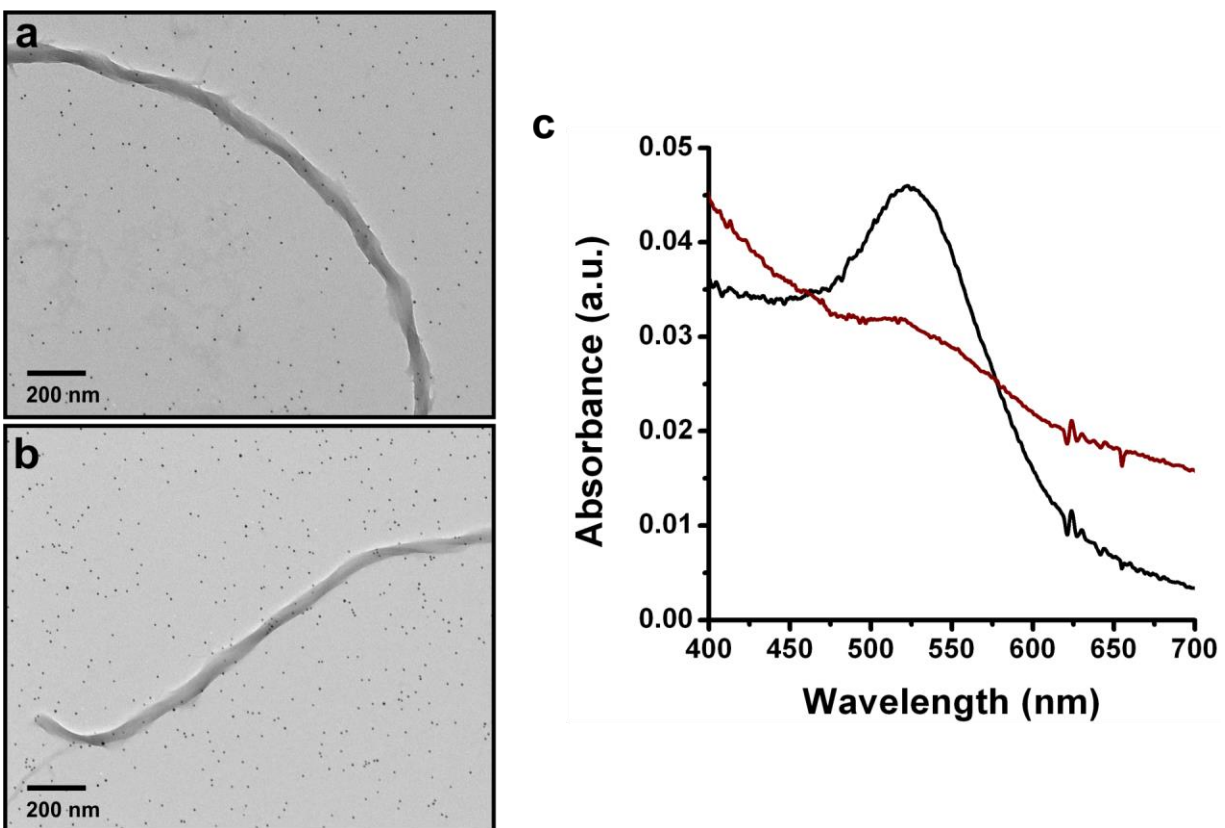


**Figure S5.84.** (a,b) TEM images 2 hrs. after addition of 5 nm gold nanoparticles (functionalized with complementary 6mer sequence) to a solution containing PO<sub>6</sub>C fibers in 50 mM CaCl<sub>2</sub>. (c) UV-Vis spectrum of free 5 nm gold nanoparticles functionalized with complementary 6mer sequence (black line) and 2 hrs. after addition to PO<sub>6</sub>C fibers (red line). The position of the LSPR band remains unchanged. The difference in signal intensity is due to different solution concentrations of gold nanoparticles.

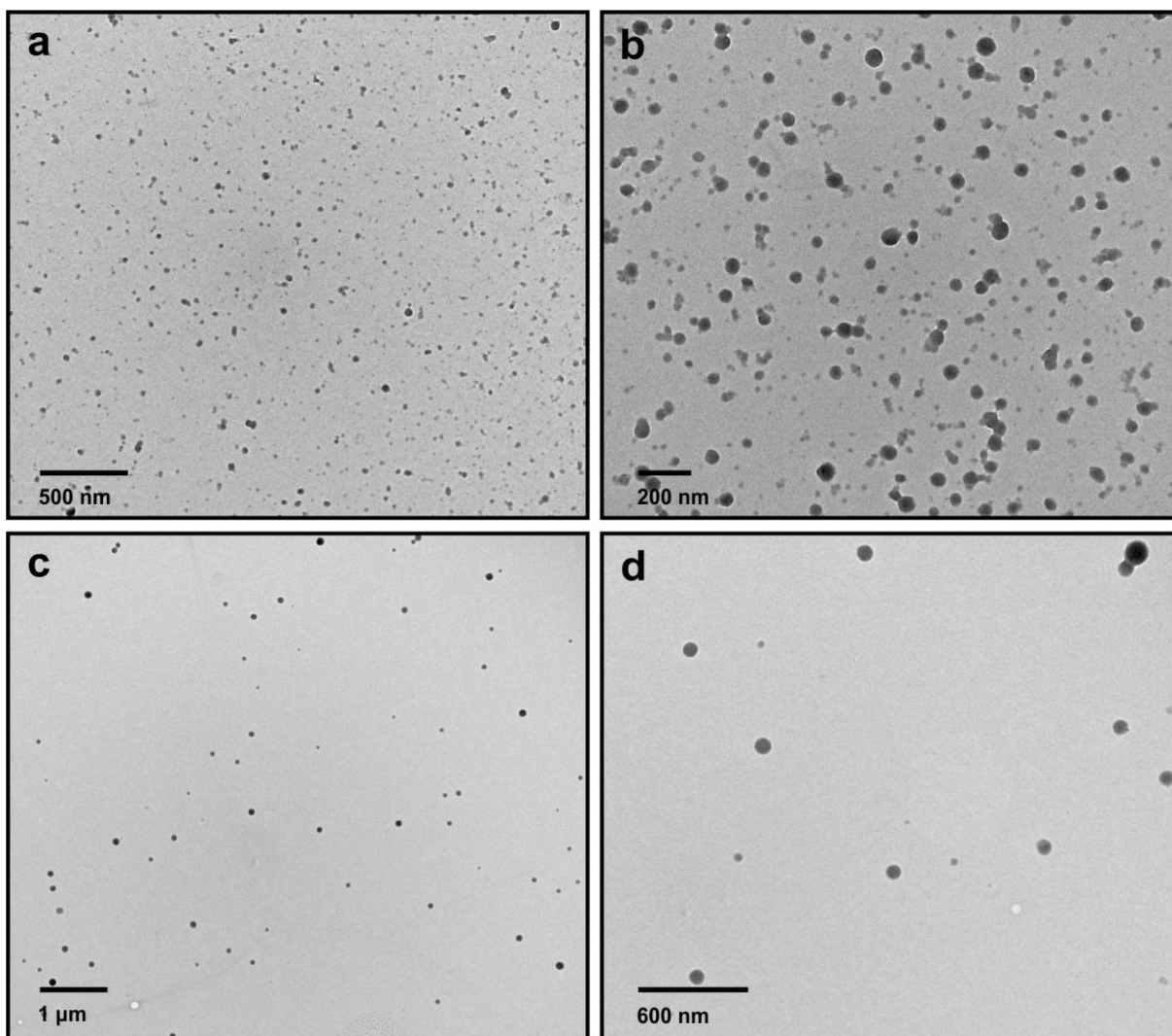


**Figure S5.85.** PO<sub>18</sub>C (500 μM) assembled in the (a,b) absence of complement and in the (c,d) presence of complement. Both experiments were conducted in 150 mM CaCl<sub>2</sub>.

## BIBLIOGRAPHY

1. Pieters, B. J. G. E.; van Eldijk, M. B.; Nolte, R. J. M.; Mecinovic, J. *Chemical Society Reviews* **2016**, *45* (1), 24-39.
2. Kelly, K. L.; Coronado, E.; Zhao, L. L.; Schatz, G. C. *The Journal of Physical Chemistry B* **2003**, *107* (3), 668-677.
3. Huang, X.; El-Sayed, M. A. *Journal of Advanced Research* **2010**, *1* (1), 13-28.
4. Lee, J.-S.; Han, M. S.; Mirkin, C. A. *Angewandte Chemie International Edition* **2007**, *46* (22), 4093-4096.
5. Lee, J.; Hernandez, P.; Lee, J.; Govorov, A. O.; Kotov, N. A. *Nat Mater* **2007**, *6* (4), 291-295.
6. Nath, N.; Chilkoti, A. *Analytical Chemistry* **2002**, *74* (3), 504-509.
7. Ko, H.; Singamaneni, S.; Tsukruk, V. V. *Small* **2008**, *4* (10), 1576-1599.
8. Song, J.; Zhou, J.; Duan, H. *Journal of the American Chemical Society* **2012**, *134* (32), 13458-13469.
9. Fan, M.; Brolo, A. G. *Physical Chemistry Chemical Physics* **2009**, *11* (34), 7381-7389.
10. Braun, G.; Pavel, I.; Morrill, A. R.; Seferos, D. S.; Bazan, G. C.; Reich, N. O.; Moskovits, M. *Journal of the American Chemical Society* **2007**, *129* (25), 7760-7761.
11. Song, C.; Wang, Y.; Rosi, N. L. *Angewandte Chemie International Edition* **2013**, *52* (14), 3993-3995.
12. Huang, P.; Lin, J.; Li, W.; Rong, P.; Wang, Z.; Wang, S.; Wang, X.; Sun, X.; Aronova, M.; Niu, G.; Leapman, R. D.; Nie, Z.; Chen, X. *Angewandte Chemie International Edition* **2013**, *52* (52), 13958-13964.
13. He, J.; Huang, X.; Li, Y.-C.; Liu, Y.; Babu, T.; Aronova, M. A.; Wang, S.; Lu, Z.; Chen, X.; Nie, Z. *Journal of the American Chemical Society* **2013**, *135* (21), 7974-7984.



14. Sonnichsen, C.; Reinhard, B. M.; Liphardt, J.; Alivisatos, A. P. *Nat Biotech* **2005**, *23* (6), 741-745.
15. Liu, G. L.; Yin, Y.; Kunchakarra, S.; Mukherjee, B.; Gerion, D.; Jett, S. D.; Bear, D. G.; Gray, J. W.; Alivisatos, A. P.; Lee, L. P.; Chen, F. F. *Nat Nano* **2006**, *1* (1), 47-52.
16. Kuzyk, A.; Schreiber, R.; Fan, Z.; Pardatscher, G.; Roller, E.-M.; Hogege, A.; Simmel, F. C.; Govorov, A. O.; Liedl, T. *Nature* **2012**, *483* (7389), 311-314.
17. Pendry, J. B. *Science* **2004**, *306* (5700), 1353-1355.
18. Shen, X. B.; Asenjo-Garcia, A.; Liu, Q.; Jiang, Q.; de Abajo, F. J. G.; Liu, N.; Ding, B. Q. *Nano Letters* **2013**, *13* (5), 2128-2133.
19. Shen, X.; Song, C.; Wang, J.; Shi, D.; Wang, Z.; Liu, N.; Ding, B. *Journal of the American Chemical Society* **2012**, *134* (1), 146-149.
20. Nykypanchuk, D.; Maye, M. M.; van der Lelie, D.; Gang, O. *Nature* **2008**, *451* (7178), 549-552.
21. Park, S. Y.; Lytton-Jean, A. K. R.; Lee, B.; Weigand, S.; Schatz, G. C.; Mirkin, C. A. *Nature* **2008**, *451* (7178), 553-556.
22. Macfarlane, R. J.; Lee, B.; Jones, M. R.; Harris, N.; Schatz, G. C.; Mirkin, C. A. *Science* **2011**, *334* (6053), 204-208.
23. Xing, H.; Wang, Z.; Xu, Z.; Wong, N. Y.; Xiang, Y.; Liu, G. L.; Lu, Y. *ACS Nano* **2012**, *6* (1), 802-809.
24. Sharma, J.; Chhabra, R.; Cheng, A.; Brownell, J.; Liu, Y.; Yan, H. *Science* **2009**, *323* (5910), 112-116.
25. Chen, C.-L.; Zhang, P.; Rosi, N. L. *Journal of the American Chemical Society* **2008**, *130* (41), 13555-13557.
26. Yu, L.; Banerjee, I. A.; Matsui, H. *Journal of the American Chemical Society* **2003**, *125* (48), 14837-14840.
27. Banerjee, I. A.; Yu, L.; Matsui, H. *Proceedings of the National Academy of Sciences* **2003**, *100* (25), 14678-14682.
28. Fu, X.; Wang, Y.; Huang, L.; Sha, Y.; Gui, L.; Lai, L.; Tang, Y. *Advanced Materials* **2003**, *15* (11), 902-906.
29. Tao, K.; Wang, J.; Li, Y.; Xia, D.; Shan, H.; Xu, H.; Lu, J. R. *Scientific Reports* **2013**, *3*, 2565.

30. Li, L.-s.; Stupp, S. I. *Angewandte Chemie International Edition* **2005**, *44* (12), 1833-1836.
31. McMillan, R. A.; Paavola, C. D.; Howard, J.; Chan, S. L.; Zaluzec, N. J.; Trent, J. D. *Nature Materials* **2002**, *1* (4), 247-252.
32. Gurunatha, K. L.; Fournier, A. C.; Urvoas, A.; Valerio-Lepiniec, M.; Marchi, V.; Minard, P.; Dujardin, E. *ACS Nano* **2016**, *10* (3), 3176-3185.
33. Lee, J.; Bhak, G.; Lee, J.-H.; Park, W.; Lee, M.; Lee, D.; Jeon, N. L.; Jeong, D. H.; Char, K.; Paik, S. R. *Angewandte Chemie International Edition* **2015**, *54* (15), 4571-4576.
34. Caswell, K. K.; Wilson, J. N.; Bunz, U. H. F.; Murphy, C. J. *Journal of the American Chemical Society* **2003**, *125* (46), 13914-13915.
35. Bromley, K. M.; Patil, A. J.; Perriman, A. W.; Stubbs, G.; Mann, S. *Journal of Materials Chemistry* **2008**, *18* (40), 4796-4801.
36. Dujardin, E.; Peet, C.; Stubbs, G.; Culver, J. N.; Mann, S. *Nano Letters* **2003**, *3* (3), 413-417.
37. Blum, A. S.; Soto, C. M.; Wilson, C. D.; Brower, T. L.; Pollack, S. K.; Schull, T. L.; Chatterji, A.; Lin, T.; Johnson, J. E.; Amsinck, C.; Franzon, P.; Shashidhar, R.; Ratna, B. R. *Small* **2005**, *1* (7), 702-706.
38. Ni, R.; Childers, W. S.; Hardcastle, K. I.; Mehta, A. K.; Lynn, D. G. *Angewandte Chemie International Edition* **2012**, *51* (27), 6635-6638.
39. Rechess, M.; Gazit, E. *Science* **2003**, *300* (5619), 625-627.
40. Fishwick, C. W. G.; Beevers, A. J.; Carrick, L. M.; Whitehouse, C. D.; Aggeli, A.; Boden, N. *Nano Letters* **2003**, *3* (11), 1475-1479.
41. Marini, D. M.; Hwang, W.; Lauffenburger, D. A.; Zhang, S.; Kamm, R. D. *Nano Letters* **2002**, *2* (4), 295-299.
42. Trent, A.; Marullo, R.; Lin, B.; Black, M.; Tirrell, M. *Soft Matter* **2011**, *7* (20), 9572-9582.
43. Liang, J.; Wu, W.-L.; Xu, X.-D.; Zhuo, R.-X.; Zhang, X.-Z. *Colloids and Surfaces B: Biointerfaces* **2014**, *114*, 398-403.
44. Jiao, D.; Geng, J.; Loh, X. J.; Das, D.; Lee, T.-C.; Scherman, O. A. *Angewandte Chemie International Edition* **2012**, *51* (38), 9633-9637.

45. Magnotti, E. L.; Hughes, S. A.; Dillard, R. S.; Wang, S.; Hough, L.; Karumbamkandathil, A.; Lian, T.; Wall, J. S.; Zuo, X.; Wright, E. R.; Conticello, V. P. *Journal of the American Chemical Society* **2016**, *138* (50), 16274-16282.
46. Dai, B.; Li, D.; Xi, W.; Luo, F.; Zhang, X.; Zou, M.; Cao, M.; Hu, J.; Wang, W.; Wei, G.; Zhang, Y.; Liu, C. *Proceedings of the National Academy of Sciences* **2015**, *112* (10), 2996-3001.
47. Hamley, I. W.; Dehsorkhi, A.; Castelletto, V. *Chemical Communications* **2013**, *49* (18), 1850-1852.
48. Cui, H.; Cheetham, A. G.; Pashuck, E. T.; Stupp, S. I. *Journal of the American Chemical Society* **2014**, *136* (35), 12461-12468.
49. Zhang, Z.; Zhu, W.; Kodadek, T. *Nature Biotechnology* **2000**, *18* (1), 71-74.
50. Heckmann, D.; Kessler, H., Design and Chemical Synthesis of Integrin Ligands. In *Methods in Enzymology*, Academic Press: 2007; Vol. Volume 426, pp 463-503.
51. Vivès, E.; Schmidt, J.; Pèlegri, A. *Biochimica et Biophysica Acta (BBA) - Reviews on Cancer* **2008**, *1786* (2), 126-138.
52. Cui, Y.; Kim, S. N.; Jones, S. E.; Wissler, L. L.; Naik, R. R.; McAlpine, M. C. *Nano Letters* **2010**, *10* (11), 4559-4565.
53. So, C. R.; Hayamizu, Y.; Yazici, H.; Gresswell, C.; Khatayevich, D.; Tamerler, C.; Sarikaya, M. *ACS Nano* **2012**, *6* (2), 1648-1656.
54. Whaley, S. R.; English, D. S.; Hu, E. L.; Barbara, P. F.; Belcher, A. M. *Nature* **2000**, *405* (6787), 665-668.
55. Slocik, J. M.; Stone, M. O.; Naik, R. R. *Small* **2005**, *1* (11), 1048-1052.
56. Chiu, C.-Y.; Li, Y.; Ruan, L.; Ye, X.; Murray, C. B.; Huang, Y. *Nature Chemistry* **2011**, *3* (5), 393-399.
57. Chen, C.-L.; Rosi, N. L. *Angewandte Chemie International Edition* **2010**, *49* (11), 1924-1942.
58. Hwang, L.; Chen, C.-L.; Rosi, N. L. *Chemical Communications* **2011**, *47* (1), 185-187.
59. Hwang, L.; Zhao, G.; Zhang, P.; Rosi, N. L. *Small* **2011**, *7* (14), 1939-1942.
60. Song, C.; Zhao, G.; Zhang, P.; Rosi, N. L. *Journal of the American Chemical Society* **2010**, *132* (40), 14033-14035.

61. Song, C.; Blaber, M. G.; Zhao, G.; Zhang, P.; Fry, H. C.; Schatz, G. C.; Rosi, N. L. *Nano Letters* **2013**, *13* (7), 3256-3261.
62. Merg, A. D.; Slocik, J.; Blaber, M. G.; Schatz, G. C.; Naik, R.; Rosi, N. L. *Langmuir* **2015**, *31* (34), 9492-9501.
63. Merg, A. D.; Boatz, J. C.; Mandal, A.; Zhao, G.; Mokashi-Punekar, S.; Liu, C.; Wang, X.; Zhang, P.; van der Wel, P. C. A.; Rosi, N. L. *Journal of the American Chemical Society* **2016**, *138* (41), 13655-13663.
64. Zhang, C.; Zhou, Y.; Merg, A.; Song, C.; Schatz, G. C.; Rosi, N. L. *Nanoscale* **2014**, *6*, 12328-12332.
65. Zhang, C.; Song, C.; Fry, H. C.; Rosi, N. L. *Chemistry – A European Journal* **2014**, *20* (4), 941-945.
66. Tang, L.; Li, S.; Xu, L.; Ma, W.; Kuang, H.; Wang, L.; Xu, C. *ACS Applied Materials & Interfaces* **2015**.
67. Zhu, Y.; Xu, L.; Ma, W.; Xu, Z.; Kuang, H.; Wang, L.; Xu, C. *Chemical Communications* **2012**, *48* (97), 11889-11891.
68. Wu, X.; Xu, L.; Liu, L.; Ma, W.; Yin, H.; Kuang, H.; Wang, L.; Xu, C.; Kotov, N. A. *Journal of the American Chemical Society* **2013**, *135* (49), 18629-18636.
69. Zhao, Y.; Belkin, M. A.; Alù, A. *Nature Communications* **2012**, *3*, 870.
70. Gansel, J. K.; Thiel, M.; Rill, M. S.; Decker, M.; Bade, K.; Saile, V.; von Freymann, G.; Linden, S.; Wegener, M. *Science* **2009**, *325* (5947), 1513-1515.
71. Xu, L. G.; Ma, W.; Wang, L. B.; Xu, C. L.; Kuang, H.; Kotov, N. A. *Chemical Society Reviews* **2013**, *42* (7), 3114-3126.
72. Pileni, M. P. *The Journal of Physical Chemistry B* **2001**, *105* (17), 3358-3371.
73. Klinkova, A.; Choueiri, R. M.; Kumacheva, E. *Chemical Society Reviews* **2014**, *43* (11), 3976-3991.
74. Huil, L. J.; Pinna, N.; Char, K.; Pyun, J. *Progress in Polymer Science* **2015**, *40*, 85-120.
75. Grzelczak, M.; Vermant, J.; Furst, E. M.; Liz-Marzan, L. M. *ACS Nano* **2010**, *4* (7), 3591-3605.
76. Moyer, T. J.; Cui, H.; Stupp, S. I. *The Journal of Physical Chemistry B* **2013**, *117* (16), 4604-4610.

77. Fitzpatrick, A. W. P.; Debelouchina, G. T.; Bayro, M. J.; Clare, D. K.; Caporini, M. A.; Bajaj, V. S.; Jaroniec, C. P.; Wang, L.; Ladizhansky, V.; Müller, S. A.; MacPhee, C. E.; Waudby, C. A.; Mott, H. R.; De Simone, A.; Knowles, T. P. J.; Saibil, H. R.; Vendruscolo, M.; Orlova, E. V.; Griffin, R. G.; Dobson, C. M. *Proceedings of the National Academy of Sciences* **2013**, *110* (14), 5468-5473.
78. Li, L.-s.; Jiang, H.; Messmore, B. W.; Bull, S. R.; Stupp, S. I. *Angewandte Chemie International Edition* **2007**, *46* (31), 5873-5876.
79. Fan, Z.; Govorov, A. O. *The Journal of Physical Chemistry C* **2011**, *115* (27), 13254-13261.
80. Rostovtsev, V. V.; Green, L. G.; Fokin, V. V.; Sharpless, K. B. *Angewandte Chemie International Edition* **2002**, *41* (14), 2596-2599.
81. Huisgen, R. *Angewandte Chemie-International Edition* **1963**, *75* (13), 604.
82. Stendahl, J. C.; Rao, M. S.; Guler, M. O.; Stupp, S. I. *Advanced Functional Materials* **2006**, *16* (4), 499-508.
83. Jiang, H.; Guler, M. O.; Stupp, S. I. *Soft Matter* **2007**, *3* (4), 454-462.
84. Nakano, K.; Sato, T.; Tazaki, M.; Takagi, M. *Langmuir* **2000**, *16* (5), 2225-2229.
85. Snyder, R. G.; Strauss, H. L.; Elliger, C. A. *The Journal of Physical Chemistry* **1982**, *86* (26), 5145-5150.
86. Habib, A.; Tabata, M.; Wu, Y. G. *Bulletin of the Chemical Society of Japan* **2005**, *78* (2), 262-269.
87. Govorov, A. O.; Gun'ko, Y. K.; Slocik, J. M.; Gerard, V. A.; Fan, Z. Y.; Naik, R. R. *Journal of Materials Chemistry* **2011**, *21* (42), 16806-16818.
88. Fan, Z.; Govorov, A. O. *Nano Letters* **2010**, *10* (7), 2580-2587.
89. Perumal, S.; Hofmann, A.; Scholz, N.; Rühl, E.; Graf, C. *Langmuir* **2011**, *27* (8), 4456-4464.
90. Zopes, D.; Stein, B.; Mathur, S.; Graf, C. *Langmuir* **2013**, *29* (36), 11217-11226.
91. Bedford, N. M.; Bhandari, R.; Slocik, J. M.; Seifert, S.; Naik, R. R.; Knecht, M. R. *Chemistry of Materials* **2014**, *26* (14), 4082-4091.
92. Tang, W.; Policastro, G. M.; Hua, G.; Guo, K.; Zhou, J.; Wesdemiotis, C.; Doll, G. L.; Becker, M. L. *Journal of the American Chemical Society* **2014**, *136* (46), 16357-16367.

93. Tamerler, C.; Oren, E. E.; Duman, M.; Venkatasubramanian, E.; Sarikaya, M. *Langmuir* **2006**, *22* (18), 7712-7718.
94. Heinz, H.; Farmer, B. L.; Pandey, R. B.; Slocik, J. M.; Patnaik, S. S.; Pachter, R.; Naik, R. R. *Journal of the American Chemical Society* **2009**, *131* (28), 9704-9714.
95. Pandey, R. B.; Heinz, H.; Feng, J.; Farmer, B. L.; Slocik, J. M.; Drummy, L. F.; Naik, R. R. *Physical Chemistry Chemical Physics* **2009**, *11* (12), 1989-2001.
96. Bedford, N. M.; Hughes, Z. E.; Tang, Z.; Li, Y.; Briggs, B. D.; Ren, Y.; Swihart, M. T.; Petkov, V. G.; Naik, R. R.; Knecht, M. R.; Walsh, T. R. *Journal of the American Chemical Society* **2016**, *138* (2), 540-548.
97. Diamanti, S.; Elsen, A.; Naik, R.; Vaia, R. *The Journal of Physical Chemistry C* **2009**, *113* (23), 9993-9997.
98. Slocik, J. M.; Govorov, A. O.; Naik, R. R. *Nano Letters* **2011**, *11* (2), 701-705.
99. Wu, X.; Xu, L.; Ma, W.; Liu, L.; Kuang, H.; Kotov, N. A.; Xu, C. *Advanced Materials* **2016**, *28*, 5907-5915.
100. Yan, W.; Xu, L.; Xu, C.; Ma, W.; Kuang, H.; Wang, L.; Kotov, N. A. *Journal of the American Chemical Society* **2012**, *134* (36), 15114-15121.
101. Guerrero-Martínez, A.; Auguie, B.; Alonso-Gómez, J. L.; Džolić, Z.; Gómez-Graña, S.; Žinić, M.; Cid, M. M.; Liz-Marzán, L. M. *Angewandte Chemie International Edition* **2011**, *50* (24), 5499-5503.
102. Yeom, B.; Zhang, H.; Zhang, H.; Park, J. I.; Kim, K.; Govorov, A. O.; Kotov, N. A. *Nano Letters* **2013**, *13* (11), 5277-5283.
103. Pashuck, E. T.; Stupp, S. I. *Journal of the American Chemical Society* **2010**, *132* (26), 8819-8821.
104. Cui, H.; Muraoka, T.; Cheetham, A. G.; Stupp, S. I. *Nano Letters* **2009**, *9* (3), 945-951.
105. Deng, M.; Yu, D.; Hou, Y.; Wang, Y. *The Journal of Physical Chemistry B* **2009**, *113* (25), 8539-8544.
106. Uesaka, A.; Ueda, M.; Makino, A.; Imai, T.; Sugiyama, J.; Kimura, S. *Langmuir* **2014**, *30* (4), 1022-1028.
107. Hamley, I. W.; Dehsorkhi, A.; Castelletto, V.; Furzeland, S.; Atkins, D.; Seitsonen, J.; Ruokolainen, J. *Soft Matter* **2013**, *9* (39), 9290-9293.

108. Yang, M.; Wang, W.; Yuan, F.; Zhang, X.; Li, J.; Liang, F.; He, B.; Minch, B.; Wegner, G. *Journal of the American Chemical Society* **2005**, *127* (43), 15107-15111.
109. Albert, S. K.; Thelu, H. V. P.; Golla, M.; Krishnan, N.; Chaudhary, S.; Varghese, R. *Angewandte Chemie International Edition* **2014**, *53* (32), 8352-8357.
110. Barth, A. *Biochimica et Biophysica Acta (BBA) - Bioenergetics* **2007**, *1767* (9), 1073-1101.
111. Pelton, J. T.; McLean, L. R. *Analytical Biochemistry* **2000**, *277* (2), 167-176.
112. Paramonov, S. E.; Jun, H.-W.; Hartgerink, J. D. *Journal of the American Chemical Society* **2006**, *128* (22), 7291-7298.
113. Zanna, N.; Milli, L.; Del Secco, B.; Tomasini, C. *Organic Letters* **2016**, *18* (7), 1662-1665.
114. Lin, Y.-J.; Chu, L.-K.; Horng, J.-C. *The Journal of Physical Chemistry B* **2015**, *119* (52), 15796-15806.
115. Serpell, L. C. *Biochimica et Biophysica Acta (BBA) - Molecular Basis of Disease* **2000**, *1502* (1), 16-30.
116. Sunde, M.; Serpell, L. C.; Bartlam, M.; Fraser, P. E.; Pepys, M. B.; Blake, C. C. F. *Journal of Molecular Biology* **1997**, *273* (3), 729-739.
117. Geddes, A. J.; Parker, K. D.; Atkins, E. D. T.; Beighton, E. *Journal of Molecular Biology* **1968**, *32* (2), 343-358.
118. Sivanandam, V. N.; Jayaraman, M.; Hoop, C. L.; Kodali, R.; Wetzel, R.; van der Wel, P. C. A. *Journal of the American Chemical Society* **2011**, *133* (12), 4558-4566.
119. Hoop, C. L.; Lin, H.-K.; Kar, K.; Hou, Z.; Poirier, M. A.; Wetzel, R.; van der Wel, P. C. A. *Biochemistry* **2014**, *53* (42), 6653-6666.
120. Sawaya, M. R.; Sambashivan, S.; Nelson, R.; Ivanova, M. I.; Sievers, S. A.; Apostol, M. I.; Thompson, M. J.; Balbirnie, M.; Wiltzius, J. J. W.; McFarlane, H. T.; Madsen, A. O.; Riekel, C.; Eisenberg, D. *Nature* **2007**, *447* (7143), 453-457.
121. Nielsen, J. T.; Bjerring, M.; Jeppesen, M. D.; Pedersen, R. O.; Pedersen, J. M.; Hein, K. L.; Vosegaard, T.; Skrydstrup, T.; Otzen, D. E.; Nielsen, N. C. *Angewandte Chemie International Edition* **2009**, *48* (12), 2118-2121.
122. Aggeli, A.; Nyrkova, I. A.; Bell, M.; Harding, R.; Carrick, L.; McLeish, T. C. B.; Semenov, A. N.; Boden, N. *Proceedings of the National Academy of Sciences* **2001**, *98* (21), 11857-11862.

123. Kremer, J. R.; Mastronarde, D. N.; McIntosh, J. R. *Journal of Structural Biology* **1996**, *116* (1), 71-76.
124. Pettersen, E. F.; Goddard, T. D.; Huang, C. C.; Couch, G. S.; Greenblatt, D. M.; Meng, E. C.; Ferrin, T. E. *Journal of Computational Chemistry* **2004**, *25* (13), 1605-1612.
125. Delaglio, F.; Grzesiek, S.; Vuister, G. W.; Zhu, G.; Pfeifer, J.; Bax, A. *Journal of Biomolecular NMR* **1995**, *6* (3), 277-293.
126. Vranken, W. F.; Boucher, W.; Stevens, T. J.; Fogh, R. H.; Pajon, A.; Llinas, M.; Ulrich, E. L.; Markley, J. L.; Ionides, J.; Laue, E. D. *Proteins: Structure, Function, and Bioinformatics* **2005**, *59* (4), 687-696.
127. Harris, R. K.; Becker, E. D.; De Menezes, S. M. C.; Granger, P.; Hoffman, R. E.; Zilm, K. W. *Magnetic Resonance in Chemistry* **2008**, *46* (6), 582-598.
128. Metz, G.; Wu, X. L.; Smith, S. O. *Journal of Magnetic Resonance, Series A* **1994**, *110* (2), 219-227.
129. Hoop, C. L.; Lin, H.-K.; Kar, K.; Magyarfalvi, G.; Lamley, J. M.; Boatz, J. C.; Mandal, A.; Lewandowski, J. R.; Wetzel, R.; van der Wel, P. C. A. *Proceedings of the National Academy of Sciences* **2016**, *113* (6), 1546-1551.
130. Boles, M. A.; Ling, D.; Hyeon, T.; Talapin, D. V. *Nature Materials* **2016**, *15* (2), 141-153.
131. Rosi, N. L.; Giljohann, D. A.; Thaxton, C. S.; Lytton-Jean, A. K. R.; Han, M. S.; Mirkin, C. A. *Science* **2006**, *312* (5776), 1027-1030.
132. Liu, Y.; Li, Y.; He, J.; Duelge, K. J.; Lu, Z.; Nie, Z. *Journal of the American Chemical Society* **2014**, *136* (6), 2602-2610.
133. He, J.; Liu, Y.; Babu, T.; Wei, Z.; Nie, Z. *Journal of the American Chemical Society* **2012**, *134* (28), 11342-11345.
134. Song, J.; Pu, L.; Zhou, J.; Duan, B.; Duan, H. *ACS Nano* **2013**, *7* (11), 9947-9960.
135. Shen, X.; Song, C.; Wang, J.; Shi, D.; Wang, Z.; Liu, N.; Ding, B. *Journal of the American Chemical Society* **2011**, *134* (1), 146-149.
136. Mastroianni, A. J.; Claridge, S. A.; Alivisatos, A. P. *Journal of the American Chemical Society* **2009**, *131* (24), 8455-8459.
137. Kalsin, A. M.; Fialkowski, M.; Paszewski, M.; Smoukov, S. K.; Bishop, K. J. M.; Grzybowski, B. A. *Science* **2006**, *312* (5772), 420-424.



138. Xie, J.; Lee, J. Y.; Wang, D. I. C. *Chemistry of Materials* **2007**, *19* (11), 2823-2830.
139. Zhang, C.; Brinzer, T.; Liu, C.; Garrett-Roe, S.; Rosi, N. L. *RSC Advances* **2015**, *5* (93), 76291-76295.
140. You, J.; Zhang, G.; Li, C. *ACS Nano* **2010**, *4* (2), 1033-1041.
141. Sanson, C.; Diou, O.; Thévenot, J.; Ibarboure, E.; Soum, A.; Brûlet, A.; Miraux, S.; Thiaudière, E.; Tan, S.; Brisson, A.; Dupuis, V.; Sandre, O.; Lecommandoux, S. *ACS Nano* **2011**, *5* (2), 1122-1140.
142. Mühligh, S.; Cunningham, A.; Scheeler, S.; Pacholski, C.; Bürgi, T.; Rockstuhl, C.; Lederer, F. *ACS Nano* **2011**, *5* (8), 6586-6592.
143. Sheikholeslami, S. N.; Alaeian, H.; Koh, A. L.; Dionne, J. A. *Nano Letters* **2013**, *13* (9), 4137-4141.
144. Qian, Z.; Hastings, S. P.; Li, C.; Edward, B.; McGinn, C. K.; Engheta, N.; Fakhraai, Z.; Park, S.-J. *ACS Nano* **2015**, *9* (2), 1263-1270.
145. Lomakin, A.; Chung, D. S.; Benedek, G. B.; Kirschner, D. A.; Teplow, D. B. *Proceedings of the National Academy of Sciences* **1996**, *93* (3), 1125-1129.
146. Hinterwirth, H.; Kappel, S.; Waitz, T.; Prohaska, T.; Lindner, W.; Lämmerhofer, M. *ACS Nano* **2013**, *7* (2), 1129-1136.
147. Rothmund, P. W. K. *Nature* **2006**, *440* (7082), 297-302.
148. Nangreave, J.; Han, D.; Liu, Y.; Yan, H. *Current Opinion in Chemical Biology* **2010**, *14* (5), 608-615.
149. Venkatesan, N.; Kim, B. H. *Chemical Reviews* **2006**, *106* (9), 3712-3761.
150. Tung, C.-H.; Stein, S. *Bioconjugate Chemistry* **2000**, *11* (5), 605-618.
151. Gour, N.; Kedracki, D.; Safir, I.; Ngo, K. X.; Vebert-Nardin, C. *Chemical Communications* **2012**, *48* (44), 5440-5442.
152. Abraham, J. N.; Gour, N.; Bolisetty, S.; Mezzenga, R.; Nardin, C. *European Polymer Journal* **2015**, *65*, 268-275.
153. Kye, M.; Lim, Y.-b. *Angewandte Chemie International Edition* **2016**, *55* (39), 12003-12007.

154. Lou, C.; Martos-Maldonado, M. C.; Madsen, C. S.; Thomsen, R. P.; Midtgaard, S. R.; Christensen, N. J.; Kjems, J.; Thulstrup, P. W.; Wengel, J.; Jensen, K. J. *Nature Communications* **2016**, *7*, 12294.
155. Gour, N.; Abraham, J. N.; Chami, M.; Castillo, A.; Verma, S.; Vebert-Nardin, C. *Chemical Communications* **2014**, *50* (52), 6863-6865.
156. Gogoi, K.; Mane, M. V.; Kunte, S. S.; Kumar, V. A. *Nucleic Acids Research* **2007**, *35* (21), e139-e139.
157. Thaner, R. V.; Eryazici, I.; Farha, O. K.; Mirkin, C. A.; Nguyen, S. T. *Chemical Science* **2014**, *5* (3), 1091-1096.
158. Seo, S. H.; Chang, J. Y.; Tew, G. N. *Angewandte Chemie International Edition* **2006**, *45* (45), 7526-7530.
159. Young, K. L.; Scott, A. W.; Hao, L.; Mirkin, S. E.; Liu, G.; Mirkin, C. A. *Nano Letters* **2012**, *12* (7), 3867-3871.
160. Barnaby, S. N.; Sita, T. L.; Petrosko, S. H.; Stegh, A. H.; Mirkin, C. A., Therapeutic Applications of Spherical Nucleic Acids. In *Nanotechnology-Based Precision Tools for the Detection and Treatment of Cancer*, Mirkin, C. A.; Meade, T. J.; Petrosko, S. H.; Stegh, A. H., Eds. Springer International Publishing: Cham, 2015; pp 23-50.
161. Banga, R. J.; Chernyak, N.; Narayan, S. P.; Nguyen, S. T.; Mirkin, C. A. *Journal of the American Chemical Society* **2014**, *136* (28), 9866-9869.
162. Zhang, C.; Hao, L.; Calabrese, C. M.; Zhou, Y.; Choi, C. H. J.; Xing, H.; Mirkin, C. A. *Small* **2015**, *11* (40), 5360-5368.
163. Cutler, J. I.; Auyeung, E.; Mirkin, C. A. *Journal of the American Chemical Society* **2012**, *134* (3), 1376-1391.
164. Miller, G. P.; Kool, E. T. *The Journal of Organic Chemistry* **2004**, *69* (7), 2404-2410.
165. Hurst, S. J.; Lytton-Jean, A. K. R.; Mirkin, C. A. *Analytical Chemistry* **2006**, *78* (24), 8313-8318.
166. Nelson, R.; Sawaya, M. R.; Balbirnie, M.; Madsen, A. O.; Riekel, C.; Grothe, R.; Eisenberg, D. *Nature* **2005**, *435* (7043), 773-778.
167. Soriaga, A. B.; Sangwan, S.; Macdonald, R.; Sawaya, M. R.; Eisenberg, D. *The Journal of Physical Chemistry B* **2015**.
168. Nesloney, C. L.; Kelly, J. W. *Bioorganic & Medicinal Chemistry* **1996**, *4* (6), 739-766.

169. Adzhubei, A. A.; Sternberg, M. J. E.; Makarov, A. A. *Journal of Molecular Biology* **2013**, *425* (12), 2100-2132.
170. Wang, L.; Feng, Y.; Sun, Y.; Li, Z.; Yang, Z.; He, Y.-M.; Fan, Q.-H.; Liu, D. *Soft Matter* **2011**, *7* (16), 7187-7190.
171. Tinland, B.; Pluen, A.; Sturm, J.; Weill, G. *Macromolecules* **1997**, *30* (19), 5763-5765.